CALIBRATING ABOVE AND BELOW SNOW LINE PRECIPITATION AS INPUTS TO MOUNTAIN HYDROLOGY MODELS

18 June 2015

Final report

from the British people

Calibrating above and below snow line precipitation as inputs to mountain hydrology models

FINAL REPORT 1SEPTEMBER 2012 – 30 JUNE 2015

Dr.W.W. Immerzeel (Utrecht University)

Prof. Dr. M.F.P. Bierkens (Utrecht University)

Dr. J. Shea (ICIMOD)

Dr. A.B. Shrestha (ICIMOD)

Dr. F. Pellicciotti (ETH Zurich)

Dr. G. Rasul (PMD)

Contents

PREFACE

DFID has granted the project "Calibrating above and below snow line precipitation as inputs to mountain hydrology models" to the consortium of Utrecht University, ETH Zurich, ICIMOD and PMD on 9 July 2012 and the contract was signed by DFID and Utrecht University by the end of August 2012. The project officially started on 1 September 2012 and ran until 30 June 2015.

This project contributes to this large knowledge gap by three main activities: literature review, field work and analysis of data and glacio-hydrological modelling. This final report summarizes the results that were achieved during the project, discusses the learnings and provides recommendations for further research.

EXECUTIVE SUMMARY

Importance of mountain precipitation

Mountains are the water towers of the world [*Viviroli et al.*, 2007], particularly for Asia, whose rivers all are fed from the High Asian Mountains such as the Hindu-Kush-Himalaya-Karokoram (HKH) range. In this area, referred to as the Third Pole together with the Tibetan Plateau [*Qiu*, 2008], snow and glacier melt are important hydrologic processes [*Immerzeel et al.*, 2010], and climate change is expected to affect melt characteristics and related runoff [*Lutz et al.*, 2014]. The Third Pole contributes the water resources to sustain the lives of nearly two billion people in Asia and provides the source of water for ten major river basins [*Immerzeel et al.*, 2010]. Water is a key resource in the region, as it sustains billions of people but also holds promise to transform the economics of some of the countries with its enormous potential for use for energy production. One of the most prominent uncertainties in Asian mountain hydrology is the spatial distribution of precipitation, which is crucial to understand the high altitude hydrology and this differential response in particular. The relation between precipitation and the Asian mountain ranges remains poorly defined due to the remoteness and the lack of reliable rainfall networks [*Bookhagen and Burbank*, 2006]. Over short horizontal distances precipitation can vary enormously due to orographic effects [*Higuchi et al.*, 1982] but precipitation gauge networks are virtually non-existing at high altitude and even if they exist they are mostly located in the valley bottoms and have difficulty in capturing snowfall. Snow accumulation measurements using snow pillows, snow courses, pits and cores from accumulation zones are also scarce and usually confined to short observation periods.

In many hydrological studies, simulation models are used and these models are forced by precipitation data observed at precipitation gauges located in valleys [*Singh and Bengtsson*, 2004; *Rees and Collins*, 2006; *Singh et al.*, 2006; *Immerzeel et al.*, 2012; *Ragettli et al.*, 2013]. Precipitation measurements are subject to large systematic errors that can amount up to 30% and even more in those cases when a significant part of precipitation falls in the form of snow and undercatch prevails [*Rubel and Hantel*, 1999; *Cheema and Bastiaanssen*, 2011]. In addition, valley stations in mountain regions are generally not representative of basin precipitation because of strong vertical precipitation lapse rates. Several regional studies show that this is particularly valid for the Karakoram.

Accurate information on precipitation distribution is crucial to glacio-hydrological modeling as outlined by [*Pellicciotti et al.*, 2012], but currently only a very limited number of stations measuring rain and snow at high altitude are available. There is a need to develop a long-term monitoring system for collecting high elevation (above snowline) and middle elevation (just below snowline) climate data in the HKH. Such short-term multi-season studies from a set of sites across the HKH range would help in calibrating precipitation inputs into mountain hydrological models.

Achievements

Observations of precipitation and temperature in the Langtang

The project contributed greatly to enhancing our understanding of high altitude precipitation patterns and the distinction between solid and liquid precipitation. The field work of the project focussed on the Langtang catchment in Nepal (Figure 1). In the Langtang catchment a network of high quality pluviometers, tipping buckets and temperature sensors were installed. The pluviometers are able to measure the total precipitation (rain and snow), the snow height and the temperature, while the cheaper tipping buckets allow accurate measurements of rain only and they are installed below the snow line. The temperature sensors are installed on the surface along an altitudinal gradient and they are used to detect whether the surface is snow covered or not. This set-up is unique in the entire Himalayas and it is probably the only site in the entire region where high altitude measurements of precipitation are made with these kinds of instruments. These measurements in combination with other meteorological and hydrological observations done by the project partners were analysed and several key findings were identified.

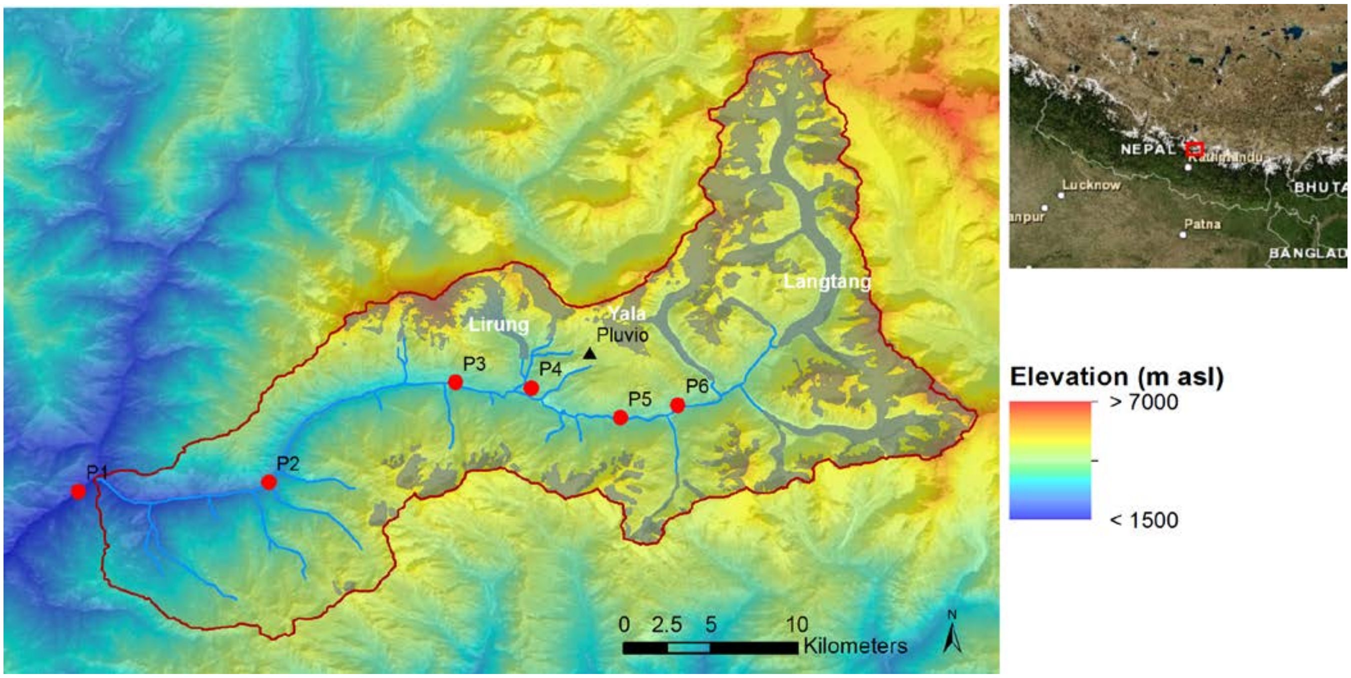

FIGURE 1THE LANGTANG RIVER BASIN WITH OUTLET NEAR SYAFRU BESI (P1), THE LOCATION OF THE TIPPING BUCKETS (P1–P6, RED DOTS), AND THE HIGH-ALTITUDE PLUVIOMETER (PLUVIO, BLACK TRIANGLE). THE GLACIERS ARE SHOWN IN GREY, AND THE NAMES OF SEVERAL REFERENCE GLACIERS IN WHITE.

Precipitation patterns in the valley are highly variable both in time and space. The Langtang catchment is located in the monsoon dominated part of the Himalayas and depending on the location in the valley between 68 and 89% falls during the monsoon season between June and September [*Immerzeel et al.*, 2014]. During monsoon there is almost daily precipitation as the moist air originating from the Bay of Bengal collides with the Himalayas. During winter the systems works completely different and precipitation is produced by disturbances from the west, which cause low pressure areas along the southern periphery of the Tibetan plateau. These low pressure areas cause cyclonic circulation which transport warm moist air from the south resulting in winter precipitation. These events are infrequent, but if they occur they can provide considerable amounts of precipitation. There is also great variation in space within the valley in precipitation. The village of Kyangjin (P4 in Figure 1) is for example twice as dry (867 mm / year) than Lama Hotel (1819 mm / year) (P2 in Figure 1) and these spatial patterns also depend on the season. During monsoon there is a general decreasing trend in precipitation following the valley gradients, while in winter an opposite pattern is observed. Precipitation also increases with altitude, but the elevation of maximum precipitation during monsoon is located at a lower elevation than during winter as a result of the different mechanisms producing the precipitation.

Temperature variations throughout the valley and seasons were also studied. In many studies temperature is assumed to decrease with altitude by about 6.5 °C per 1000 meter elevation gain. This lapse rate is generally a very important parameter in modelling studies as it determines the temperature at the higher areas where snow and ice are melting. It is also a very sensitive parameter, for example, an error of 2 °C / 1000 meter could results in a temperature difference of 4 °C between the valley floor and this may greatly impact the amount of melt water modelled. The temperature observations revealed a very clear seasonal cycle and a high correlation with elevation throughout the year, which is expected, however the lapse rates show great seasonal variation. During monsoon the temperature decreases only by 4.6 °C degrees / 1000 m, where as in winter the lapse rate is -

5.8 °C / 1000 m. The steepest lapse rate is observed in the pre-monsoon season from March to mid-June (- 6.4 °C / 1000m). There is also strong variation in diurnal variations throughout the valley.

Impact on water availability projections

These strong variations in temperature and precipitation in time and space play determine for a large part the amount of water generated in such catchments. Water availability projections are very commonly made using hydrological simulation models and these models are forced by temperature and precipitation time series. In many case accurate observational data is absent and in those cases publically available gridded datasets are used, but these are grossly inaccurate at high-altitudes and possess a resolution that is much too coarse to be of use for high-resolution hydrological assessments [*Palazzi et al.*, 2013]. In other cases just a single station is used and crude assumptions are made for the spatial variation in precipitation and temperature. To illustrate how important the use of local observations are, the hydrological model TOPKAPI-ETH [*Immerzeel et al.*, 2014; *Ragettli et al.*, 2015] was used and five different cases were analyzed ([*Immerzeel et al.*, 2014], Figure 2). The figure shows the relative difference from a reference run where only observations of a single station are used and precipitation does not vary in space and temperature is lapsed using the environmental lapse rate of -6.5 °C / 1000m. Run 5 is the optimum run where all observations are used and run 1 to 4 are intermediate runs where different amounts of observations are used. The results show that run5 is the most realistic run as it simulated the snow line most accurately and the differences in the amount of runoff, snow melt, glacier melt and rain are striking. The runoff is much higher for the case when all observations are used. This has two primary reasons: (i) the real temperature lapse rates are shallower and this result in higher temperature at higher altitude and more melt, (ii) there is more precipitation at high altitude because of the positively observed precipitation gradients.

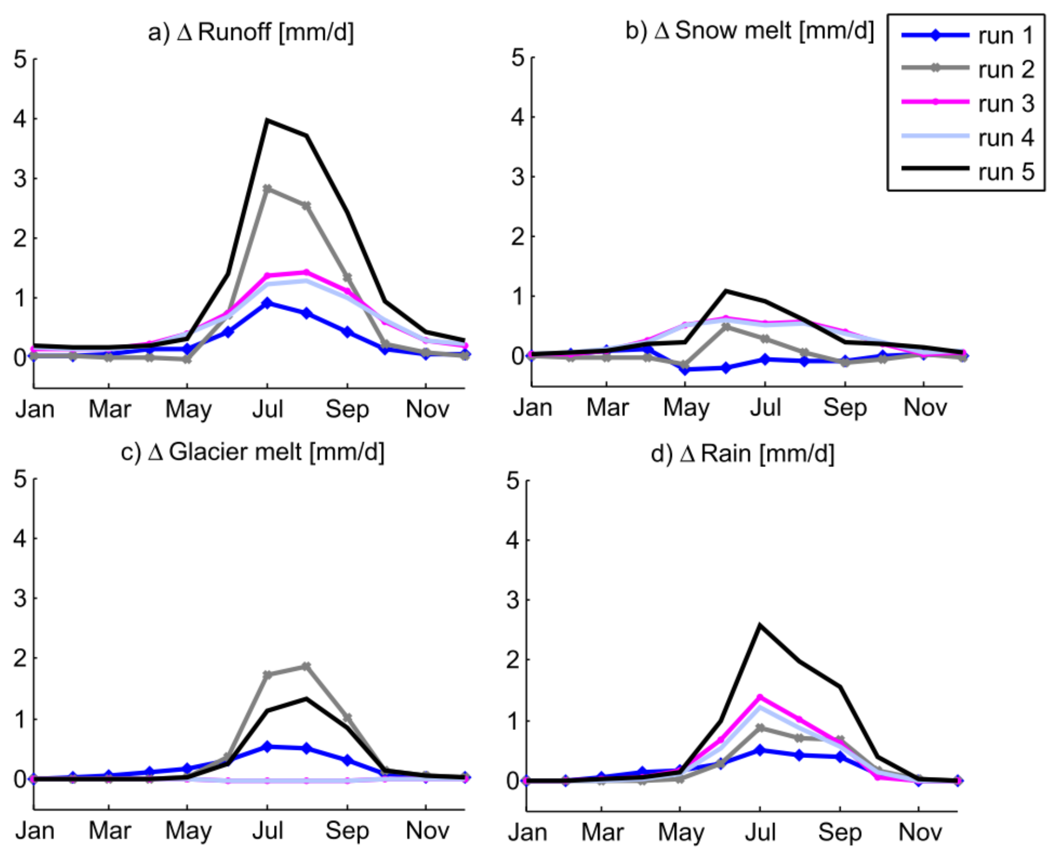

FIGURE 2 EFFECT OF USING DIFFERENT CONFIGURATIONS FOR PRECIPITATION GRADIENTS AND TEMPERATURE LAPSE RATES ON MEAN MONTHLY SIMULATED RUN- OFF, SNOW MELT, GLACIERMELT, AND RAIN. THE FIGURE SHOWS THE MONTHLY MEAN DIFFERENCES WITH RESPECT TO THE REFERENCE RUN [*IMMERZEEL ET AL.*, 2014].

Transferability to comparable catchments

The Himalayas show great variation in climate and even within a single country such as Nepal there are considerable climate differences between the west and the east. For the Everest region potential effects of climate change on future glacier evolution was assessed using a high resolution glacier model, locally observed datasets of precipitation and temperature, glacier mass balances and ice thicknesses and remote sensing datasets [*Shea et al.*, 2015]. Using the APHRODITES gridded dataset [*Yatagai et al.*, 2012] and an elevation model, temperature lapse rates were computed and the seasonal pattern in temperature lapse rates showed good agreement with what was directly observed in the Langtang. For precipitation the APHRODITES gridded precipitation dataset was used and corrected using precipitation gradients partly based on the Langtang observations and this showed the best model performance. However, an independent check with local observations showed mixed results from very good for one station to very poor for another. Although there is scope to transfer observed temperature lapse rates and precipitation gradients within similar climate zones, it is concluded that further investigations into high-elevation precipitation gradients, through field studies, remote sensing derivatives, and/or the use of high-resolution numerical weather models, will help to increase our understanding of glacier nourishment in the region.

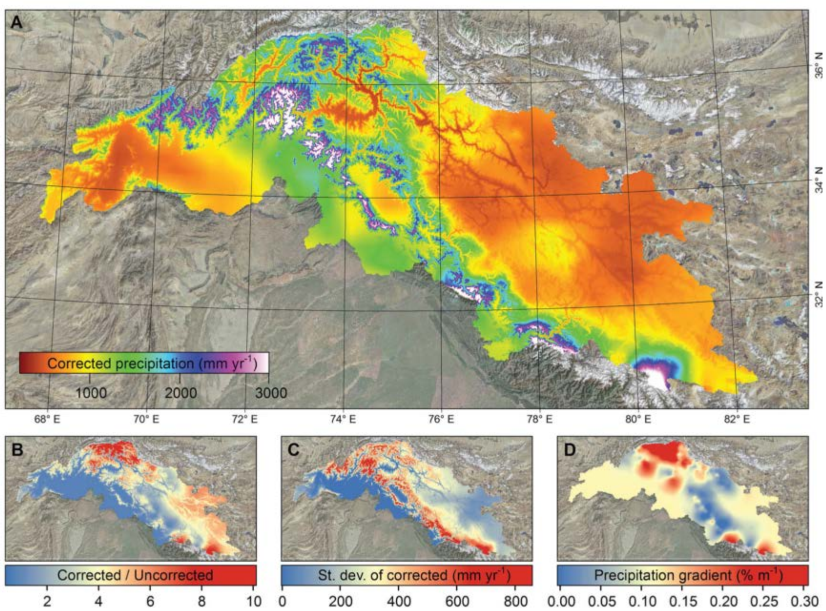

FIGURE 3 CORRECTED PRECIPITATION AND ESTIMATED UNCERTAINTY FOR THE UPPER INDUS. (A) SHOWS THE AVERAGE MODELLED PRECIPITATION FIELD FOR THE PERIOD 2003–2007, (B) SHO WS THE RATIO OF CORRECTED PRECIPITATION TO THE UNCORRECTED APHRODITE PRECIPITATION FOR THE SAME PERIOD, (C) SHOWS THE ERROR AND (D) SHOWS THE AVERAGE PRECIPITATION GRADIENT [*IMMERZEEL ET AL.*, 2015].

Alternatives to estimate high altitude precipitations

Although there is an evident need for more references sites across the Himalayas representative for the entire range of climates, a complete coverage of the entire region with an observational network is simply too expensive and logistically unfeasible. However, other types of information could also be used to approximate the high altitude precipitation. This approached was tested for the upper Indus basin. In this region very large glaciers are found, yet most datasets available indicate very small amounts of precipitation in this region, and this seems counterintuitive. To estimate the amount of snow fall required to sustain these large glacier systems information on the glacier mass balances measured from space was used. For each large glacier system the average annual melt was computed and it was estimate how much snowfall was required to match the observed mass balance. This information was then used to generate a new map of upper Indus precipitation [*Immerzeel et al.*, 2015]. The results were quite striking and there are regions, in particular the Karakoram mountain range, where the precipitation at high altitude may have been underestimated by a factor 10. The results were validated by runoff observations and the approach has a lot of potential to improve high altitude precipitation estimates in high altitude, glacierised areas which are scarce in observations.

Conclusions

It is evident that the high mountains of Asia are of great important in supplying water to more than 25% percent of the global precipitation. Climate change is likely to affect the timing and patterns of water availability and an accurate understanding of the water cycle in this region is imperative. A first step in understanding the water cycle is to quantify solid and liquid precipitation. In this project importance advances were made in this field and the following conclusions are drawn:

- There is a great variation in precipitation even within a relatively small Himalayan catchment. There are very large seasonal differences, diurnal difference, and spatial differences. These differences are caused by the complex interaction of the topography, the monsoon during summer and westerly disturbances during winter.
- Temperature varies very strongly with elevation, season and between day and night. The temperature decrease with altitude is less than the environmental lapse rate as a result of local circulation and seasonal humidity. The use of a constant annual lapse rate is incorrect and may result in erroneous temperature fields.
- The use of local observation and incorporation of spatial variation in precipitation and temperature has a profound impact on rain – snow portioning, snow melt, glacier melt and river runoff and it is essential to incorporate this information in water availability and climate change impact studies.
- Results of local studies may to some extent be transferred to nearby catchments under similar climatic conditions, if local observations are not available. However utmost care should be taken to verify the datasets using as much local observations as possible.
- If for budgetary, logistical or safety reasons local meteorological observations cannot be obtained then there are proxies, such as the mass balances of glaciers, which may be used to make a first order assessment of high altitude precipitation.

Challenges

Doing field-based research in high altitude regions of Asia is very challenging for several reasons and these need to be acknowledged:

- The logistics of organising field expeditions to the Himalayas are complex. The accessibility is poor and there is a strong dependence on local people, their knowledge of the mountains and their strength and endurance.
- Working at high altitude poses the risk of Acute Mountain Sickness (AMS) caused by the lack of oxygen at high altitude. Proper care should be taken beforehand and sufficient medical knowledge and precautionary measures should be taken.
- The weather in the mountain is highly unpredictable. Twice during a field expedition of the project, a cyclone originating from the Bay of Bengal caused large amounts of snowfall which prevented access to several observational sites.
- Nepal is located in a tectonically very active area and the Gorkha earthquake which occurred at the end of the project on 25 April 2015 has hit Nepal and the Langtang catchment in particular very hard. Many people lost their lives, villages were severely damaged and the majority of the hydro-meteorological equipment is destroyed beyond repair.
- Working in strong partnerships and international cooperation is essential for being able to successfully conduct this type of research. The partnership between ICIMOD, ETH, Utrecht University, PMD and

Kathmandu University was successful and none of the outputs would have been possible without this partnership.

- Local institutes and universities like the Department of Hydrology and Meteorology, Kathmandu University and the Tribhuvan University are the obvious partner to manage such observational networks. Yet, these are complex instruments and the capacity of these institutes needs to be further developed until they can independently manage such high altitude observatories.
- Many regions in high mountain Asia are located in geopolitical unstable areas and security and permitting issues can constrain scientific research considerably. This was experienced first handed when a nearby terrorist attack in Pakistan forced the project to cancel the fieldwork in this region.
- Data management is important, but it is sometime challenging to quality control, homogenise and store the data in a high quality manner.

Future directions

The following recommendations are made:

- The 2015 Ghorka earthquake has destroyed much of the Langtang high altitude observatory. It is strongly recommended to rebuild this site as a benchmark catchment for the entire Himalayas. There is a lot of knowledge about this valley, it is relatively accessible and it is more effective to rebuild this site than to start over elsewhere from scratch.
- More catchments like the Langtang should be equipped with hydro-meteorological instruments to improve the scientific basis for water availability projections. Only when we understand the past we can project into the future. These new catchments should be located in contrasting climate zones from the east (upper Brahmaputra) to the west (upper Indus). Selection criteria should be based on representativeness, accessibility and security.
- The capacity of local institutes, government organisations and universities should be improved by hands-on training in the field. A critical component is a transparent selection procedure of candidates which should be based on intellectual capacity, physical and mental strength and motivation.
- International collaboration should be promoted and mechanisms should be in place which ensures long term commitment, maintenance of observatories and central data management.

PROJECT DELIVERABLES

Peer reviewed publications

The project has resulted or contributed significantly to several peer reviewed publications. The abstracts of those scientific papers are presented here and the full papers are attached in annex 1.

Title	**The importance of observed gradients of air temperature and precipitation for modeling runoff from a glacierised watershed in the Nepalese Himalayas**
Journal	Water Resources Research (March 2014)
Authors	Immerzeel, W.W., Petersen, L. Ragettli, S. Pellicciotti, F.
Impact factor	3.71
Open Access	Yes

Abstract:

The performance of glaciohydrological models which simulate catchment response to climate variability depends to a large degree on the data used to force the models. The forcing data become increasingly important in high-elevation, glacierized catchments where the interplay between extreme topography, climate, and the cryosphere is complex. It is challenging to generate a reliable forcing data set that captures this spatial heterogeneity. In this paper, we analyze the results of a 1 year field campaign focusing on air temperature and precipitation observations in the Langtang valley in the Nepalese Himalayas. We use the observed time series to characterize both temperature lapse rates (LRs) and precipitation gradients (PGs). We study their spatial and temporal variability, and we attempt to identify possible controlling factors. We show that very clear LRs exist in the valley and that there are strong seasonal differences related to the water vapor content in the atmosphere. Results also show that the LRs are generally shallower than the commonly used environmental lapse rates. The analysis of the precipitation observations reveals that there is great variability in precipitation over short horizontal distances. A uniform valley wide PG cannot be established, and several scale-dependent mechanisms may explain our observations. We complete our analysis by showing the impact of the observed LRs and PGs on the outputs of the TOPKAPI-ETH glaciohydrological model. We conclude that LRs and PGs have a very large impact on the water balance composition and that short-term monitoring campaigns have the potential to improve model quality considerably.

Title	**Unraveling the hydrology of a Himalayan watershed through integration of high resolution in- situ data and remote sensing with an advanced simulation model**
Journal	Advances in Water Resources (February 2015)
Authors	Ragettli, S., Pellicciotti, F., Immerzeel, W. W., Miles, E.S., Petersen, L., Heynen, M., Shea, J. M., Stumm, D., Joshi, S., Shrestha, A.B.
Impact factor	2.78
Open Access	No

Abstract:

The hydrology of high-elevation watersheds of the Hindu Kush-Himalaya region (HKH) is poorly known. The correct representation of internal states and process dynamics in glacio-hydrological models can often not be verified due to missing in situ measurements. We use a new set of detailed ground data from the upper Langtang valley in Nepal to systematically guide a state-of-the art glacio-hydrological model through a parameter assigning process with the aim to understand the hydrology of the catchment and contribution of snow and ice processes to runoff. 14 parameters are directly calculated on the basis of local data, and 13 parameters are calibrated against 5 different datasets of in situ or remote sensing data. Spatial fields of debris thickness are reconstructed through a novel approach that employs data from an Unmanned Aerial Vehicle (UAV), energy balance modeling and statistical techniques. The model is validated against measured catchment runoff (Nash–Sutcliffe efficiency 0.87) and modeled snow cover is compared to Landsat snow cover. The advanced representation of processes allowed assessing the role played by avalanching for runoff for the first time for a Himalayan catchment (5% of annual water inputs to the hydrological system are due to snow redistribution) and to quantify the hydrological significance of sub-debris ice melt (9% of annual water inputs). Snowmelt is the most important contributor to total runoff during the hydrological year 2012/2013 (representing 40% of all sources), followed by rainfall (34%) and ice melt (26%). A sensitivity analysis is used to assess the efficiency of the monitoring network and identify the timing and location of field measurements that constrain model uncertainty. The methodology to set up a glacio-hydrological model in high-elevation regions presented in this study can be regarded as a benchmark for modelers in the HKH seeking to evaluate their calibration approach, their experimental setup and thus to reduce the predictive model uncertainty.

Title	**A comparative high-altitude meteorological analysis from three catchments in the Nepalese Himalaya**
Journal	International Journal of Water Resources Development (April 2015)
Authors	Shea, J.M., Wagnon, P., Immerzeel, W. W., Biron, R., Brun, F., Pellicciotti, F.,
Impact factor	0.895
Open Access	Yes

Abstract:

Meteorological studies in high-mountain environments form the basis of our understanding of catchment hydrology and glacier accumulation and melt processes, yet high-altitude (.4000m above sea level, asl) observatories are rare. This research presents meteorological data recorded between December 2012 and November 2013 at seven stations in Nepal, ranging in elevation from 3860 to 5360m asl. Seasonal and diurnal cycles in air temperature, vapour pressure, incoming short-wave and long-wave radiation, atmospheric transmissivity, wind speed, and precipitation are compared between sites. Solar radiation strongly affects diurnal temperature and vapour pressure cycles, but local topography and valley-scale circulations alter wind speed and precipitation cycles. The observed diurnal variability in vertical temperature gradients in all seasons highlights the importance of in situ measurements for melt modelling. The monsoon signal (progressive onset and sharp end) is visible in all data-sets, and the passage of the remnants of Typhoon Phailin in mid-October 2013 provides an interesting case study on the possible effects of such storms on glaciers in the region.

Title	**Modelling glacier change in the Everest region, Nepal Himalaya**
Journal	The Cryosphere (May 2015)
Authors	Shea, J.M., Immerzeel, W.W., Wagnon, P., Vincent, C., Bajracharya, S.
Impact factor	4.374
Open Access	Yes

Abstract:

In this study, we apply a glacier mass balance and ice redistribution model to examine the sensitivity of glaciers in the Everest region of Nepal to climate change. High- resolution temperature and precipitation fields derived from gridded station data, and bias-corrected with independent station observations, are used to drive the historical model from 1961 to 2007. The model is calibrated against geodetically derived estimates of net glacier mass change from 1992 to 2008, termini position of four large glaciers at the end of the calibration period, average velocities observed on selected debris-covered glaciers, and total glacierized area. We integrate field-based observations of glacier mass bal- ance and ice thickness with remotely sensed observations of decadal glacier change to validate the model. Between 1961 and 2007, the mean modelled volume change over the Dudh Koshi basin is $-6.4 \pm 1.5 km^3$, a decrease of 15.6% from the original estimated ice volume in 1961. Modelled glacier area change between 1961 and 2007 is $-101.0 \pm 11.4 km^2$, a decrease of approximately 20% from the initial extent. The modelled glacier sensitivity to future climate change is high. Application of temperature and precipitation anomalies from warm/dry and wet/cold end-members of the CMIP5 RCP4.5 and RCP8.5 ensemble results in sustained mass loss from glaciers in the Everest region through the 21st century.

Title	**Reconciling high altitude precipitation in the upper Indus basin with glacier mass balances and river runoff**
Journal	Hydrology and Earth System Sciences Discussion (May 2015)
Authors	Immerzeel, W.W., Wanders, N., Lutz, A.F., Shea, J.M., Bierkens, M. F. P.
Impact factor	3.642
Open Access	Yes

Abstract:

Mountain ranges in Asia are important water suppliers, especially if downstream cli- mates are arid, water demands are high and glaciers are abundant. In such basins, the hydrological cycle depends heavily on high altitude precipitation. Yet direct observations of high altitude precipitation are lacking and satellite derived products are of insufficient resolution and quality to capture spatial variation and magnitude of mountain precipitation. Here we use glacier mass balances to inversely infer the high altitude precipitation in the upper Indus Basin and show that the amount of precipitation required to sustain the observed mass balances of the large glacier systems is far beyond what is observed at valley stations or estimated by gridded precipitation products. An independent validation with observed river flow confirms that the water balance can indeed only be closed when the high altitude precipitation is up to a factor ten higher than previously thought. We conclude that these findings alter the present understand- ing of high altitude hydrology and will have an important bearing on climate change impact studies, planning and design of hydropower plants and irrigation reservoirs and the regional geopolitical situation in general.

Equipment and Field studies

During the project course several field trips were conducted which are summarized below. The objective of these field studies was to install hydro-meteorological equipment, to build capacity of regional scientists and to maintain and download the data.

In the beginning of the project the following equipment was procured at Koenders instruments in the Netherlands and shipped to Nepal:

1. Three advanced pluviometers including
   - OTT Pluvio2 precipitation gauge
   - Campbell SR50A acoustic sensor to measure snow depth
   - JENOPTIK SHM30 optoelectronic laser sensor for determining snow depths to compare with the acoustic snow depth sensor (optional instead of SR50A)
   - Campbell temperature sensor (109) including radiation shield
   - Campbell data logger (CR200)
   - Iridium based satellite communication
   - Solar panel
   - Casing for batteries and data logger
   - Mounting structures (tripod and structure Pluvio2)
   - Satellite modem and data package subscription

2. Twenty temperature loggers to distinguish between liquid and solid precipitation. These temperature loggers will be installed at the surface at various locations along an altitudinal profile.
3. Eight tipping buckets (Casella) to be installed at lower altitude (below the snow line) equipped with simple event loggers. These measurements are essential to understand the valley precipitation lapse rates.

All equipment was delivered to Utrecht University and shipped to Nepal in two shipments.

A training was organised at Koenders instruments on 5 March 2013. During the training the setup of the pluviometer was demonstrated and tested and based on the training a detailed field manual was developed. This manual is attached in Annex 2.

FIELD TRIP MAY 2013

A first field trip was conducted in May 2013 in the Langtang catchment in Nepal and Dr. W.W. Immerzeel, Dr. F. Pellicciotti and Dr. J. Shea participated. Part of the equipment was installed (Figure 4) including one pluviometer, two tipping buckets and 9 temperature loggers.

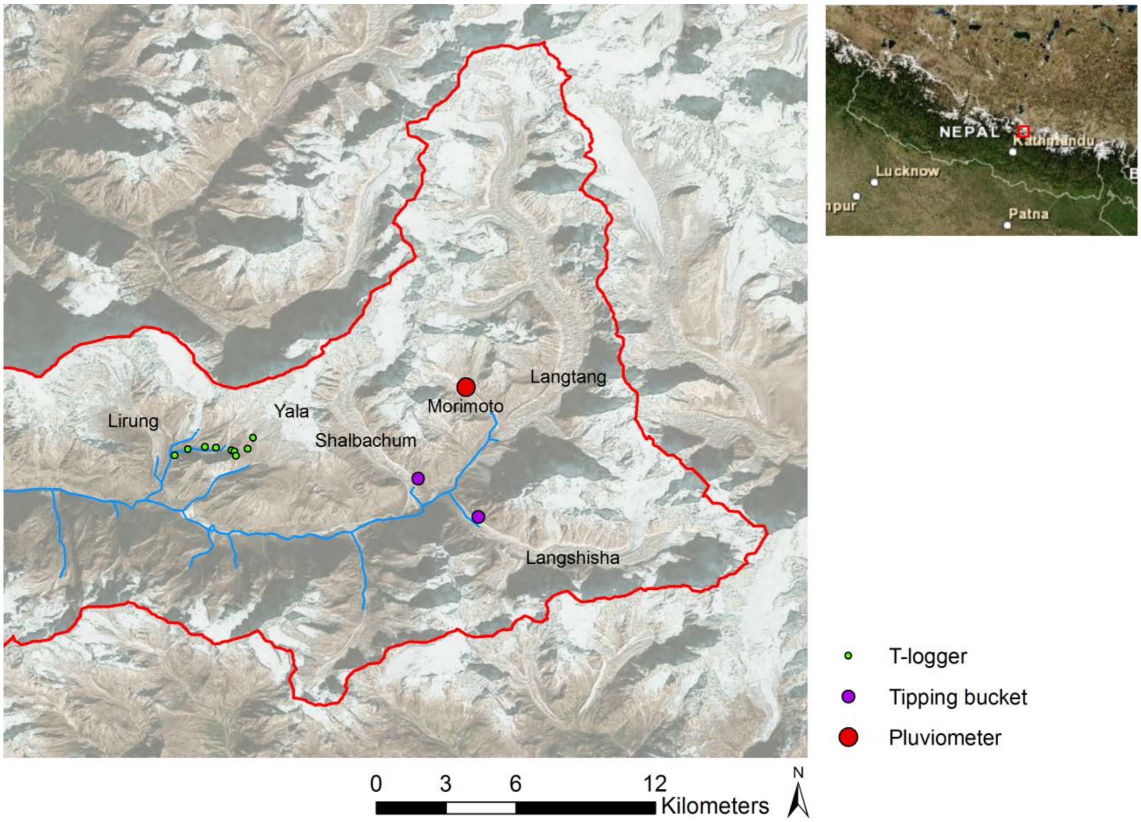

FIGURE 4 EQUIPMENT INSTALLED DURING THE MAY 2013 FIELD TRIP

- The pluviometer including temperature sensor and snow depth gauge was installed on the lateral moraine of the Morimoto glacier at an elevation of 4919 m. asl (Figure 5). The installation was conducted successful and initial tests shows that the systems logs data successfully.
- Two tipping buckets were installed near Langshisha Karka; one on the south side of the valley (4452 m asl) and one on the north side (4312 m asl)
- An elevation transect of surface temperature loggers was installed. The elevation ranges from 4116 to 4960 m asl at approximately 100 m intervals. These are intended to be used to identify the snow line position, e.g. if the surface is snow free the diurnal temperature ranges will be very large and this information can be used to discriminate the snow line position.

FIGURE 5 THE HIGH ALTITUDE PLUVIOMETER AT MORIMOTO GLACIER

FIELD TRIP OCTOBER 2013

A second field trip was organised in October 2013 to the Langtang area in Nepal and in this field trip Dr. W.W. Immerzeel (Utrecht University), Dr. J. Shea (ICIMOD), Dr. F. Pellicciotti (ETH), Mr. Waqar Ali (PMD) and Mr. Muhammad Atif Wazir (PMD) participated. During this trip the first data were downloaded and the remaining equipment was installed including two Pluviometers, 6 tipping buckets and the remaining surface temperature loggers (Figure 6).

- The pluviometers including temperature sensors and snow depth gauges were installed on the lateral moraine of the Langshisha glacier at an elevation of 4452 m. asl and towards the Ganja La pass at an elevation of 4361 m. asl (Figure 6). The installation was conducted successful and initial tests shows that the systems logs data successfully.
- Six tipping buckets were installed:
  - Three tipping buckets in an elevation profile towards Ganja La. One tipping bucket was also installed at the same location as the pluviometer to be able to make comparisons.
  - Three tipping buckets along the main valley at Nunthang (3974 m asl), Langshisha Karka (4104 m asl) and Morimoto basecamp (4617 m asl)
- An elevation transect of surface temperature loggers was installed. The elevation ranges from 4002 to 4875 m asl at approximately 100 m intervals. These are intended to be used to identify the snow line position, e.g. if the surface is snow free the diurnal temperature ranges will be very large and this information can be used to discriminate the snow line position. The final positions of the temperature loggers will be confirmed after the entire team has returned.

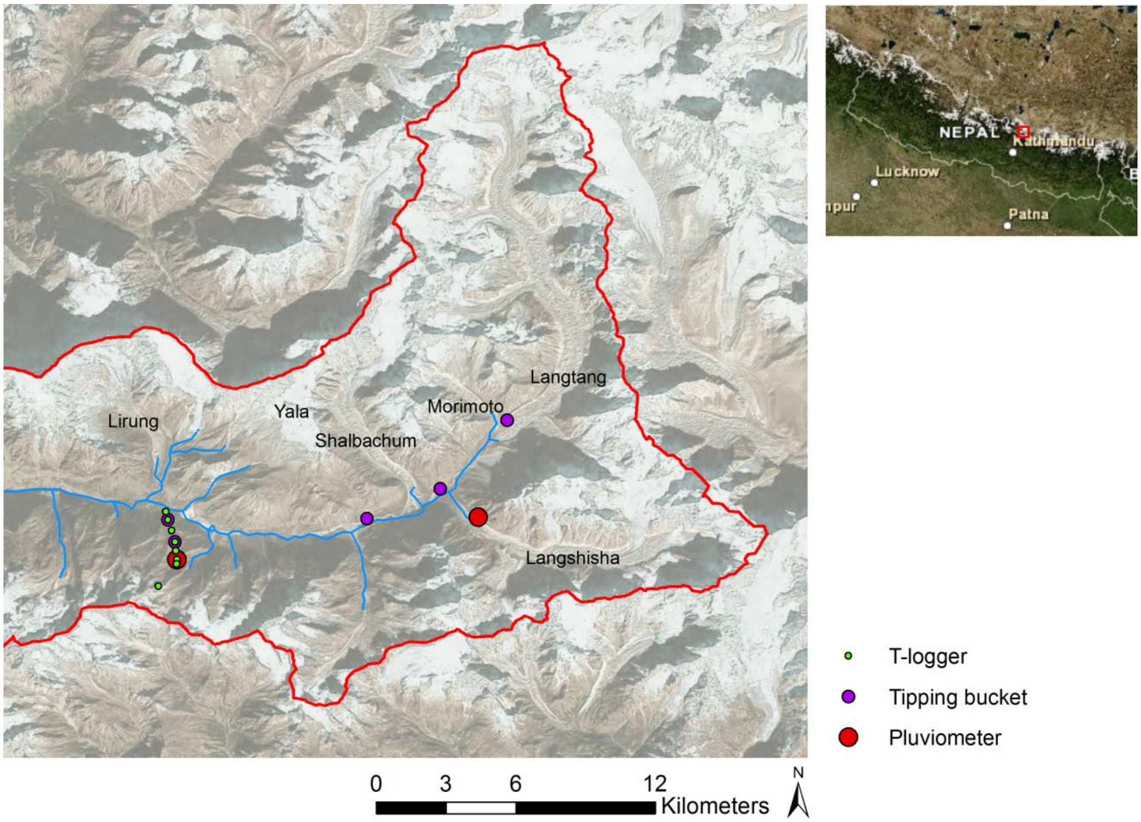

FIGURE 6 EQUIPMENT INSTALLED DURING THE OCTOBER 2013 FIELD TRIP

During the October 2013 field trip the first data from the equipment installed during the May trip was downloaded:

- The team downloaded the data from temperature loggers. We were able to download data from 5 temperature loggers. One T-logger was missing and three T-loggers were covered by snow and these will be tracked down during the next year's field trip.
- The team downloaded the data from the two tipping buckets on the Shalbachum and Langshisha lateral moraines (Figure 5).
- The team tried to visit the Morimoto pluviometer, but the conditions were very tough. Just before the October field trip, the remnants of cyclone Phaelin had passed over Nepal causing an unusual amount of snow at high altitude. In the end the team reached the site, but the pluviometer was completely full as a result of the cyclone precipitation, the contents were frozen and the bucket even contained a dead bird (Figure 7). In addition there were strong winds and extremely low temperatures and the team had to withdraw and was unable to download the data and empty the bucket. In spring next year we will attempt to fix this problem.

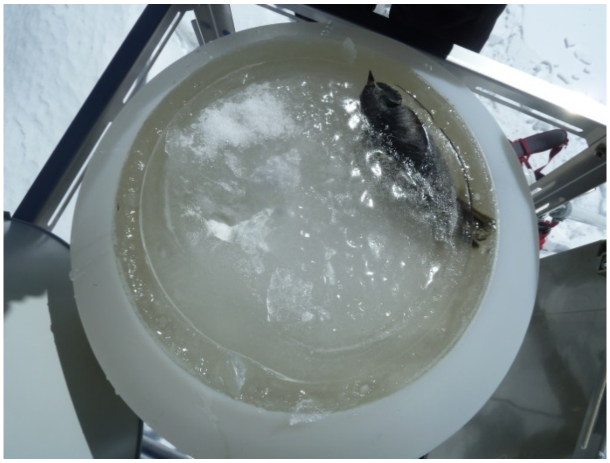

FIGURE 7 HIGH ALTITUDE PLUVIOMETER AT MORIMOTO BASECAMP

FIELD TRIP MAY 2014

In May 2014 a field trip was organized and Dr W.W. Immerzeel, Dr. J. Shea and Dr. F. Pellicciotti joined the trip from the project consortium. The trip coincided with a training organized by ICIMOD and financially supported by the Regional Office for Science, Technology and the Environment (REOSA) of the American Embassy in Kathmandu. This provided us with a unique opportunity to train and demonstrate the DFID instruments to a large group of regional members (Figure 8). During the trip the following activities were undertaken (Figure 10):

- All tipping buckets (3x) and surface temperature loggers (5x) on the south side of the valley were downloaded
- The pluviometer at Ganja La was maintained and the data downloaded. The system did not work continuously, because the solar panel did not have enough capacity to charge the battery. A second solar panel was installed in October 2014 and the systems is now working satisfactory.
- All surface temperature loggers (8x) towards the Yala glacier were successfully downloaded, except one that could not be found under the snow.
- The tipping buckets in the valley towards Langshisha and the three near Langshisha (4x) were downloaded
- The pluviometer at Langshisha was maintained and the data were downloaded
- The tipping bucket near Morimoto basecamp was downloaded.
- The pluviometer at Morimoto was repaired and the power has been restored to the system. An error was identified in the wiring of the solar panel and the system now works fine.

Figure 8 REOSA training participants

FIELD TRIP OCTOBER 2014

In October 2014 a maintenance field trip was organized and Dr. J. Shea, Prof. Steven de Jong (UU) and Mr. P. Kraaijenbrink (UU) joined the trip from the project consortium. During the trip the cyclone HudHud brought an unexpected amount of snow (about 1 meter in 24 hours), similar to the previous year (Figure 9). The team was still able to reach most instruments, only the surface temperature loggers towards Yala could not be found. The following activities were conducted:

- All tipping buckets (3x) and surface temperature loggers (5x) on the south side of the valley were downloaded
- The pluviometer at Ganja La was maintained and the data downloaded. A second solar panel has been installed in October 2014 and the system works fine again.
- The tipping buckets in the valley towards Langshisha and the three near Langshisha (4x) were downloaded
- The pluviometer at Langshisha was maintained and the data were downloaded
- The tipping bucket near Morimoto basecamp was downloaded.
- The pluviometer at Morimoto was maintained and downloaded.

The final setup of the instruments supported by the project is shown in Figure 10.

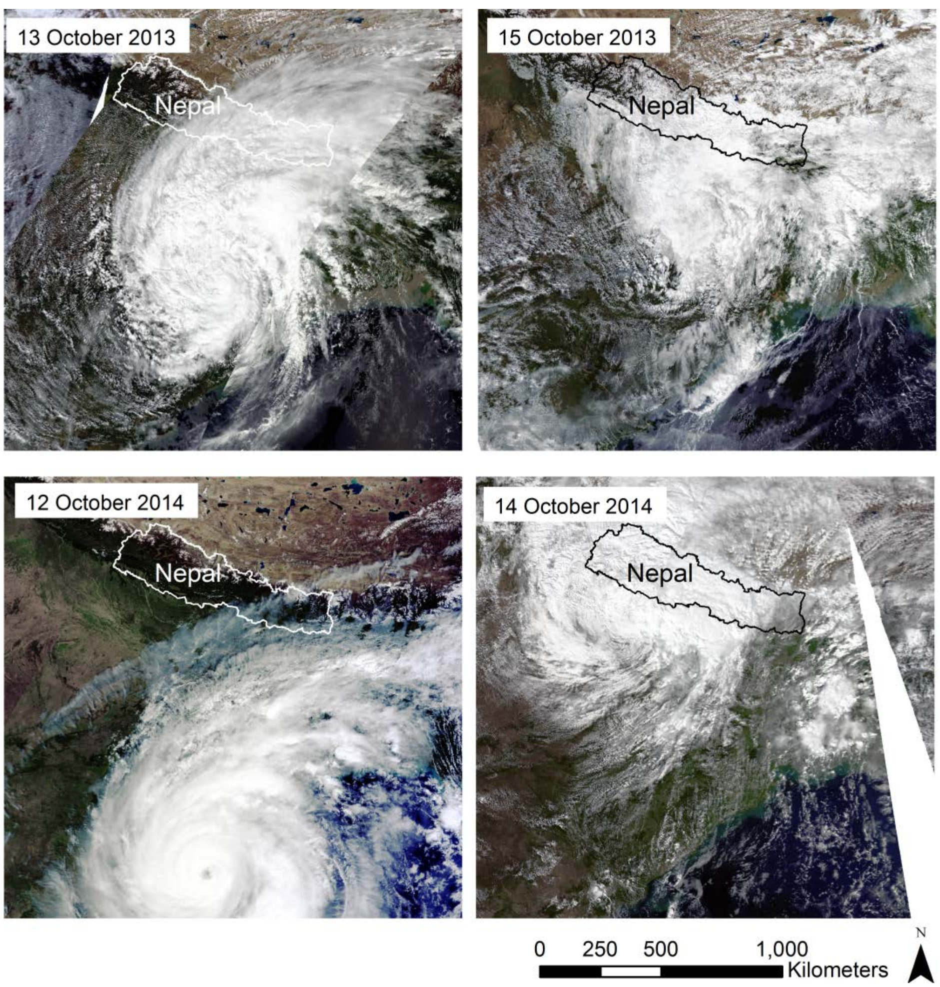

Figure 9 Cyclones in October 2013 and 2014

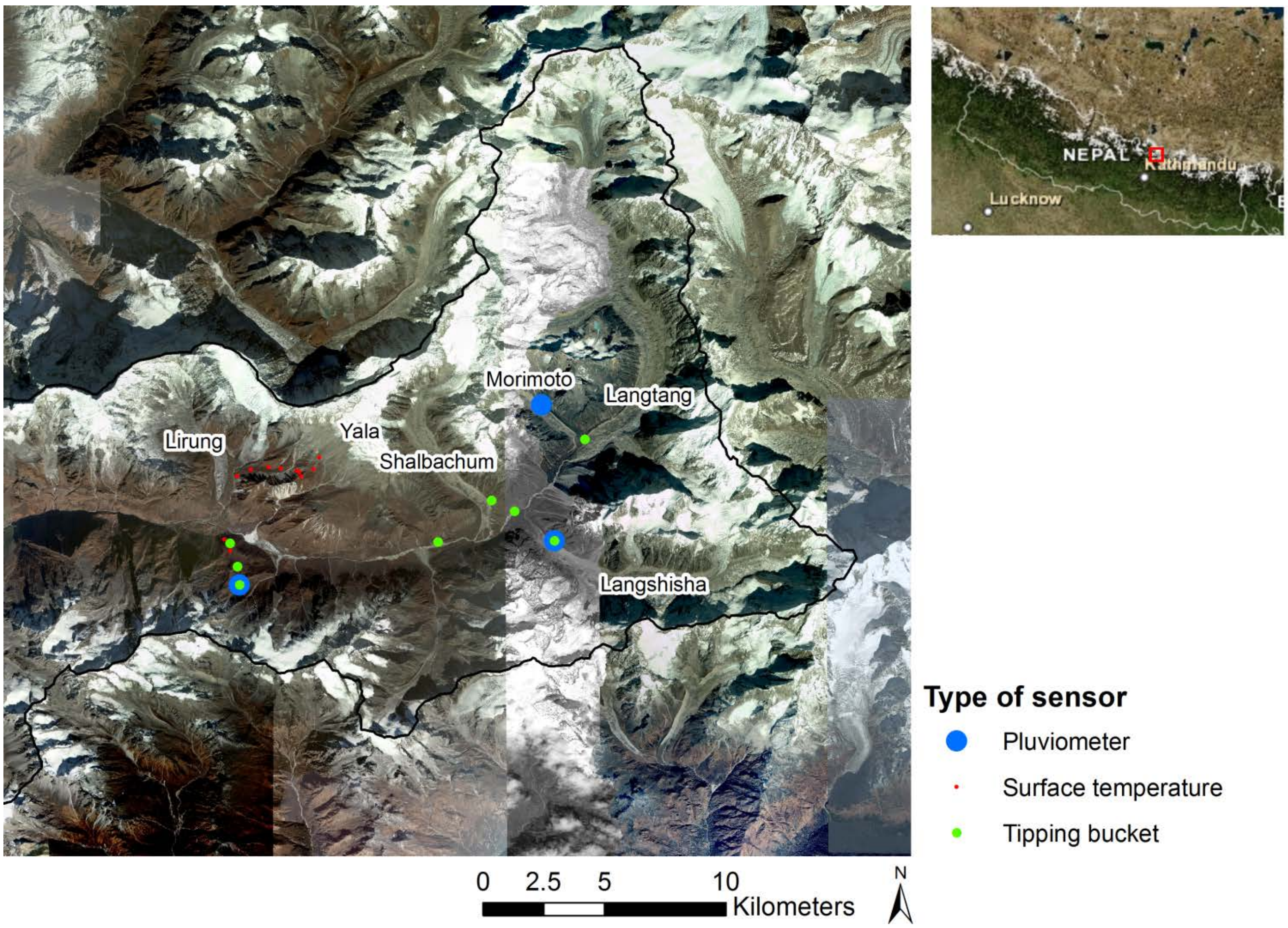

Figure 10 Locations and type of all instruments installed (October 2014)

Datasets

All datasets that were collected are being uploaded to ICIMOD dataportal (rds.icimod.org, Figure 11), where they will be made publicly available after quality control.

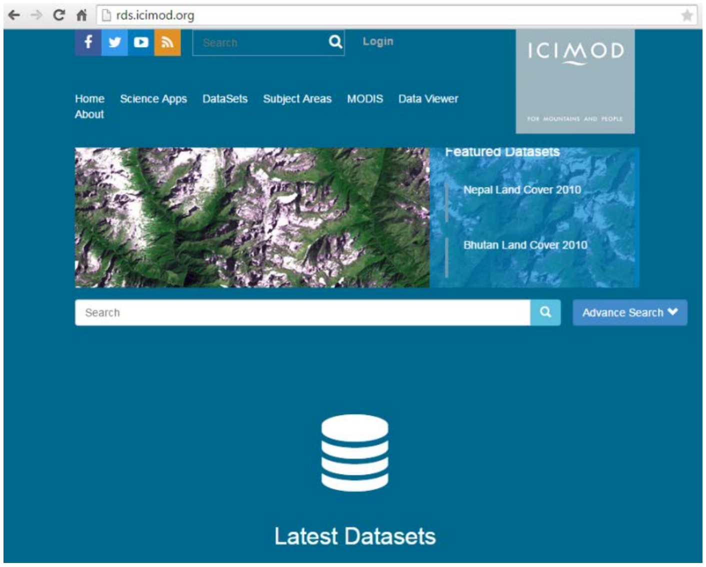

Figure 11 ICIMOD data portal

UPTAKE AND ENGAGEMENT WITH BENEFICIARIES

Capacity building

- In all field trips we employ local porters as much as possible and we also involved them actively in the setup of the pluviometer
- We worked very successfully together with Mr. Waqar Ali (PMD) and Mr. Muhammad Atif Wazir (PMD) in the field in October 2013. There was substantial mutual learning and spending so much time together in challenging conditions laid the foundations of successful future collaborations.

FIGURE 12 MR. WAQAR ALI, MR ATIF WAZIR, DR. JOSEPH SHEA, DR WALTER IMMERZEEL AND TEAM OF LOCAL PORTERS WHO ASSISTED THE INSTALLATION

- The combination with the REOSA training in May 2014 was very successful. A large group of regional participants was trained in the use of this kind of equipment. The group was very enthusiastic and indicated that the training and learning experience had great value for their respective careers.

Outreach

We worked together with ScienceMedia to develop a professional documentary of the project. This was quite successful and generated significant media attention and the movie has been viewed over 2000 times on YouTube. It was also screened at an international conference in Kathmandu.

The documentary can be viewed at http://youtu.be/xTLgpd4Wyxw.

In March 2015 ICIMOD organised the International Glaciological Society international symposium (www.icimod.org/igs2015) in Kathmandu. To maximize the outreach of the project the funds budgeted for a final workshop were used to support regional students to attend the conference. From 1 March to 6 March 2015, 245 scientists, researchers, and students met in Kathmandu, Nepal for the International Glaciological Society Symposium on Glaciology in High Mountain Asia. The symposium was sponsored and hosted by the International Centre for Integrated Mountain Development, and additional funding for student travel support was provided by a number of international agencies. The symposium was designed to highlight research advances in glaciology, with a particular focus on the glaciers of High Mountain Asia. The HMA region includes the Himalayas, the Hindu Kush, the Karakoram, the Pamirs, the Tien Shan, and the Tibetan Plateau. The glaciers of HMA were a notable 'blank spot' in the 2007 IPCC report, and while some research had been conducted in time for the 2013 IPCC report, there had not been a scientific symposium focused specifically on the glaciers of the region. With an innovative conference format that included less formality, time for discussions and synthesis, networking opportunities, and fantastic science, the IGS Symposium has had a major impact on both the science of glaciology in the region, and on the way scientific symposia should operate. The forthcoming papers of the Annals of Glaciology related to glaciology in High Mountain Asia will ensure that the region receives greater scientific attention and scrutiny. A summary report of the conference is attached as Annex 3.

CHALLENGES, DISAPPOINTMENTS AND LEARNINGS

We had to deal with several challenges throughout the project which were beyond our control. Listed below are the challenges we had to deal with during the normal project cycle. On 25 April Nepal was hit by a severe earthquake, and the impacts are described in a separate chapter.

- Initially we planned to have two research sites: one in Pakistan (Shimshal) and one in Nepal (Langtang). The trip to Pakistan was planned for July 2013 and we spent a large amount of time preparing for the expedition and getting the research and security permissions. Just before we planned to send the equipment to Pakistan nine foreigners were killed in the basecamp of Nanga Parbat about 100 km from the place where we intended to do the fieldwork. After consulting with DFID (Jean-Marion Aitken and Chetan Kumar) we decided to cancel the expedition and focus the research on the exclusively on the Langtang catchment. We considered it important though that the Pakistan Meteorological Department remained involved in the project, and so we invited two Pakistan colleagues to join the October expedition. In order to keep working in Pakistan and in the upper Indus, which is a crucial region both scientifically and in terms of importance of melt water for downstream people, we have developed an approach where we use glacier mass balance information to estimate high altitude precipitation (see Hydrology and Earth System Sciences paper in the Annex 1)
- Cyclone Phaelin passed over Nepal mid October 2013 causing unexpected rainfall and snow in the Himalayas (Figure 9). This has complicated our work in several ways. It was very difficult to reach the site of the pluviometer installed at Morimoto basecamp in May 2013 and the work at high altitude was extremely challenging given the large amount of snow. Nevertheless the installation of the two new Pluvios, the tipping buckets and the temperature loggers has been successful.
- The satellite communication to transmit data is not working, probably due to the position of the satellites and the mountainous terrain. We were not able to repair the satellite communication of the pluviometers. We have had intensive contact with the manufacturer and it seems that the angle of the satellites is too low to be able to make a good connection in such a mountainous environment. This is not a critical problem as the systems need to be visited anyway bi-annually to empty the buckets and for general maintenance.
- Some of the tipping buckets were set to a too small recording interval and therefore the memory storage was full soon after the data loggers had been started. This has now been corrected.
- Due to the heavy snow fall due to the cyclone Hudhud some of the surface temperature loggers could not be found during the October 2014 trip.

VALUE FOR MONEY

The consortium has taken all possible measures to ensure value for money while maintaining excellent quality standards in this project. The measures include:

- For the May trip the flight was paid for by ICIMOD separately as part of the REOSA training
- The travel and field costs for the October 2014 trip were charged to the DFID funded UAV project.
- The project aligns very well with the Cryospheric Monitoring Programme (CMP) that ICIMOD presently conducts. Part of the CMP project is a long-term monitoring programme in the Langtang catchment and this would also ensure maintenance of the stations beyond the duration of the project. In addition in this programme valuable auxiliary data is collected that can be used for the modelling activities planned for this project.
- The expenditure is as planned and the budget has not been exceeded so far.
- Research proposed by the Norwegian Water and Energy Resources Directorate (NVE) will complement the snowline precipitation study with additional sensors to be installed near Langtang Valley in April/May 2015

THE NEPAL EARTHQUAKE AND THE FUTURE

On April 25, 2015 Nepal was hit by a severe earthquake and the Langtang area was hit particularly hard and more than 350 people died in the region due to a very large avalanche that buried the village of Langtang completely.

The entire valley is now inhabited and everyone has been evacuated to Kathmandu and the high altitude areas are not accessible by foot now. However, plans for reconstruction in the valley are ongoing and hopefully after the monsoon, Kyangjin (which is the highest village) will become inhabited again and the community will have a chance to recover.

The earthquake also has a severe impact on the scientific research being conducted in the region. ICIMOD, ETH and Utrecht University have spent considerable funds and efforts to make the Langtang catchment into a unique observatory for meteorological, glaciological and hydrological observations. During a reconnaissance flight over the area it was found that a lot the equipment has been damaged and/or fallen over.

FIGURE 13 DAMAGE AFTE RTHE EARTHQUAKE. THE PLUVIO AT LANGSHISHA (TOP LEFT), GANJA LA (TOP RIGHT), MORIMOTO (BOTTOM LEFT) AND THE VILLAGE OF KYANGJIN WHERE MANY ROOFS ARE BLOWN OFF DIE TO AVALANCHE WINDS.

Although a full damage assessment required a field visit, which may hopefully be conducted before the monsoon we have observed that:

- Two out of the three pluvio systems have fallen over. The system at Morimoto is still standing.

- We do not the status of the tipping buckets, but it is likely that due to the enormous avalanche winds they are damaged or have disappeared.
- We do not know the status of the temperature sensors

We propose the following for the future:

- We aim at repairing the stations as soon as technically and logistically feasible. This option is much cheaper and practical then trying to start such an observatory at another location.
- We hope to conduct a field visit before the monsoon. Permits have been obtained for this and the plan is to fly by helicopter to Kyangjin and visit all the stations and make a damage assessment.
- We plan to procure new sensors and spare materials during the monsoon months and we can the hopefully complete all repairs in October 2015.
- Funding is being sought to support this work and we would be interested to explore with DFID if a new project can be formulated, which could cover the above outlined activities, possibly in combination with a number of new research ideas.

A report with a status assessment after the earthquake is attached in Annex 4.

REFERENCES

Bookhagen, B., and D. W. Burbank (2006), Topography, relief, and TRMM-derived rainfall variations along the Himalaya, *Geophys. Res. Lett.*, *33*(8), 1–5, doi:10.1029/2006GL026037.

Cheema, M. J. M., and W. G. M. Bastiaanssen (2011), Local calibration of remotely sensed rainfall from the TRMM satellite for different periods and spatial scales in the Indus Basin, *Int. J. Remote Sens.*, (November), 1–25, doi:10.1080/01431161.2011.617397.

Higuchi, K., Y. Ageta, T. Yasunari, and J. Inoue (1982), Characteristics of precipitation during the monsoon season in high-mountain areas of the Nepal Himalaya, *IAHS*, *138*, 21–30.

Immerzeel, W. W., L. P. H. Van Beek, and M. F. P. Bierkens (2010), Climate change will affect the Asian water towers, *Science*, *328*, 1382–1385, doi:10.1126/science.1183188.

Immerzeel, W. W., L. P. H. Beek, M. Konz, a. B. Shrestha, and M. F. P. Bierkens (2012), Hydrological response to climate change in a glacierized catchment in the Himalayas, *Clim. Change*, *110*, 721–736, doi:10.1007/s10584-011-0143-4.

Immerzeel, W. W., L. Petersen, S. Ragettli, and F. Pellicciotti (2014), The importance of observed gradients of air temperature and precipitation for modeling runoff from a glacierised watershed in the Nepalese Himalayas, *Water Resour. Res.*, *50*(3), 2212–2226, doi:10.1002/2013WR014506.

Immerzeel, W. W., N. Wanders, A. F. Lutz, J. M. Shea, and M. F. P. Bierkens (2015), Reconciling high altitude precipitation in the upper Indus basin with glacier mass balances and river runoff, *HESSD*.

Lutz, A. F., W. W. Immerzeel, A. B. Shrestha, and M. F. P. Bierkens (2014), Consistent increase in High Asia ' s runoff due to increasing glacier melt and precipitation, *Nat. Clim. Chang.*, *4*, 1–6, doi:10.1038/NCLIMATE2237.

Palazzi, E., J. Von Hardenberg, and A. Provenzale (2013), Precipitation in the Hindu-Kush Karakoram Himalaya : Observations and future scenarios, *J. Geophys. Res. Atmos.*, *118*(November 2012), 85–100, doi:10.1029/2012JD018697.

Pellicciotti, F., C. Buergi, W. W. Immerzeel, M. Konz, B. Arun, and A. B. Shrestha (2012), Challenges and Uncertainties in Hydrological Modeling of Remote Hindu Kush – Karakoram – Himalayan (HKH) Basins : Suggestions for Calibration Strategies, *Mt. Res. Dev.*, *32*(1), 39–50.

Qiu, J. (2008), The third pole, *Nature*, *454*, 393–396.

Ragettli, S., F. Pellicciotti, R. Bordoy, and W. W. Immerzeel (2013), Sources of uncertainty in modeling the glaciohydrological response of a Karakoram watershed to climate change, *Water Resour. Res.*, *49*(9), 6048–6066, doi:10.1002/wrcr.20450.

Ragettli, S., F. Pellicciotti, W. W. Immerzeel, E. S. Miles, L. Petersen, M. Heynen, J. M. Shea, D. Stumm, S. Joshi, and A. B. Shrestha (2015), Unraveling the hydrology of a Himalayan watershed through integration of high resolution in- situ data and remote sensing with an advanced simulation model, *Adv. Water Resour.*

Rees, H. G., and D. N. Collins (2006), Regional differences in response of flow in glacier-fed Himalayan rivers to climatic warming, *Hydrol. Process.*, *20*, 2157−2169.

Rubel, F., and M. Hantel (1999), Correction of daily rain gauge measurement in the Baltic sea drangae basin, *Nord. Hydrol.*, *30*, 191–208.

Shea, J. M., W. W. Immerzeel, P. Wagnon, C. Vincent, and S. Bajracharya (2015), Modelling glacier change in the Everest region , Nepal Himalaya, *Cryosph.*, *9*, 1105–1128, doi:10.5194/tc-9-1105-2015.

Singh, P., and L. Bengtsson (2004), Hydrological sensitivity of a large Himalayan basin to climate change, *Hydrol. Process.*, *18*(13), 2363–2385, doi:10.1002/hyp.1468.

Singh, P., M. Arora, and N. K. Goel (2006), Effect of climate change on runoff of a glacierized Himalayan basin, *Hydrol. Process.*, *20*(9), 1979–1992, doi:10.1002/hyp.5991.

Viviroli, D., H. H. Dürr, B. Messerli, M. Meybeck, and R. Weingartner (2007), Mountains of the world, water towers for humanity: Typology, mapping, and global significance, *Water Resour. Res.*, *43*(7), 1–13, doi:10.1029/2006WR005653.

Yatagai, A., N. Yasutomi, A. Hamada, A. Kitoh, K. Kamiguchi, and O. Arakawa (2012), APHRODITE : constructing a long-term daily gridded precipitation dataset for Asia based on a dense network of rain gauges, *Geophys. Res. Abstr.*, *14*(9), 1401 – 1415.

ANNEX 1: PEER REVIEWED PUBLICATIONS

AGU PUBLICATIONS

Water Resources Research

RESEARCH ARTICLE

10.1002/2013WR014506

Key Points:

- Precipitation is variable and uniform precipitation gradients cannot be derived
- Temperature lapse rates are not constant throughout the year and shallow
- Temperature lapse rates and precipitation gradients are key inputs in modeling

Correspondence to:
W. W. Immerzeel,
w.w.immerzeel@uu.nl

Citation:
Immerzeel, W. W., L. Petersen, S. Ragettli, and F. Pellicciotti (2014), The importance of observed gradients of air temperature and precipitation for modeling runoff from a glacierized watershed in the Nepalese Himalayas, *Water Resour. Res.*, *50*, 2212–2226, doi:10.1002/2013WR014506.

Received 1 AUG 2013
Accepted 17 JAN 2014
Accepted article online 22 JAN 2014
Published online 12 MAR 2014

The importance of observed gradients of air temperature and precipitation for modeling runoff from a glacierized watershed in the Nepalese Himalayas

W. W. Immerzeel[1,2,3], L. Petersen[2], S. Ragettli[2], and F. Pellicciotti[2]

[1]Department of Physical Geography, Utrecht University, Utrecht, Netherlands, [2]Hydrology and Water Resources Management, Institute of Environmental Engineering, ETH Zurich, Zurich, Switzerland, [3]International Centre for Integrated Mountain Development, Kathmandu, Nepal

Abstract The performance of glaciohydrological models which simulate catchment response to climate variability depends to a large degree on the data used to force the models. The forcing data become increasingly important in high-elevation, glacierized catchments where the interplay between extreme topography, climate, and the cryosphere is complex. It is challenging to generate a reliable forcing data set that captures this spatial heterogeneity. In this paper, we analyze the results of a 1 year field campaign focusing on air temperature and precipitation observations in the Langtang valley in the Nepalese Himalayas. We use the observed time series to characterize both temperature lapse rates (LRs) and precipitation gradients (PGs). We study their spatial and temporal variability, and we attempt to identify possible controlling factors. We show that very clear LRs exist in the valley and that there are strong seasonal differences related to the water vapor content in the atmosphere. Results also show that the LRs are generally shallower than the commonly used environmental lapse rates. The analysis of the precipitation observations reveals that there is great variability in precipitation over short horizontal distances. A uniform valley wide PG cannot be established, and several scale-dependent mechanisms may explain our observations. We complete our analysis by showing the impact of the observed LRs and PGs on the outputs of the TOPKAPI-ETH glaciohydrological model. We conclude that LRs and PGs have a very large impact on the water balance composition and that short-term monitoring campaigns have the potential to improve model quality considerably.

1. Introduction

The Himalayas and Tibetan plateau form the source areas of Asia's major river systems, yet their hydrology is poorly understood due to inaccessibility, the large variation in climates over short horizontal distances, and the absence of observations [*Immerzeel et al.*, 2010]. Hydrological modeling is a challenging task in such environments, as the availability of hydrometeorological data sets at high altitude is extremely limited, a high model resolution is required to account for the large spatiotemporal variability of climate and physiography, and many key processes such as orographic precipitation and glacier melt under debris-covered glaciers are poorly understood [*Viviroli et al.*, 2011; *Ragettli et al.*, 2013a]. Little is known about the variability in space and time of climate drivers such as temperature and precipitation in these high-elevation catchments with extreme topography. For this reason simple approaches have been used to distribute point observations in space to create gridded input to spatially distributed models [*Tahir et al.*, 2011; *Immerzeel et al.*, 2012b]. As a result, the major challenge in such studies is dealing with internal processes, e.g., an underestimation of precipitation can be compensated in the model by an overestimation of melt [*Pellicciotti et al.*, 2012]. Yet well-targeted field campaigns, even of short duration, have the potential to overcome these challenges [*Pellicciotti et al.*, 2012; *Ragettli and Pellicciotti*, 2012].

In the Nepalese Himalayas several precipitation mechanisms can be distinguished as a result of large-scale circulation in combination with mesoscale orographical and thermal induced circulation [*Ueno and Yamada*, 1990]. Depending on the mechanism, the altitude dependence may also vary. *Seko* [1987] hypothesized that at the large scale, the monsoon season from June to September is the dominant mechanism, and that during the monsoon the total precipitation amount decreases from Kathmandu (1400 m) upward. *Bookhagen and Burbank* [2006] confirm this, and they show a strong relationship with the topography and monsoon rainfall. Their work shows that there are two topography-related zones of high rainfall: one at around 1200 m elevation and a second one at 2100 m. At higher elevation the precipitation (at a larger scale) gradually decreases with elevation.

However, at the valley-scale convective precipitation occurs, which is associated with thermal circulation in the valley, and the precipitation near 5300 m was significantly higher than at 3800 m. This contradicts with the large-scale hypothesis of a negative relation between elevation and precipitation [*Ueno and Yamada*, 1990].

During winter, precipitation is produced by synoptic disturbances from the west. Westerly troughs develop over the west side of the Tibetan plateau and move eastward along the southern periphery of the plateau. Associated with the intrusion of troughs is a warm southerly moist air flow, bringing precipitation in the Himalaya which is amplified at high altitude. Winter precipitation generally occurs on a limited number of days, but the daily amounts can be considerable [*Seko*, 1987; *Shiraiwa et al*., 1992; *Steinegger et al*., 1993].

Air temperature variability is strongly controlled by the onset of the monsoon and the marked seasonality typical of the region [*Kattel et al*., 2012]. The premonsoon and monsoon seasons are the warmest [*Shiraiwa et al*., 1992], and the diurnal temperature cycle is also strongly affected by this seasonality. During the monsoon, temperature fluctuations during the day are smaller [*Takahashi et al*., 1987; *Shiraiwa et al*., 1992; *Fujita et al*., 1998; *Fujita and Sakai*, 2000] as the thick cloud cover attenuates dissipation of heat through nocturnal surface radiative cooling [*Shiraiwa et al*., 1992].

While temporal variability is relatively well understood at both seasonal and diurnal scales, spatial variation is more complex, due to the steep and rough topography, development of valley and katabatic winds, and the presence of debris on many of the glacier tongues [*Fujita and Sakai*, 2000]. They concluded that constant lapse rates (LRs) should therefore not be used for melt calculations.

Little is known about variability of air temperature in the valley and how strong its elevation dependency is. Most of the previous studies in Langtang derived LRs from only a few points and did not analyze the strength of that relationship in terms of correlation [*Fujita and Sakai*, 2000]. *Kattel et al*. [2012] analyzed temperature LRs for the entire southern slopes of the central Himalayas in Nepal, and they found strong variability in the annual cycle of LRs, with the highest values in the premonsoon season, and minima in monsoon and winter. While the study of *Kattel et al*. [2012] has shed light on LRs variability, it focuses on a very large region and coarse temporal resolution, and LR variability at the catchment scale, where local processes may be important, remains largely unknown.

In this study we analyze seasonal observed LRs and precipitation gradients (PGs) based on a 2012–2013 field campaign in the Langtang valley in the greater Himalaya in Nepal (Figure 1). Our aim is to further our understanding of temperature and precipitation variability, to discuss their potential controlling mechanisms, and to test how sensitive simulations with a glaciohydrological model are to observed LRs and PGs.

1.1. Study Area

In this study we focus on the upper Langtang catchment in the central Himalaya in Nepal (Figure 1). The Langtang River is part of the Trishuli River system in the monsoon-dominated central part of the Himalayas. Its drainage area upstream of Syafru Besi is 585 km^2, of which 155 km^2 is glacierized. The glacier tongues below 5200 m are generally debris covered. The elevation ranges from 1406 m in Syafru Besi to the summit of Langtang Lirung at 7234 m. The Langtang River flows through the main valley (Figure 1), which is typically U shaped. The climate is dominated by monsoon circulation, with predominant easterly winds in the summer and westerly winds from October to May.

2. Data and Methods

2.1. Meteorological Setup

Following the main Langtang valley six tipping buckets and six temperature loggers were installed between Syafru Besi (1406 m above sea level (asl)) and Numthang (3981 m asl) (see Figure 1 and Table 1). At each site an ARG100 tipping bucket was mounted on a steel pole at about 1 m above the surface (Figure 2b). This low-cost tipping bucket is originally designed by the Institute of Hydrology, Wallingford, UK. The ARG100 has a funnel diameter of 254 mm, a funnel rim height of 340 mm, and a sensitivity of 0.2 mm of

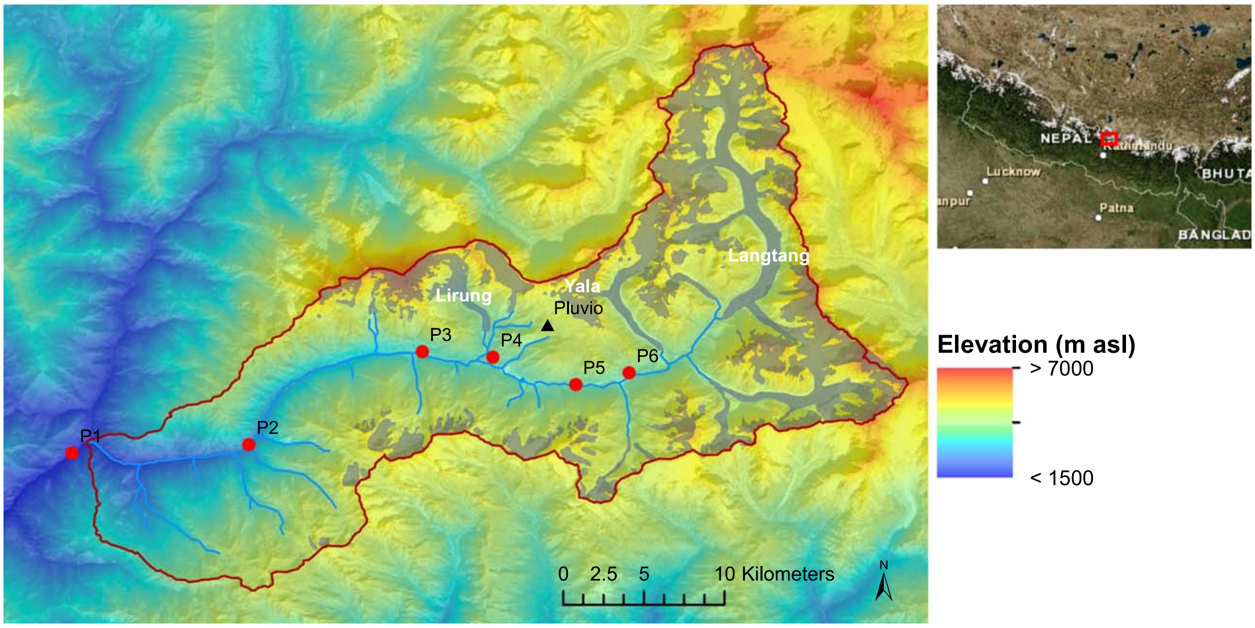

Figure 1. The Langtang River basin with outlet near Syafru Besi (P1), the location of the tipping buckets (P1–P6, red dots), and the high-altitude pluviometer (Pluvio, black triangle). The glaciers are shown in grey, and the names of several reference glaciers in white. Kyangjin is located at P4.

rain per tip. The ARG100 is equipped with a simple HOBO event data logger controlled using the dedicated BoxCar pro software. The temperature loggers (henceforth referred to as "TLoggers") are HOBO TidbiT v2 UTBI-001 from Onset. They were programmed to record air temperature at a 5 and 10 min interval. The loggers were fixed in PVC cylinders allowing natural ventilation through channelization of air flow and covered with an aluminum foil to shield the sensors from direct incoming shortwave radiation. Temperature measurements over snow surfaces are known to be strongly affected by radiation effects [*Huwald et al*., 2009], but given that all T-loggers are below the snow line the effect in this study will be limited. The cylinders were mounted on a metal pole at a distance of 2 m above the surface (see Figure 2c). They have an accuracy of 0.2°C in the range 0–50°C. Data were downloaded in August and October 2012 and in May 2013.

At an altitude of 4831 m asl on the slopes close to Yala glacier a more advanced pluviometer was installed that consists of an OTT Pluvio2 sensor, a Campbell SR50A sonic ranging sensor, and a Campbell temperature probe (109-L) (Figure 1 and Table 1). Hereafter the entire system consisting of the three sensors is referred to as Pluvio, whereas we refer to the precipitation gauge itself as Pluvio2. The Pluvio2 is based on the weighing principle, and it has an accuracy of 1% of the measured amount. The Pluvio2 has a capacity of 750 mm and measures both liquid and solid precipitations, and it complies with WMO (World Meteorological Organization, Geneva) guidelines for precipitation monitoring. The SR50A is a rugged, acoustic sensor that provides a noncontact method for determining snow depth. The SR50A determines depth by emitting an ultrasonic pulse and then measuring the elapsed time between the emission and return of the pulse. The 109-L sensor is a rugged, accurate probe that measures temperature of air, soil, or water from −50 to +70°C. It was placed in an unaspirated radiation shield (Campbell MET20) to avoid errors due to direct

Table 1. Overview of Stations, Locations, Elevation, and Sensors[a]

Description	Code	Latitude	Longitude	Average T (°C)	Elevation (m asl)	Relative Distance (m)	Sensors
Syafru Besi	P1	28.1574	85.3322	16.9	1406	0	TB, TL
Lama Hotel	P2	28.1621	85.4307	10.7	2370	9098	TB, TL
Langtang	P3	28.2140	85.5275	5.6	3539	18,563	TB, TL
Kyangjin	P4	28.2110	85.5669	4.0	3857	22,143	TB, TL
Jathang	P5	28.1956	85.6130	2.8	3875	26,206	TB, TL
Numthang	P6	28.2022	85.6428	2.8	3981	29,013	TB, TL
Near Yala	Pluvio	28.2290	85.5970	−1.8	4831	25,112	PL, UDG, TS

[a]TB, ARG100 tipping bucket; TL, Onset HOBO TidbiT v2 temperature logger; PL, OTT Pluvio2; UDG, Campbell SR50A sonic ranging sensor; TS, Campbell temperature probe 109-L inside radiation shield.

10.1002/2013WR014506

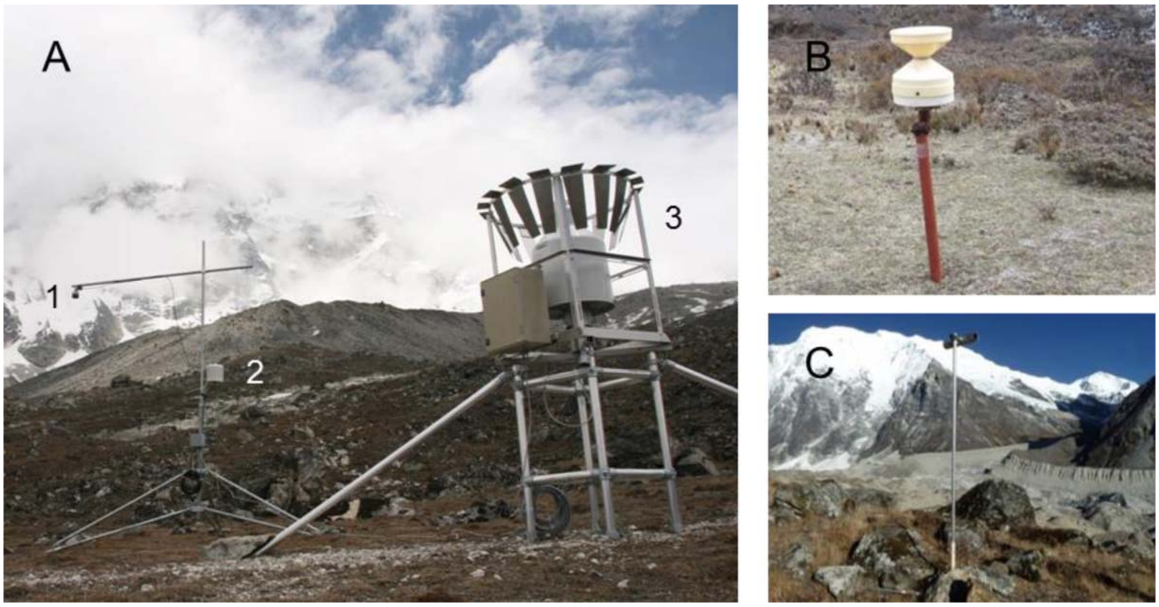

Figure 2. Setup of the instruments. (a) The high-altitude pluviometer (1, Campbell SR50A sonic ranging sensor; 2, Campbell temperature probe 109-L inside radiation shield; 3, OTT Pluvio2 including windshield), (b) a ARG100 tipping bucket, and (c) the Onset HOBO TidbiT v2 temperature logger inside its radiation shield.

radiation. The SR50A and the 109-L were installed on a tripod at 3 and 1.5 m heights above the surface, respectively. The Pluvio2 was installed on an aluminum scaffold, and the top of the Pluvio2 is at 2.5 m above the surface. The Pluvio2 includes a windscreen, and all sensors were connected to a Campbell CR200 data logger. Data of all three sensors were acquired at a 15 min interval. Data were downloaded, and batteries and antifreeze were replaced in October 2012 and May 2013.

2.2. Quality Control and Preprocessing

The data of the ARG100 tipping buckets, the temperature logger data, and the Pluvio data were all quality checked and the following corrections were made.

A yak was tied to the pole of the ARG100 at P5 sometime between 28 July and 8 August. This tilted the ARG100, and no precipitation was measured while there was considerable rainfall at P6. The P5 time series was corrected using the P6 precipitation and the average P5/P6 ratio on days with precipitation from the preceding period.

From 30 March 2013 onward the ARG100 at P2 was blocked by leaves, and no rainfall was observed from this date onward. The P2 time series was corrected using P3 precipitation and the average P2/P3 ratio on days with precipitation from the preceding period.

During the monsoon all tipping buckets were well below the snow line, but in some occasions during winter the temperature was below zero on days with precipitation. In those cases, the tipping bucket data were corrected using the Pluvio2 data and the ratio of the Pluvio2 data and the respective tipping bucket on days with above zero temperature.

Due to memory limitations and a delayed download, the TLogger's data record has a gap from 28 September until 1 November 2012. This period is not considered in the analysis. The TLogger in Kyangjin was not operating before 1 November; therefore, the data were replaced by temperature measurements from an automatic weather station at the same location.

The SR50-A data were corrected for the varying speed of sound as a result of air temperature variation.

2.3. Data Analysis

All tipping bucket data were aggregated to daily values, and the Pluvio data to both hourly and daily. Precipitation gradients were analyzed as a function of elevation, distance along the valley, latitude, and longitude both annually and seasonally. For the runs with the TOPKAPI-ETH model PGs were calculated from P4

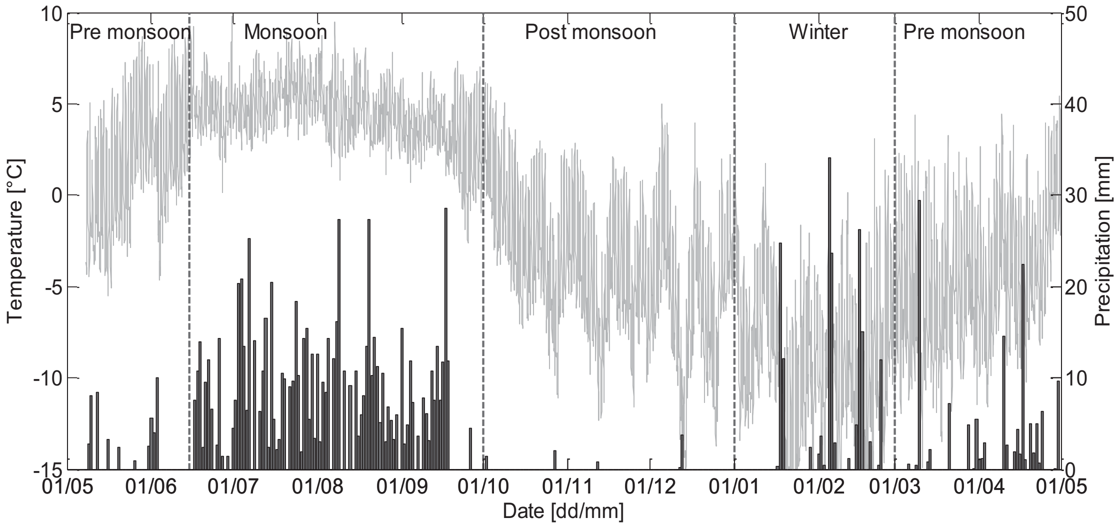

Figure 3. Daily precipitation (bars) and hourly temperature (grey line) at the location of the high-altitude pluviometer (Pluvio in Figure 1). The dotted vertical lines show the delineation of the different seasons.

upward. Both seasonal and annual PGs were derived, and distinction was made between a longitudinal and a vertical PG. These were derived by analyzing annual and seasonal precipitation sums of P4, P6, and Pluvio and their respective east-west distances and elevation differences, e.g., two linear equations with two unknowns were solved to derive the PGs. We define a vertical PG (% m^{-1}) as

$$\mathrm{PG} = 100 \times \frac{P1 - P2}{z1 - z2} = \frac{\mathrm{d}P}{\mathrm{d}z} \tag{1}$$

where $P1$ and $P2$ are the precipitation sums of the highest and lowest points (in mm) and $z1$ and $z2$ are their respective elevations. For the longitudinal PG we use the same equation, but $z1 - z2$ is the distance between the two points. The longitudinal PG is positive from east to west by convention.

All temperature data were aggregated to hourly values for the analysis. Temperature lapse rates were calculated as a regression through all points in the temperature-elevation space [*Petersen and Pellicciotti*, 2011] and are a measure of how strongly temperature is linearly controlled by altitude. Air temperature is normally assumed to increase or decrease linearly with elevation [*Marshall and Sharp*, 2009] under well-mixed atmospheric conditions [*Lundquist et al*., 2008], so that a LR (°C m^{-1}) can be defined as [*Petersen and Pellicciotti*, 2011]:

$$\mathrm{LR} = \frac{T1 - T2}{z1 - z2} = \frac{\mathrm{d}T}{\mathrm{d}z} \tag{2}$$

where $T1$ and $T2$ are the air temperatures of the highest and lowest points (in °C), and $z1$ and $z2$ are their elevations (m). We calculate the LRs from regression of all values, as this allows calculating the strength of the relationship between air temperature and elevation [*Petersen and Pellicciotti*, 2011; *Kattel et al*., 2012]. The measure of the strength of the altitudinal dependence is provided through the correlation coefficients of the linear regression. A strongly negative (steep) lapse rate indicates that temperature decreases rapidly with elevation, whereas the decrease is slower for a less negative (shallow) lapse rate [*Pepin and Losleben*, 2002; *Chutko and Lamoureux*, 2009; *Petersen and Pellicciotti*, 2011].

Temperature lapse rates were calculated for the entire year of record and separately for the main seasons. The seasons were identified based on the literature and from analysis of the precipitation and temperature records. Figure 3 shows the time series of air temperature and precipitation at the location of the Pluvio.

Based on these observations we define four distinct seasons.

Table 2. Overview of the Four Identified Seasons, Mean Temperature (T in °C), and Seasonal Precipitation (P in mm)

			P1		P2		P3		P4		P5		P6		Pluvio	
Season	Start	End	*T*	*P*	*T*	*P*	*T*	*P*	*T*	*P*	*T*	*P*	*T*	*P*	*T*	*P*
Premonsoon	8/5/12	14/6/12	23.6	107	15.8	98	10.1	156	7.8	142	7.5	156	7.6	136	1.9	181
	1/3/13	30/4/13														
Monsoon	15/6/12	30/9/12	20.7	960	14.9	1613	11.1	712	9.4	589	9.2	621	9.1	597	4.6	809
Postmonsoon	1/10/12	30/11/12	11.7	13	6.7	7	1.7	9	0.9	6	−1.9	7	−1.4	7	−3.8	8
Winter	1/12/11	28/2/13	15.2	135	8.2	102	2.0	98.8	0.2	130	−1.0	125	−1.2	132	−6.8	169

The premonsoon season from March to mid-June is characterized by relatively high temperatures gradually increasing toward the monsoon onset. The diurnal variability of temperature is high, and there are only few, rather small precipitation events.

The monsoon season lasts from mid-June until end of September. There is almost constant daily precipitation, and temperature is relatively high with small diurnal variability.

The postmonsoon season spans over the months of October, November, and December and shows nearly no precipitation and a steady decrease in temperature. Diurnal fluctuations of temperature increase again after the monsoon and are comparable to those of the premonsoon period.

The winter season (January and February) is characterized by the lowest temperatures, and precipitation occurs mostly in the form of snow at higher altitudes, with a few extreme events where daily precipitation exceeds the maximal values of monsoon precipitation.

This division agrees with what was reported by *Shiraiwa et al*. [1992] and *Kattel et al*. [2012]. The seasons, together with their mean temperature and precipitation, are summarized in Table 2. All results are reported separately for the four seasons defined above.

2.4. Glaciohydrological Modeling

We test the effect of using different precipitation gradients and temperature lapse rates on the outputs of a distributed glaciohydrological model. The model used for this purpose is the TOPKAPI-ETH model, which has been frequently used for simulations of glacier melt and runoff in high-elevation catchments [*Finger et al*., 2011, 2012; *Ragettli and Pellicciotti*, 2012; *Ragettli et al*., 2013a, 2013b]. The physical basis of the process representation allows setting up the model using data obtained locally, in ad hoc short-term field campaigns, to estimate model parameters [*Ragettli and Pellicciotti*, 2012].

The model requires daily input of measured precipitation and temperature, and station data from Kyangjin are used for this purpose. Daily cloud transmissivity coefficients are derived from the range of observed diurnal variations of air temperature at Kyangjin [*Pellicciotti et al*., 2011]. Temperature and precipitation are extrapolated to every model grid cell (resolution: 100 m) using spatially constant LRs and PGs.

Gravitational snow transport is simulated using a slope-dependent maximum snow holding depth [*Bernhardt and Schulz*, 2010]. If the snow depth of a model grid cell exceeds the cells' maximum snow holding depth, snow is redistributed to the next lower cell in flow direction. Snow and glacier melt in TOPKAPI-ETH are computed using an Enhanced Temperature-Index approach [*Pellicciotti et al*., 2005, 2008]. The model was thoroughly set up and tested using an extensive data set collected in 2012–2013, and calibration was conducted against data of different nature [*Ragettli and Pellicciotti*, 2013]. Melt parameters are estimated using data from ablation stake measurements on Lirung and Yala glacier (Figure 1) during the period November 2011 to May 2013 [*Ragettli and Pellicciotti*, 2013]. Melt parameters are different for debris-covered and debris-free glacier areas, in order to take into account the melt reducing effect of the thick debris cover observed on many glaciers within the study area. Validation of the simulated snow cover recession after winter (March–June) against Moderate Resolution Imaging Spectroradiometer (MODIS)/Terra and MODIS/Aqua daily fractional snow cover indicates very good model performance. The coefficient of determination (r^2) for the period 2012–2013 between daily observed and daily simulated snow cover was 0.92 using Aqua satellite data and 0.93 using Terra satellite data.

In this study, we run the model with five different combinations of the observed LRs and PGs, and we compare the results with a reference run where precipitation is constant with increasing elevation and the

Table 3. Configuration of TOPKAPI-ETH Model Runs[a]

	PGv	PGh	LR
Reference run			ELR
Run 1			Mean annual observed
Run 2			Mean seasonal observed
Run 3	Mean annual observed	Mean annual observed	ELR
Run 4	Mean seasonal observed	Mean seasonal observed	ELR
Run 5	Mean seasonal observed	Mean seasonal observed	Mean seasonal observed

[a]PGv and PGh are the vertical and horizontal precipitation gradients, and LR is the temperature lapse rate. The values of PGv and PGh can be found in Table 4.

Table 4. Vertical (PGv) and Longitudinal (PGh) Precipitation Gradients in % m^{-1}

Season	PGv	PGh
Premonsoon	0.031	−0.0004
Monsoon	0.040	−0.0005
Postmonsoon	0.039	0.0022
Winter	0.053	0.0006
Annual	0.041	−0.0003

standard environmental lapse rate (ELR, −0.0065°C/m) is used to extrapolate temperature data. The configurations of the different runs are reported in Table 3. The values of observed seasonal and annual LRs are shown in Table 5. For assessing how sensitive a glaciohydrological model is to PGs we consider only the area from P4 upward, as the TOPKAPI-ETH model is available from the stream gauge at P4 upward, and there is a more consistent longitudinal and vertical PG from P4 upward. The PGs used to force the model are shown in Table 4. The model is forced with precipitation and temperature data from the Department of Hydrology and Meteorology for a period of 8 years (2003–2010). The first year is used to initialize the simulations. We therefore discuss mean differences in model outputs with respect to the reference run for the period 2004–2010.

3. Results and Discussion

3.1. Precipitation

Figure 4 shows the seasonal precipitation sums and wet day frequencies. There is a strong variation in precipitation in the valley over short horizontal distances. The maximum precipitation is at P2 (1819 mm), and the minimum precipitation is at P4 (867 mm), e.g., a 52% decrease of precipitation within a distance of 14 km. P2 is the wettest location only during the monsoon, and since P2 is located after the first steep ascend in the valley (Table 1), it seems plausible that the wet convective monsoon air mass is orographically forced at this elevation. During winter and the premonsoon this is not observed, and this may be related to differences in circulation patterns and a more stratiform type of precipitation. The majority of rainfall falls during the monsoon, and this ranges from 68% of the annual precipitation in P4 to 89% in P2. There is also strong variation in the wet day frequencies (Figure 4). During the monsoon there is precipitation nearly every day ranging from 70% of the days at Pluvio to 86% at P5. In winter the wet day frequencies are much lower, and there is only occasional precipitation ranging from 17% (P1) to 31% (P6) of the total number of days.

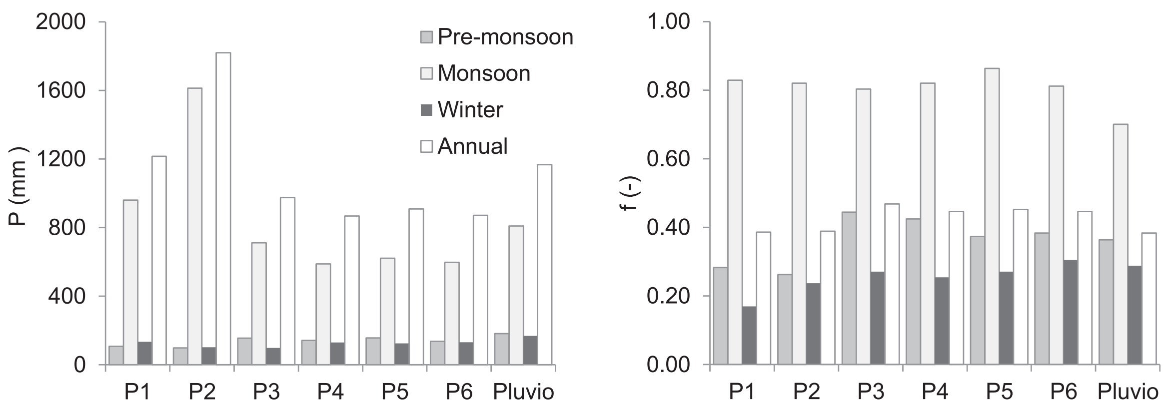

Figure 4. Annual, premonsoon, monsoon, and winter (left) precipitation sums and (right) wet day frequency based on observations from 8 May 2012 until 30 April 2013.

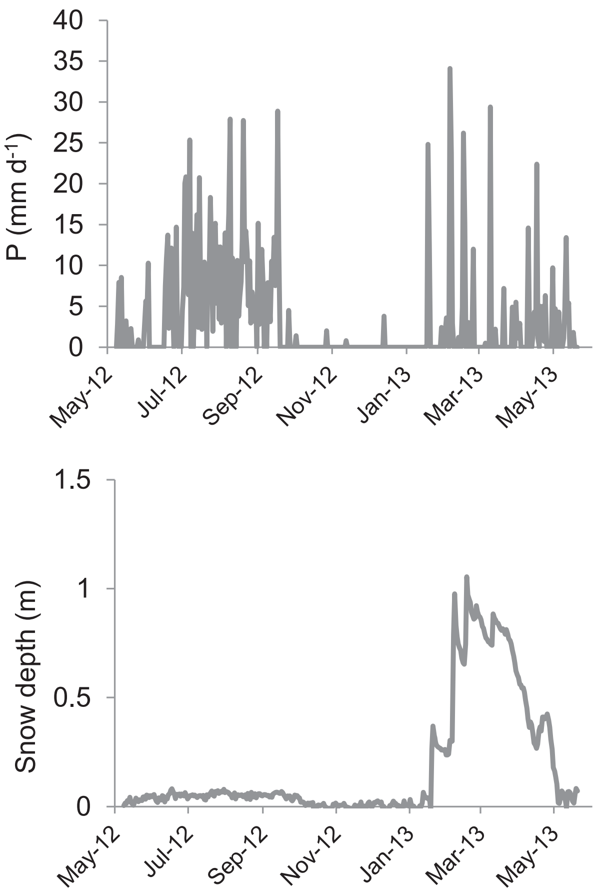

Figure 5. (top) Daily precipitation and (bottom) snow depth at Pluvio.

There are also considerable differences in the daily precipitation intensities during both the monsoon and winter seasons. The most extreme precipitation occurred in P2 during the monsoon (58 mm/d). No clear spatial trends can be identified in the rainfall intensities. Although the wet day frequency is much lower during the winter, the precipitation intensities are generally higher. The distribution of the intensities during winter is more skewed than the monsoon intensities, e.g., during winter there are a few events with a relatively extreme amount of precipitation, whereas during the monsoon the intensities are more or less normally distributed around the mean.

The premonsoon shows a clear diurnal precipitation pattern. During the morning it is relatively dry and most precipitation occurs during the later afternoon (5.00–7.00 P.M.), decreasing again during the evening and the night. During the other seasons we also observe a diurnal pattern, but without the distinct peak during the late afternoon. This distinct peak may be explained by the fact that the air is already relatively moist in this season, which in combination with relatively abrupt radiative cooling results in the late afternoon peak during the premonsoon.

We analyzed large-scale wind direction and speed using *u* and *v* winds at the geopotential height of 500mb derived from the ERA-INTERIM reanalysis data set [*Dee et al.*, 2011]. The analysis shows a distinct intraannual pattern. During winter, 500 mb wind speeds are much higher than during monsoon. In winter, there is a strong northwestern wind from the Tibetan plateau, whereas during the monsoon the wind comes from the southeast. This is in agreement with the mechanisms which we outline in section 1.

No consistent trend in the entire valley is evident between precipitation and elevation, relative distance along the valley, longitude, or latitude. We hypothesize that during monsoon there is a strong upvalley wind that leads to the formation of convective cumulus clouds during the day, and this causes a strong precipitation peak at P2 after the first steep ascent in the valley. Even at night weak upvalley winds continue to flow during the monsoon, because radiative cooling is suppressed due to the presence of stratus in the evening [*Seko*, 1987]. In winter, precipitation is associated with synoptic scale disturbances of stratiform type, with less pronounced diurnal variation and a stronger elevation dependence [*Seko*, 1987].

From P4 upward, PGs can be discerned, and the PGs that were used in the glaciohydrological modeling are shown in Table 4. A positive vertical PG is observed in all seasons that ranges from 31% to 53% increase in precipitation over a 1000 m in elevation rise during the premonsoon and winter, respectively. Calculated longitudinal PGs are negative during premonsoon and monsoon and positive during winter, and several studies have used or suggested the existence of longitudinal gradients [*Seko*, 1987; *Konz et al.*, 2007; *Immerzeel et al.*, 2012b].

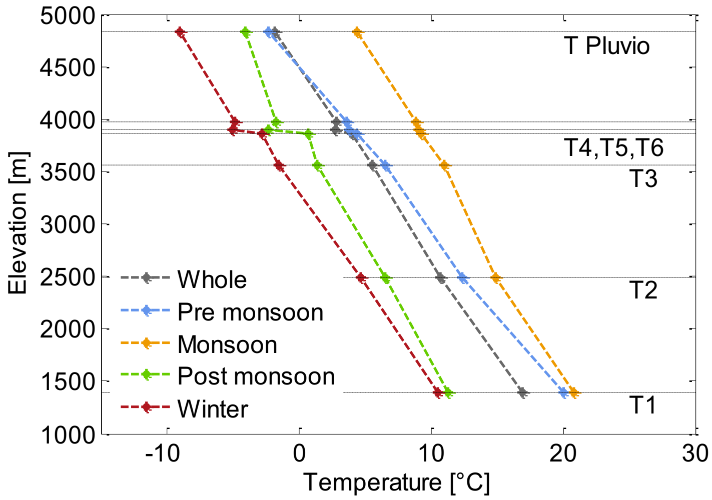

Figure 6. Mean temperature at all locations plotted against elevation for the entire period (8 May 2012 to 1 May 2013), premonsoon, monsoon, postmonsoon, and winter.

During winter a significant part of the precipitation falls in the form of snow at high altitude (Figure 5). The first snow fall occurred on 18 January 2013, and the maximum snow depth at Pluvio was 1.1 m on 17 February 2013. By 4 May 2013 the snowpack was completely depleted. Snow falls during a few isolated events only, and there were only 6 days when there was more than 10 cm of increase in snow depth. By using the total precipitation and snow depth increments on these days we estimate that the average density of the fresh snow falling on those days is 115 $\pm$ 48 kg m^{-3}. In total we estimate that 211 mm falls in the form of snow (17.5% of the annual precipitation).

3.2. Temperature

The mean temperatures versus elevation at all locations are shown in Figure 6, and the corresponding LRs calculated from linear regression are reported in Table 5. The increase in temperature from winter to monsoon is obvious throughout the valley. Temperature and elevation are highly correlated (Table 5), indicating that the relationship is strong, and temperature can be predicted accurately as a function of elevation [*Kattel et al.*, 2012].

Figure 6 also shows that the linearity in the elevation-temperature relation seems to be interrupted during winter and postmonsoon for P4 and P5. These are the coldest seasons and the atmosphere is stable. In combination with the fact that beyond P4 the valley widens and the slopes become less steep, cold air pooling may explain this anomaly in LR [*Lundquist et al.*, 2008].

While temperatures are highest during monsoon, the LR ($-$0.0046°C/m) is less negative than in winter ($-$0.0058°C/m) as during monsoon the temperature decrease with elevation is attenuated by the presence of a consistent cloud cover, which reduces radiative cooling. Premonsoon season has the steepest lapse rate ($-$0.0064°C), indicating that differences in temperature between the locations are largest during this time, whereas the postmonsoon season shows a LR ($-$0.0049°C/m) similar, but slightly steeper, than during monsoon. The most prominent reasons for the seasonal differences in LRs are differences in relative humidity. Under humid conditions, such as during the monsoon, the condensation of water droplets warm the air during lifting, resulting in more shallow LRs.

The peak in LR in premonsoon season is consistent with the observations for the entire southern slopes of the central Himalayas and might also be related to the vertical gradient of premonsoon snow cover, e.g., deep snow cover at high elevations and none at lower elevations [*Kattel et al.*, 2012]. Snow-covered surface has a high albedo and from the limited net radiation that remains a significant part, is used for snow melt. The sensible heat flux is therefore generally limited, which in combination with strong radiative cooling from the cold surface, results in relatively low air temperatures. In addition, some of the differences among

Table 5. Mean, Minimum, and Maximum Values of the Diurnal Cycle for Lapse Rate (LR) and Correlation (*r*) for the Seasons of Premonsoon, Monsoon, Postmonsoon, and Winter Between Mean, Minimum and Maximum Temperatures

Season	Mean LR (°C/m)	Minimum LR (°C/m)	Maximum LR (°C/m)	Mean *r*	Minimum *r*	Maximum *r*
Premonsoon	−0.0064	−0.0070	−0.0054	0.989	0.943	0.997
Monsoon	−0.0046	−0.0053	−0.0040	0.990	0.956	0.997
Postmonsoon	−0.0049	−0.0059	−0.0034	0.944	0.814	0.982
Winter	−0.0058	−0.0067	−0.0045	0.969	0.900	0.987

10.1002/2013WR014506

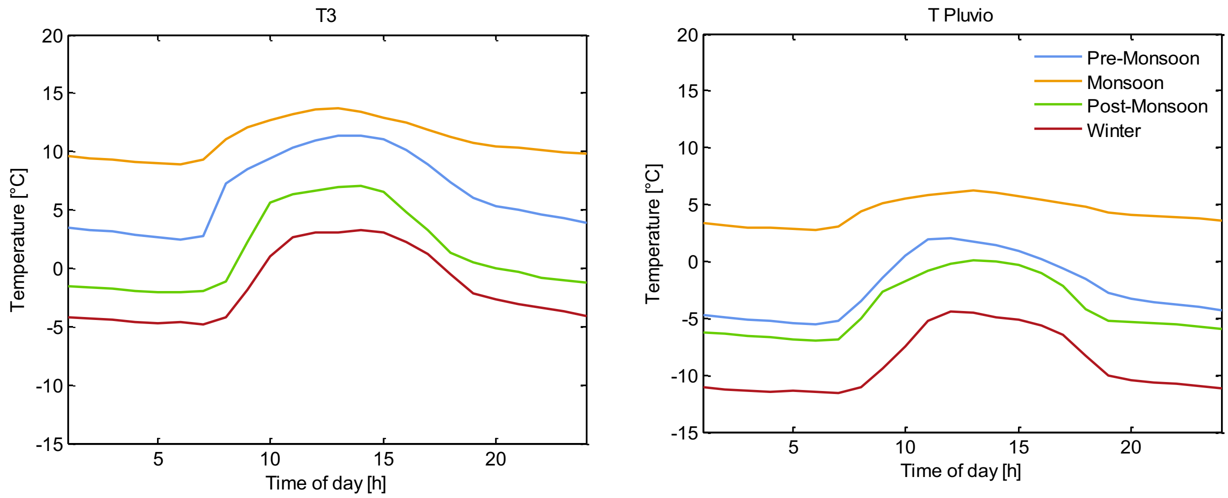

Figure 7. Mean diurnal cycle temperature at P3 and Pluvio for the premonsoon season (blue), monsoon season (orange), postmonsoon season (green), and winter season (red line).

locations during premonsoon might be explained to changing weather patterns within the valley (scattered showers, partial cloud cover, and partial clear sky with high incoming radiation), whereas in postmonsoon the climate is stable with high incoming shortwave radiation flux.

Over all seasons, and especially during monsoon and postmonsoon, the observed LRs are shallower than the values of the commonly used ELR of -0.0065°C/m, indicating that in the Langtang valley, the decrease of air temperature with elevation is less rapid than commonly assumed for free atmosphere conditions. This is important for redistribution of air temperature used to force glaciohydrological models, as use of the ELR would result in lower air temperatures in the upper sections of the valley and higher temperatures in the lower sections. The mean annual observed lapse rate (-0.0054°C/m), which is also lower than the ELR, is an average of distinct seasonal values that we consider separately for glaciohydrological modeling (Table 3).

Our results generally agree with studies in other mountainous regions of the world [*Minder et al*., 2010; *Mizukami et al*., 2013]. *Minder et al*. [2010], for example, find for the Cascade mountain range in the United States LR ranging between -0.0039 and -0.0052°C/m with strong seasonal variation and the most shallow LRs during the season with the highest relative humidity. They also show that a high-resolution mesoscale weather model (MM5) is capable of accurately simulating the observed LRs, probably due to accurate simulation of spatiotemporal variations in atmospheric moisture. Although such models are currently unavailable for the Himalaya, it would certainly be recommendable for a future study to explain the physical processes underlying Himalayan LR variation.

Figure 7 shows that the diurnal range is strongly reduced during the monsoon, and this can be attributed to the influence of a thick cloud cover [*Takahashi et al*., 1987; *Shiraiwa et al*., 1992]. The diurnal range generally decreases with altitude.

The regression lapse rate through all locations for every hour of the day was calculated for all four seasons, and values are reported in Table 5 together with the corresponding correlation coefficients. Correlation coefficients for *mean* and *maximum* temperature LRs are very high, especially for the maximum temperature LRs, and vary between 0.944 and 0.997 (Table 5). However, correlation coefficients between *minimum* temperature and elevation are lower and more variable, with values between 0.814 and 0.956 (Table 5). This indicates that the relationship between temperature and elevation for low temperature is weaker and other factors have an influence [*Kattel et al*., 2012]. Several studies have suggested that factors such as humidity, cloudiness, wind velocity, valley orientation, and the general drainage patterns of cold air from higher grounds are stronger controls over minimum temperature than elevation [*Lundquist et al*., 2008; *Gouvas et al*., 2011]. The very high correlation for *maximum* temperature-elevation relationship seems on the opposite to indicate that elevation is the main control on air temperature variability under high temperature conditions, which occur mainly during the day (Figure 7). Correlation coefficients between *mean* temperature

10.1002/2013WR014506

Table 6. Median and Standard Deviation (σ) of the Simulated Equilibrium Line Altitude (ELA) at Yala Glacier (5130–5750 m asl) of Each Run

	Median (m asl)	σ (m)
Reference run	ELA below glacier	
Run 1	5264	33
Run 2	5510	54
Run 3	ELA below glacier	
Run 4	ELA below glacier	
Run 5	5403	26

and elevation are lowest in postmonsoon and winter, increase in March–May, and reach the highest values during monsoon (with a value of 0.990), in very good agreement with findings from *Kattel et al.* [2012]. The lower correlation coefficients during postmonsoon and winter have also been attributed to inversions [*Kattel et al.*, 2012].

The LRs found here result in temperature differences up to several degrees over the elevation range typical of the Langtang catchment, and their diurnal variability temperature is relevant for numerous processes, such as melt and evapotranspiration, all occurring within certain periods of the day.

3.3. Glaciohydrological Model Simulations

We test the effect of the observed PGs and LRs on the sensitivity of the outputs of the TOPKAPI-ETH glaciohydrological model using the five runs listed in Table 3. Runs 1 and 2 are to examine impact of different LRs (observed annual LR versus seasonal LR), runs 3 and 4 are for assessing the impact of different PGs (annual mean versus seasonal PG), and run 5 is used to show impact of combination of seasonal PGs and LRs. Run 5 can be considered as the optimum run using the best information available. The simulated equilibrium line altitude (ELA) values for Yala glacier—a benchmark glacier in the region—are consistent with information from the literature: field-based measurements locate the ELA at Yala at about 5400 m [*Sugiyama et al.*, 2013]. The median elevation of the simulated ELA by run 5 for the period 2004–2010 is exactly 5403 m asl (with a standard deviation of 26 m between different years, Table 6). The simulated ELA at Yala by the other

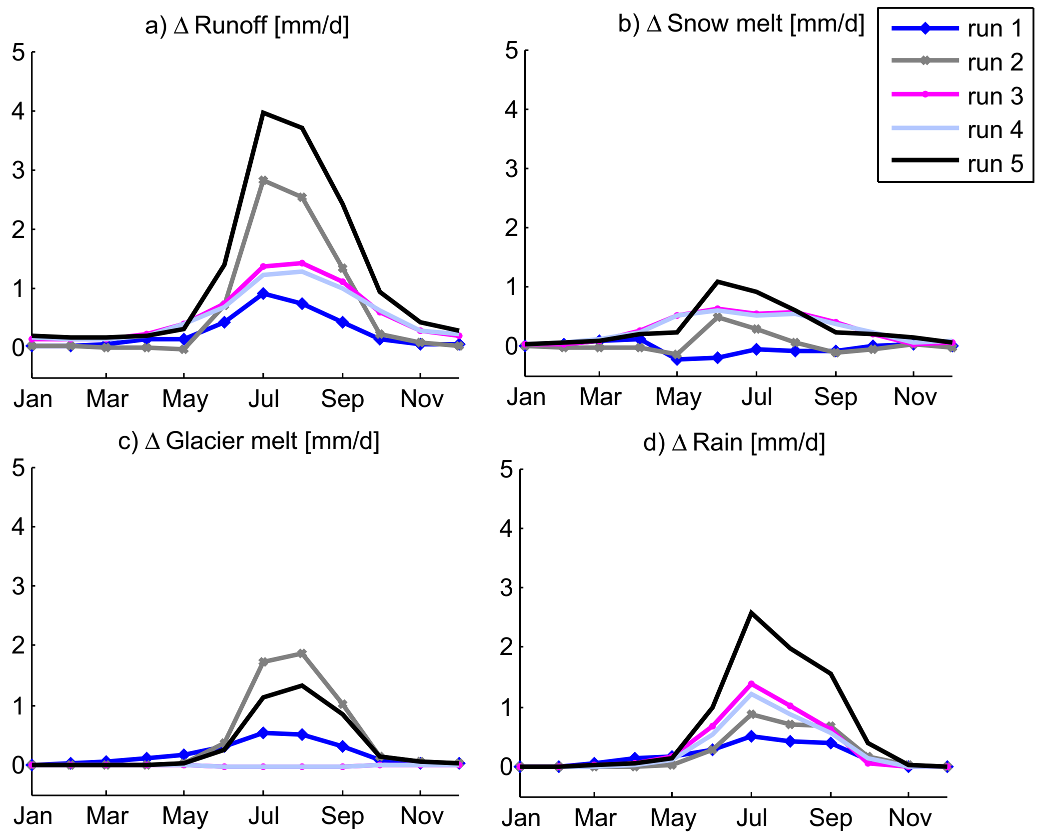

Figure 8. Effect of using different configurations for precipitation gradients and temperature lapse rates on mean monthly simulated runoff, snow melt, glacier melt, and rain. The figure shows the monthly mean differences with respect to the reference run (run-reference run) (Table 3), simulated for the period 2004–2010.

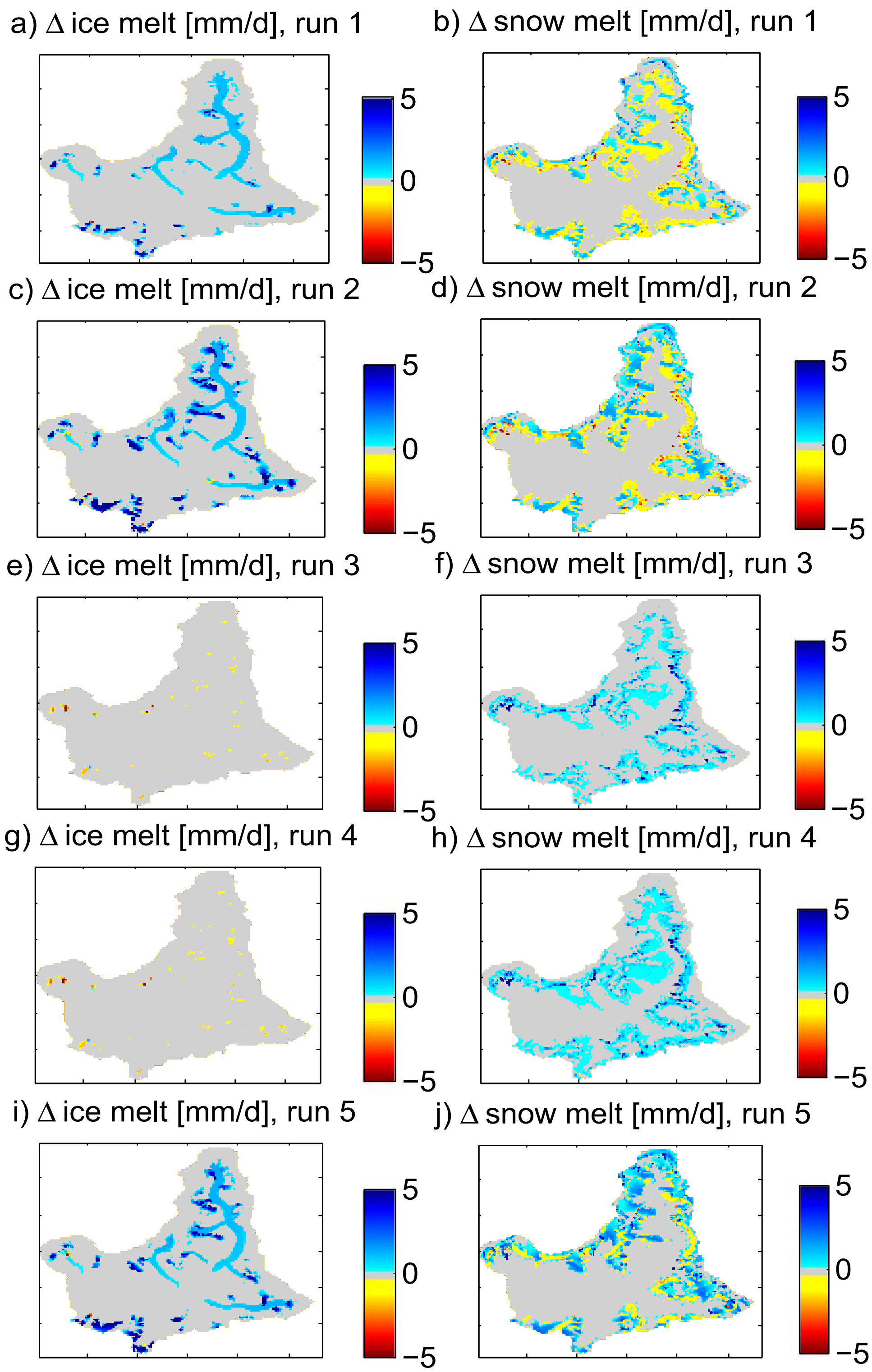

Figure 9. Effect of using different configurations for precipitation gradients and temperature lapse rates on the spatial distribution of mean annual simulated runoff, snow melt, glacier melt, and rain. The maps show the differences with respect to the reference run (run-reference run; Table 3) simulated for the period 2004–2010.

runs is mostly below that value (reference run, run 1, runs 3 and 4) or above (run 2). Validation against measured streamflow—the most common approach to validate glaciohydrological models—is not possible for Langtang because reliable streamflow data are not available for this period.

In runs 1 and 2 the temperatures are higher because the observed temperature lapse rates are shallower than the ELR. But since precipitation remains the same as for the reference run, less snow accumulation and more rain at lower elevations are simulated. Consequently, at lower elevations the model simulates also less snowmelt (yellow areas in Figures 9b and 9d). At higher elevations, in the accumulation areas of glaciers where annual snow accumulation exceeds annual snowmelt, the model simulates more snowmelt because of higher temperatures. Glacier-ice melt increases owing to less snow on glaciers and more melt due to higher temperatures (Figures 8c, 9a, and 9c). The highest increases of runoff, snow melt, and ice melt are simulated for run 2 and during July and August, due to very shallow temperature lapse rates during the monsoon period.

In runs 3 and 4 the overall precipitation is higher. With respect to the reference run, negative horizontal valley gradients lead only to less precipitation in a very small portion of the catchment, the valley bottom east of Kyangjin, where most of the precipitation falls in the form of rain. Everywhere else precipitation is higher due to the application of the observed steep elevation gradients. As the snow/rain transition remains at the same elevation as for the reference run, we simulate more snowfall and for areas below the equilibrium line altitude, more snowmelt (blue areas in Figures 9f and 9h). Overall simulated ice melt does not change significantly (Figure 8c). More snow accumulation also means more redistribution of snow due to gravitational snow transport. As a consequence, snowmelt below steep slopes increases disproportionately to the increases in precipitation (dark blue areas in Figures 9f and 9h). Since the thicker snowpack persists for a longer period on top of the glacier ice, increased avalanching can at some places significantly reduce ice melt (as it is the case for some Lirung glacier grid cells, dark red pixels in Figures 9e and 9g).

Concerning run 5, the mean monthly differences to the reference run are proportional to the differences reported for run 2, where the same temperature lapse rates were used (Figure 8a). Ice melt increases with respect to the reference run, despite more precipitation, but slightly less than in run 2 (Figure 8c). These model results suggest that the system is very sensitive to both changes in LRs and PGs: the effect of changing both at the same time leads to the strongest increase of simulated runoff with respect to the reference run (Figure 8a). However, using the observed monsoon temperature LRs for simulations (runs 2 and 5) has the most significant effect on simulated runoff, comparing to the other runs and the case where no observed data are used for simulations.

Based on these results, we therefore stress the importance of using observed LRs and PGs in glaciohydrological modeling studies, and also studies in other regions of the world confirm this [*Petersen and Pellicciotti*, 2011; *Pellicciotti et al*., 2014]. Short-term, low-cost campaigns can already provide crucial information that will greatly enhance the quality of such simulations.

4. Conclusions

In this study we analyze observed LRs and PGs acquired during a 1 year field campaign in 2012–2013 in the Langtang catchment in the central Himalaya in Nepal. We use these observations to improve our understanding of precipitation and temperature patterns in a catchment with extreme relief, and we discuss possible controlling mechanisms. We also illustrate how sensitive simulations with a glaciohydrological model are to observed LRs and PGs, and we draw the following conclusions.

There are four clearly detectable seasons over the year: a premonsoon season with a gradual increase in temperature and occasional precipitation; the monsoon season with daily precipitation, high temperatures, and a reduced diurnal range in temperature; a postmonsoon seasons with no precipitation and a gradual decrease in temperature; and the winter season with very low temperatures and frequent precipitation in the form of strong events and snowfall.

The precipitation patterns are complex, and PGs for the entire valley cannot be derived. There is a strong seasonal difference in the precipitation patterns and their controlling mechanisms. In the upper part of the catchment we do however identify a positive PG, which on an annual basis is 41% per 1000 m elevation rise. Our highest precipitation gauge was located at 4831 m, and despite the logistical constraints, it is important to extend the monitoring of precipitation at this and higher altitudes to be able to better constrain PGs and identify the altitude with maximum precipitation per season. The variation we identify also suggests that the use of satellite derived [*Huffman et al*., 2007] or large-scale gridded precipitation products

[*Yatagai et al*., 2012], which have a resolution in the order of 25 km, are questionable without further spatial downscaling using local information. The way precipitation fields are generated for glaciohydrological models needs to be reconsidered, and the use of field radars, hyperresolution weather models, and innovative proxies [*Immerzeel et al*., 2012a] is needed to further our understanding of precipitation dynamics in a monsoon-dominated climate with extreme topography.

The temperature analysis shows that valley LRs exist, and that there is a high correlation between temperature and elevation for all seasons. However, the LRs are shallower than the ELR, and there is high temporal variability on a seasonal and diurnal scale. These findings confirm other studies in mountain regions in the United States [*Minder et al*., 2010; *Mizukami et al*., 2013]. Both the temporal variability and the specific values should therefore be taken into account when generating input fields to glacier mass balance and runoff models.

LRs and PGs have a very large impact on the outputs of the glaciohydrological model used. The impact of the LRs is particularly large, and in specific months an increase of glacier melt of 400% is modeled. This is caused by the fact that the critical elevation below which snow falls as rain and below which melt occurs moves up just above the tongues of the main glaciers, and as a result the melt is amplified. Temperature measurements are relatively cheap, and a single year of observations has already great added value in constraining model parameters. Only the model run using measured seasonal LRs and PGs produces model output that compares well with observations of the ELA at Yala glacier, a benchmark glacier in the region [*Sugiyama et al*., 2013]. The Himalaya region is in urgent need for more complete analyses regarding the health of its glaciers [*Cogley*, 2011]. Our results are therefore of high relevance, given the fact that modeling studies are required to bridge the gap between process understanding at the point scale and remote sensing studies focusing on glacier changes.

Acknowledgments
The authors thank Mark Williams, Jessica Lundquist, and one anonymous reviewer for their constructive suggestions for improving this manuscript. The authors are grateful to all the people who assisted with the data collection, and in particular, Prashant Baral, Sonika Shahi, Martin Heynen, and Simon Wicki. The authors are very grateful to the HKH Cryosphere Monitoring Project implemented by the International Centre for Integrated Mountain Development (ICIMOD) and supported by the Norwegian Ministry of Foreign Affairs. They would also like the thank the project partners for their help in carrying out this study and for providing data in particular the Himalayan Cryosphere, Climate and Disaster Research Center of Kathmandu University and the Department of Hydrology and Meteorology and the Department of National Parks and Wildlife Conservation of the Government of Nepal. This study was partially funded by the Netherlands Organization for Scientific Research through their VENI program and by the South Asia Research Hub of the UK Department for International Development (DFID).

References

Bernhardt, M., and K. Schulz (2010), SnowSlide: A simple routine for calculating gravitational snow transport, *Geophys. Res. Lett.*, *37*, L11502, doi:10.1029/2010GL043086.

Bookhagen, B., and D. W. Burbank (2006), Topography, relief, and TRMM-derived rainfall variations along the Himalaya, *Geophys. Res. Lett.*, *33*, L08405, doi:10.1029/2006GL026037.

Chutko, K. J., and S. F. Lamoureux (2009), The influence of low-level thermal inversions on estimated melt-season characteristics in the central Canadian Arctic, *Int. J. Climatol.*, *29*(2), 259–268, doi:10.1002/joc.1722.

Cogley, J. G. (2011), Present and future states of Himalaya and Karakoram glaciers, *Ann. Glaciol.*, *52*(59), 69–73.

Dee, D. P., et al. (2011), The ERA-Interim reanalysis: Configuration and performance of the data assimilation system, *Q. J. R. Meteorol. Soc.*, *137*(656), 553–597, doi:10.1002/qj.828.

Finger, D., F. Pellicciotti, M. Konz, S. Rimkus, and P. Burlando (2011), The value of glacier mass balance, satellite snow cover images, and hourly discharge for improving the performance of a physically based distributed hydrological model, *Water Resour. Res.*, *47*, W07519, doi:10.1029/2010WR009824.

Finger, D., G. Heinrich, A. Gobiet, and A. Bauder (2012), Projections of future water resources and their uncertainty in a glacierized catchment in the Swiss Alps and the subsequent effects on hydropower production during the 21st century, *Water Resour. Res.*, *48*, W02521, doi:10.1029/2011WR010733.

Fujita, K., and A. Sakai (2000), Air temperature environment on the debris-covered area of Lirung Glacier, Langtang Valley, Nepal Himalayas, in *Debris-Covered Glaciers*, edited by M. Nakawo, C. F. Raymond, and A. Fountain, *IAHS Publ. 264*, pp. 83–88. Int. Assoc. of Hydrol. Sci., Wallingford, U. K.

Fujita, K., N. Takeuchi, and K. Seko (1998), Glaciological observations of Yala Glacier in Langtang Valley, Nepal Himalayas, 1994 and 1996, *Bull. Glacier Res.*, *16*, 75–81.

Gouvas, M. A., N. K. Sakellariou, and H. D. Kambezidis (2011), Estimation of the monthly and annual mean maximum and mean minimum air temperature values in Greece, *Meteorol. Atmos. Phys.*, *110*, 143–149, doi:10.1007/s00703-010-0111-y.

Huffman, G. J., R. F. Adler, D. T. Bolvin, G. Gu, E. J. Nelkin, K. P. Bowman, Y. Hong, E. F. Stocker, and D. B. Wolff (2007), The TRMM Multisatellite Precipitation Analysis (TMPA): Quasi-global, multiyear, combined-sensor precipitation estimates at fine scales, *J. Hydrometeorol.*, *8*(1), 38–55, doi:10.1175/JHM560.1.

Huwald, H., C. W. Higgins, M.-O. Boldi, E. Bou-Zeid, M. Lehning, and M. B. Parlange (2009), Albedo effect on radiative errors in air temperature measurements, *Water Resour. Res.*, *45*, W08431, doi:10.1029/2008WR007600.

Immerzeel, W. W., L. P. H. Van Beek, and M. F. P. Bierkens (2010), Climate change will affect the Asian water towers, *Science*, *328*(5984), 1382–1385, doi:10.1126/science.1183188.

Immerzeel, W. W., F. Pellicciotti, and A. B. Shrestha (2012a), Glaciers as a proxy to quantify the spatial distribution of precipitation in the Hunza basin, *Mt. Res. Dev.*, *32*(1), 30–38, doi:10.1659/MRD-JOURNAL-D-11–00097.1.

Immerzeel, W. W., L. P. H. Beek, M. Konz, a. B. Shrestha, and M. F. P. Bierkens (2012b), Hydrological response to climate change in a glacierized catchment in the Himalayas, *Clim. Change*, *110*, 721–736, doi:10.1007/s10584-011-0143-4.

Kattel, D. B., T. Yao, K. Yang, L. Tian, G. Yang, and D. Joswiak (2012), Temperature lapse rate in complex mountain terrain on the southern slope of the central Himalayas, *Theor. Appl. Climatol.*, *113*(3–4), 671–682, doi:10.1007/s00704-012-0816-6.

Konz, M., S. Uhlenbrook, L. Braun, A. Shrestha, and S. Demuth (2007), Implementation of a process-based catchment model in a poorly gauged, highly glacierized Himalayan headwater, *Hydrol. Earth Syst. Sci.*, *11*(1993), 1323–1339.

Lundquist, J. D., N. Pepin, and C. Rochford (2008), Automated algorithm for mapping regions of cold-air pooling in complex terrain, *J. Geophys. Res.*, *113*, D22107, doi:10.1029/2008JD009879.

Marshall, S. J., and M. J. Sharp (2009), Temperature and melt modeling on the Prince of Wales Ice Field, Canadian High Arctic, *J. Clim.*, *22*(6), 1454–1468, doi:10.1175/2008JCLI2560.1.

Minder, J. R., P. W. Mote, and J. D. Lundquist (2010), Surface temperature lapse rates over complex terrain: Lessons from the Cascade Mountains, *J. Geophys. Res.*, *115*, D14122, doi:10.1029/2009JD013493.

Mizukami, N., M. Clark, A. Slater, L. Brekke, M. Elsner, J. Arnold, and S. Gangopadhyay (2013), Hydrologic implications of different large-scale meteorological model forcing datasets in mountainous regions, *J. Hydrometeorol.*, doi:10.1175/JHM-D-13-036.1, in press.

Pellicciotti, F., B. Brock, U. Strasser, P. Burlando, M. Funk, and J. Corripio (2005), An enhanced temperature-index glacier melt model including the shortwave radiation balance: Development and testing for Haut Glacier d'Arolla, Switzerland, *J. Glaciol.*, *51*(175), 573–587.

Pellicciotti, F., J. Helbing, V. Favier, and J. Corripio (2008), A study of the energy balance and melt regime on Juncal Norte Glacier, semi-arid Andes of central Chile, using melt models of different complexity, *Hydrol. Processes*, *22*(19), 3980–3997, doi:10.1002/hyp.7085.

Pellicciotti, F., T. Raschle, T. Huerlimann, M. Carenzo, and P. Burlando (2011), Transmission of solar radiation through clouds on melting glaciers: A comparison of parameterisations and their impact on melt modelling, *J. Glaciol.*, *57*, 367–381.

Pellicciotti, F., M. Konz, W. W. Immerzeel, and A. B. Shrestha (2012), Challenges and uncertainties in hydrological modelling of remote Hindu Kush-Himalayan (HKH) basins: Suggestions for calibration strategies, *Mt. Res. Dev.*, *32*, 39–50.

Pellicciotti, F., S. Ragettli, M. Carenzo, and J. McPhee (2014), Changes of glacier in the Andes of Chile and priorities for future work, *Sci. Total Environ.*, doi:10.1016/j.scitotenv.2013.10.055, in press.

Pepin, N., and M. Losleben (2002), Climate change in the Colorado Rocky Mountains: Free air versus surface temperature trends, *Int. J. Climatol.*, *22*(3), 311–329, doi:10.1002/joc.740.

Petersen, L., and F. Pellicciotti (2011), Spatial and temporal variability of air temperature on a melting glacier: Atmospheric controls, extrapolation methods and their effect on melt modeling, Juncal Norte Glacier, Chile, *J. Geophys. Res.*, *116*, D23109, doi:10.1029/2011JD015842.

Ragettli, S., and F. Pellicciotti (2012), Calibration of a physically based, spatially distributed hydrological model in a glacierized basin: On the use of knowledge from glaciometeorological processes to constrain model parameters, *Water Resour. Res.*, *48*, W03509, doi:10.1029/2011WR010559.

Ragettli, S., and F. Pellicciotti (2013), A framework for the application of physically-oriented glacio-hydrological models in the Himalaya-Karakorum region based on a new approach of uncertainty evaluation, *AGU,* Fall Meet., Abstract C11A-0639.

Ragettli, S., F. Pellicciotti, R. Bordoy, and W. W. Immerzeel (2013a), Sources of uncertainty in modeling the glacio-hydrological response of a Karakoram watershed to climate change, *Water Resour. Res.*, *49*, 1–19, doi:10.1002/wrcr.20450.

Ragettli, S., G. Cortés, J. McPhee, and F. Pellicciotti (2013b), An evaluation of approaches for modelling hydrological processes in high-elevation, glacierized Andean watersheds, *Hydrol. Process*, doi:10.1002/hyp.10055.

Seko, K. (1987), Seasonal variation of altitudinal dependence of precipitation in Langtang Valley, Nepal Himalayas, *Bull. Glacier Res.*, *5*, 41–47.

Shiraiwa, T., K. Ueno, and T. Yamada (1992), Distribution of mass input on glaciers in the Langtang Valley, Nepal Himalayas, *Bull. Glacier Res.*, *10*, 21–30.

Steinegger, U., L. N. Braun, G. Kappenberger, and G. Tartari (1993), Assessment of annual snow accumulation over the past 10 years at high elevations in the Langtang Region, *IAHS Publ. 218*, pp. 155–166, Int. Assoc. of Hydrol. Sci., Wallingford, U. K.

Sugiyama, S., K. Fukui, K. Fujita, K. Tone, and S. Yamaguchi (2013), Changes in ice thickness and flow velocity of Yala Glacier, Langtang Himal, Nepal, from 1982 to 2009, *Ann. Glaciol.*, *54*(64), 157–162, doi:10.3189/2013AoG64A111.

Tahir, A. A., P. Chevallier, Y. Arnaud, L. Neppel, and B. Ahmad (2011), Modeling snowmelt-runoff under climate scenarios in the Hunza River basin, Karakoram Range, Northern Pakistan, *J. Hydrol.*, *409*, 140–117.

Takahashi, S., H. Motoyama, K. Kawashima, Y. Morinaga, K. Seko, H. Iida, H. Kubota, and N. R. Turadahr (1987), Meteorological features in Langtang Valley, Nepal Himalayas, 1985–1986, *Bull. Glacier Res.*, *5*, 35–40.

Ueno, K., and T. Yamada (1990), Diurnal variation of precipitation in Langtang valley, Nepal Himalayas, *Bull. Glacier Res.*, *8*, 93–101.

Viviroli, D., et al. (2011), Climate change and mountain water resources: Overview and recommendations for research, management and policy, *Hydrol. Earth Syst. Sci.*, *15*(2), 471–504, doi:10.5194/hess-15-471-2011.

Yatagai, A., N. Yasutomi, A. Hamada, A. Kitoh, K. Kamiguchi, and O. Arakawa (2012), APHRODITE: Constructing a long-term daily gridded precipitation dataset for Asia based on a dense network of rain gauges, *Bull. Am. Meteorol. Soc.*, *93*(9), 1401–1415.

Advances in Water Resources 78 (2015) 94–111

Contents lists available at ScienceDirect

Advances in Water Resources

journal homepage: www.elsevier.com/locate/advwatres

Unraveling the hydrology of a Himalayan catchment through integration of high resolution in situ data and remote sensing with an advanced simulation model

S. Ragettli [a,*], F. Pellicciotti [a], W.W. Immerzeel [a,b], E.S. Miles [c], L. Petersen [a], M. Heynen [a], J.M. Shea [d], D. Stumm [d], S. Joshi [d], A. Shrestha [d]

[a] Institute of Environmental Engineering, ETH Zurich, Zurich, Switzerland
[b] Department of Physical Geography, Utrecht University, Utrecht, Netherlands
[c] Scott Polar Research Institute, University of Cambridge, Cambridge, UK
[d] International Centre for Integrated Mountain Development, Kathmandu, Nepal

ARTICLE INFO

Article history:
Received 8 May 2014
Received in revised form 2 December 2014
Accepted 25 January 2015
Available online 2 February 2015

Keywords:
Himalayas
Mountain hydrology
Debris covered glaciers
Glacier mass balance
In situ measurements
Runoff modeling

ABSTRACT

The hydrology of high-elevation watersheds of the Hindu Kush-Himalaya region (HKH) is poorly known. The correct representation of internal states and process dynamics in glacio-hydrological models can often not be verified due to missing in situ measurements. We use a new set of detailed ground data from the upper Langtang valley in Nepal to systematically guide a state-of-the art glacio-hydrological model through a parameter assigning process with the aim to understand the hydrology of the catchment and contribution of snow and ice processes to runoff. 14 parameters are directly calculated on the basis of local data, and 13 parameters are calibrated against 5 different datasets of in situ or remote sensing data. Spatial fields of debris thickness are reconstructed through a novel approach that employs data from an Unmanned Aerial Vehicle (UAV), energy balance modeling and statistical techniques. The model is validated against measured catchment runoff (Nash–Sutcliffe efficiency 0.87) and modeled snow cover is compared to Landsat snow cover. The advanced representation of processes allowed assessing the role played by avalanching for runoff for the first time for a Himalayan catchment (5% of annual water inputs to the hydrological system are due to snow redistribution) and to quantify the hydrological significance of sub-debris ice melt (9% of annual water inputs). Snowmelt is the most important contributor to total runoff during the hydrological year 2012/2013 (representing 40% of all sources), followed by rainfall (34%) and ice melt (26%). A sensitivity analysis is used to assess the efficiency of the monitoring network and identify the timing and location of field measurements that constrain model uncertainty. The methodology to set up a glacio-hydrological model in high-elevation regions presented in this study can be regarded as a benchmark for modelers in the HKH seeking to evaluate their calibration approach, their experimental setup and thus to reduce the predictive model uncertainty.

1. Introduction

The Hindu Kush-Himalaya region (HKH) holds the largest volume of ice outside the polar regions and thus stores important freshwater resources [36]. Climate change is expected to have significant consequences on snowmelt and glacier runoff across the region (e.g. [42,53]). Understanding the present hydrological regimes and climatological and glaciological processes of high-elevation catchments is thus vital. This requires better insights into the present composition of runoff and interactions between climate, glaciers, snow and soil.

Our knowledge of high-altitude snow/ice and its response to climate is still incomplete [10,16]. In the Himalayas, fieldwork is difficult due to the remoteness of glaciers as well as logistical, financial and political obstacles. For this reason, in recent years the focus has been on remote sensing approaches used to reconstruct snow cover, frontal and areal changes of glaciers and ice volumetric changes (e.g. [29,46,83]). However, in the light of possible changes in the snow- and glacier-energy balance due to climatic changes, there is a strong call for more in situ measurements across the Himalayas and models that integrate those data in space and time [10,16,77]. Local processes and effects

* Corresponding author at: ETH Zurich, Institute of Environmental Engineering, Stefano-Franscini-Platz 5, 8093 Zurich, Switzerland. Tel.: +41 44 633 27 30.

E-mail address: ragettli@ifu.baug.ethz.ch (S. Ragettli).

http://dx.doi.org/10.1016/j.advwatres.2015.01.013
0309-1708/

that are difficult to study using remotely sensed data could explain regional differences and temporal changes in glacier mass balance across the region, such as the glacier expansion in the central Karakorum known as the 'Karakorum anomaly' [33]. Recent studies on the spatial variability of glacier extension and mass balance across the HKH point at the importance of varying monsoon and westerly winds influence on the local climate [46,93], but also of gravitational redistribution of snow, glacier flow dynamics and the interplay between glacier surface characteristics such as debris cover and albedo, topography and energy fluxes reaching the glacier surface [34].

Glacio-hydrological models are indispensable tools to study these effects and to understand the characteristics of a catchment and its response to climate. They are however subject to a number of factors that complicate their applicability in high elevation regions: (i) the lack of representative data to force the models [37,67], (ii) simplifications in model structure due to insufficient process understanding and the scarcity of detailed information about glacio-hydrological processes [37] and (iii) parametric uncertainty due to insufficient quality or paucity of data for model calibration and validation (e.g. [75]). A growing number of studies have assessed the relation between snow- and/or glacier changes and runoff production at the catchment scale in the HKH using models (e.g. in the Central Himalaya: [41,42,48,49,59,70], or in the Karakorum: [9,66,75]). However, the applied models were calibrated using a maximum of two response variables (usually runoff and/or remotely sensed snow cover). Many studies have not included observations about the cryosphere other than initial glacier outlines (e.g. [59,70,75]). The use of only one or two response variables increases the risk that many combinations of parameters yield the same result, which leads to a large degree of predictive uncertainty [8]. Also, most previous modeling studies do not use meteorological data from stations above 4000 m asl – where most glaciers are. Finally, data scarcity is also the reason why the effect of variable debris thickness on glacier melt is rarely considered and why there is no previous modeling study in the HKH region which reproduces observed avalanche patterns.

The present study has two main goals. First, to provide high resolution (temporally and spatially) simulations of the full water balance of a high-elevation catchment in the HKH to improve our understanding of the role of cryospheric processes for streamflow generation. These simulations (i) incorporate high elevation data as model inputs, (ii) make use of state-of-the art algorithms to model the relevant processes, and (iii) use local data to constrain parametric uncertainty and limit equifinality problems. The second goal is to provide recommendations on network design and the timing and location of field measurements, in order to collect the data that can be most efficiently used to constrain the uncertainties of the glacio-hydrological model. For this purpose we developed an approach that assesses the capacity of model parameters and variables to explain uncertainty in a given model output [75]. For the present study this approach is also used to assess the effectiveness of ongoing monitoring programs within the study catchment, the upper Langtang catchment in Nepal.

This study presents thus a methodological framework to set up a glacio-hydrological model for a high-elevation Himalayan catchment. We make use of a unique set of ground data combined with high resolution satellite observations to inform our choice of model parameters. Through advanced high-resolution modeling we provide a fundamental understanding of the role of individual processes for streamflow generation in a Himalayan head-water catchment. The methodology enables a detailed assessment of the state of the glaciers within the catchment, their role in runoff production and the processes controlling their response to climate.

2. Study area and climate

This study focuses on the upper Langtang catchment, located approximately 50 km north of Kathmandu, Nepal (Fig. 1). The catchment has an area of 350 km^2, with a total glacier portion of 33.8%, of which 27% are debris covered. Only at the less steep slopes along the main river sparse forest and grassland exists (approximately 1.5% of the catchment area [48]). Boulders and scree cover the steep slopes and high plateaus. The outlet of the upper Langtang catchment is at 3650 m asl (Fig. 1a).

The tongues of the largest glaciers within the catchment are debris covered (Table 1). Field observations indicate that the composition of the debris layer is highly heterogeneous, from very fine silt to large boulders exceeding several meters in height. The largest glacier is Langtang Glacier, in the northeast of the catchment. The Lirung Glacier, with the greatest elevation range (4040–7180 m asl) has been the site of several glaciological investigations in the past [57,78–80]. Other glaciological studies focused on Yala Glacier, a non-debris covered glacier [1,4,22,24,25,88]. Glacierization and snow cover in the catchment have been documented by Iida et al. [38], Shiraiwa et al. [84] and Steinegger et al. [86] and more recently by Pellicciotti et al. [68].

The climate in the Langtang valley is monsoon dominated and approximately 70% of the annual precipitation falls during the monsoon (mid-June–September, [43]). Outside of this period precipitation is limited and is produced by the occasional passage of westerly troughs during post-monsoon (October–November) or winter (December–February). Localized convective precipitation events occur during the pre-monsoon (March–mid-June, [43]). Seasonally, temperatures are highest during the monsoon, with rising (falling) temperatures during the pre-monsoon (post-monsoon) periods.

3. Data and methods

The modeling approach presented in this study aims at making maximal use of in situ data for the estimation and calibration of model parameters. The instruments that have been installed since May 2012 and that provide data for this study are

- Two permanent automatic weather stations (AWSs) at Kyangjing (AWS K, 3862 m asl) and near Yala Glacier (AWS Y, 5090 m asl).
- A pluviometer and a sonic ranging sensor near Yala Glacier (Pluvio, 4831 m asl) [43].
- Two temporary AWSs on Lirung Glacier (AWS L-G, 4164 m asl) and on Yala Glacier (AWS Y-G, 5204 m asl).
- Tipping buckets and temperature sensors (T-Loggers) installed at various locations in the main valley [43].
- T-Loggers installed on Lirung Glacier.
- Stakes installed on Yala Glacier for mass balance observations [4].
- Newly equipped hydrological stations for runoff measurements at the outlet and near Lirung Glacier.

The characteristics and locations of the hydro-meteorological stations are provided in Table 2. Locations are shown in Fig. 1. Station data are complemented by data measured manually in the field (debris thickness, snow density, terminus position of Lirung Glacier). New rating curves were obtained in 2012 and 2013 for Langtang Khola (at the outlet of the upper Langtang catchment) and Lirung Khola (near Lirung Glacier) by tracer (constant-rate injection) and current meter measurements and coincident observations of stream height from an automated pressure level transducer at Lirung Khola and a radar water level sensor at Langtang

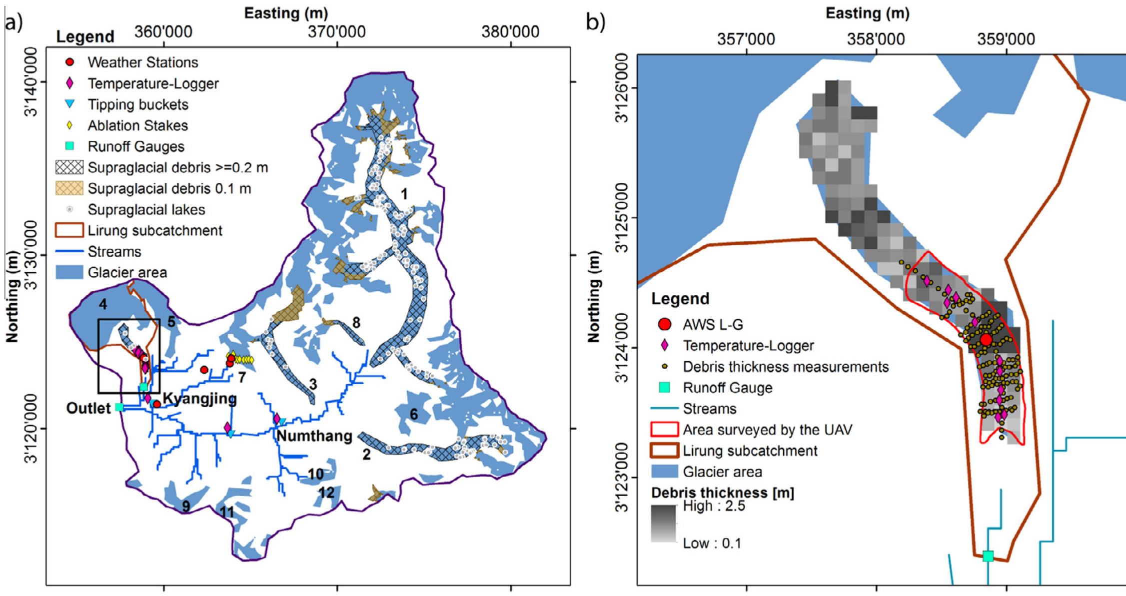

Fig. 1. (a) Map of the upper Langtang catchment showing the position of meteorological stations and streamgauges (Table 2), tipping buckets and temperature loggers, ablation stakes and Landsat ETM+ derived supraglacial lakes. The numbers on the map indicate the locations of glaciers listed in Table 1. (b) Map of the glacier tongue of Lirung Glacier. The Unmanned Aerial Survey System (UAV) range shows the area that has been mapped by airborne stereo imagery in May and October 2013. The debris thickness values within the UAV range indicate reconstructed debris thickness, and outside the UAV range the randomly sampled reconstructed debris thickness.

Table 1
Names and characteristics of glaciers within the upper Langtang valley.

Name	ID	Area [km^2]	Elevation range [m asl]	Mean elevation [m asl]	Debris cover (%)	Mean slope (%)	Main aspect [°]	Mass balance [m w.e./a]	AAR (%)	IC rank	IC rank elev. corrected
Langtang	1	57.1	4490–7160	5510	35	46	230	−0.13	55	9	12
Langshisha	2	16.8	4420–6840	5520	33	43	310	−0.21	50	7	10
Shalbachum	3	11.6	4210–6690	5380	37	49	147	−0.36	37	8	11
Lirung	4	11.3	4040–7180	5490	10	94	130	−0.80	22	6	3
Kimoshung	5	4.2	4400–6360	5610	0	39	215	0.69	83	10	6
Langshisha Ri	6	2.7	4970–6270	5770	0	47	191	0.52	78	12	7
Yala	7	1.6	5170–5630	5370	0	42	211	−0.17	44	3	5
Ghanna	8	1.4	4720–5860	5150	56	45	71	−0.57	24	5	9
Urkin Kangari	9	1.3	5110–5450	5300	0	23	11	−0.92	13	1	2
Gangchenpo 1	10	1.3	4990–5880	5450	0	46	292	0.58	56	4	4
Kanja La	11	1.2	5100–5830	5320	0	29	45	−0.71	28	2	1
Gangchenpo 2	12	1.1	5140–6300	5760	0	72	220	0.16	29	11	8

Only glaciers with an area larger than 1 km^2 are shown. Locations of glaciers are indicated in Fig. 1a. *Mass Balance*, Accumulation area ration (*AAR*) and information content (*IC*) ranks are modeling results that correspond to the model setup tested by case 8 (Table 4). *Slope* is the ratio between vertical and horizontal distance, *Aspect* is expressed clockwise from north.

Table 2
Characteristics and location of the hydro-meteorological stations used in this study.

Station	Code	Elevation (m asl)	Latitude	Longitude	Location	Period of functioning
AWS Kyangjing	AWS K	3862	28.2108	85.5695	Kyangjing village	01 May 2012–17 Nov 2013
AWS Lirung Glacier	AWS L-G	4164	28.2349	85.5613	Lirung Glacier tongue	13 May 2012–25 Oct 2012, 9 May 2013–23 Oct 2013
AWS Yala	AWS Y	5090	28.2325	85.6121	Close to Yala Glacier	01 May 2012–17 Nov 2013
AWS Yala Glacier	AWS Y-G	5204	28.2352	85.6127	Yala Glacier ablation area	7 Jun 2012–20 Jun 2012
Pluviometer Yala	Pluvio	4831	28.2290	85.5970	near Yala	08 May 2012–11 Jun 2013
Lirung Khola streamgauge	Lirung Q	3971	28.2199	85.5617	Outlet Lirung subcatchment	1 May 2013–17 Nov 2013
Langtang Khola streamgauge	Langtang Q	3652	28.2091	85.5475	Study catchment outlet	01 Apr 2012–17 Nov 2013

Khola. We also use remotely sensed data of snow cover (Landsat ETM+ and MODIS) and stereo imagery provided by an Unmanned Aerial Vehicle (UAV). Landsat ETM+ data were atmospherically-corrected via the LandCor implementation of the 6S radiative transfer model [50,94]. The UAV dataset is used to obtain high-resolution digital elevation models (DEMs) of Lirung Glacier that provide surface height changes and is described in detail in [40].

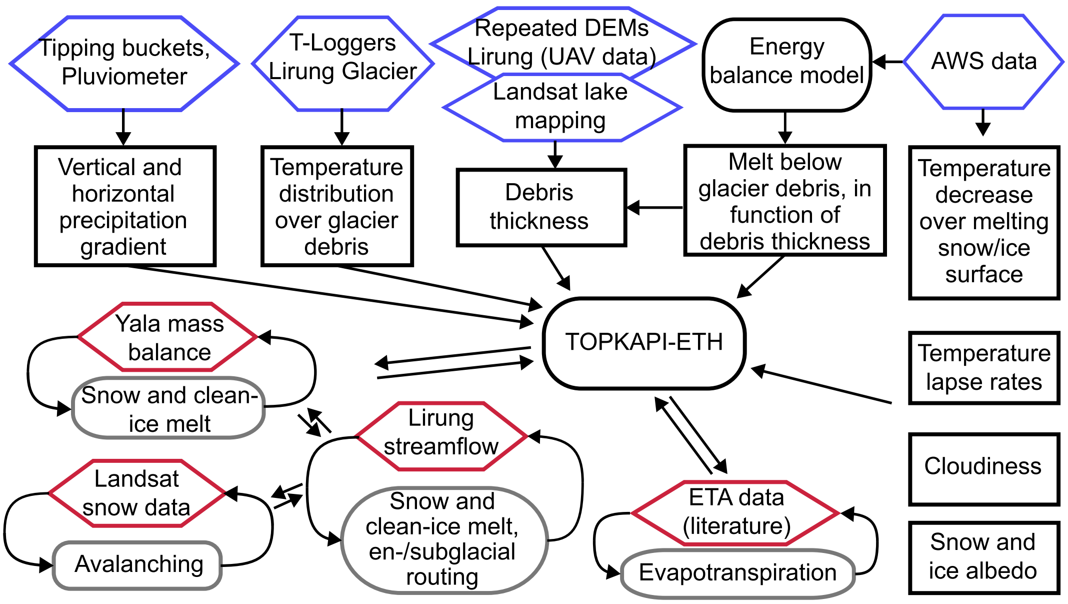

Fig. 2. Scheme of the methodology developed to estimate optimal model parameters for the upper Langtang valley making maximal use of available in situ data. Rectangular boxes represent model parameters that are directly calculated using local data (blue hexagons). Those parameters are kept fixed during the calibration of other model components – represented by gray rounded shapes – against the calibration datasets (red hexagons). (For interpretation of the references to color in this figure legend, the reader is referred to the web version of this article.)

Sections 3.2–3.9, describe how the data are used by the model as input, for parameter estimation and for model validation. An overview about how the local data are used for calibration of TOPKAPI-ETH parameters is provided in Fig. 2.

3.1. The glacio-hydrological model TOPKAPI-ETH

The model used in this study is the process-oriented, distributed model TOPKAPI-ETH. The model has been applied in numerous hydrological studies of high-elevation watersheds in the Andes [73,74], Alps [18–20] and Karakorum [66,75]. In this study, TOPKAPI-ETH is applied with a grid resolution of 100 m and an hourly temporal resolution. In comparison with previous TOPKAPI-ETH applications, the model structure is identical except for the new glacier debris component, which now allows taking into account the effect of a spatially variable debris thickness on melt. The most important model components and parameters are listed in Table 3. Details about the model components are presented in Sections 3.3–3.8.

3.2. Input data

The model requires air temperature, precipitation and cloudiness as input data. Hourly temperature and precipitation are measured in Kyangjing (Fig. 1) at AWS K and extrapolated to every model grid cell (see Section 3.3). The ratio of measured incoming shortwave radiation and modeled potential clear-sky radiation at AWS K is used to calculate cloud transmissivity (*CT*) factors. Potential clear-sky global irradiance is simulated with a non parametric model based on Iqbal [44] accounting for the position of the sun relative to every grid cell at each time step. The vectorial algebra approach proposed by Corripio [17] is used for the interaction between the solar beam and terrain geometry. The hourly CT factors, which are constant in space, multiply the modeled clear-sky incoming shortwave radiation.

The high temporal resolution chosen constrains the possible simulation period, as AWS K providing the hourly input data was installed on 1 May 2012. We use the period between 1 May 2012 and 17 Nov 2012 to initialize the model. The annual water balance and runoff simulations are calculated for the period 18 Nov 2012–17 Nov 2013.

3.2.1. DEM, glacier and debris maps

A 30 m resolution ASTER Global Digital Elevation Model (GDEM) dataset (available on <http://gdem.ersdac.jspacesystems.or.jp>) resampled to 100 m resolution is used in this study. The vertical accuracy is between 10 and 15 m in area with slopes less than 30° [26,60].

For the debris covered glaciers in the valley, accounting for 82% of the total glacier area, the debris and glacier maps are provided by Pellicciotti et al. [68], where glaciers were manually delineated using three Landsat scenes from 2008, 2009 and 2010. For other glaciers, we use information from two available regional glacier maps: (i) a map based on a semi-automated object-based classification method using Landsat TM7 imagery around the period 2003 [3]; and (ii) a map of manually delineated glacier outlines based on Landsat images taken from 1999 to 2003 [61]. The final glacier and debris maps are shown in Fig. 1a. Since the simulation period in this study is only 1.5 years, no changes of glacier or debris area over time are assumed.

3.3. Extrapolation of meteorological input data

Temperature is extrapolated to every grid cell using hourly lapse rates calculated between air temperature measured at AWS K (3862 m asl) and AWS Y (5090 m asl). Seasonal and diurnal variability of temperature lapse rates in the Langtang valley are discussed in detail by Immerzeel et al. [43].

To account for the cooling effect of snow and ice surfaces, when extrapolated air temperatures over these surfaces are above 0 °C, the lapsed air temperatures are corrected with the parameter T_{mod}. T_{mod} is constant and calculated from the mean difference between air temperature extrapolated at AWS Y and measured at AWS Y-G (Table 3). Local air temperature variations over debris are also accounted for with a constant parameter ($T_{moddebris}$), as debris has been shown to warm up to very high values during the day

Table 3
Summary of all TOPKAPI-ETH parameters that are included in the calibration scheme (Fig. 2).

Name	Unit	Description	Value(s)	Reference or calibration data	Comments
Distribution of meteorological input					
PGv	% km^{-1}	Vertical precipitation gradient	Seasonal	AWS K, Pluvio, Tipping buckets	Values as in [43]
PGh	% km^{-1}	Horizontal precipitation gradient	Seasonal	AWS K, Pluvio, Tipping buckets	Values as in [43]
LR	°C m^{-1}	Temperature lapse rate	Hourly	AWS K, AWS Y	Measured hourly lapse rates
T_{mod}	°C	Temperature decrease over snow and bare- ice	0.71	AWS Y, AWS Y-G	Mean difference between lapsed temperatures from AWS Y and measured at AWS Y-G; standard deviation 0.46 °C
$T_{moddebris}$	°C	Temperature increase over glacier debris	0.75	AWS K, Lirung T-Loggers	Mean temperature difference between lapsed temperatures and interpolated temperatures between Lirung T-Loggers, debris covered Lirung Glacier tongue, 1 May–30 Sep 2013. Standard deviation over 117 grid cells: 0.07°C
Avalanching					
SGR_a, SGR_C	m, –	Snow holding depth dependent on the slope angle; exponential regression function	250, 0.17245	Landsat snow cover	Calibration against avalanched snow cover on the Lirung debris covered glacier tongue, 9 and 25 Oct 2013: mean difference in snow cover 0.01 km^2 or 6.25%
Snow-& ice melt					
α_1	–	Albedo of fresh snow	0.83	AWS Y	Mean measured fresh snow albedo at AWS Y of 12 snowfall events in 2013; standard deviation 0.04
α_2	–	Decay of snow albedo	0.34	AWS Y, Yala stakes	(1) Calibration simulated against measured albedo at AWS Y, 20 April–24 June 2013, RMSE 0.16. (2) calibration against Yala MB (Fig. 4)
α_{reset}	mm d^{-1}	Threshold precipitation rate to reset snow albedo	1	AWS Y	Minimum precipitation rate of 12 observed snowfall events in 2013 at AWS Y
$\alpha_{glacier}$	–	Albedo of bare-ice (glacier surface)	0.25	AWS Y-G	Mean measured value; standard deviation 0.03
SRF		ETI melt model (Eq. (1))	0.00625	Yala MB, Lirung Q	Calibration results in Fig. 4
TF		ETI melt model (Eq. (1))	0.18	Yala MB, Lirung Q	Calibration results in Fig. 4
T_T, P_T	°C	Threshold temperature for melt onset and for for precipitation state transition	1	Literature	With daily time steps often around 0°C [11,39,48], but higher values with hourly time steps (snow depth observations by sonic ranging sensor and measured temperatures at Pluvio)
Subdebris ice melt					
TF_{d1}, TF_{d2}		Debris-ETI melt model (Eq. (2) and (4))	0.03, 0.8	AWS L-G, Energy balance melt model (EB model)	Calibration results in Figs. 3 and 4
SRF_{d1}, SRF_{d2}		Debris-ETI melt model (Eq. (2) and (5))	0.005, 7	AWS L-G, EB model	Calibration results in Figs. 3 and 4
lag_1, lag_2	m^{-1}, –	Debris-ETI melt model (Eq. (2) and (3))	16, 2	AWS L-G, EB model	Calibration results in Figs. 3 and 4
α_{debris}	–	Debris albedo	0.15	AWS L-G	Median of measured debris albedo at AWS L-G, 10 May to 22 Oct 2013, standard deviation 0.03
d	*m*	Debris thickness	0.1–2.5	UAV, EB model, field data Lirung	See Fig. 4
Glacial meltwater routing					
K_{ice}	*h*	Storage constant for ice melt	72	Lirung Q	Calibration results in Fig. 4
K_{snow}	*h*	Storage constant for snowmelt on glaciers	240	Lirung Q	Calibration results in Fig. 4
Evapotranspiration					
CropF	–	Crop factors of evapotranspiration	0.05–1.30	Literature	Calibration against measured actual evapotranspiration (ETA) in Kyangjing by Sakai et al. [81], 15 July–29 August 1996. Simulated ETA during the same period in 2013: 95.3% of measured ETA in 1996
ET_{debris}	%	Evaporation from glacier debris, per mm monsoon precipitation	25	Literature	Value adopted from Sakai et al. [81]

[13]. The correction is based on observations at temperature loggers installed on Lirung Glacier during the monsoon period in 2012 and 2013 (Fig. 1b, Table 3).

Seasonal horizontal and vertical precipitation gradients are taken from [43]. The study found vertical precipitation gradients in the Langtang valley with between 31%–53% precipitation increase per kilometer vertical distance, depending on the season of the year. The horizontal valley gradient was derived from precipitation data recorded at tipping buckets (Fig. 1a) installed in the upper Langtang valley but was found to be relatively weak (mostly less than ±0.6% per kilometer). Previous modeling studies [41,42,48,49] have used a stronger horizontal valley gradient of −3% km^{-1}, based on observations by Shiraiwa et al. [84]. No new data are available in the eastern half of the catchment (Fig. 1a), and the observations by Shiraiwa et al. [84] are only based on snow pack data from five locations in the winter 1989/1990. Thus, we test the effect on simulated streamflow and snow cover of different assumptions of horizontal precipitation gradients upstream of the easternmost tipping bucket (Numthang), after calibration of all other model parameters. The horizontal precipitation gradients are tested independently for pre-monsoon/monsoon (March–September) and for post-monsoon/winter (October–February).

3.4. Avalanching

Gravitational snow transport is modeled using the approach by Bernhardt and Schulz [7], where a maximum snow holding depth is defined as an exponential function of slope. Snow exceeding the threshold depth is moved to the next model grid cell downwards. The two parameters of the exponential regression function (SGR_a, SGR_C) need to be calibrated. Since for safety reasons it is impossible to measure the maximum snow holding depth in the field, modeled avalanche patterns are calibrated against Landsat ETM+ snow cover (SC) data at the upper end of the debris covered Lirung Glacier tongue. The area above Lirung tongue has a mean slope of more than 100% and ranges from 4500 to 7200 m asl. It is known from field observations that avalanches are very common at this location after major snowfall events and avalanche cones are large enough to be identified by Landsat 30 m resolution imagery. Two Landsat SC images from October 2013 are chosen for comparison (October 9th and 25th). Twelve more images from 2013 would be available, but are not suitable for comparison due to clouds or extensive snow cover. The scene from 9 October 2013 shows only 1.4% snow cover in the catchment for the elevation range 4365–4520 m asl (which comprises the upper end of Lirung tongue), while at the same elevation on Lirung Glacier 71.4% of the area was snow covered. For calibration of the avalanching model component, TOPKAPI-ETH is run for more than 150 possible parameter combinations of SGR_a and SGR_C. Other model parameters are independently defined (Fig. 2) and maintained constant. The optimal parameter combination is determined by choosing the model run which shows the lowest mean difference in total snow cover over the debris covered tongue.

To constrain the possibility that the simultaneous calibration of snow and bare-ice melt parameters (Section 3.5) affects the calibration of gravitational snow transport parameters, we perform several calibration iterations. The iteration loop ends when optimal parameters SGR_a and SGR_C do not vary anymore from one iteration to the next.

3.5. Snow- and bare-ice melt

Snow- and bare-ice (debris-free) melt is computed using an Enhanced Temperature-Index (ETI) approach [64,65]:

$$\mathrm{M}_i = \begin{cases} \mathrm{TF} \cdot \mathrm{T}_i + \mathrm{SRF} \cdot \mathrm{I}_i \cdot (1 - \alpha_i) & \mathrm{T}_i \geqslant \mathrm{T}_T \\ 0 & \mathrm{T}_i < \mathrm{T}_T \end{cases} \quad (1)$$

Melt (M, mm w.e. h^{-1}) in each grid cell i is a function of an air temperature (T, °C) dependent term including an empirical temperature factor TF (mm w.e. $\mathrm{h}^{-1}\,°\mathrm{C}^{-1}$) and a shortwave radiation dependent term that uses the distributed incoming shortwave radiation (I, Wm^{-2}), an empirical parameter SRF (m^2mm w.e. W^{-2} h^{-1}) and snow or ice albedo (α). T_T is the threshold air temperature for melt onset.

Bare-ice albedo is constant in space and is calculated as the mean ratio of incoming and reflected shortwave radiation measured at AWS Y-G during June 2012. The decrease of fresh snow albedo (α_1) is modeled as a logarithmic decay in function of cumulated daily maximum positive air temperatures, controlled by an empirical parameter α_2 [12]. Each time precipitation exceeds a snowfall threshold rate α_{reset}, snow albedo is reset to α_1. The parameters α_1, α_2 and α_{reset} are estimated using data measured at AWS Y. Details are provided in Table 3.

The parameters TF and SRF are calibrated simultaneously against the observed mass balances at eight ablation stakes on Yala Glacier and against measured runoff at the outlet of the Lirung Glacier subcatchment (Fig. 2). The advantage of this approach is that the uncertainty in parameter identification can be reduced by evaluating the model against a number of responses representing different aspects of the hydrological functioning of the catchment (e.g. [2]). The effect of potential measurement errors on optimal parameters can also be mitigated [5].

Lirung runoff data are discussed in Section 3.7. The mass balance obtained from stake readings between 10 November 2011 and 3 November 2012 and the location of the stakes on Yala Glacier are described in [4]. The present study uses stake readings from 3 November 2012, 8 May 2013 and 18 November 2013. The mass balances calculated between 3 November 2012 and 8 May 2013 are not used for calibration, to prevent possible error compensation due to inaccuracies in simulated winter snow accumulation.

The parameter α_2 is also included in the calibration against Yala mass balance observations (5190–5501 m asl), to obtain a second estimate of snow albedo evolution. Albedo parameters are kept constant when calibrating TF and SRF against Lirung runoff. Therefore, an optimal α_2 is determined for each pair TF-SRF on the basis of the Yala mass balance data, and this α_2 is then used for each pair TF-SRF during calibration against Lirung streamflow.

3.6. Sub-debris ice melt

The presence of supraglacial debris strongly affects ablation (e.g. [13,62,95]). For this study, TOPKAPI-ETH was modified to account for the debris thickness feedback on melt. The sub-debris ice ablation model implemented is based on work by Mabillard [54] and has been tested on Miage and Arolla glacier in the Alps [15]. Ice melt below debris is calculated using a modified version of the ETI melt model that can take into account the melt reducing effect of varying debris thickness and hereafter is called debris-ETI (dETI) model:

$$\mathrm{M}_i(t) = \begin{cases} \mathrm{TF}_d \cdot \mathrm{T}_i(t - lag) + \mathrm{SRF}_d \cdot \mathrm{I}_i(t - lag) \cdot (1 - \alpha_i) & \mathrm{T}_i \geqslant \mathrm{T}_T \\ 0 & \mathrm{T}_i < \mathrm{T}_T \end{cases} \quad (2)$$

where $M_i(t)$ is simulated melt (mm w.e. h^{-1}) for each grid cell i and time step t, T is air temperature (°C), I is incoming shortwave radiation ($\mathrm{W\,m}^{-2}$), α is debris albedo and T_T is the threshold air temperature for melt onset. In contrast to the original ETI equation (Eq. (1)), a parameter lag has been introduced. This parameter has a unit h and varies in function of debris thickness, to take into account that the effect of air temperature and shortwave radiation on melt is temporally delayed by the debris:

$$lag = lag_1 \cdot d - lag_2 \quad (3)$$

where d is debris thickness (units of m) and lag_1 and lag_2 are two empirical parameters. Both SRF_d and TF_d (Eq. (2)) also vary with debris thickness:

$$\mathrm{TF}_d = \mathrm{TF}_{d1} \cdot d^{-\mathrm{TF}_{d2}} \quad (4)$$

$$\mathrm{SRF}_d = \mathrm{SRF}_{d1} \cdot e^{-\mathrm{SRF}_{d2} \cdot d} \quad (5)$$

TF_{d1}, TF_{d2}, SRF_{d1} and SRF_{d2} are empirical parameters which need to be calibrated. The physics of the energy exchange between surface and atmosphere and within the debris layer is best represented by physically-based models. Energy balance (EB) models have very good performance when high quality input data are available (e.g. [65,76]), but their use is more questionable at the distributed scale or with extrapolated data [28]. We therefore assume that a dEB model provides the best estimates of ablation at the location of AWS Lirung Glacier (AWS L-G). The dETI model is compared to the debris-EB (dEB) model of Reid and Brock [76] at AWS L-G to ensure appropriate parameter selection. To test the validity of the dEB model, modeled surface temperatures were validated against measured data [92]. This study uses the dEB results for a debris thickness range of 0.1–2.5 m and for the period 19 May 2013–21 Oct 2013 (Fig. 3). The parameters of the dETI model are calibrated against the outputs of the dEB model by minimizing the mean of the root mean square error of hourly melt rates for the tested range of debris thickness.

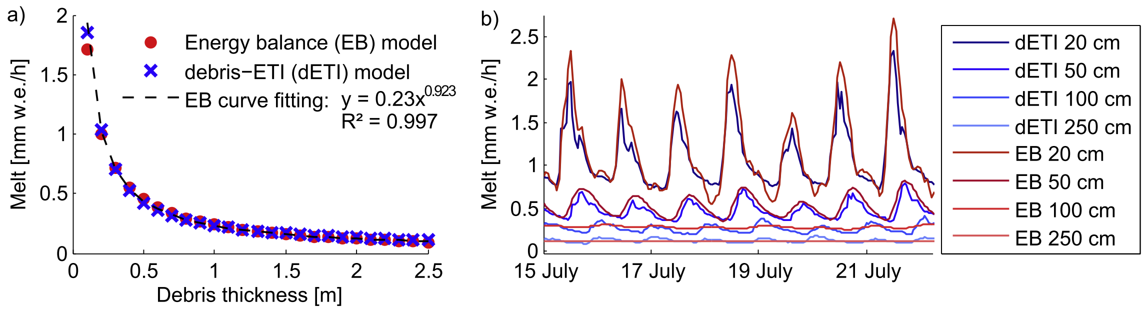

Fig. 3. (a) Energy balance (EB) and debris-enhanced temperature index (dETI) melt model outputs for given debris thicknesses (simulations for the period 19 May 2013–21 Oct 2013). The dashed line represents the Østrem curve that has been fitted to the results of the EB model. (b) Close-up view of model results corresponding to debris thicknesses of 20, 50, 100 and 150 cm for the period 15–22 July 2013.

More than 350'000 possible parameter combinations of lag_1, lag_2, TF_{d1}, TF_{d2}, SRF_{d1} and SRF_{d2} were tested.

3.6.1. Debris thickness estimation

The surface properties of a debris covered glacier are highly heterogeneous, with a rugged topography, ice cliffs and supraglacial ponds [6,68]. Ground-based observations of debris thickness can only provide a rough estimate of the debris thickness distribution, and were conducted only on Lirung Glacier (the transects where debris thickness was mapped are shown in Fig. 1b). The debris was mostly too thick to be sampled by manual methods (in 92.8% of all cases debris was thicker than 50 cm). Debris thickness can be estimated by methods that are based on remote sensing such as the ones described by Mihalcea et al. [55], Zhang et al. [95], and Foster et al. [21] or by Fujita and Sakai [23]. Empirical methods such as Mihalcea et al. [55] are site specific and require large amount of in situ data for calibration. The more physically based method by Foster et al. [21] failed to reconstruct the thick debris of Lirung Glacier, likely because of the assumption of a linear temperature gradient within the debris and lack of knowledge of surface temperature distribution [69]. In this study, we therefore propose a new approach that makes use of several available datasets to map debris thickness.

First, two high resolution DEMs obtained from UAV flights at the beginning (19 May) and at the end (21 Oct) of the ablation season 2013 are used to quantify the mass loss at Lirung Glacier glacier between the two dates. The glacier surface height changes are aggregated to the TOPKAPI-ETH 100 m grid and converted into meter water equivalents (m w.e.) of melt assuming a density of ice of 900 kg m^{-3}. The Østrem curve is derived using the dEB model at the location of AWS L-G as described in Section 3.6. This curve (equation indicated in Fig. 3a) is used to assign a debris thickness to each TOPKAPI-ETH glacier grid cell in the UAV survey from the cell ablation rate, assuming that the Østrem curve is the same over the entire tongue.

Vertical emergence of the glacier would cause an error in the quantification of ice loss and therefore in the debris thickness estimates. Overall this error is likely to be limited as the flow velocity of the Lirung Glacier is very small [40]. However, there is a small region near AWS L-G (Fig. 1b) where emergence occurs [40]. From field observations we know that this area is characterized by thick debris cover. In order to prevent unrealistic debris thickness values due to very small elevation changes or increasing surface height, maximum debris thickness is limited to 2.5 m.

The inverse Østrem approach is used to calculate debris thickness on the lower half of the Lirung Glacier tongue, in the area covered by the UAV survey (Fig. 1b). Then, the thickness of all debris covered glacier areas are sampled from the debris thickness estimates from Lirung Glacier, and satellite imagery is used to distinguish between the most important debris surface characteristics for the random sampling. The presence of lakes and ice cliffs affect the reconstructed debris thickness estimates, and they are taken into account in an indirect way. A supraglacial lake map from May 2012 is thus used to identify the concentration of supraglacial ponds. A map of supraglacial cliffs is not available, thus we assume that the fraction of cliffs correlates with the presence of lakes [95]. If a 50 m elevation band of a debris covered glacier includes supraglacial ponds, the debris thickness of those grid cells is sampled randomly from 50 m elevation bands within the UAV survey area that do include ponds. The same is done for 50 m elevation bands that do not include ponds, and separately for the lowest 50 m elevation band of each debris covered glacier, in order to account for the effect of frontal ablation on reconstructed debris thickness. The spatial density of supraglacial lakes and cliffs is thus used as a proxy for spatial variations in the equivalent debris thickness when sampling the debris thickness estimates from Lirung Glacier. The supraglacial lake map is described in Pellicciotti et al. [68] and is constructed from Landsat ETM+ multispectral data. The locations of the ponds are indicated in Fig. 1a.

Few previous studies have shown a mild dependency of debris thickness on elevation [21,47,95], but these relationships were all obtained along one longitudinal profile neglecting the transverse variability, which our field observations showed was large. At Lirung Glacier, thick debris accumulated through rockfall and avalanches appears right below the glacier cirque. On the basis of our observations from the field a gradual increase of debris thickness along the entire glacier is not evident for such glaciers. Due the lack of an established functional dependence of thickness on elevation or other topographical variables we thus apply the random sampling approach described above. However, 12.9% of the total debris covered area at the upper end of the tongues is excluded from the random sampling, and only a shallow debris thickness of 0.1 m is assumed here (Fig. 1a) in accordance with the results of Zhang et al. [95], who found that debris thickness varied between 0 and 20 cm in the uppermost section of debris covered area. We assign such shallow debris thickness to glacier area where a discrepancy exists between the manually and a automatically [63] delineated debris cover map, assuming that only the manual method correctly classifies the shallow debris cover of such areas.

3.7. Glacier meltwater routing

Meltwater from the glacier is routed to the glacier outlet (i.e. the lowest grid cell of the glacier) using the linear reservoir approach, which has been commonly used for the transformation of surface meltwater into glacier discharge (e.g. [32,45,73]). We distinguish two reservoirs for snow and ice, respectively. The two storage coefficients (K_{snow} and K_{ice}) are calibrated together with the melt parameters TF and SRF against hourly runoff measured between 1 May 2013 and 17 Nov 2013 at the outlet of the Lirung subcatchment (prior to this period the stream was frozen). More than 1500 possible combinations of the parameters TF, SRF, K_{snow} and K_{ice} are tested. The Nash–Sutcliffe (N&S) efficiency criterion [58] is used for model evaluation. As a second criterion, we reject all parameter combinations that result in a mean daily runoff amplitude higher or lower than ±50% of the measured mean daily amplitude.

As 71.3% of the Lirung subcatchment area is glacierized, it can be assumed that the independent calibration of evapotranspiration parameters (Section 3.8) does not interfere with the calibration of storage coefficients and melt parameters.

3.8. Evapotranspiration and drainage

Water routing outside the glacier areas is based on the kinematic wave concept, whereby soil drainage and channel- and overland flow are represented by nonlinear reservoir differential equations [51,52]. The soil-, surface- and channel routing is based on properties that in theory are physically measurable. However, soil and surface roughness parameters aggregate spatially and temporally heterogeneous properties of the real system. The aggregate nature of parameters makes it difficult to specify them directly and unambiguously from point observations made in the field. Considering the large number of properties that need to be specified (eight parameters per soil type and layer), a systematic identification of soil parameters on the basis of in situ data or through calibration is thus difficult. Soil parameters for this study are therefore exclusively estimated based on literature [19,75,82]. We define nine different soil classes (assigned as a function of three slope categories and thee elevation categories) and two soil layers. The suitability of the soil configuration and the standard parameters to represent seasonal soil water storage is discussed in Section 5.2.

Potential evapotranspiration from non-glacierized cells is calculated using the Priestly–Taylor equation [71], in which net radiation is assumed to be a function of incoming shortwave radiation, albedo, and air temperature through an empirical equation. Crop factors (*CropF*) determine the potential crop evapotranspiration. Actual evapotranspiration (ETA) depends on the available soil moisture content within the superficial soil layer, which is calculated by the model. Since no recent field observations of ETA are available, the modeled ETA at Kyangjing (Fig. 1a) is compared to the magnitude of lysimetric estimates by Sakai et al. [81] during the monsoon period (Table 3). The same publication also provides an estimate about evaporation from glacier debris. The estimate of 25% evaporation of liquid precipitation on debris covered glacier area during the monsoon period is considered by subtracting that amount from precipitation over debris.

3.9. Model validation

At the outlet of the upper Langtang catchment (Fig. 1a), hourly discharge is estimated from stage heights recorded by a radar water level sensor (Ott RLS) at 15-min intervals. In contrast to most glacio-hydrological studies, catchment runoff is not used for parameter calibration, and can thus be used for model validation.

A second dataset that has not been used for calibration and that is used for model validation is observed fractional snow cover (fSC) data from MODIS and Landsat imagery. MYD10A1 and MOD10A1 data from the MODIS Aqua and Terra platforms with 500 m resolution are downloaded from <www.nsidc.org>. Images with more than 10% cloud cover over the study catchment are discarded due to the risk of cloud/snow confusion [30,31,91]. TOPKAPI-ETH fSC is then calculated for each corresponding 500 × 500 m MODIS grid area. The root mean square error of daily snow cover is calculated using the minimum difference between simulated and observed fSC at each MODIS grid cell, comparing simulated fSC at 9 am and at 17 pm. Landsat fSC is also calculated for the MODIS 500 × 500 m areas, so that TOPKAPI-ETH fSC can be validated also against Landsat (although only available for a few dates), and Landsat can be compared against MODIS. The advantage of using the MODIS fSC product rather than the binary product is that small scale variation in SC (typical for high-elevation areas, e.g. [74]) modeled by TOPKAPI-ETH and observed by Landsat do not have to be averaged out for comparison against MODIS.

3.10. Sensitivity analysis

In order to test the effect of parametric uncertainty on simulated streamflow volumes, we perform a regional sensitivity analysis [35,85]. TOPKAPI-ETH is run in a Monte-Carlo way with 1000 parameter sets where the parameters of the model are varied randomly within ±10% of their calibrated value (or ±0.1 °C for parameters with temperature units). The Monte-Carlo simulations are used to evaluate the effect of relative changes in single parameters on the model outputs. Following the approach of Ragettli et al. [75], the 1000 parameter sets are partitioned in two groups: parameter sets that lead to more than average and to less than average simulated streamflow volumes, over a certain time period. The maximum vertical distance between cumulative distribution functions (CDFs) of single model parameters within the two groups is used to assess if a parameter significantly contributes to the resulting uncertainty in simulated streamflow, a property which hereafter is called 'information content' (IC). Soil-, routing- and evapotranspiration parameters are excluded from the information content analysis since the focus of this study is on the cryospheric processes that affect the annual water balance. Precipitation gradients and temperature lapse rates are also excluded since it has already been shown previously that the model is very sensitive to those parameters in the upper Langtang catchment [43].

To identify the characteristics of the catchment (such as elevation, slope or debris cover) that increase the model sensitivity, we calculate the information content distribution in space [75]. Areas of high information content indicate the locations where information about the hydrological system can most efficiently constrain runoff uncertainty. For this spatial IC analysis we look at the difference between cumulative distribution functions (associated with the two groups of parameter sets) of the simulated mass balance in each glacier grid cell (hereafter called 'cell information content'). We calculate also the mean cell information content for each glacier and put the result in relation to glacier characteristics (such as mean elevation, slope or debris cover; Table 1).

4. Results

4.1. Parameter calibration

The results of the parameter calibration are shown in Table 3. For constant parameters that are estimated directly on the basis of measured data, standard deviation in measured parameter values are provided (T_{mod}, $T_{moddebris}$, α_1, $\alpha_{glacier}$, α_{debris}).

Over the monitored period, the dETI model reproduces energy-balance modeled melt with a mean difference of 0.019 mm w.e. h^{-1} (Fig. 3a). The largest differences occur for debris thicknesses of 0.1 m, where the dETI model overestimates total melt by 550 mm w.e. over the ablation period (0.15 mm w.e. h^{-1}). However, this error is negligible considering that reconstructed mean debris thicknesses over the Lirung tongue are never less than 0.2 m (see Section 4.2). Diurnal melt rate variability and amplitude estimated from the EB model overall are well-simulated by the dETI model (Fig. 3b). Diurnal melt rate variability in debris thicker

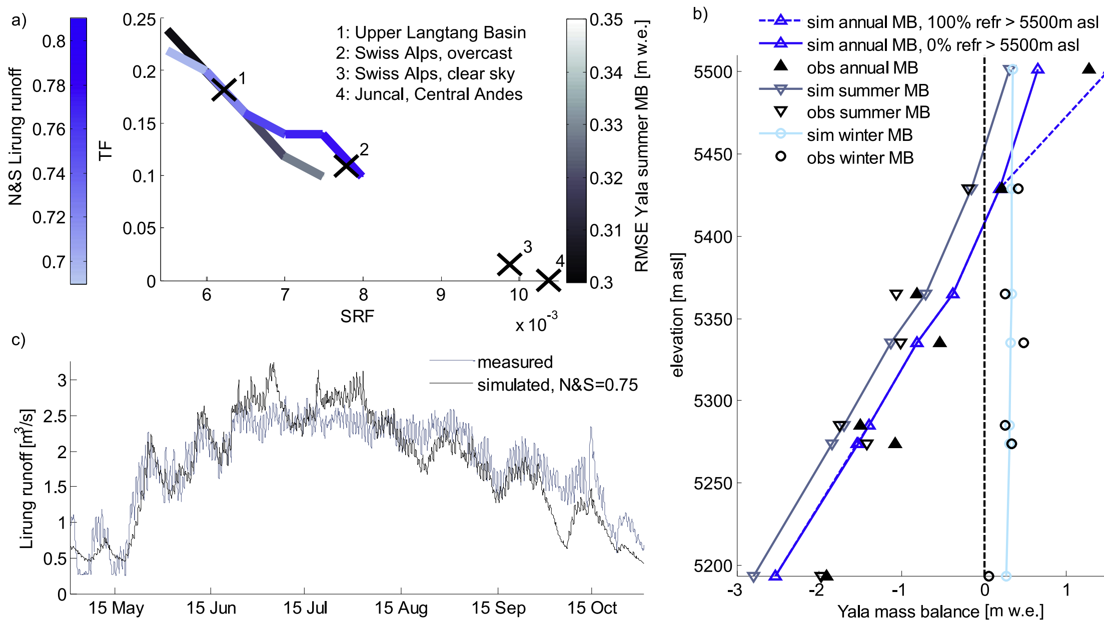

Fig. 4. (a) Optimal parameter combinations of the parameters *SRF* and *TF* for various places on Earth [14], reflecting the dependence of the parameters on local climatic conditions. The colored lines indicate the highest achieved model efficiency (Nash–Sutcliffe, *N&S*, of simulated Lirung runoff, and root mean square error, *RMSE*, with respect to Yala mass balance observations) and parameter *TF* that corresponds to each tested value of *SRF*. The parameter combination where the two lines cross is assumed to represent the optimal solution for the Upper Langtang Basin. (b) Simulated (sim) and observed (obs) summer (8 May 2013–18 Nov 2013), winter (3 Nov 2012–8 May 2013) and annual Yala mass balance (MB). The blue dotted line connects the simulated annual MB that was calculated assuming 100% refreezing of meltwater above 5500 m asl. (c) Measured and simulated runoff at Lirung streamgauge. Model results shown in (b) and (c) are simulated using a parameter combination $SRF = 0.00625$ and $TF = 0.18$.

than 1 m is overestimated by the dETI model, but the magnitude of daily melt is similar.

The melt factors SRF and TF are calibrated simultaneously against Yala summer mass balance (MB) stake observations and Lirung runoff (Fig. 4). The calibration against Lirung runoff results in an optimal *SRF* which is higher, and an optimal *TF* which is lower than the corresponding parameters calibrated against Yala MB. Several parameter combinations result in an acceptable model performance (N&S higher than 0.7, RMSE Yala MB lower than 0.35 m w.e.). To identify the best combination with respect to both datasets, we look at the highest model efficiency and values of TF that correspond to each tested value of SRF (Fig. 4a). For an *SRF* value of 0.00625 calibration against both datasets yields an optimal value of *TF* of 0.18. It is therefore assumed that this parameter combination represents the optimum of all possible parameter combinations, given the differences in meteorological conditions, possible modeling and measurement errors that may have led to the differences in model results.

The modeled Yala Glacier MB and Lirung discharge for *SRF* equal to 0.00625 and *TF* equal to 0.18 are presented in Fig. 4b and c. Note that the observed Yala winter MB was not used for calibration (Fig. 4b). As only annual MB is observed at 5501 m asl we do not use this point for calibration. The modeled annual MB at this location exhibits the largest departure from observations (underestimation by 0.6 m w.e.). It is possible that at this elevation, which was above the equilibrium line altitude (ELA), meltwater refreezes in the snow layer [56]. Model results are therefore also shown for the assumption that 100% of melted snow refreezes at 5501 m asl, which yields a better result comparing to the MB observations. The largest error in simulated summer MB appears at the elevation of the lowest ablation stake, at 5194 m asl (simulated MB more negative by 0.7 m w.e.). However, the MB measurements are affected also by small scale topography and wind-effects that cannot be reproduced by the model, as well as by measurement errors.

The comparison of measured with simulated runoff at the outlet of the Lirung subcatchment (Fig. 4c) reveals that the model overestimates the inter-seasonal variability of runoff, especially for the period after 1 July 2013. Increasing the storage coefficients (optimal values presented in Table 3) can smooth out the inter-seasonal variability but would lead to further underestimation of the daily runoff amplitude.

4.2. Reconstructed debris thickness and melt below debris

Mean reconstructed debris thicknesses for the Lirung tongue are shown in Fig. 5 together with modeled and observed surface height change as a function of elevation. Only one 50 m elevation band contains a supraglacial pond ('Lake 1') that can be identified from Landsat ETM+ data. Debris thickness of debris covered glacier area including lakes but not mapped by the UAV flights is thus sampled from there (Section 3.6.1). This Section (4070–4120 m asl) is characterized by variable but relatively low debris thickness (mostly less than 1 m). Another large supraglacial pond ('Lake 2') is just above the UAV mapped area, but smaller ponds and many cliffs follow in glacier flow direction (4170–4220 m asl). This section of the glacier is characterized by reconstructed debris thicknesses between 1 and 2 m. The lowest debris thickness values (0.2–0.9 m) are calculated for the area near the glacier snout. The reconstructed debris thickness has to be understood as a proxy for all surface features of debris covered glacier area that contribute to melt (Section 3.6.1). Our observations show that debris covered glacier area with a more rugged surface – and therefore more supraglacial ponds – experiences more pronounced glacier surface changes over the ablation season (Fig. 5). This is respected by the model even though no information about supraglacial cliffs and their contribution to glacier melt is available.

Fig. 5 also shows comparison of modeled surface change to observed surface changes. Overall the agreement is very high, with a mean error in simulated surface change of 0.16 m (equivalent to a

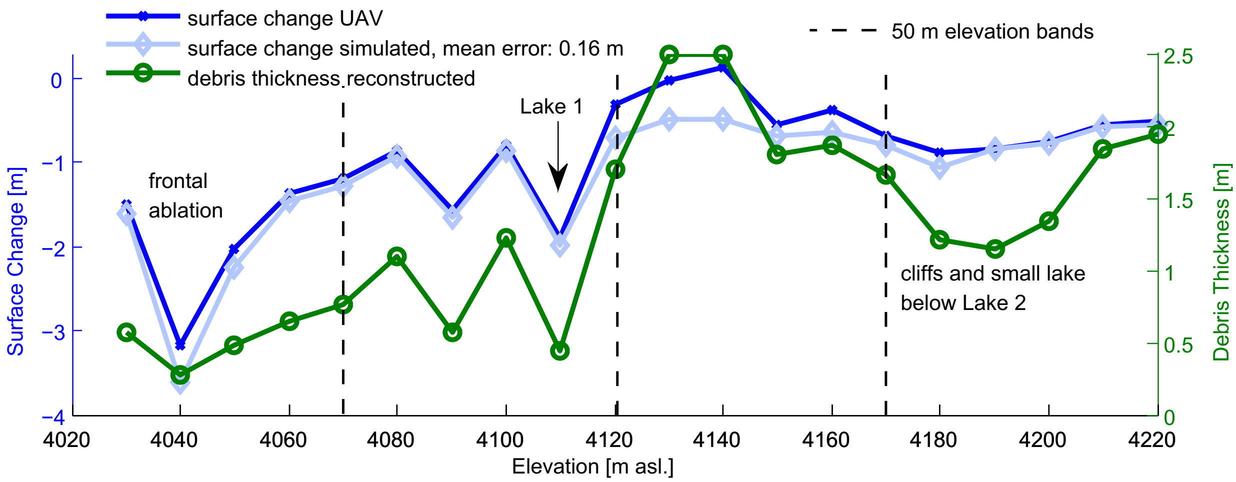

Fig. 5. Surface height changes documented by an Unmanned Aerial Survey System (UAV) between 19 May and 21 October 2013, simulated surface changes corresponding to the same period assuming an ice density of 900 kg m^{-3}, and reconstructed debris thickness. The figure shows mean values for each 10 m elevation band of Lirung Glacier. 50 m elevation bands are used to assign different categories of debris covered area (frontal ablation, supraglacial lake area or not supraglacial lake area) to debris outside the UAV range (Fig. 1b) for the random sampling of reconstructed debris thickness values.

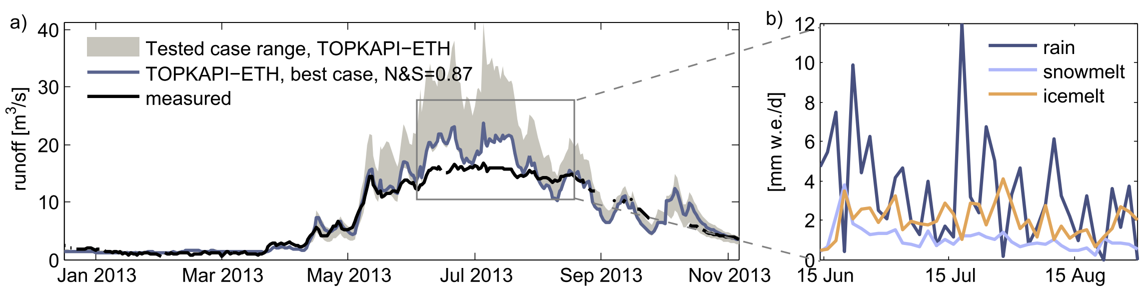

Fig. 6. (a) Simulated and measured daily runoff at Langtang Khola streamgauge. The tested case range corresponds to the model outputs simulated with the tested model setups indicated in Table 4. The 'best case' corresponds to case 8 in Table 4. (b) Running 72 h mean values of water balance components corresponding to case 8 model outputs.

difference of less than 1 mm w.e. ice melt per day). More significant differences to observed surface change appear for very shallow debris thickness (4040 m asl in Fig. 5, 0.5 m difference) and for very thick debris (4120–4140 m asl in Fig. 5, 0.4–0.6 m difference). Note however that the overestimation of surface change at 4120–4140 m asl is partly due to vertical emergence of the glacier at this location [43], so the comparison should be treated with care here. The good results confirm the applicability of the dETI melt model on the distributed scale and suggest a realistic reproduction of air temperature and incoming shortwave radiation during the ablation period in 2013.

4.3. Model validation against remotely sensed snow cover and catchment runoff

The previous two sections showed that the available in situ data could be successfully used to constrain model parameters. However, uncertainty prevails about hydro-meteorological processes in parts of the catchment where no data are available. Model validation against catchment runoff and catchment snow cover thus reveals if the locally collected in situ data is representative also of the rest of the catchment. Moreover, validation against both catchment runoff and snow cover allows testing a range of assumptions about two processes about which no in situ data are available yet: precipitation in the east of the catchment (east of Numthang, see Section 3.3) and melting conditions above 5500 m asl (see Section 4.1). Figs. 6a and 7 present ranges of catchment runoff and snow cover simulated by multiple model runs using the fixed parameters discussed above, but with a horizontal precipitation gradient east of Numthang ($PGh2_{winter}$ and PGh_{summer}) varying between 0 and −10% km^{-1} and a coefficient of refreezing (CFR, % of total melt above 5500 m asl) varying between 0 and 100% (Table 4). The uncertainty in simulated runoff due to the tested assumptions is very large during the monsoon period (around 10 m^3 s^{-1} uncertainty from mid-June to end of July, equivalent to 33% of total runoff, Fig. 6a). The uncertainty in simulated snow cover is mostly around 20% of the catchment area, but more constant in time (Fig. 7).

Goodness-of-fit measures are provided in Table 4. The *N&S* value of the tested assumption varies between −0.5 (case 1: PGh2 zero, CFR 0%) and 0.89 (case 10: PGh2 −10% km^{-1} in summer and winter, CFR 100%). The mean root mean square error (RMSE) in simulated fractional snow cover in comparison to MODIS varies between 41.1% (case 9: $PGh2_{winter}$ and PGh_{summer} −10% km^{-1}, CFR 0%) and 23.6% (case 8: $PGh2_{winter}$ zero and PGh_{summer} −10% km^{-1}, CFR 100%). Note that during the monsoon period, MODIS fSC images are very much affected by clouds and are therefore not used for comparison. Comparison against Landsat SC is also possible, although only few images are available over the year. Here, the tested cases 1–8 perform about equally well (Table 4). Regarding the *N&S* values, cases 6, 8 and 10 perform very well (*N&S* $\geqslant$0.87, Table 4). Considering all criteria together, case 8 can be considered as best performing. Simulated catchment runoff and snow cover using the assumptions associated to case 8 are therefore presented in Figs. 6 and 7 as the best run. Parameter values shown in Table 3 and assumptions about precipitation distribution and melt above

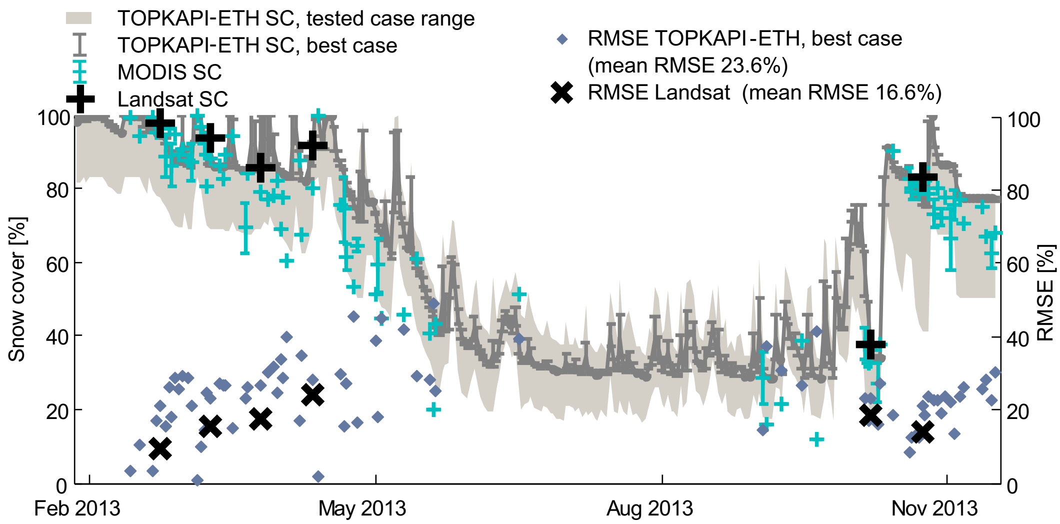

Fig. 7. Remotely sensed MODIS and Landsat snow cover (SC) and snow cover simulated by the model (TOPKAPI-ETH). The tested case range corresponds to the model outputs simulated with the tested model setups indicated in Table 4. The 'best case' corresponds to case 8 in Table 4. The error bars that are shown for MODIS SC correspond to the differences in SC observed by Terra and Aqua satellites. The error bars in 'best case' TOPKAPI-ETH SC correspond to simulated daily fluctuations between 9 am and 17 pm. The TOPKAPI-ETH root mean square error (*RMSE*) is calculated using always the minimum difference between simulated and observed fractional snow cover at each MODIS grid cell. Landsat *RMSE* values are calculated in the same way and should be regarded as a benchmark for model comparison against MODIS.

Table 4
Configuration of model setups that are tested against catchment runoff, MODIS snow cover (SC) and Landsat SC.

Case	PGh2 summer	PGh2 winter	CFR	Runoff N&S	MODIS SC mean RMSE (%)	Landsat SC mean RMSE (%)	Precipitation mm/a	Snowmelt mm/a	Ice melt mm/a	GMB mm/a
1	0	0	0	−0.50	23.9	16.8	1388	581	166	0.23
2	0	0	100	0.14	24.0	16.8	1388	511	164	0.40
3	−3	−3	0	0.07	23.9	17.6	1121	514	192	−0.16
4	−3	−3	100	0.55	24.0	17.6	1121	444	188	0.00
5	−10	−3	0	0.51	24.1	19.7	792	406	272	−0.67
6	−10	−3	100	0.89	24.0	19.6	792	337	244	−0.45
7	−10	0	0	0.47	23.7	17.5	943	441	263	−0.46
8	−10	0	100	0.87	23.6	17.6	943	366	238	−0.23
9	−10	−10	0	0.52	41.1	42.5	658	353	291	−0.86
10	−10	−10	100	0.89	35.7	36.3	658	288	255	−0.62

PGh2 is the horizontal precipitation gradient (% km^{-1}) applied east of Numthang (Fig. 1a), *CFR* is the coeffient of refreezing (%) applied to elevations higher than 5500 m asl. Other parameters are identical to the values indicated in Table 3. N&S is the Nash–Sutcliffe efficiency coefficient and RMSE is the root mean square error. *Precipitation*, *Snowmelt*, *Icemelt* and mean glacier mass balance (*GMB*) represent model outputs.

5500 m asl tested in case 8 are used to model the water balances in the following Section 4.4 and for the sensitivity analysis in Section 4.5.

4.4. Simulated water balance

The simulated magnitudes of all components of the water balance are shown in Fig. 8a and Table 5 for the upper Langtang basin and for the Lirung subcatchment. Total ice melt amounts to 26% of all positive water balance components (providing water input to the hydrological system) for the entire basin (43% for Lirung subcatchment). Snowmelt amounts to 40% (38% for Lirung) and rainfall contributes by 33% (19% for Lirung). The steep topography of the Lirung subcatchment results in a high importance of gravitational snow transport for the annual water balance: 16% of the annual water input originates from melt of snow that has been avalanched (43% of total snowmelt; Fig. 8a). On the larger scale it is only 4.5% of total water input or 11% of total snowmelt. Only 8% of total Lirung ice melt originates from sub-debris ablation (Fig. 8a). This value is substantially higher for other debris covered glaciers (Langtang: 49%, Langshisha: 30%, Shalbachum: 69%). Overall, 33% of total ice melt in Langtang originates from sub-debris ablation, which is equivalent to 8.6% of total water input.

Overall, the water input at Lirung subcatchment is much higher than for the entire basin (1923 mm w.e. in Lirung and 906 mm w.e. in Langtang, Fig. 8a). Measured monsoonal streamflow volumes at Lirung hydrological station amount to 15.8% of measured streamflow at Langtang Khola station, although Lirung subcatchment represents only 4.4% of the total catchment area. This is likely due to decreasing precipitation from west to the east, high elevations and strong vertical precipitation gradients and an important fraction of Lirung Glacier area that has a south aspect and is not mantled in debris.

The magnitude of runoff production decreases from west to east (Fig. 8b). Areas in the east of the study catchment receive very little precipitation in form of rain due to lower temperatures at higher elevations and a strong horizontal precipitation gradient during the warm period. The relative importance of ice melt as a water input increases up-valley. In the northeastern section of the upper Langtang basin (that includes Langtang Glacier) ice melt represents

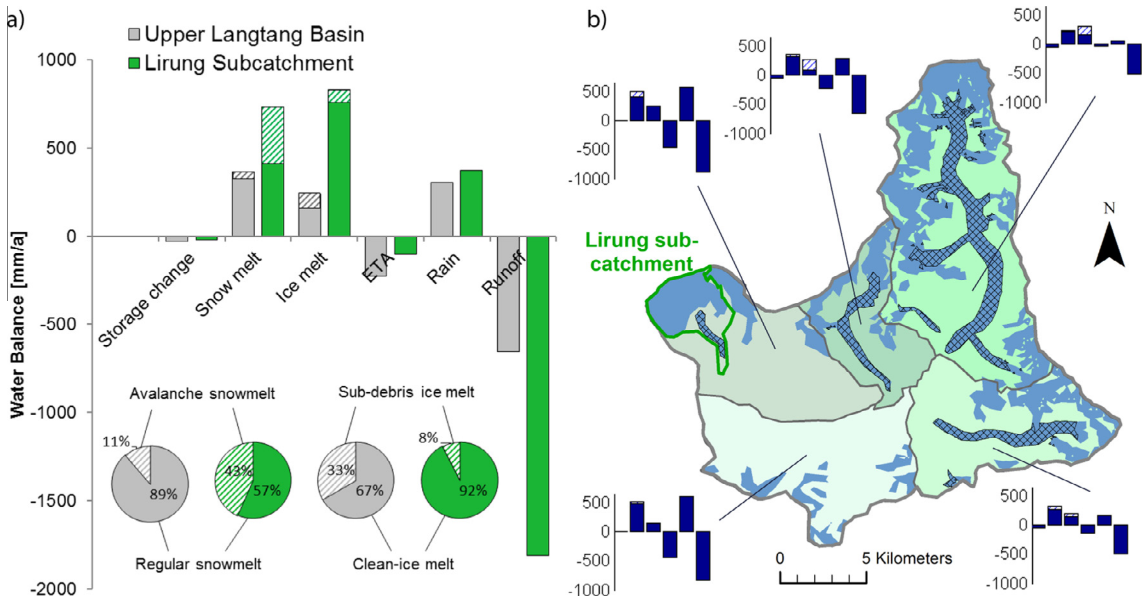

Fig. 8. Simulated water balance for the year 18 Nov 2012–17 Nov 2013: (a) upper Langtang basin and Lirung subcatchment, (b) five sub-sections of the watershed. The components of the water balance are storage changes (soil-, channel-, surface- and englacial reservoir water), snow- and icemelt, evapotranspiration (*ETA*), rain and runoff (always shown in the same order). Hatched patterns show snow- and icemelt from avalanched snow and from debris covered areas, respectively. The sum of positive and negative components of the water balance is always zero.

Table 5
Mean values of the water balance components calculated for (1) the upper Langtang catchment and (2) the Lirung subcatchment.

	Annual		Post-monsoon		Winter		Pre-monsoon		Monsoon	
	(1)	(2)	(1)	(2)	(1)	(2)	(1)	(2)	(1)	(2)
Total inputs										
Rain	305.7	370.7	42.0	37.9	0.0	0.0	30.3	35.1	233.4	297.7
Snow melt										
Regular	324.5	414.9	64.7	48.8	12.5	13.5	181.4	190.4	65.8	162.2
Avalanched	41.2	317.4	0.4	15.9	0.1	2.9	8.4	60.5	32.4	238.1
Ice melt										
Bare-ice	158.6	767.6	3.1	34.8	0.6	7.9	18.7	136.1	136.3	588.8
Sub-debris	79.3	63.5	2.6	6.0	0.2	1.3	12.5	14.9	63.9	41.2
Residuals										
Storage change	−28.6	−21.0	−13.0	32.6	19.2	17.1	−54.2	−74.0	19.6	3.3
Losses										
Evapotranspiration	−228.4	−101.9	−17.1	−6.6	−3.0	−2.4	−61.9	−31.5	−146.3	−61.4
Outflow	−652.4	−1811.0	−82.8	−169.4	−29.6	−40.4	−135.2	−331.4	−405.0	−1270.0

Seasonal values are shown for post-monsoon (1 October–31 November), winter (1 December–28 February), pre-monsoon (1 March–15 June) and monsoon (16 June–30 September) periods of the hydrological year 2012/2013. *Avalanched snow melt* is here defined as snow that would not have melted if it was not transported to lower elevations. *Storage change* represents changes in soil-, channel-, surface- and englacial water reservoirs. Values are expressed in milimeter water equivalents.

Table 6
Results of the regional sensitivity analysis: ranking of parameters regarding their information content for simulated annual and seasonal streamflow volumes.

Rank	Annual	Winter	Pre-monsoon	Monsoon	Post-monsoon	Behavioral
1	SRF	SGR_a	α_1	SRF	α_1	SRF
2	α_1	α_1	SRF	α_1	SRF	α_1
3	T_{mod}	SRF	SGR_a	T_{mod}	T_T	SGR_a
4	SGR_a	T_{mod}	T_{mod}	SGR_a	α_2	T_{mod}
5	T_T	α_2	T_T	T_T	T_{mod}	d
6	TF_{d1}		α_2	TF_{d1}	P_T	TF
7	d			d	SGR_a	TF_{d1}
8	TF			TF		TF_{d2}
9				TF_{d2}		

For the category *Behavioral*, parameters are ranked according to their information content regarding the Nash–Sutcliffe efficiency criteria. Only parameters exceeding the α threshold of the Kolmogorov–Smirnov test are shown. Parameters are described in Table 3.

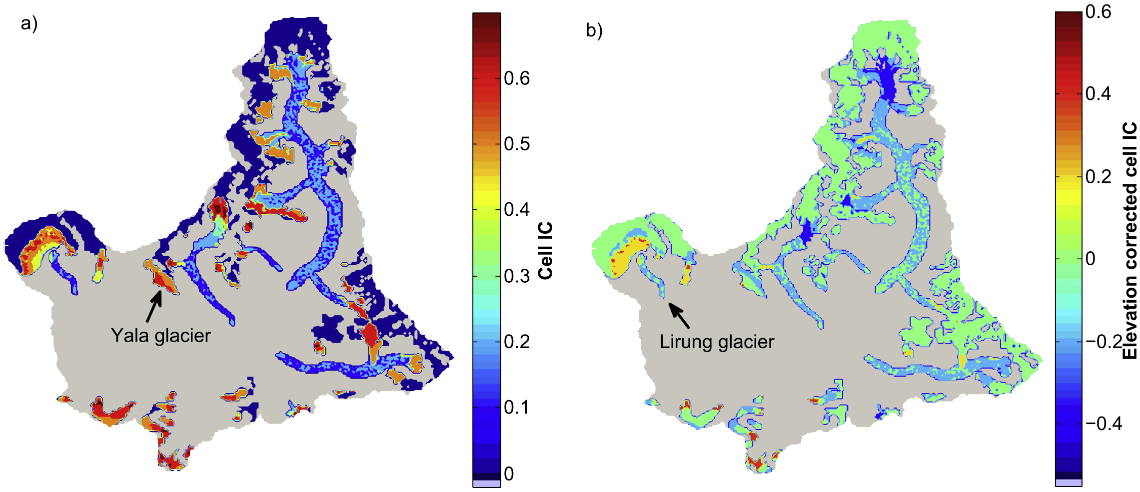

Fig. 9. Spatial distribution of information content (IC) and elevation corrected IC (where the median value for each 100 m elevation band is subtracted from the cell IC values), calculated for the monsoon period 2013 (16 June–31 September).

50% of all water sources, whereas half of the total ice melt originates from debris covered areas. Snowmelt represents 37%–47% of annual water inputs in all five subareas defined in Fig. 8b. Table 5 shows that meltwater inputs from regular snow are highest during the pre-monsoon period (March–mid-June), whereas meltwater inputs from avalanched snow peak during the monsoon period. This applies to both the whole basin and to the Lirung subcatchment, and can be explained by heavy snowfalls during the monsoon period in steep areas located at <shigh elevations.

4.5. Information content

The ranking of parameters with highest information content (IC) for annual and seasonal streamflow simulations is provided in Table 6. Parameters that do not exceed the significance level (α) are not shown. Parameter significances are calculated with the Kolmogorov–Smirnov test [85], with α equal to $5\%/n$, where n is the number of parameters that are included in the analysis (20). The IC-ranks in Table 6 are shown separately for the annual variation in total runoff, the seasonal variations and for the variation in model efficiency (Langtang Khola N&S). For the latter, the 1000 parameter sets are divided into two groups separating parameter sets that lead to higher and lower than median N&S. This is called 'behavioral' partitioning (e.g. [89]). Uncertainty in parameters with a high rank in this category significantly affects the calculated N&S values.

Four parameters (SRF, α_1, T_{mod}, SGR_a) have a high IC in all categories. While SRF, α_1 and T_{mod} have a direct effect on simulated melt (Eq. (2)), SGR_a affects simulated gravitational snow movement. The ranks of the four parameters vary, but SRF has the highest IC for annual and monsoonal streamflow as well as with respect to the behavioral classification. Sub-debris melt parameters that have a significant IC for both annual streamflow volumes and behavioral classification are TF_{d1} (Eq. (4)) and debris thickness (d).

IC-ranks with respect to monsoonal streamflow are almost identical as annual streamflow IC-ranks (Table 6), which means that uncertainty in annual streamflow volumes is mostly determined by the processes that are relevant during the monsoon period. Monsoonal cell-IC is shown in Fig. 9a. Debris covered areas generally have a lower IC than non-debris covered area, whereas IC decreases with debris thickness. Generally, cell IC strongly depends on elevation. The cell IC is highest for non-debris covered glacier area at about 5200 m asl (just below the ELA) such as at Yala Glacier (Fig. 9a). In order to determine which characteristics other than elevation affect cell IC, the basin-wide median cell IC of each 100 m elevation band is subtracted from the cell IC values ('elevation corrected cell IC', Fig. 9b). Elevation corrected cell IC is especially high at the tongues of glaciers in the southwest of the catchment (such as Urkin Kangari or Kanja La), or at Lirung Glacier just above the debris covered area.

Table 1 provides the ranks of glaciers according to the glacier-wide mean cell IC and elevation corrected cell IC. Yala Glacier has the third highest mean cell IC and Lirung Glacier the third highest mean elevation corrected cell IC (Table 1). The highest mean values are calculated in both categories for Urkin Kangari and Kanja La glaciers. We observe that glaciers with a high elevation corrected IC ranks often have a north aspect. An exception is Lirung Glacier which has a south-east aspect. Lirung is by far the steepest glacier in the Langtang catchment (Table 1), which seems to have an effect on model sensitivity and therefore cell-IC. We also calculated the ranks of glaciers with respect to elevation corrected IC for different seasons. The ranks for the monsoon season are nearly identical to those indicated in Table 1. Lirung Glacier has the highest pre-monsoon rank. The highest rank regarding the post-monsoon season is obtained for Kimoshung Glacier. This glacier has a large accumulation area and a low reaching, southward oriented non-debris covered tongue. Temperatures during the post-monsoon period are just high enough that the last 600 m of the tongue (<4700 m asl) are exposed to temperatures above the melting threshold, while for the tongues of other non-debris covered glaciers this is not the case.

5. Discussions

5.1. Model calibration

The calibration approach designed for this study resulted in parameter values that would have been different if no local data had been available for their estimation. This is exemplified by SRF and TF: with only runoff data available for calibration, SRF would be higher and TF lower (Fig. 4a). If SRF and TF had not been calibrated but taken from literature, the chosen parameters would again be different, as the optimal parameter combinations for other high-elevation regions shown in Fig. 4a suggest. Literature values and the calibrated values of TF and SRF indicate that the temperature dependent energy balance components become more important and the shortwave radiation component less important as cloudiness increases (Fig. 4a). The monsoon dominated climate of the Langtang valley, where the ablation period coincides with the main accumulation period, is different from the climate of other sites where the ETI model has been applied. This study demonstrates thus not only that it is of high importance to use local data for parameter calibration, but also that parameter uncertainty cannot be sufficiently constrained if only one response variable is available for calibration.

The calibration of the snow albedo parameter α_2 also resulted in a high value (0.34, Table 3) previously not reported in literature [75]. α_2 is calibrated against snow albedo measured at AWS Y and a second time against Yala mass balance (MB) observations. There is thus evidence that snow albedo in the Central Himalaya might decrease more rapidly than in other regions. Saturation of snow due to monsoonal rain and dust deposition due to rain-on-snow events may be possible reasons.

While the vast majority of model applications in remote high-elevation catchments use daily time steps, this is to our knowledge the first application of a distributed glacio-hydrological model at an hourly resolution. An advantage of simulating processes with hourly time steps is that the comparison with measured hourly data (e.g. runoff) allows for a more thorough model evaluation. Another advantage is that temperature thresholds have a better physical basis at the hourly resolution. Snow depths measured by a sonic ranging sensor next to the pluviometer at 4831 m asl (Table 2) and air temperature measured at the same location [43] reveals that the mean daily air temperature of days with snowmelt are often well below 0 °C. During hours with above threshold air temperature melt occurs which can be modeled by simulations at hourly resolution but not daily. Other parameters that are affected by the temporal resolution of the simulations are the storage coefficients. Due to the hourly time step, the storage coefficients are conditioned to account for diurnal fluctuations (Fig. 4c). At a coarser time step, these coefficients would be higher to match better the inter-seasonal variability.

Regarding the use of remotely sensed snow cover for model evaluation, Fig. 7 shows the RMSE values of Landsat compared against MODIS snow cover. While Landsat provides high resolution, high quality images of snow cover, the MODIS product is unvalidated in the HKH region and of relatively low spatial resolution. The RMSE calculated between Landsat and MODIS SC can thus be considered as a benchmark for model comparison, since it can be assumed that the error of any model with respect to MODIS cannot be lower than the difference in snow cover between Landsat and MODIS. Landsat vs. MODIS RMSE values are lower by only a few percent than model vs. MODIS RMSE values (Fig. 7), which attests a good performance of the model. However, this questions the utility of MODIS SC for model calibration (such as conducted for the upper Langtang catchment by Konz et al. [49], as in that case the model may be tuned to erroneous observations.

The stepwise scheme for model calibration allowed the identification of knowledge gaps that did not emerge from previous glacio-hydrological model applications in the upper Langtang catchment [11,27,41,42,48,49,72], possibly due to error compensation. The parameters listed in Table 3 were not found to be sufficient to describe the processes at very high elevations (above 5500 m asl) and the precipitation distribution in the east of the catchment. Two additional parameters thus had to be introduced (*CFR* and *PGh*2, Table 4). More precipitation data from the east of the catchment and information about melting conditions above 5500 m asl are required to validate the model setup identified as optimal (Table 4). Measured catchment runoff (Fig. 6a, Table 4) and the annual point mass balance at 5501 m asl (Fig. 4b) suggests that snowmelt from perennial snow refreezes within the snowpack and does thus not contribute to runoff. Snow conditions above 5500 m asl are additionally affected by uncertainty about blowing wind sublimation, a process that can be important at high elevation in the Central Himalaya [90] and that is not considered by the model. Observed Lirung Glacier runoff suggests that the model does not overestimate melt without a parameter *CFR* (and *CFR* was thus only applied to areas outside the Lirung subcatchment). However, an underestimation of precipitation at the flanks of Langtang Lirung peak (7227 m asl), an important orographic barrier, may compensate for an overestimation of meltwater contribution to runoff from above 5500 m asl.

5.2. Simulated water balance and runoff

Snowmelt, rain and ice melt all contribute by at least 26% to the simulated annual water balance (Fig. 8, Table 5). There is a strong seasonal variability in the relative importance of the water balance components: during the hydrological year 2012/2013, snowmelt represented the most important water input to the hydrological system from March to May (84% of all sources) and again in October (57%). In June and in July the hydrology of the catchment was dominated by rainfall (45%) and in August/September by meltwater inputs from ice ablation (47%). Storage changes (derived from changes in soil-, channel-, surface- and englacial reservoir volumes) are the most important contributors to runoff during winter (Table 5). Changes in annual storage between the beginning and the end of the hydrological year are negligible (Fig. 8, Table 5). Racoviteanu et al. [72] have shown that in November 2008 and 2009, an important fraction of channel runoff (30%) had the isotope signature of groundwater. This means that an important fraction of meltwater or rain is routed through the ground. Base flow in winter is reproduced well by the model (Fig. 6a), which suggests that inter-seasonal storage changes are not over- or underestimated or that the soil configuration (Section 3.8) does not need to be revisited. However, the model overestimates catchment runoff during the main monsoon period (Fig. 6a). If the streamflow measurements can be trusted, this overestimation might be due to underestimation of groundwater storage or an underestimation of runoff that is leaving the catchment through the groundwater and not through the channel. Rainfall is an important but also very variable water balance component during this period (Fig. 6b), but the variability in rainfall input to the hydrological system is almost not visible in measured Langtang runoff (Fig. 6a), while some of the variability appears in simulated runoff. It is rather unlikely that the model overestimates rainfall, since precipitation and temperatures are measured at various locations in the valley, and used by the model directly as input data or to estimate meteorological gradients. The effect on streamflow of variable rainfall input to the hydrological system must therefore be buffered by the soil if streamflow data are correct. However, measured monsoon runoff in Himalayan high-elevation catchments must be treated with care. Tracer experiments for the calculation of the rating curve are rarely conducted during the peak monsoon period in July/August, due to difficult road conditions, and the rating curve might therefore not be representative of peak flows. Recorded stage heights may also underestimate peak flows since the radar sensor cannot measure water levels within a very short distance. Peak runoff according to the stage height measurements in 2013 was 17 $m^3\ s^{-1}$. The maximum discharge measured by tracer experiments at Langtang Khola on 1 July 2012 was not much below that value (14.95 $m^3\ s^{-1}$). However, the tracer experiments were carried out just before intensive monsoon rainfall set in (in total 36.1 mm precipitation measured in Kyangjing on 3 and 4 July 2012). We cannot therefore be sure that the rating curves represent well discharge after intensive monsoon precipitation. Observations by Fukushima et al. [27] show that for the very wet year 1985/1986 (1224.5 mm w.e. precipitation) monsoon mean daily runoff (measured at a location about 1.3 km upstream of the current gauge) exceeded 30 $m^3 s^{-1}$ every day during July/August. The simulated peak value of 23.8 $m^3 s^{-1}$ of the present study is therefore within the range of observed values. Since the results of all previous glacio-hydrological model applications in the basin [11,27,41,42,48,49,72] are highly sensitive to measured discharge, this highlights the importance of using other in situ data instead of the lumped catchment response for the calibration of model parameters.

5.3. Simulated glacier mass balances

The model simulations of accumulation and ablation resulted in a negative glacier mass balance (−0.24 m w.e. a^{-1}) for the hydrological year 2012/2013, using the model setup that performs best with respect to all available observed data (case 8 in Table 4). Annual mass balances calculated for single glaciers (reported in Table 1) vary between −0.92 m w.e. a^{-1} (Urkin Kangari) and 0.69 m w.e. a^{-1} (Kimoshung). This range of values probably overestimates the actual differences between glaciers. Kimoshung glacier has a large accumulation area that is shielded towards the south by a ridge higher than 6000 m asl. Monsoon clouds moving up-valley may be blocked by that ridge and extrapolated precipitation and therefore mass balance overestimated as a result. Glacier area of Urkin Kangari or of other small, non-debris covered glaciers in the south may be overestimated due to a not up to date glacier mask. The model probably provides more accurate simulations for Yala Glacier, where the monitoring network is dense (Fig. 1). Here, an annual mass balance of −0.17 m w.e. a^{-1} is simulated (Table 1), while the ELA is located at 5400 m asl (Fig. 4b). [22] locate the ELA at Yala Glacier for the periods 1982–96 and 1996–2009 at the same elevation, using GPS and ground-penetrating radar measurements. The ELA in 2011/2012 was slightly higher (5450 m asl, [4], but the year 2013 was characterized by much more post-monsoon precipitation than in 2012. Only 1.3 mm w.e. of precipitation was measured at AWS K in October/November 2012, but 150 mm w.e. during the same period in 2013 due to the cyclone Phailin. Overall, 924.5 mm w.e. precipitation were measured in Kyangjing during the period 18 Nov 2012–17 Nov 2013 which is 284 mm w.e. more than the annual average of the years 1990–2010. This can explain why [88] calculate a mean thinning rate of Yala Glacier for the years 1982–1996 (−0.69 m w.e. a^{-1}) and 1996–2009 (−0.75 m w.e. a^{-1}) that is substantially lower than the modeled mass balance in this study.

The annual mass balances of debris covered glaciers are all negative (Table 1). Melt rates of debris covered areas differ fundamentally from melt rates of bare ice at similar elevations, even when taking into account that supraglacial lakes and cliffs contribute to melt. At 4800 m asl, the annual mean melt rate of bare-ice glacier area is 0.55 m w.e. d^{-1}, whereas the mean melt rate of debris covered area at the same elevation is only 0.07 m w.e. d^{-1}. In comparison to a model run where the presence of supraglacial debris is ignored, melt rates from debris covered glacier area are reduced on average by 84%. Previous studies assumed a reduction of 50% [11] to 70% [42,48] obtained with a constant in time and uniform in space reduction factor.

5.4. Collection of local data

Data collection in 2012 and 2013 at locations on- or near glaciers was concentrated mainly at Lirung and Yala (Fig. 1). Yala was chosen because it is considered as a ‘benchmark glacier’ for the Himalayan region [22], which has been well investigated in the last 20 years. Lirung Glacier was chosen because of its relatively easy access, previous studies [57,78–80] and because it offered an ideal case to study cliffs and supra-glacial ponds [87]. The information content analysis (Tables 1 and 6 and Fig. 9) allows assessing the effectiveness of ongoing monitoring programs to (i) reduce the uncertainty in model parameters that lead to uncertainty in modeled streamflow, and to (ii) verify that the locations are well chosen in the sense that defining parameter at specific sites effectively leads to less uncertainty in modeled streamflow.

The parameter with the highest information content, *SRF*, was determined by calibration against two different datasets (Lirung streamflow and Yala mass balance). However, the simulations of streamflow and glacier melt are affected by a number of other processes (e.g. temperature distribution, snowfall amounts, albedo, etc.). The model certainly does not represent all these processes perfectly, a fact that may affect the calibrated value of *SRF*. For the design of future field campaigns it would therefore be advisable to install an AWS on bare-ice during the ablation season. Calibration of *SRF* (and *TF*) against the outputs of an energy balance model at the point scale could provide robust parameter estimates (e.g. [73]) that are not affected by potential errors in other model components. AWS Y-G could be used for that purpose, but during the previous field campaign did not measure all the input data necessary to an EB model (e.g. wind speed) due to technical problems. Fresh snow albedo (α_1) is the parameter with the second highest ranks in Table 6 and was determined using the observed snow albedo of 12 snowfall events at AWS Y (Table 3). Since AWS Y is a permanent weather station, future data can be used for a more complete statistical analysis. SGR_a seems to be an important parameter (Table 6). For safety reasons it is not advisable to measure snow depths in avalanche areas; the function that relates snow holding depth to slope will therefore always have to be determined by indirect methods such as by calibration against remotely sensed avalanche patterns, as in this study. Finally, to limit the discussion to the parameters that are among the top five in annual IC in Table 6, T_{mod} and T_T are temperature related parameters which in theory can be directly determined with the current monitoring setup. However, those are parameters whose uncertainty is naturally high. T_{mod} is associated with the variability of air temperature over glacierized surfaces, which is high especially during the day, poorly understood and controlled by katabatic flows and energy fluxes in the glacier boundary layer. T_T is an empirical parameters that is normally assumed or calibrated, but depends also on meteorological conditions, the energy balance at the glacier surface and on the cold content of the snow pack. Given this, it is unrealistic to determine a single optimal value for T_{mod} and T_T. It is therefore recommended to vary these parameters following a Monte Carlo procedure to provide robust projections of simulated streamflow.

Regarding the choice of the locations for fieldwork, the results of the information content analysis are encouraging. Yala Glacier has the third highest mean IC and Lirung Glacier the third highest IC if elevation effects are omitted (Table 1). In the case of Yala Glacier the model is sensitive to the transition from a snow covered to an ice exposed surface, which due to changes in albedo leads to strong variations in simulated melt. Field campaigns in the region should therefore always focus on elevations above and below the potential location of the ELA. If the approximate elevation of the ELA is known, this value should be used as a response variable for model calibration. For the present study, the ablation stakes confirmed that the model reproduces the ELA correctly at Yala Glacier. Regarding Lirung Glacier, the fieldwork was concentrated on the tongue, while it is the steep area above the glacier cirque that has a high information content. Fieldwork on the tongue is necessary to fill the data gap which exists about processes on debris covered glaciers. However, measured glacier runoff allowed the uncertainty in modeled meltwater contribution from higher elevations to also be constrained. Avalanching is an important process on Lirung (Fig. 8), and remotely sensed avalanche patterns were therefore evaluated at a very relevant location.

The high IC of Urkin Kangari and Kanja La glaciers does not mean that the monitoring program needs to be entirely transferred to the southern side of the basin, since glaciers there are relatively small. The sum of all cell IC of all glacier area in the south-west of the catchment is still less than the sum of all cell IC calculated for Langtang Glacier only. However, temperature and precipitation data and an updated glacier map would be beneficial in order to assess if the model represents the glacio-meteorological conditions correctly in the south-west.

6. Conclusions

New detailed in situ data from the upper Langtang catchment, the core study catchment of various institutions doing research in the Central Himalaya, are used to set up a state-of-the-art glacio-hydrological model and provide a fundamental understanding of the complex hydrology of this Himalayan catchment. The model is used to quantify processes that have been previously suggested to be important in Himalayan catchments but never quantified before. We use it to provide estimates of the contribution of glaciers and snow to catchment runoff and their spatial and temporal variability.

14 parameters are directly calculated on the basis of local data, and 13 parameters are calibrated against 5 different datasets (Table 3, Fig. 2). Measured catchment runoff and remotely sensed snow cover – datasets that are used in previous modeling studies in the region to tune model parameters but in high-elevation regions are often affected by significant uncertainties – are not used for model calibration but only for validation. All parameter values derived in this study can be directly linked to physical processes that can be observed. The methodology to derive various parameter values can be regarded as a benchmark for future efforts to calibrate glacio-hydrological models. However, the systematic approach to estimate model parameters based on local data also revealed further data gaps, not often discussed in literature, that are significantly affecting the performance of glacio-hydrological models. As such, there remains uncertainty about snowmelt contribution to runoff from perennial snow (>5500 m asl) and about the spatial variability of precipitation. However, by employing all 27 model parameters that are included in the calibration scheme, and by making realistic assumptions about the spatial variability of precipitation and melt at high elevations, the model is capable of reproducing observed catchment runoff and snow cover accurately.

The systematic integration of detailed local information on physical processes enhances the capacity of the model to unravel the full water balance of the study catchment. Snowmelt is the most important contributor to total runoff during the hydrological year 2012/2013 (representing 40% of all sources), followed by rainfall (34%) and ice melt (26%). From March to May and again in October snowmelt represented the most important streamflow source. In June and in July the hydrology of the catchment was dominated by rainfall and in August/September by meltwater inputs from ice ablation. Note that these results might differ slightly for years with considerably different meteorological conditions than during the hydrological year 2012/2013.

A novel approach is used to generate maps of spatially varying debris thickness. The role of supraglacial lakes and cliffs on the total melt of a debris covered glacier is indirectly taken into account by attributing more shallow debris to model grid cells that contain lakes and cliffs. In combination with a new sub-debris melt model, we provide the first estimation of the melt reducing effect of supraglacial debris in the upper Langtang catchment that is based on in situ data. We find that melt rates on average are reduced by 84%, which is more than assumed by previous modeling studies [11,42,48]. In spite of the lower melt rates below debris, simulated annual glacier mass balances of debris covered glaciers are of similar magnitude than those of non debris covered glaciers. Overall, the mass balance of glacierized area of the upper Langtang catchment for the hydrological year 2012/2013 was -0.24 m w.e. One third of total ice melt originated from the debris covered glacier parts.

The analysis of the spatial distribution of information content confirms the effectiveness of the current monitoring setup, since the installed network is concentrated at locations where the uncertainty in glacier mass balance due to uncertainty in model parameters significantly affects uncertainty in simulated catchment runoff. The analysis underlines that it is fundamental for the performance of a glacio-hydrological model to represent well the ELA, as previous studies have concluded (e.g. [72]). The information content analysis also reveals that a significant portion of runoff uncertainty can be attributed to uncertainty in modeling gravitational snow redistribution, although only about 5% of total water inputs to the hydrological system originate from melted snow that had been moved by avalanches. Since avalanching can have locally and temporarily an important effect on the water balance, this processes need to be considered by glacio-hydrological models in the Central Himalaya. With respect to potential applications of the model for future projections, an effort should be made to collect the relevant data to integrate melt from supraglacial cliffs and lakes explicitly into the model, in order to further improve its predictive skills.

Acknowledgments

This study was part of the HKH Cryosphere Monitoring Project (CMP) implemented by the International Centre for Integrated Mountain Development and supported by the Norwegian Ministry of Foreign Affairs. The authors would like to thank the CMP project partners for their help in carrying out this study, including the Himalayan Cryosphere, Climate and Disaster Research Center, Kathmandu University; Central Department of Hydrology and Meteorology, Tribhuvan University; Department of Hydrology and Meteorology, Government of Nepal; and Water and Energy Commission Secretariat, Government of Nepal. This study was partially funded by the USAID High Mountain Glacier Watershed Programs Climber-Scientist (Grant No. CCRDCS0010), which is warmly acknowledge for its support, and by the South Asia Research Hub of the UK Department for International Development (DFID). Stefan Rimkus did all the necessary modifications in the code of TOPKAPI-ETH and Anna Chesnokova and Simon Wicki helped with the energy balance modeling of Lirung Glacier which is gratefully acknowledged. The authors would like to thank very much all the people that contributed to the data collection. The authors are grateful to Koji Fujita and two anonymous reviewers for providing thoughtful and useful reviews. Special thanks go to Paolo Burlando for supporting Silvan Ragettli's work at ETH.

References

[1] Ageta Y, Iida H, Watanabe O. Glaciological studies on Yala Glacier in Langtang Himal, Glacial Studies in Langtang Valley, Report of the Boring Project 1981–82 in the Nepal Himalaya, 2, 41–47; 1984.

[2] Anderton S, Latron J, Gallart F. Sensitivity analysis and multi-response, multi-criteria evaluation of a physically based distributed model. Hydrol Processes 2002;16(2):333–53. http://dx.doi.org/10.1002/hyp.336.

[3] Bajracharya SR, Shrestha B. The status of glaciers in the Hindu Kush-Himalayan Region. Kathmandu, Nepal: ICIMOD; 2011.

[4] Baral P et al. Preliminary results of mass-balance observations of Yala Glacier and analysis of temperature and precipitation gradients in Langtang Valley, Nepal. Ann Glaciol 2014;55(66):9–14. http://dx.doi.org/10.3189/2014AoG66A106.

[5] Bárdossy a, Singh SK. Robust estimation of hydrological model parameters. Hydrol Earth Syst Sci 2008;12(6):1273–83. http://dx.doi.org/10.5194/hess-12-1273-2008.

[6] Benn D et al. Response of debris-covered glaciers in the Mount Everest region to recent warming, and implications for outburst flood hazards. Earth-Sci Rev 2012;114(1–2):156–74. http://dx.doi.org/10.1016/j.earscirev.2012.03.008.

[7] Bernhardt M, Schulz K. SnowSlide: a simple routine for calculating gravitational snow transport. Geophys Res Lett 2010;37(11):L11502. http://dx.doi.org/10.1029/2010GL043086.

[8] Beven K. Uniqueness of place and process representations in hydrological modelling. Hydrol Earth Syst Sci 2000;4(2):203–13. http://dx.doi.org/10.5194/hess-4-203-2000.

[9] Bocchiola D, Diolaiuti G, Soncini a, Mihalcea C, D'Agata C, Mayer C, Lambrecht a, Rosso R, Smiraglia C. Prediction of future hydrological regimes in poorly gauged high altitude basins: the case study of the upper Indus, Pakistan. Hydrol Earth Syst Sci 2011;15(7):2059–75. http://dx.doi.org/10.5194/hess-15-2059-2011.

[10] Bolch T et al. The state and fate of Himalayan glaciers. Science 2012;336(6079):310–4. http://dx.doi.org/10.1126/science.1215828.

[11] Braun L, Grabs W, Rana B. Application of a conceptual precipitation-runoff model in the Langtang Khola Basin, Nepal Himalaya. IAHS Publ 1993;218:221–37.

[12] Brock B, Willis I, Sharp M. Measurement and parameterization of albedo variations at Haut Glacier d'Arolla, Switzerland. J Glaciol 2000;46:675–88. http://dx.doi.org/10.3189/172756500781832675.

[13] Brock BW, Mihalcea C, Kirkbride MP, Diolaiuti G, Cutler MEJ, Smiraglia C. Meteorology and surface energy fluxes in the 2005–2007 ablation seasons at the Miage debris-covered glacier, Mont Blanc Massif, Italian Alps. J Geophys Res 2010;115(D09106). http://dx.doi.org/10.1029/2009JD013224.

[14] Carenzo M, Pellicciotti F, Rimkus S, Burlando P. Assessing the transferability and robustness of an enhanced temperature-index glacier-melt model. J Glaciol 2009;55(190):258–74. http://dx.doi.org/10.3189/002214309788608804.

[15] Carenzo M, Pellicciotti F, Mabillard J, Reid T, Brock BW. An enhanced debris temperature index model accounting for thickness effect. Adv Water Resour (in preparation). 2015.

[16] Cogley JG. Himalayan glaciers in the balance. Nature 2012;488(7412):468–9. http://dx.doi.org/10.1038/488468a.

[17] Corripio J. Vectorial algebra algorithms for calculating terrain parameters from DEMs and solar radiation modelling in mountainous terrain. Int J Geog Inf Sci 2003;17(1):1–23. http://dx.doi.org/10.1080/713811744.

[18] Fatichi S, Rimkus S, Burlando P, Bordoy R. Does internal climate variability overwhelm climate change signals in streamflow? The upper Po and Rhone basin case studies. Sci Total Environ 2014;493:1171–82. http://dx.doi.org/10.1016/j.scitotenv.2013.12.014.

[19] Finger D, Pellicciotti F, Konz M, Rimkus S, Burlando P. The value of glacier mass balance, satellite snow cover images, and hourly discharge for improving the performance of a physically based distributed hydrological model. Water Resour Res 2011;47(7):1–14. http://dx.doi.org/10.1029/2010WR009824.

[20] Finger D, Heinrich G, Gobiet A, Bauder A. Projections of future water resources and their uncertainty in a glacierized catchment in the Swiss Alps and the subsequent effects on hydropower production during the 21st century. Water Resour Res 2012;48(2):1–20. http://dx.doi.org/10.1029/2011WR010733.

[21] Foster LA, Brock BW, Cutler MEJ, Diotri F. A physically based method for estimating supraglacial debris thickness from thermal band remote-sensing data. J Glaciol 2012;58(210):677–91. http://dx.doi.org/10.3189/2012JoG11J194.

[22] Fujita K, Nuimura T. Spatially heterogeneous wastage of Himalayan glaciers. Proc Nat Acad Sci USA 2011;108(34):14011–4. http://dx.doi.org/10.1073/pnas.1106242108.

[23] Fujita K, Sakai a. Modelling runoff from a Himalayan debris-covered glacier. Hydrol Earth Syst Sci 2014;18(7):2679–94. http://dx.doi.org/10.5194/hess-18-2679-2014.

[24] Fujita K, Takeuchi N, Seko K. Glaciological observations of Yala Glacier in Langtang Valley, Nepal Himalayas, 1994 and 1996. Bull Glacier Res 1998;16:75–81.

[25] Fujita K, Thompson LG, Ageta Y, Yasunari T, Kajikawa Y, Sakai A, Takeuchi N. Thirty-year history of glacier melting in the Nepal Himalayas. J Geophys Res 2006;111(D03109):1–6. http://dx.doi.org/10.1029/2005JD005894.

[26] Fujita K, Suzuki R, Nuimura T, Sakai A. Performance of ASTER and SRTM DEMs, and their potential for assessing glacial lakes in the Lunana region, Bhutan Himalaya. J Glaciol 2008;54(185):220–8. http://dx.doi.org/10.3189/002214308784886162.

[27] Fukushima Y, Watanabe O, Higuchi K. Estimation of streamflow change by global warming in a glacier-covered high mountain area of the Nepal Himalaya. IAHS Publ 1991;205:181–8.

[28] Gabbi J, Carenzo M, Pellicciotti F, Bauder A, Funk M. A comparison of empirical and physically-based glacier surface melt models for long-term simulations of glacier response. J Glaciol 2014;60(224):1140–54. http://dx.doi.org/10.3189/2014JoG14J011.

[29] Gardelle J, Berthier E, Arnaud Y, Kääb A. Region-wide glacier mass balances over the Pamir-Karakoram-Himalaya during 1999–2011. Cryosphere 2013;7(4):1263–86. http://dx.doi.org/10.5194/tc-7-1263-2013.

[30] Hall D, Riggs G. Accuracy assessment of the MODIS snow products. Hydrol Processes 2007;1547:1534–47. http://dx.doi.org/10.1002/hyp.

[31] Hall DK, Riggs Ga, Salomonson VV, DiGirolamo NE, Bayr KJ. MODIS snow-cover products. Remote Sensing Environ 2002;83(1–2):181–94. http://dx.doi.org/10.1016/S0034-4257(02)00095-0.

[32] Hannah DM, Gurnell AM. A conceptual, linear reservoir runoff model to investigate melt season changes in cirque glacier hydrology. J Hydrol 2001;246(1–4):123–41. http://dx.doi.org/10.1016/S0022-1694(01)00364-X.

[33] Hewitt K. The Karakoram anomaly? Glacier expansion and the 'elevation effect', Karakoram Himalaya. Mt Res Dev 2005;25(4):332–40. http://dx.doi.org/10.1659/0276-4741(2005) 0250332:TKAGEA2.0.CO;2.

[34] Hewitt K. Glacier change concentration, and elevation effects in the Karakoram Himalaya, Upper Indus Basin. Mt Res Dev 2011;31(3):188–200. http://dx.doi.org/10.1659/MRD-JOURNAL-D-11-00020.1.

[35] Hornberger GM, Spear RC. An approach to the preliminary analysis of environmental systems. J Environ Manage 1981;12(1):7–18.

[36] Huss M, Farinotti D. Distributed ice thickness and volume of all glaciers around the globe. J Geophys Res 2012;117(F4):F04010. http://dx.doi.org/10.1029/2012JF002523.

[37] Huss M, Zemp M, Joerg PC, Salzmann N. High uncertainty in 21st century runoff projections from glacierized basins. J Hydrol 2014;510:35–48. http://dx.doi.org/10.1016/j.jhydrol.2013.12.017.

[38] Iida H, Watanabe O, Mulmi D, Thapa K. Glacier distribution in the Langtang river region, Nepal, Glacial Studies in Langtang Valley. Report of the Boring Project 1981–82 in the Nepal Himalaya: 2; 1984. p. 117–20.

[39] Immerzeel W, Van Beek L, Bierkens M. Climate change will affect the Asian water towers. Science 2010;328(5984):1382–5. http://dx.doi.org/10.1126/science.1183188.

[40] Immerzeel W, Kraaijenbrink P, Shea J, Shrestha AB, Pellicciotti F, Bierkens M, de Jong S. High-resolution monitoring of Himalayan glacier dynamics using unmanned aerial vehicles. Remote Sensing Environ 2014;150:93–103. http://dx.doi.org/10.1016/j.rse.2014.04.025a.

[41] Immerzeel WW, Beek LPH, Konz M, Shrestha AB, Bierkens MFP. Hydrological response to climate change in a glacierized catchment in the Himalayas. Clim Change 2012;110:721–36. http://dx.doi.org/10.1007/s10584-011-0143-4.

[42] Immerzeel WW, Pellicciotti F, Bierkens MFP. Rising river flows throughout the twenty-first century in two Himalayan glacierized watersheds. Nat Geosci 2013;6(8):1–4. http://dx.doi.org/10.1038/ngeo1896.

[43] Immerzeel WW, Petersen L, Ragettli S, Pellicciotti F. The importance of observed gradients of air temperature and precipitation for modeling runoff from a glacierized watershed in the Nepalese Himalayas. Water Resour Res 2014;50:1–15. http://dx.doi.org/10.1002/2013WR014506b.

[44] Iqbal M. An introduction to solar radiation. London: Academic Press; 1983. 390 p.

[45] Jansson P, Hock R, Schneider T. The concept of glacier storage: a review. J Hydrol 2003;282(1–4):116–29. http://dx.doi.org/10.1016/S0022-1694(03)00258-0.

[46] Kääb A, Berthier E, Nuth C, Gardelle J, Arnaud Y. Contrasting patterns of early twenty-first-century glacier mass change in the Himalayas. Nature 2012;488(7412):495–8. http://dx.doi.org/10.1038/nature11324.

[47] Kirkbride MP, Deline P. The formation of supraglacial debris covers by primary dispersal from transverse englacial debris bands. Earth Surf Processes Landforms 2013;38(15):1779–92. http://dx.doi.org/10.1002/esp.3416.

[48] Konz M, Uhlenbrook S, Braun L. Implementation of a process-based catchment model in a poorly gauged, highly glacierized Himalayan headwater. Hydrol Earth Syst Sci 2007;11:1323–39. http://dx.doi.org/10.5194/hess-11-1323-2007.

[49] Konz M, Finger D, Bürgi C, Normand S, Immerzeel WW. Calibration of a distributed hydrological model for simulations of remote glacierized Himalayan catchments using MODIS snow cover data. IAHS Publ 2010;340:465–73.

[50] Kotchenova SY, Vermote EF, Matarrese R, Klemm FJ. Validation of a vector version of the 6S radiative transfer code for atmospheric correction of satellite data. Part I: path radiance. Appl Opt 2006;45(26):6762–74. http://dx.doi.org/10.1364/AO.45.006762.

[51] Liu Z, Todini E. Towards a comprehensive physically-based rainfall-runoff model. Hydrol Earth Syst Sci 2002;6:859–81. http://dx.doi.org/10.5194/hess-6-859-2002.

[52] Liu Z, Todini E. Assessing the TOPKAPI non-linear reservoir cascade approximation by means of a characteristic lines solution. Hydrol Processes 2005;19(10):1983–2006. http://dx.doi.org/10.1002/hyp.5662.

[53] Lutz A, Immerzeel W, Shrestha A, Bierkens M. Consistent increase in High Asia's runoff due to increasing glacier melt and precipitation. Nat Clim Change 2014;4:587–92. http://dx.doi.org/10.1038/NCLIMATE2237.

[54] Mabillard J. Distributed modelling of changes in glacier mass balance and runoff on Miage glacier [Master thesis]. Italy: Institute of Environmental Engineering, ETH–Zurich; 2012.

[55] Mihalcea C, Mayer C, Diolaiuti G, Lambrecht A, Smiraglia C, Tartari G. Ice ablation and meteorological conditions on the debris-covered area of Baltoro glacier, Karakoram, Pakistan. Ann Glaciol 2006;43(1):292–300. http://dx.doi.org/10.3189/172756406781812104.

[56] Mukhopadhyay B. Detection of dual effects of degradation of perennial snow and ice covers on the hydrologic regime of a Himalayan river basin by stream water availability modeling. J Hydrol 2012;412–413:14–33. http://dx.doi.org/10.1016/j.jhydrol.2011.06.005.

[57] Naito N, Nakawo M, Aoki T, Asahi K, Fujita K, Sakai A, et al. Surface flow on the ablation area of the Lirung Glacier in Langtang Valley, Nepal Himalayas. Bull Glacier Res 1998;16:67–73.

[58] Nash JE, Sutcliffe JV. River flow forecasting through conceptual models. Part I–A discussion of principles. J Hydrol 1970;10(3):282–90. http://dx.doi.org/10.1016/0022-1694(70)90255-6.
[59] Nepal S, Krause P, Flügel W-A, Fink M, Fischer C. Understanding the hydrological system dynamics of a glaciated alpine catchment in the Himalayan region using the J2000 hydrological model. Hydrol Processes 2013;28:1329–44. http://dx.doi.org/10.1002/hyp.9627.
[60] Nuimura T, Fujita K, Yamaguchi S, Sharma RR. Elevation changes of glaciers revealed by multitemporal digital elevation models calibrated by GPS survey in the Khumbu region, Nepal Himalaya, 1992–2008. J Glaciol 2012;58(210):648–56. http://dx.doi.org/10.3189/2012JoG11J061.
[61] Nuimura T et al. The GAMDAM glacier inventory: a quality controlled inventory of Asian glaciers. Cryosphere Discuss 2014;8(3):2799–829. http://dx.doi.org/10.5194/tcd-8-2799-2014.
[62] Østrem G. Ice melting under a thin layer of moraine, and the existence of ice cores in moraine ridges. Geografiska Annaler 1959;41(4):228–30.
[63] Paul F, Huggel C, Kääb A. Combining satellite multispectral image data and a digital elevation model for mapping debris-covered glaciers. Remote Sensing Environ 2004;89(4):510–8. http://dx.doi.org/10.1016/j.rse.2003.11.007.
[64] Pellicciotti F, Brock B, Strasser U, Burlando P, Funk M, Corripio J. An enhanced temperature-index glacier melt model including the shortwave radiation balance: development and testing for Haut Glacier d Arolla, Switzerland. J Glaciol 2005;51(175):573–87. http://dx.doi.org/10.3189/172756505781829124.
[65] Pellicciotti F, Helbing J, Rivera A, Favier V, Corripio J, Araos J, et al. A study of the energy balance and melt regime on Juncal Norte Glacier, semi-arid Andes of central Chile, using melt models of different complexity. Hydrol Processes 2008;22:3980–97. http://dx.doi.org/10.1002/hyp.7085.
[66] Pellicciotti F, Buergi C, Immerzeel WW, Konz M, Shrestha AB. Challenges and uncertainties in hydrological modeling of remote Hindu Kush-Karakoram-Himalayan (HKH) basins: suggestions for calibration strategies. Mt Res Dev 2012;32(1):39–50. http://dx.doi.org/10.1659/MRD-JOURNAL-D-11-00092.1.
[67] Pellicciotti F, Ragettli S, Carenzo M, McPhee J. Changes of glaciers in the Andes of Chile and priorities for future work. Sci Total Environ 2014;493:1197–210. http://dx.doi.org/10.1016/j.scitotenv.2013.10.055.
[68] Pellicciotti F, Stephan C, Miles E, Immerzeel WW, Bolch T. Mass balance changes of debris-covered glaciers in the Langtang Himal in Nepal between 1974 and 1999. J Glaciol 2015;61(225):1–14. http://dx.doi.org/10.3189/2015JoG13J237.
[69] Petersen L, Schauwecker S, Brock B, Immerzeel W, Pellicciotti F. Deriving supraglacial debris thickness using satellite data on the Lirung Glacier in the Nepalese Himalayas. Geophys Res Abstr 2013;15(10):244.
[70] Prasch M, Mauser W, Weber M. Quantifying present and future glacier melt-water contribution to runoff in a central Himalayan river basin. Cryosphere 2013;7(3):889–904. http://dx.doi.org/10.5194/tc-7-889-2013.
[71] Priestley C, Taylor R. On the assessment of surface heat flux and evaporation using large-scale parameters. Mon Weather Rev 1972;100(2):81–92. http://dx.doi.org/10.1175/1520-0493(1972)100<0081:OTAOSH 2.3.CO;2.
[72] Racoviteanu AE, Armstrong R, Williams MW. Evaluation of an ice ablation model to estimate the contribution of melting glacier ice to annual discharge in the Nepal Himalaya. Water Resour Res 2013;49(9):5117–33. http://dx.doi.org/10.1002/wrcr.20370.
[73] Ragettli S, Pellicciotti F. Calibration of a physically based, spatially distributed hydrological model in a glacierized basin: on the use of knowledge from glaciometeorological processes to constrain model parameters. Water Resour Res 2012;48(3):1–20. http://dx.doi.org/10.1029/2011WR010559.
[74] Ragettli S, Cortez G, McPhee J, Pellicciotti F. An evaluation of approaches for modeling hydrological processes in high-elevation, glacierized Andean watersheds. Hydrol Processes 2013;28(23):5674–95. http://dx.doi.org/10.1002/hyp.10055a.
[75] Ragettli S, Pellicciotti F, Bordoy R, Immerzeel W. Sources of uncertainty in modeling the glaciohydrological response of a Karakoram watershed to climate change. Water Resour Res 2013;49(9):6048–66. http://dx.doi.org/10.1002/wrcr.20450b.
[76] Reid TD, Brock BW. An energy-balance model for debris-covered glaciers including heat conduction through the debris layer. J Glaciol 2010;56(199):903–16. http://dx.doi.org/10.3189/002214310794457218.
[77] Rohrer M, Salzmann N, Stoffel M, Kulkarni AV. Missing (in-situ) snow cover data hampers climate change and runoff studies in the Greater Himalayas. Sci Total Environ 2013;468–469(Supplement S60–S70). http://dx.doi.org/10.1016/j.scitotenv.2013.09.056.
[78] Sakai A, Nakawo M, Fujita K. Melt rate of ice cliffs on the Lirung Glacier, Nepal Himalayas, 1996. Bull Glacier Res 1998;16:57–66.
[79] Sakai A, Takeuchi N, Fujita K, Nakawo M. Role of supraglacial ponds in the ablation process of a debris-covered glacier in the Nepal Himalayas. IAHS Publ 2000;265:119–30.
[80] Sakai A, Nakawo M, Fujita K. Distribution characteristics and energy balance of ice cliffs on debris-covered glaciers, Nepal Himalaya. Arctic Antarctic Alpine Res 2002;34(1):12–9. http://dx.doi.org/10.2307/1552503.
[81] Sakai A, Fujita K, Kubota J. Evaporation and percolation effect on melting at debris-covered Lirung Glacier, Nepal Himalayas, 1996. Bull Glaciol Res 2004;21:9–15.
[82] Saxton KE, Rawls WJ. Soil water characteristic estimates by texture and organic matter for hydrologic solutions. Soil Sci Soc Am J 2006;70(5):1569–78. http://dx.doi.org/10.2136/sssaj2005.0117.
[83] Shangguan D et al. Glacier changes in the Koshi River basin, central Himalaya, from 1976 to 2009, derived from remote-sensing imagery. Ann Glaciol 2014;55(66):61–8. http://dx.doi.org/10.3189/2014AoG66A057.
[84] Shiraiwa T, Ueno K, Yamada T. Distribution of mass input on glaciers in the Langtang Valley, Nepal Himalayas. Bull Glacier Res 1992;10:21–30.
[85] Spear RC, Hornberger GM. Eutrophication in peel inlet. 2. Identification of critical uncertainties via generalized analysis. Water Res 1980;14(1):43–9. http://dx.doi.org/10.1016/0043-1354(80)90040-8.
[86] Steinegger U, Braun L, Kappenberger G, Tartari G. Assessment of annual snow accumulation over the past 10 years at high elevations in the Langtang region. IAHS Publ 1993;218:155–66.
[87] Steiner JF, Pellicciotti F, Buri P, Evan S, Immerzeel WW. Modeling ice cliff backwasting on a debris covered glacier in the Nepalese Himalayas. J Glaciol. 2014: p. 1–17 (under review).
[88] Sugiyama S, Fukui K, Fujita K, Tone K, Yamaguchi S. Changes in ice thickness and flow velocity of Yala Glacier, Langtang Himal, Nepal, from 1982 to 2009. Ann Glaciol 2013;54(64):157–62. http://dx.doi.org/10.3189/2013AoG64A111.
[89] Tang Y, Reed P, Wagener T, van Werkhoven K. Comparing sensitivity analysis methods to advance lumped watershed model identification and evaluation. Hydrol Earth Syst Sci 2007;11(2):793–817. http://dx.doi.org/10.5194/hess-11-793-2007.
[90] Wagnon P et al. Seasonal and annual mass balances of Mera and Pokalde glaciers (Nepal Himalaya) since 2007. Cryosphere 2013;7(6):1769–86. http://dx.doi.org/10.5194/tc-7-1769-2013.
[91] Wang X, Xie H, Liang T. Evaluation of MODIS snow cover and cloud mask and its application in Northern Xinjiang, China. Remote Sensing Environ 2008;112(4):1497–513. http://dx.doi.org/10.1016/j.rse.2007.05.016.
[92] Wicki S. Energy balance modelling over the debris-covered Lirung Glacier [Master thesis]. Nepalese Himalaya: Department of Environmental Engineering, ETH Zurich; 2014.
[93] Yao T et al. Different glacier status with atmospheric circulations in Tibetan Plateau and surroundings. Nat Clim Change 2012;2(9):663–7. http://dx.doi.org/10.1038/nclimate1580.
[94] Zelazowski P, Sayer AM, Thomas GE, Grainger RG. Reconciling satellite-derived atmospheric properties with fine-resolution land imagery: insights for atmospheric correction. J Geophys Res 2011;116(D18308):1–15. http://dx.doi.org/10.1029/2010JD015488.
[95] Zhang Y, Fujita K, Liu S, Liu Q, Nuimura T. Distribution of debris thickness and its effect on ice melt at Hailuogou glacier, southeastern Tibetan Plateau, using in situ surveys and ASTER imagery. J Glaciol 2011;57(206):1147–57. http://dx.doi.org/10.3189/002214311798843331.

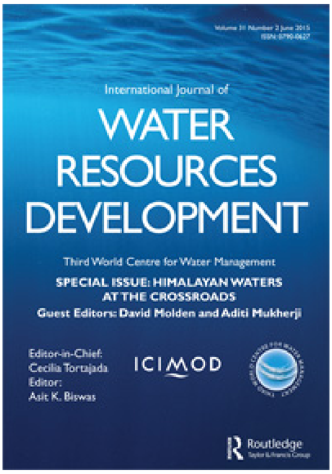

International Journal of Water Resources Development
Publication details, including instructions for authors and subscription information:
http://www.tandfonline.com/loi/cijw20

A comparative high-altitude meteorological analysis from three catchments in the Nepalese Himalaya

J.M. Shea[a], P. Wagnon[ab], W.W. Immerzeel[c], R. Biron[b], F. Brun[b] & F. Pellicciotti[d]

[a] International Centre for Integrated Mountain Development, Kathmandu, Nepal
[b] IRD/UJF-Grenoble 1/CNRS/G-INP, LTHE UMR5564, LGGE UMR5183, Grenoble, France
[c] Department of Physical Geography, Utrecht University, the Netherlands
[d] Department of Environmental Engineering, ETH Zürich, Switzerland

Published online: 18 Apr 2015.

To cite this article: J.M. Shea, P. Wagnon, W.W. Immerzeel, R. Biron, F. Brun & F. Pellicciotti (2015) A comparative high-altitude meteorological analysis from three catchments in the Nepalese Himalaya, International Journal of Water Resources Development, 31:2, 174-200, DOI: 10.1080/07900627.2015.1020417

To link to this article: http://dx.doi.org/10.1080/07900627.2015.1020417

International Journal of Water Resources Development, 2015
Vol. 31, No. 2, 174–200, http://dx.doi.org/10.1080/07900627.2015.1020417

A comparative high-altitude meteorological analysis from three catchments in the Nepalese Himalaya

J.M. Shea[a*], P. Wagnon[a,b], W.W. Immerzeel[c], R. Biron[b], F. Brun[b] and F. Pellicciotti[d]

[a]*International Centre for Integrated Mountain Development, Kathmandu, Nepal;* [b]*IRD/UJF–Grenoble 1/CNRS/G-INP, LTHE UMR5564, LGGE UMR5183, Grenoble, France;* [c]*Department of Physical Geography, Utrecht University, the Netherlands;* [d]*Department of Environmental Engineering, ETH Zürich, Switzerland*

(*Received 29 September 2014; accepted 14 February 2015*)

Meteorological studies in high-mountain environments form the basis of our understanding of catchment hydrology and glacier accumulation and melt processes, yet high-altitude (>4000 m above sea level, asl) observatories are rare. This research presents meteorological data recorded between December 2012 and November 2013 at seven stations in Nepal, ranging in elevation from 3860 to 5360 m asl. Seasonal and diurnal cycles in air temperature, vapour pressure, incoming short-wave and long-wave radiation, atmospheric transmissivity, wind speed, and precipitation are compared between sites. Solar radiation strongly affects diurnal temperature and vapour pressure cycles, but local topography and valley-scale circulations alter wind speed and precipitation cycles. The observed diurnal variability in vertical temperature gradients in all seasons highlights the importance of *in situ* measurements for melt modelling. The monsoon signal (progressive onset and sharp end) is visible in all data-sets, and the passage of the remnants of Typhoon Phailin in mid-October 2013 provides an interesting case study on the possible effects of such storms on glaciers in the region.

Keywords: meteorology; glaciers; water resources; monsoon; Himalaya; Nepal

Introduction

High-altitude catchments in Asia play a pivotal role in regional hydrology and water resources (Immerzeel, van Beek, & Bierkens, 2010; Viviroli, Dürr, Messerli, Meybeck, & Weingartner, 2007). Glacier melt, snow melt, and rainfall contributions to streamflow vary across the region (Lutz, Immerzeel, Shrestha, & Bierkens, 2014) and are ultimately determined by the interactions between terrain and atmospheric circulation patterns. However, future climate changes are projected to substantially impact snow and glacier water resources (Lutz et al., 2014), and warming signals appear to be enhanced at high elevations (Rangwala & Miller, 2012). Identification of glacier responses to climate change in this large and remote area is challenging, but nevertheless required to quantify glacier contribution to water resources (Immerzeel, Pellicciotti, & Bierkens, 2013; Kaser, Grosshauser, & Marzeion, 2010) and sea-level rise (Gardner et al., 2013), or to reliably project their response to twenty-first-century climate changes (Marzeion, Jarosch, & Hofer, 2012; Radić & Hock, 2011).

Glaciers are good climatic indicators (Oerlemans, 2001), and recent studies have demonstrated that glaciers across the Karakoram-Himalaya region experience contrasting patterns of volume change (Gardelle, Berthier, Arnaud, & Kääb, 2013; Kääb, Berthier,

*Corresponding author. Email: joseph.shea@icimod.org

Nuth, Gardelle, & Arnaud, 2012). Over the last decade, Karakoram glaciers have been in balanced conditions or slightly gaining mass (the so-called Karakoram anomaly; Hewitt, 2005) though glaciers in the Himalaya have been shrinking at an accelerated rate since the beginning of the twenty-first century (Azam et al., 2014a; Bolch et al., 2012). Spatial patterns of glacier change have been linked to both climatic changes (Shrestha & Aryal, 2011) and the geomorphologic characteristics of glaciers (i.e. debris-covered versus clean glaciers (Scherler, Bookhagen, & Strecker, 2011). From west to east, the region is subject to different climate systems, with an increased influence of the Asian and Indian summer monsoons and simultaneously decreased influence of westerly storm systems (Bookhagen & Burbank, 2006).

Long-term, high-resolution meteorological records at glacier elevations are an essential prerequisite to (1) place the observed glacier changes in the context of current climatic change and (2) calibrate and validate statistically and dynamically downscaled climate fields (Maussion et al., 2014; Mölg, Maussion, Yang, & Scherer, 2012), which are essential for spatially distributed models of glacier–climate response and hydrology. But in this region, where glaciers are located at high altitudes in remote environments that are difficult to access, the collection of long-term and high-quality meteorological data is challenging. Consequently, year-round meteorological observations at high-altitude glacier stations are extremely scarce in the Himalaya (Table 1), especially in comparison with other mountain regions such as the European Alps. Nevertheless, before making any projections of future glacier change, understanding how glaciers respond to the present climate is necessary, and this requires combining meteorological records at glacier elevations with glaciological monitoring.

Table 1. A summary of selected high-elevation automatic weather stations (AWS) in the HKH region, with elevation (Z) and on- or off-glacier designation, station type (A = year-round, S = seasonal/temporary), and type of observations: T = temperature, RH = relative humidity, P = precipitation, u = wind speed, θ = wind direction, $K\downarrow$ = downwelling short-wave radiation, $L\downarrow$ = downwelling long-wave radiation, p = atmospheric pressure.

Site	Z (m)	Station type	Observations	Period	Country/ source
Pyramid	5035 (off)	A	$T, RH, P, u, \theta, K\downarrow, L\downarrow, p$	1994–2014	Nepal/1, 2
Khumbu	5350 (on)	S	T, RH, u	1999	Nepal/3
Everest S. Col	7986 (off)	S	T	1998	Nepal/4
EB050 Khumbu	5160 (on)	S	P	1976	Nepal/5
Mera	5360 (on)	A	$T, RH, u, \theta, K\downarrow, L\downarrow, p$	2009–2010, 2012–2014	Nepal/6
AX010	4958 (off)	S	T, P	1973–1978	Nepal/7
Hidden Valley	5055 (off)	S	T, RH, P, p	1974	Nepal/8
Tibetan Plateau	4070, 4420	A	$K\downarrow, L\downarrow$	1998, 2003	China/9
Zhadang	5400, 5660, 5800	A	$T, RH, P, u, \theta, K\downarrow, L\downarrow, p$	2005–2011	China/10, 11
Baltoro	5033 (on)	S	$T, RH, u, \theta, K\downarrow, L\downarrow, p$	2004	Pakistan/12
Baltoro	4022 (off)	A	$T, RH, u, \theta, K\downarrow, L\downarrow, p$	2004	Pakistan/12

Sources: Ageta, Ohata, Tanaka, Ikegami, and Higuchi (1980); Bollasina, Bertolani, and Tartari (2002); Diodato et al. (2012); Higuchi (1977); Higuchi, Ageta, Yasunari, and Inoue (1982); Mihalcea et al. (2006); Mölg et al. (2012); Moore and Semple (2004); Takeuchi (2000); Wagnon et al. (2013); Yang, He, Tang, Qin, and Cheng (2010); Zhang et al. (2013).

Combined glaciological and meteorological studies have already been conducted in various mountain ranges such as the Alps (Oerlemans, 2000), the Andes (Favier, Wagnon, & Ribstein, 2004; Hardy, Vuille, Braun, Keimig, & Bradley, 1998), Africa (Nicholson, Prinz, Mölg, & Kaser, 2013), and Tibet (Mölg et al., 2012; Zhang et al., 2013). Similar studies are still needed in the Karakoram-Himalaya region, though some short-term studies have been published (Azam et al., 2014b; Fujita, Sakai, & Chhetri, 1997; Immerzeel, Petersen, Ragettli, & Pellicciotti, 2014; Takahashi et al., 1987). This article presents first analyses of high-quality meteorological data-sets recorded in three distinct catchments in the Nepal Himalaya where glaciological monitoring is simultaneously performed. Long-term mass balance and meteorological observations at selected benchmark glaciers representative of various climates in Nepal are required to better understand the climate–glacier relationship and inform models and projections.

During the melt season, observations of radiative fluxes and surface height changes are required for calibration of empirical and physically based snow and ice melt models (Hock, 2005; Pellicciotti et al., 2008; Ragettli & Pellicciotti, 2012). On-glacier observations of temperature, relative humidity and wind speeds can also be used to evaluate the effect of katabatic flows on meteorological variables within the surface boundary layer (Petersen & Pellicciotti, 2011; Shea & Moore, 2010). High-altitude precipitation is perhaps the most important meteorological variable to consider with respect to both glacier mass balance and the hydrological water balance (Rasmussen et al., 2012). Gradients of precipitation in mountainous environments are subject to both vertical and horizontal variability (Barry, 2012), are affected by the mechanism of precipitation, and are often defined by an elevation of maximum precipitation. In monsoon-dominated Langtang Valley, orographic uplift and valley-scale convection result in precipitation maxima at relatively low elevations (ca. 2000 m), while winter synoptic events result in precipitation maxima at higher elevations (Bookhagen & Burbank, 2006; Immerzeel et al., 2014). However, given the uncertainties and complexity of solid precipitation analyses (Marks, Winstral, Reba, Pomeroy, & Kumar, 2013) and the limited number of stations, solid precipitation and precipitation gradients are not addressed in this study.

The main objective of this paper is to characterize and compare meteorological conditions in different high-altitude glacierized catchments in Nepal, assessed from *in situ* measurements. The following sections describe the study areas and measurements and identify data gaps and sources of error, describe the calculation of derived quantities and gradients, and compare and contrast meteorological quantities between stations and between basins. We also assess temperature and vapour pressure gradients in the Langtang catchment, and examine the high-altitude meteorological impacts of Typhoon Phailin, a large post-tropical cyclone that crossed the study area in October 2013. Based on these analyses, key points are emphasized that need to be addressed for distributed energy balance studies, glacio-hydrological modelling (spatial variability of meteorological variables), or downscaling studies.

Study area and methods

Nepal contains a glacierized area of approximately 3900 km^2 (Bajracharya, Maharjan, Shrestha, Bajracharya, & Baidya 2014; http://rds.icimod.org), 90% of which is located at elevations between 4500 and 6500 m asl. The climate in central and eastern Nepal is dominated by the Indian monsoon, with nearly 80% of total annual precipitation occurring between June and October (Bookhagen & Burbank, 2006; Wagnon et al., 2013). The Himalaya form a large orographic barrier which can produce strong horizontal and vertical gradients of temperature and precipitation, but field-based studies of other meteorological parameters are limited. Furthermore, the climate stations operated by the Department of Hydrology and Meteorology of the Government of Nepal are mostly below 3000 m (http://www.dhm.gov.np) and thus are difficult to reconcile with high-altitude glaciological and hydrological studies.

Station locations and specifications

Combined glacier and meteorological modelling studies have been initiated by the International Centre for Integrated Mountain Development (ICIMOD) and the GLACIOCLIM project (through the Institut de Recherche pour le Développement). Through these projects, detailed meteorological observations (Table 2) have been collected at five stations, located in three catchments in Nepal: Langtang, Dudh Kosi, and Hidden Valley (Figure 1). This study compares and contrasts diurnal and seasonal patterns of air temperature (T), vapour pressure (e_a), wind speed (u), incoming solar radiation ($K\downarrow$), incoming longwave radiation ($L\downarrow$), and precipitation (P).

Meteorological observations were collected at the Kyanging and Yala Base Camp stations in Langtang Valley, at the Changri Nup and Mera Glacier stations in Dudh Kosi Valley, and at the Rikha Samba station in Hidden Valley (Figure 1). Precipitation observations were collected at Kyanging, Yala Base Camp, Yala2 and Morimoto stations in Langtang Valley, and at the Pyramid observatory near Changri Nup glacier. Station instrumentation and specifications, as well as some morphological features, are given in Table 2. All stations were off-glacier, except the Changri Nup station, which was on the debris-covered part of the glacier, and the Mera Glacier station, which was on a clean-ice glacier. The approximate measurement height at all stations was 2.0 m. The Pyramid, Yala2 and Morimoto precipitation gauges were shielded with Nipher and Tretyakov-type wind shields, respectively, while the Kyanging and Yala Base Camp precipitation sites were unshielded. A ventilated radiation shield working only during daytime was used for air temperature measurements at the Changri Nup and Mera glaciers. Meteorological observations were sampled at a frequency between 10 and 60 seconds, and recorded as 10-to-30-minute averages by Campbell Scientific and Real Time Solutions data-loggers. For all analyses in this paper, hourly averages were constructed from the data of the preceding hour.

Identification of errors

Errors in meteorological observations are not uncommon, particularly in harsh, high-elevation environments. From the five meteorological stations and three additional precipitation stations, a period of overlap from 1 December 2012 to 30 November 2013 was identified. The following steps were taken to address erroneous observations.

- Where available, data warnings and flags are used to remove spurious precipitation observations at the Pluvio sites (see Table 2).
- Night-time power losses occurred at the Changri Nup station starting in April 2013. Mean daily values at this site are used for illustrative purposes only, and when evaluating the mean daily cycle, mean hourly values are computed only for periods where more than 80% of observations are available.
- Incoming short-wave and long-wave radiation at the Mera Glacier station were affected by water ingress into the CNR4 housing. Radiation measurements from 5 September to 30 November 2013 were discarded for this analysis.

Table 2. Station locations, measurements, sensors, and morphological setting (T = temperature, RH = relative humidity, u = wind speed, θ = wind direction, $K\downarrow$ = downwelling short-wave radiation, $L\downarrow$ = downwelling long-wave radiation, P = precipitation).

Station (distance from Kyanging)	Elevation (m)	Latitude (°)	Longitude (°)	Parameters	Sensors	Morphological setting
Changri Nup (122 km)	5363	27.983	86.783	T/RH u, θ $K\downarrow, L\downarrow$	RMYoung 05103-5 Vaisala HMP45C Kipp&Zonen CNR4	AWS on a flat part of the debris-covered area of the glacier; valley open to the east
Mera (130 km)	5360	27.718	86.897	T/RH u, θ $K\downarrow, L\downarrow$	RMYoung 05103-5 Vaisala HMP155C Kipp&Zonen CNR4	AWS on Naulek Glacier (clean), drilled into the ice surface; tiltmeter
Pyramid (125 km)	5035	27.95	86.82	P	Geonor T-200B (shielded)	Flat grassy moraine
Kyanging	3862	28.211	85.570	T/RH u, θ $K\downarrow, L\downarrow$ P	Rotronic SC2 RMYoung 015043 Kipp&Zonen CNR4 OttPluvio 400 (unshielded)	Flat grassy side-valley
Morimoto (13 km)	4919	28.253	85.682	P	OttPluvio 400 (shielded)	Glacier moraine crest; rocky debris
Yala Base Camp (5 km)	5090	28.233	85.612	T/RH u, θ $K\downarrow, L\downarrow$ P	Rotronic SC2 RMYoung 015043 Kipp&Zonen CNR4 OttPluvio 400 (unshielded)	Bedrock knob below Yala Glacier
Yala2 (4 km)	4831	28.229	85.597	P	OttPluvio 400 (shielded)	Scree
Rikha Samba (212 km)	5310	28.799	83.515	T/RH u $K\downarrow$	Rotronic SC2 RMYoung 015043 Kipp&Zonen CMP6	Scree/bedrock

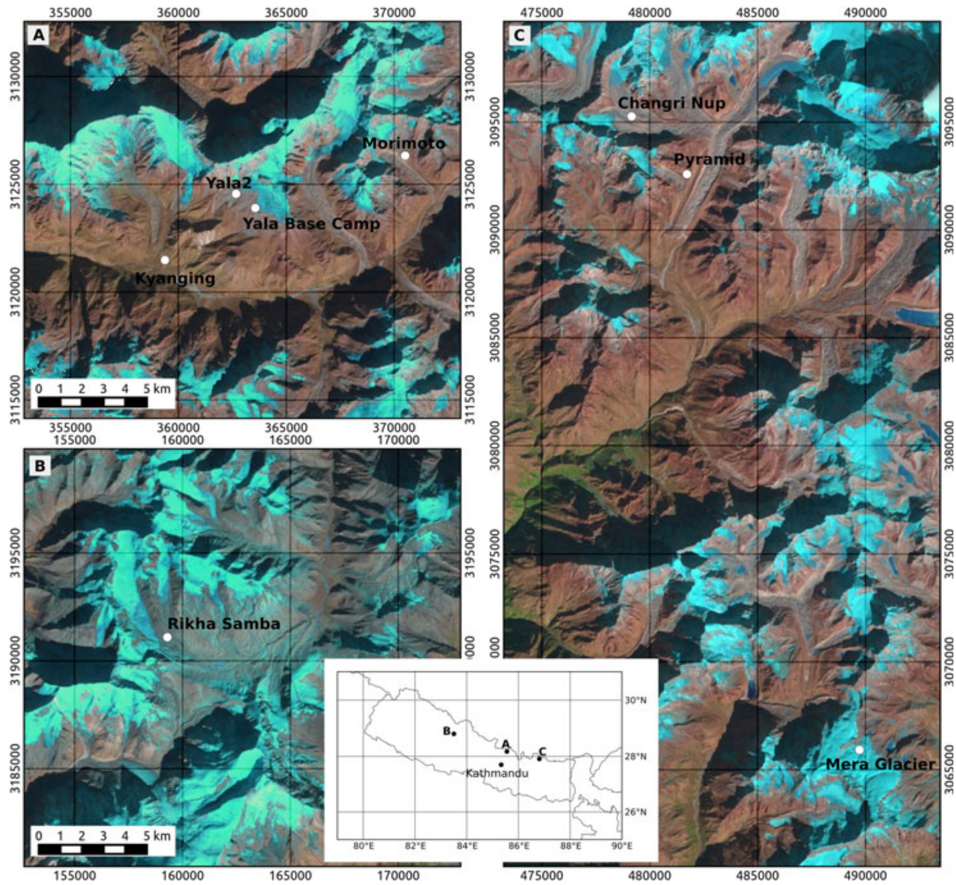

Figure 1. Location of meteorological and precipitation stations in (a) Langtang Valley, (b) Hidden Valley, and (c) DudhKosi, with location map of Nepal. Station location maps are given in UTM 45N projection.

- Values of $K\downarrow$ lower than $7\,\mathrm{W\ m^{-2}}$ are set to zero, and the maximum albedo ($\alpha = K\downarrow/K\uparrow$) was assumed to be 0.95. For observations where α exceeds 0.95 (i.e. where snowfall or dew/frost has reduced the amount of incoming solar radiation), $K\downarrow$ was recalculated as $K\uparrow/0.95$.
- Precipitation data at the Pyramid site are extracted from the bucket weight, which is recorded with a GeonorT-200B at 15-minute intervals. To extract the precipitation at each time step, we first calculate the change in bucket content, which is supposed to be always positive given that evaporation is blocked with a layer of oil spread out over the water. However, the vibrating device used to weigh the bucket is sensitive to external perturbations such as wind, which results in a background noise, i.e. small positive or negative changes for every 15-minute time step. To smooth the signal and avoid any negative precipitation values, each negative change recorded over a 15-minute time step is compensated by summing it with the neighbouring positive changes. In this way, the accumulated precipitation recorded over the entire period remains unchanged.
- While there are a number of empirical corrections for gauge undercatch based on air temperature and wind speed (Førland et al., 1996; Michelson, 2004; Wagnon et al.,

2009), these corrections need to be calibrated for different regions. Future research will be specifically focused on solid precipitation, rain/snow thresholds, and gauge undercatch issues, which do not substantially affect the results presented here.

Derived meteorological quantities and methods of comparison

To calculate vapour pressure we first calculate the saturation vapour pressure (e_s) following Teten's formulae (Bolton, 1980):

$$e_{\mathrm{s}} = \begin{cases} 6.108 \times 10^{\frac{9.5T}{T+265.5}}, \ T < 0 \\ 6.108 \times 10^{\frac{7.5T}{T+237.3}}, \ T > 0 \end{cases} \tag{1}$$

where T is the observed air temperature in °C. Actual vapour pressure (in hPa) is calculated from e_s and relative humidity (RH), which ranges from 0 to 100%:

$$e_{\mathrm{a}} = e_{\mathrm{s}} RH \tag{2}$$

Bulk daily atmospheric transmissivity (τ, unitless) is calculated as the ratio between observed mean daily incoming solar radiation and mean daily extraterrestrial solar radiation ($K\downarrow_{ex}$),

$$\tau = \frac{K\downarrow}{K\downarrow_{\mathrm{ex}}\ \tau_{\mathrm{cs}}} \tag{3}$$

where $K\downarrow_{ex}$ (W m^{-2}) was calculated for the latitude and longitude of each site (Table 2) using the United States National Renewable Energy Laboratory's online solar calculator (http://www.nrel.gov/midc/srrl_bms/), and τ_{cs} is the clear sky atmospheric transmissivity. We estimate τ_{cs} for each site by fitting daily $K\downarrow$ observations with $K\downarrow_{ex}\tau_{cs}$. To facilitate τ comparisons with the Changri Nup record, which is missing early-morning insolation data (usually between 1 and 2 hours after sunrise) between April and October 2013, mean daily $K\downarrow_{ex}$ at Changri Nup was recalculated by excluding the morning hours when observations were missing.

To compare the seasonal and diurnal patterns of each meteorological data-set, we first divide the year into four seasons: winter (December–February), pre-monsoon (March–May), monsoon (June–September), and post-monsoon (October–November). These divisions are arbitrary, but similar to those noted by Bonasoni et al. (2010). Mean daily values and total daily P are calculated for each station to examine seasonal trends and variability. For each station we also calculate the hourly mean and standard deviation to examine diurnal cycles of temperature, vapour pressure and wind speed in each season. Wind speeds and directions at each site are also compared with wind rose plots. For each hour, season and station we define a mean precipitation intensity (mm h^{-1}) for all hourly observations where $P > 0.1$ mm ($N_{P>0.1}$), and calculate an hourly precipitation frequency as $N_{P>0.1}/N$, where N is the total number of hourly observations. Gradients of near-surface temperature (γ_T) and vapour pressure (γ_{ea}) provide important information for distributed melt models. In Langtang Valley, where two stations are separated by only 2 km horizontally but by 1300 m in elevation, γ_T and γ_{ea} are computed as:

$$\gamma_{\mathrm{T}} = \frac{T_1 - T_2}{Z_1 - Z_2} \tag{4}$$

$$\gamma_{ea} = \frac{ea_1 - ea_2}{Z_1 - Z_2} \tag{5}$$

where Z_1 and Z_2 are elevations of the automatic weather stations. Gradients of near-surface temperature are a large source of uncertainty in temperature-indexed hydrological models (Immerzeel et al., 2014; Petersen & Pellicciotti, 2011), and melt modelling at hourly timescales requires understanding of sub-diurnal variability in temperature lapse rates. We thus examine seasonal variations in mean daily temperature gradients, and compare hourly temperature gradients calculated (a) for each season and (b) for snow-cover conditions at the Yala Base Camp site, as the presence of snow can affect near-surface temperatures.

In energy-balance models, the calculation of both sensible and latent heat fluxes requires estimates of near-surface T and e_a. Information about γ_T can also be used to infer the elevation of the zero-degree isotherm, which affects both precipitation phase (liquid or solid) and the sign of the sensible heat flux. The vapour pressure immediately above a melting snow or ice surface at 0°C is fixed at 6.11 hPa. The elevation of the 6.11 hPa isoline (obtained from γ_{ea}) thus impacts the sign of the latent heat flux, which controls the energy gain (condensation) or loss (evaporation or sublimation) at the surface (Shea & Moore, 2010).

From the computed temperature and vapour pressure gradients, we derive the approximate elevations of the 0 °C isotherm ($Z_{T=0}$) and the 6.11 hPa isoline ($Z_{ea=6.11}$) as:

$$Z_{T=0} = \frac{-T_K}{\gamma_T} + Z_K \tag{6}$$

$$Z_{ea=6.11} = \frac{6.11 - ea_K}{\gamma_{ea}} + Z_K \tag{7}$$

where Z_K is the elevation of the Kyanging station. For glaciers in monsoon climates, these quantities provide important information about the phase of precipitation at different elevations, and have a significant control on the sign of the sensible and latent heat fluxes.

Results

Comparison of seasonal variations in meteorological components

Time series of meteorological variables recorded at the Kyanging, Yala Base Camp, Rikha Samba, and Changri Nup and Mera Glacier stations illustrate the seasonal variation of meteorological variables across the region (Figure 2).

Temperature and vapour pressure

Air temperatures at all sites are strongly correlated at daily time step ($r = 0.93–0.97$), with high variability in the post-monsoon and winter months, and reduced variability in the monsoon. Temperatures at the Changri Nup station are elevated in the pre-monsoon period (after 21 April 2013) due to the missing early-morning (approximately 03:00–07:00) data. At the Mera Glacier site, mean daily temperatures do not exceed 3°C, a consequence of excess energy at the surface being directed to snow and ice melt. Vapour pressures calculated from air temperature and relative humidity are also highly correlated at daily time step ($r = 0.95–0.97$). However, the seasonal evolution of vapour pressure is different between low elevation (Kyanging) and high elevation (Yala, Changri Nup, Rikha Samba,

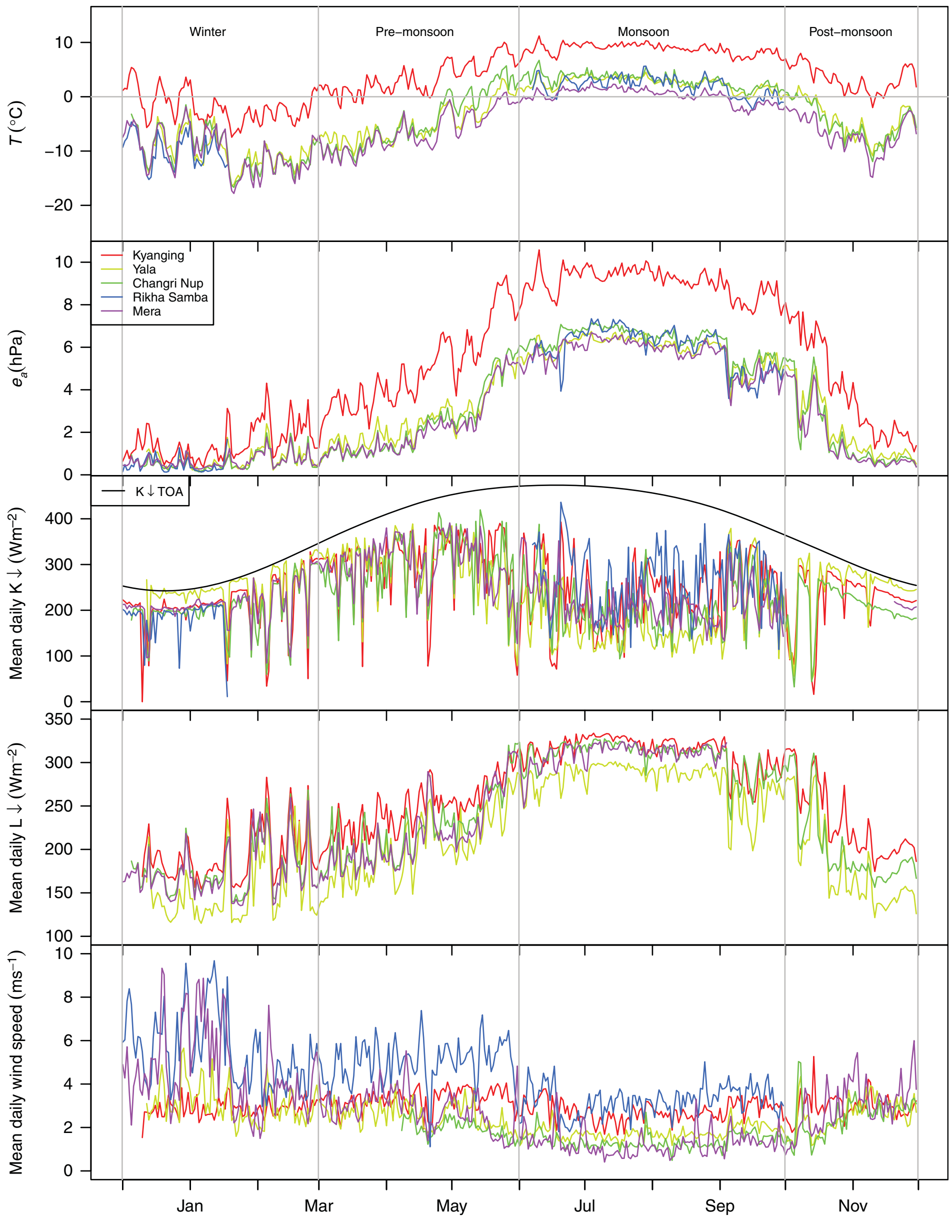

Figure 2. Summary of mean daily 2012–2013 meteorological data. From top to bottom, air temperature (T), vapour pressure (e), incoming short-wave radiation ($K\downarrow$), incoming long-wave radiation ($L\downarrow$), and wind speed (u). Climatological seasons (see text) are shown as vertical grey lines, and extraterrestrial global radiation calculated for 28N, 85E is given in black.

Mera). In winter, vapour pressures at all sites are extremely low (<2 hPa). Moisture advection and increased temperatures in the pre-monsoon season lead to elevated vapour pressures at all sites, but the increase is greatest at Kyanging. During the monsoon, vapour pressures at Kyanging remain 3–4 hPa higher than the high-elevation sites, but this difference is reduced to less than 1 hPa by the end of the post-monsoon.

Incoming short-wave and long-wave radiation

At all stations, increased cloudiness in the pre-monsoon leads to reductions in mean daily $K\downarrow$, and low values of $K\downarrow$ during the monsoon (Figure 2). Compared to incoming solar radiation at the top of the atmosphere (K_{TOA}), the Kyanging and Yala sites exhibit significantly different incoming short-wave radiation during the monsoon, which is probably related to cloud formation and valley circulation patterns. Similarly, Rikha Samba appears to have a higher mean incoming solar radiation. A sharp drop in vapour pressures at the high-elevation sites near the beginning of September corresponds with an increase in $K\downarrow$. The relative absence of clouds during the post-monsoon and winter seasons is also evident, as $K\downarrow$ parallels the extraterrestrial radiation. Correlations in mean daily $K\downarrow$ are moderate ($r = 0.55$–0.80) between the Kyanging, Yala Base Camp, Changri Nup, and Mera stations, and low ($r = 0.01$–0.41) between Rikha Samba and all other stations. The low correlations point towards the differences between cloud formation processes in windward and leeward sites, and the influence of the monsoon; Rikha Samba is the most westerly site, and is also the only site of our study located on the north side of the main mountain range, i.e. on its leeward slope.

Downwelling long-wave radiation (not measured at Rikha Samba) shows a minimum in the winter months, a gradual increase through the pre-monsoon, and a stable maximum for much of the monsoon (Figure 2). The break in the monsoon recorded in both the vapour pressure and solar radiation time series results in a steep decline in $L\downarrow$, which recovers until the end of September, and then declines rapidly during the post-monsoon period. Values for $L\downarrow$ are greatest at the lowest-elevation station (Kyanging), and lowest at the Yala station. Inter-station correlations in mean daily $L\downarrow$ range between 0.92 and 0.99 at daily time steps, and the highest correlation occurs between the Mera Glacier and Changri Nup stations.

Wind speed

Observed wind speeds are greatest at the Rikha Samba and Mera Glacier sites, and are particularly strong (greater than 4 m s^{-1}) during the winter and pre-monsoon (Figure 2). Wind speeds at all sites decrease during the monsoon, and exhibit reduced variability. Correlations in mean daily u are positive between all stations, with the greatest correlation ($r = 0.76$) between the Changri Nup and Yala Base Camp stations. The lowest correlation in mean daily u ($r = 0.10$) is found between the Kyanging and Mera Glacier stations. A surprisingly low correlation ($r = 0.26$) is also observed between the Kyanging and Yala Base Camp stations, which are only separated by 5 km horizontally (Table 2).

Precipitation

Daily precipitation totals in 2012–2013 demonstrate (1) the strong seasonality of precipitation, (2) differences in the magnitude of precipitation events between the Langtang and Dudh Kosi sites, and (3) the extraordinary precipitation amounts received during the passage of remnants of Typhoon Phailin in October 2013 (Figure 3). Winter and pre-monsoon precipitation events are sporadic, but with some significant accumulation totals, whereas precipitation occurs almost daily during the monsoon. Total annual precipitation observed at the Kyanging and Pyramid stations was 924.0 and 521.5 mm, respectively, with 56.5% and 70.0% of the precipitation occurring between June and September (Table 3). The share of monsoon precipitation in the annual total typically averages 80% in the region (Shea et al., in review; Wagnon et al., 2013). However, due to

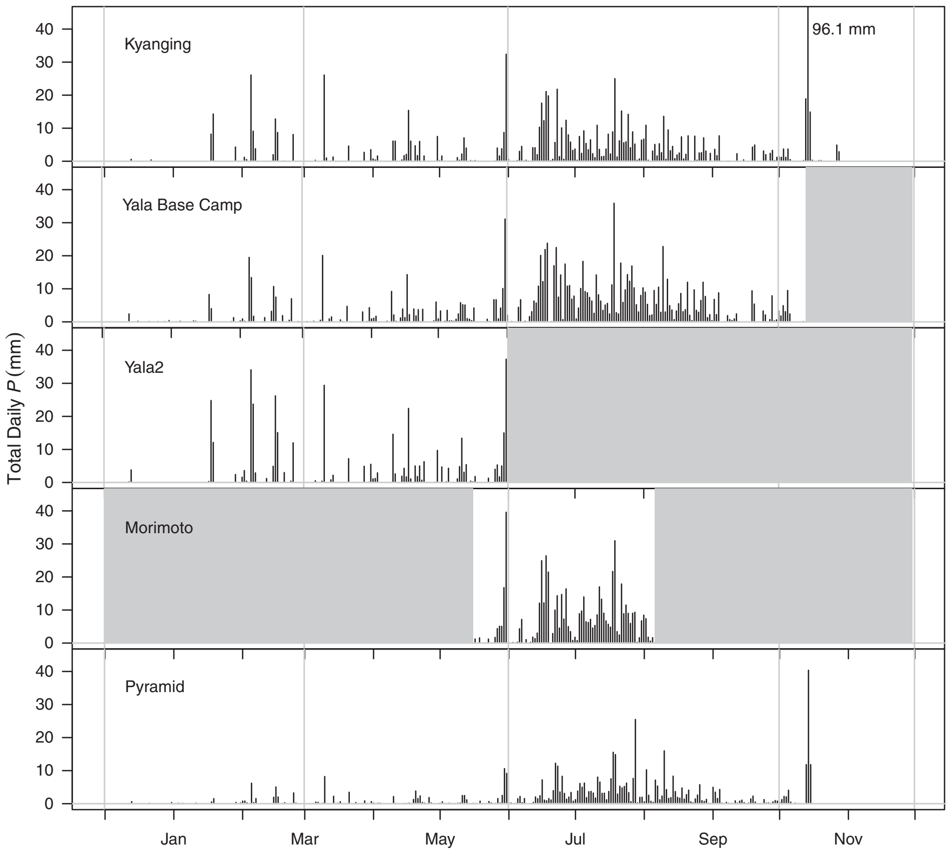

Figure 3. Total daily precipitation at Kyanging, Yala Base Camp, Yala2, Morimoto and Pyramid stations. Periods with no data are indicated in grey.

three-day precipitation totals of 129.9 mm and 63.9 mm at Kyanging and Pyramid during the Typhoon Phailin event (11–13 October 2013), the post-monsoon precipitation totals are elevated (Table 3). At Kyanging, 96.1 mm of precipitation fell during the second day of the event, and the Pluvio station at Yala overflowed during the event.

Previous studies of Kyanging meteorological data observed mean annual precipitation totals of 646.5 mm (Racoviteanu, Armstrong, & Williams, 2013), which is 30% less than that observed in this study, and a transect of tipping bucket stations in the valley recorded annual precipitation totals between 867 and 1819 mm (Immerzeel et al., 2014). While

Table 3. Seasonal and annual precipitation totals, 2012–2013. Morimoto precipitation totals were not calculated due to missing data. Relative contributions are given in parentheses for stations with a full year of data.

	Total precipitation, mm				
Site	DJF	MAM	JJAS	ON	Total
Kyanging	100.2 (11%)	136.9 (15%)	535.4 (58%)	151.5 (16%)	924.0 (100%)
Pyramid	27.0 (5%)	57.0 (11%)	371.9 (70%)	75.6 (14%)	531.5 (100%)
Yala Base Camp	85.8	157.9	746.4	–	–
Yala2	172.7	205.1	–	–	–

meteorological variability may explain some of the 30% difference between historical and 2012–2013 precipitation observations, a more likely explanation is that our measurements were automated, in contrast to the historical measurements, which were manual. Manual measurements are collected by an observer and are integrated over an approximate 24-hour period. Historical measurements may be subject to both systematic and random errors due to evaporation, measurement errors, and data transcription. This measurement bias has potentially large implications for the development, calibration and testing of hydrological and glaciological models in the region, and should be considered in future studies.

Kyanging, Yala Base Camp and Yala2 precipitation totals during the common period of record (1 December 2012–1 June 2013) are 269.5, 274.9 and 415.1 mm, respectively. The 150% higher precipitation observed during this period at the Yala2 station is probably due to the effects of the wind shield installed only at this location. Indeed, precipitation during the winter and pre-monsoon seasons occurs primarily as snowfall, and gauge accumulation totals are thus highly sensitive to wind speed (Yang, Goodison, Ishida, & Benson, 1998). Precipitation totals at Kyanging and Yala Base Camp are nearly identical during the winter and pre-monsoon but these totals are probably both under-estimated due to gauge undercatch. However, during the monsoon Yala Base Camp received 143 mm more precipitation than Kyanging – nearly 150% of the Kyanging value. This higher value, observed at two unshielded measurement sites, is probably due to orographic or convective effects that exist during the monsoon (Immerzeel et al., 2014).

Atmospheric transmissivity

Net all-wave radiation is the greatest contributor to the surface energy balance of high-altitude snowpacks and glaciers (Wagnon, Ribstein, Francou, & Pouyaud, 1999). Atmospheric transmissivity, which regulates the amount of short-wave radiation reaching the surface, is a function of atmospheric water vapour content, impurities, and clouds. As observations of short-wave radiation may be difficult to establish at high-elevation sites, atmospheric transmissivity is typically parameterized and used to scale global solar radiation at the top of the atmosphere.

Our estimates of clear-sky transmissivity (τ_{cs}) range from 0.98 (Yala Base Camp) to 0.85 (Rikha Samba). Time series of bulk daily transmissivity (τ; Figure 4) illustrates the synoptic (large-scale) nature of winter precipitation events, which result in correlated reductions in τ at the Langtang and Dudh Kosi sites. Similar reductions in transmissivity are also observed during the Typhoon Phailin event. During the pre-monsoon, steady declines in τ are observed in the Kyanging, Yala Base Camp, Mera Glacier and Changri Nup records, sporadically interrupted by sharp decreases due to precipitation events. Atmospheric transmissivity values at these sites are lowest during the monsoon, and the monsoon break in September results in sharply reduced vapour pressures (Figure 2) and a concomitant increase in atmospheric transmissivity. In contrast, transmissivity values at Rikha Samba are higher during the monsoon, and the monsoon break is not clearly defined by changes in τ.

Comparison of diurnal cycles in meteorological components

Temperature and vapour pressure

Temperature and vapour pressure exhibit strong diurnal cycles that reflect daytime solar heating (Figures 5 and 6). Minimum daily temperatures at the Yala and Kyanging sites occur at 07:00, while maximum temperatures are observed between 15:00 and 16:00.

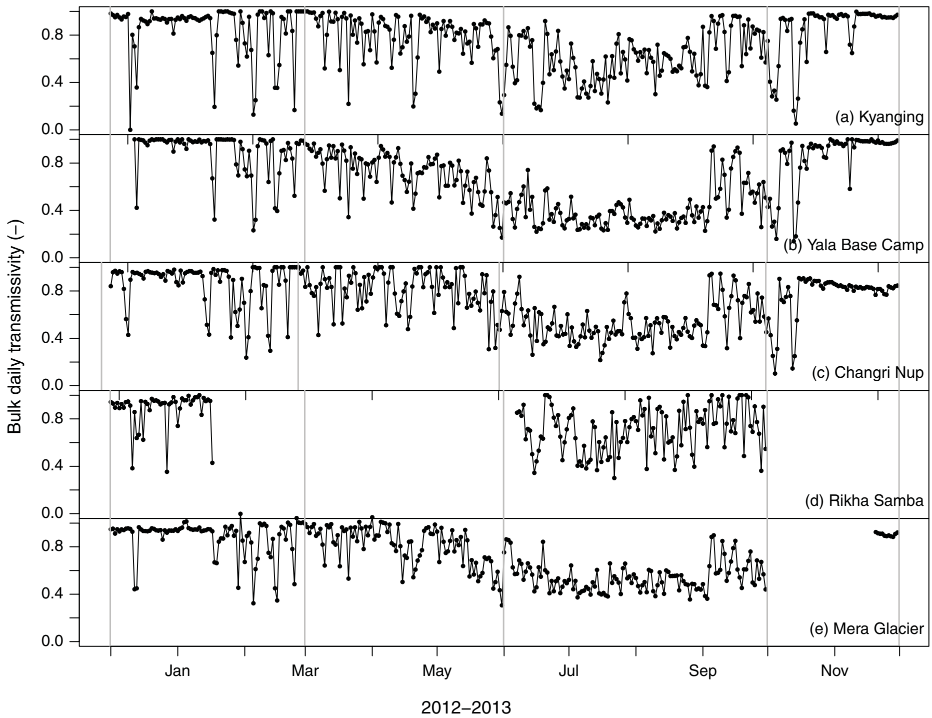

Figure 4. Bulk atmospheric transmissivity, 2012–2013, at (a) Kyanging, (b) Yala Base Camp, (c) Changri Nup, (d) Rikha Samba, and (e) Mera Glacier.

Maximum temperatures during the monsoon occur at 13:00 at Rikha Samba, and at 12:00 at Changri Nup. At all sites, the diurnal range of mean hourly air temperature (Figure 5) is strongly reduced during the monsoon. At Changri Nup, post-monsoon temperatures exhibit a marked early-afternoon maximum, in comparison with other records. Examination of the hourly records at Changri Nup suggests that this peak results from strong solar heating and relatively low wind speeds after the Typhoon Phailin snowfall event. In contrast, the daily temperature cycles at Mera Glacier show that peak temperatures occur in mid-morning (09:00), and the daily cycle is damped as surplus energy at the surface is directed to snow and ice melt, as opposed to increased air temperatures.

Vapour pressures follow a similar diurnal pattern (Figure 6), with maximum vapour pressures observed in late afternoon, and minima between 07:00 and 08:00. In pre- and post-monsoon seasons, the cycle is more gradual than that observed for temperature. Diurnal variations and absolute values of vapour pressure are lowest in winter, and the range of observed hourly vapour pressures is greatest in the post-monsoon.

Downwelling long-wave radiation

Unsurprisingly, diurnal cycles in $L\downarrow$ follow a pattern similar to mean daily temperatures and vapour pressures (Figure 7). Minimum values are observed at approximately 08:00 in all seasons, and increase towards late-afternoon/early-evening (16:00–20:00) maxima. The diurnal range and the standard deviation of observed $L\downarrow$ are lowest for the monsoon, and greatest in the post-monsoon. In the winter months, the diurnal signal of $L\downarrow$ is weak in

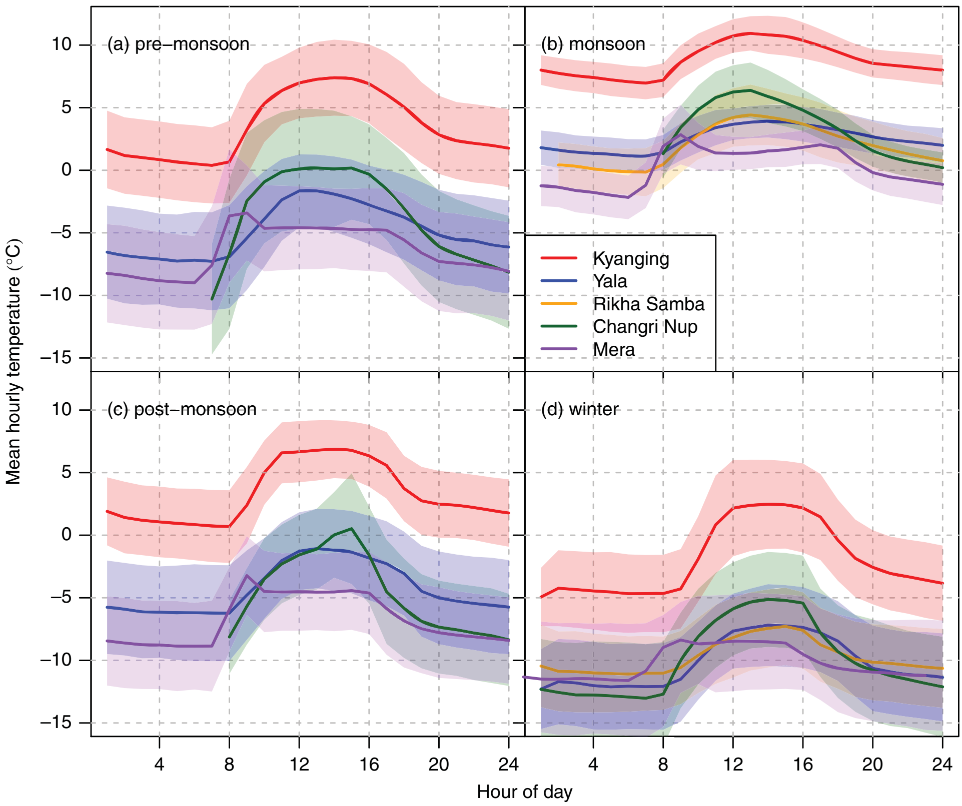

Figure 5. Cycles of mean daily temperature, for (a) pre-monsoon, (b) monsoon, (c) post-monsoon, and (d) winter. Solid lines show the hourly mean (calculated for periods where greater than 80% of observations were available), and the shaded portions give mean plus or minus standard deviation.

spite of the substantial warming observed (Figure 5) and appears to follow the vapour pressure cycle more closely. Changri Nup and Mera Glacier long-wave radiation cycles are very similar over their common periods of record.

Precipitation

At high altitudes, the timing and magnitude of precipitation can have a significant impact on glacier melt totals, as the phase is determined by air temperature. In the pre-monsoon, the frequency of precipitation is greatest in the late afternoon at all sites (Figure 8). Precipitation frequency during the monsoon is characterized by minima in the early morning (6:00–7:00), and two maxima in the mid-afternoon (13:00–16:00) and the middle of the night (23:00–2:00), with relatively high frequencies of occurrence throughout the day. In the post-monsoon and winter seasons, precipitation frequencies are generally low, with a slight tendency towards greater frequencies in the late afternoon.

Precipitation intensities are greatest in the pre- and post-monsoon seasons, with a maximum observed mean intensity of 5 mm h^{-1} at Kyanging. There do not appear to be any consistent diurnal patterns of precipitation intensity except in the pre-monsoon season, when intensities are greatest in the afternoon. Higuchi (1977) suggested that 60% of the total precipitation at Rikha Samba was received between 17:40 and 05:40. We find similar

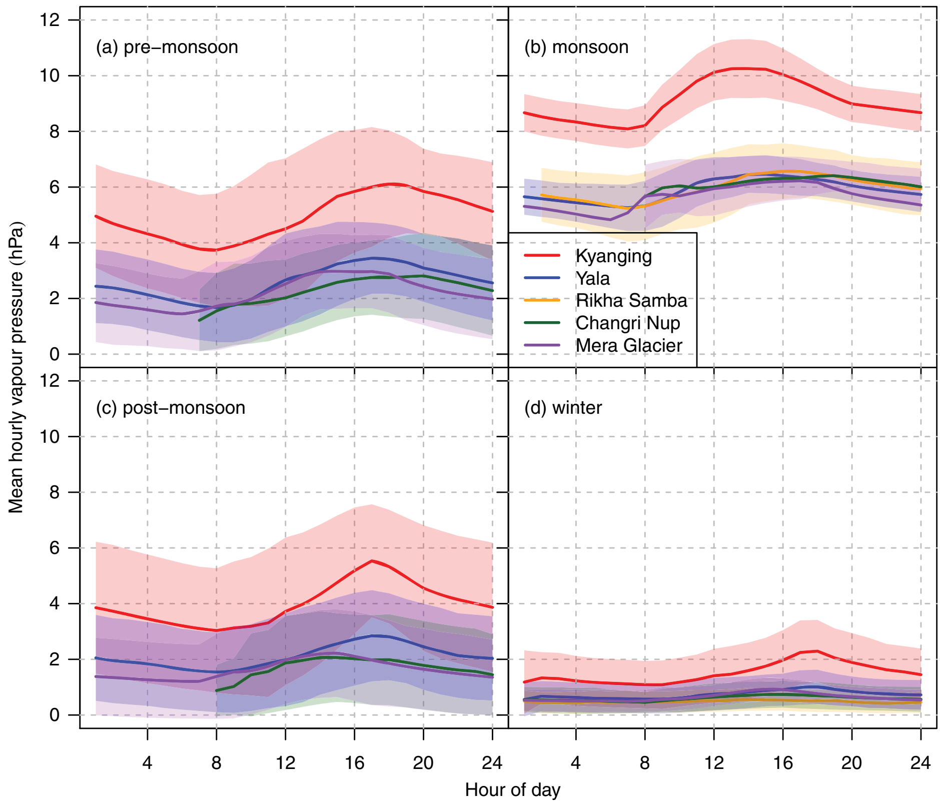

Figure 6. As in Figure 5, but for vapour pressure.

values at our stations, where between 49.3% (at Yala2) and 69.2% (at Pyramid) of total monsoon precipitation occurs between 17:00 and 05:00.

Wind speed and direction

In mountainous terrain, wind speed and direction are products of synoptic and valley-scale circulations, and topographic exposure (Whiteman, 2000). Wind speeds regulate the turbulent transfer of sensible and latent heat over melting snow and ice surfaces (Hock, 2005), but are among the most difficult meteorological parameters to model accurately in complex terrain (Jiménez et al., 2012).

Wind roses for the five sites demonstrate the dominance of valley winds at the Kyanging and Yala Base Camp stations, and the exposure of stations to synoptic-scale flows at Rikha Samba and Mera Glacier (Figure 9). Diurnal wind speed cycles are given in Figure 10. At Kyanging, the predominant wind direction is up-valley (westerly), with a secondary down-valley wind maximum. The Kyanging site (Figure 1) is above the main valley floor, on the northern slope, and daytime heating occurs in all seasons (Figure 5). Maximum mean wind speeds of 5–7 m s^{-1} occur between 15:00 and 16:00 at Kyanging. In all seasons except the post-monsoon, wind speeds at Yala Base Camp follow a similar pattern, though maximum wind speeds are lower (3–5 m s^{-1}). Wind directions at Yala Base Camp also follow a bi-modal distribution (Figure 9), with dominant up-valley (south-west) winds, and secondary down-glacier (north-east) winds.

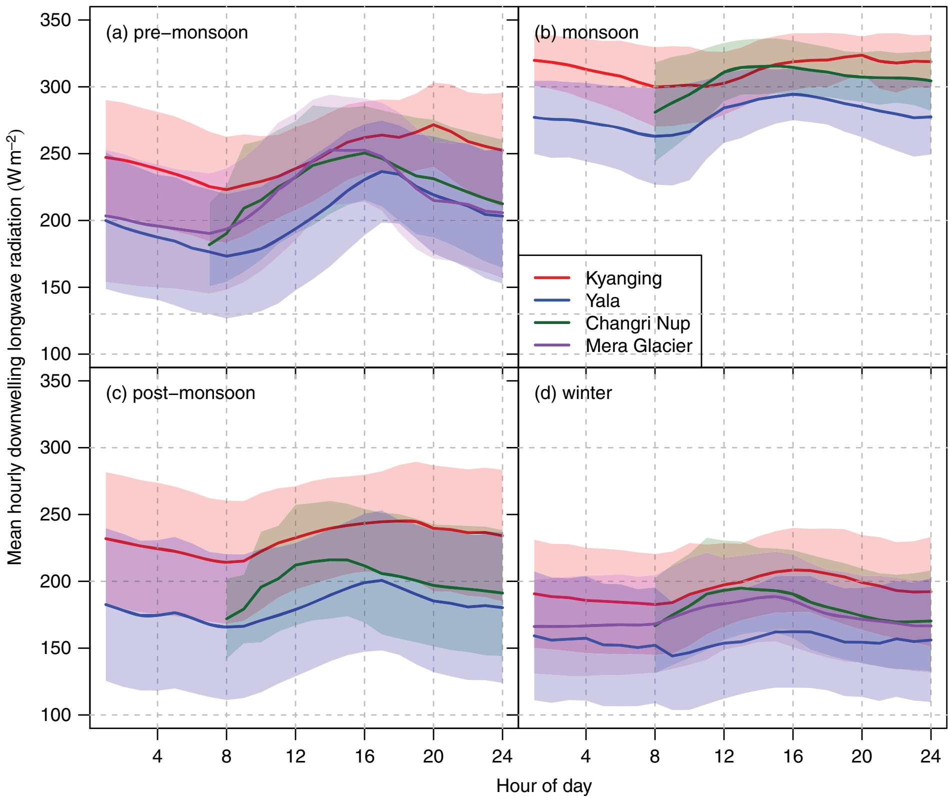

Figure 7. As in Figure 5, but for downwelling long-wave radiation. Data for the Mera Glacier station are missing in the monsoon and post-monsoon.

At Changri Nup, mid-afternoon wind maxima occur in the pre-monsoon and monsoon (Figure 10), but the maximum wind speed is the lowest of all four stations (2–3 m s^{-1}), also partly due to the fact that there is a large data gap in this series (no data between December 2012 and March 2013). Wind directions at Changri Nup are mainly from the south-west, which suggests that valley wind circulations are weak, and that this on-glacier station is influenced by glacier katabatic winds. At Rikha Samba, the distribution of wind direction is also bimodal. The dominant wind direction is from the north-west, with a secondary maximum from the south (up-valley). The greatest wind speeds, observed in winter (Figure 2), result from the channelling of synoptic-scale winds (Figure 1). At Rikha Samba, strong valley circulation results in up-valley wind maxima that average 5 m s^{-1} at 16:00 during the monsoon. Finally, at the Mera Glacier station there is no evidence of valley wind circulation. Winds are almost entirely from the west and reach up to 12 m s^{-1}, a result of the exposure of the station to synoptic-scale winds.

Temperature and vapour pressure gradients

Temperature and vapour pressure gradients computed from the hourly data observed at the Kyanging and Yala stations (Figures 11 and 12) highlight the importance of having multiple stations at different elevations. While vertical gradients would ideally be calculated with a number of stations at different elevations, this two-station gradient reflects a common measurement scenario. At daily scales, vertical temperature gradients

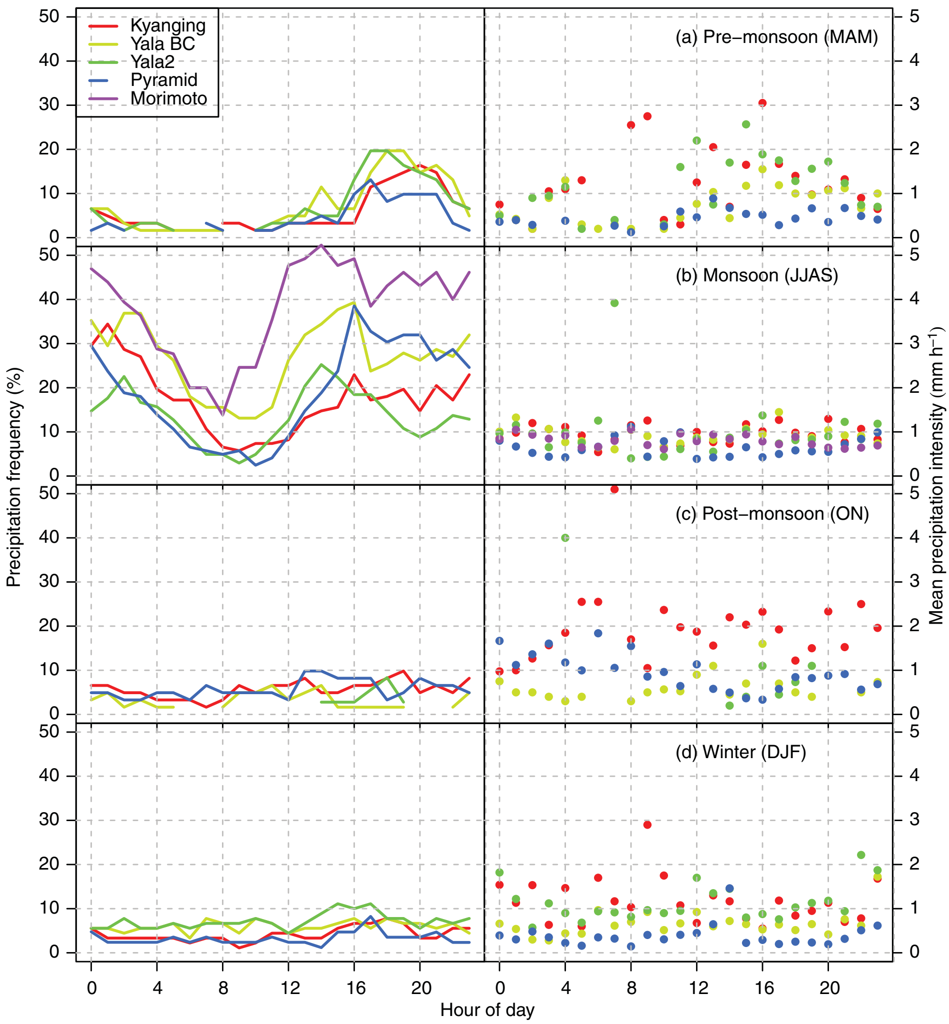

Figure 8. Hourly precipitation frequency (%, left column) and intensity (mm h^{-1}, right column) for (a) pre-monsoon, (b) monsoon, (c) post-monsoon, and (d) winter.

vary from -6 to -8°C km^{-1} during the winter and post-monsoon, and are least negative during the monsoon (-4 to -5°C km^{-1}). This is consistent with previous results reported from a transect of temperature loggers in Langtang Valley that covered a greater elevation range (Immerzeel et al., 2014), but different from the values reported by Fujita and Sakai (2000). The derived height of the estimated 0°C isotherm varies from approximately 3000 m asl in the winter to 6000 m asl during the monsoon. Glaciers in the region are situated mainly between 5000 and 6000 m (Bajracharya et al., 2014), which would suggest that a majority of glaciers in the basin experienced melt and liquid precipitation during the monsoon. During the Typhoon Phailin event in October 2013, $Z_{T=0}$ increased to 7000 m asl for a short duration.

Calculated vapour pressure gradients (Figure 12) range from 0 to -3 hPa km^{-1}, with the most negative values occurring during the monsoon. The strong gradient during monsoon results in $Z_{ea=6.11}$ values of approximately 5000 m asl, and lower values for the

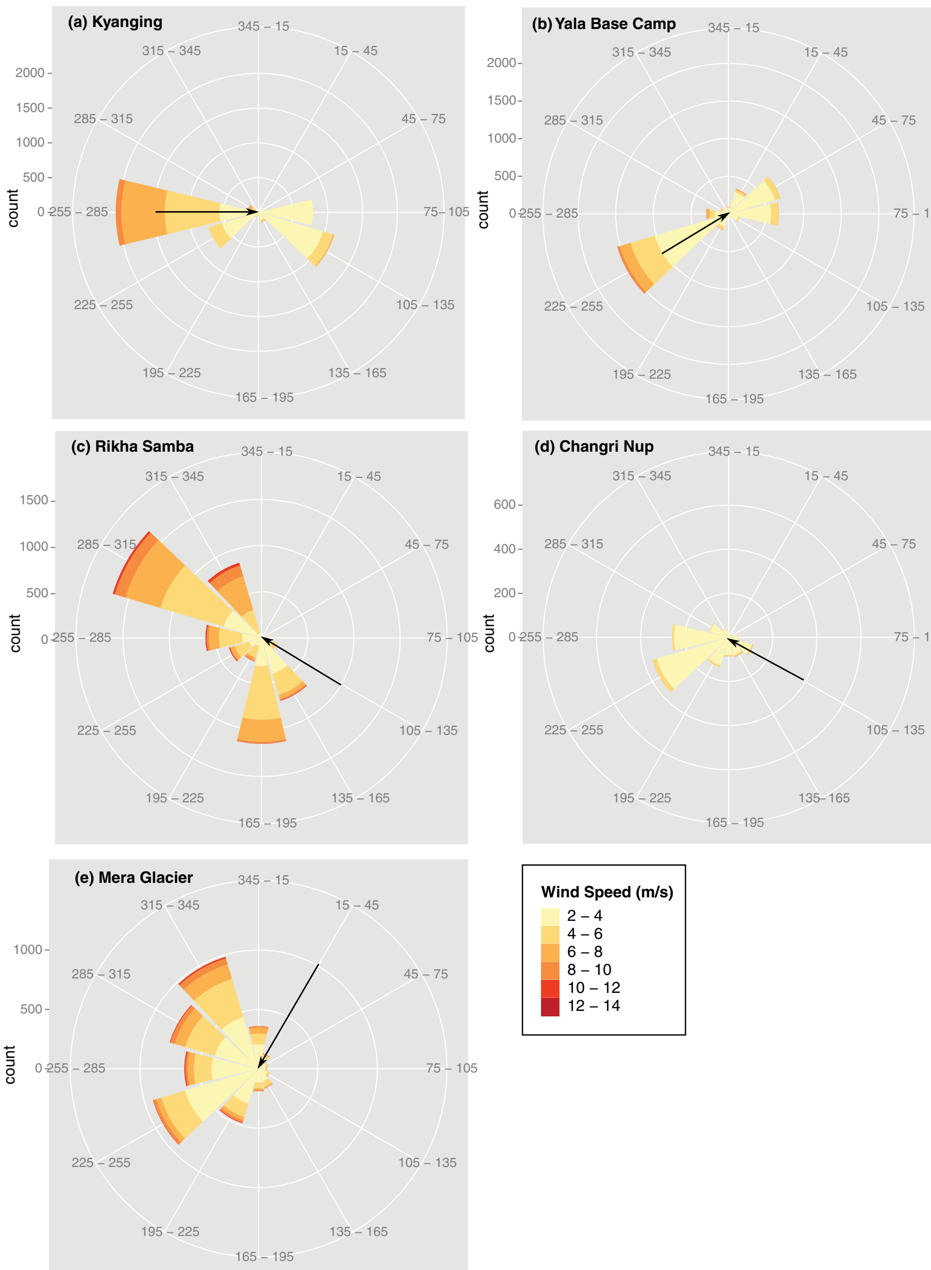

Figure 9. Wind roses for (a) Kyanging, (b) Yala Base Camp, (c), Rikha Samba, (d) Changri Nup, and (e) Mera Glacier automatic weather stations, 2012–2013. Up-valley wind directions are indicated by arrows.

rest of the year. This information suggests that glaciers in the region experience primarily evaporation/sublimation (energy loss) from the surface, which has implications for both energy balance melt models and glacier mass balance.

The diurnal cycle of hourly temperature gradients (Figure 13) calculated for the Kyanging – Yala Base is similar in all seasons and snow conditions. Vertical gradients are

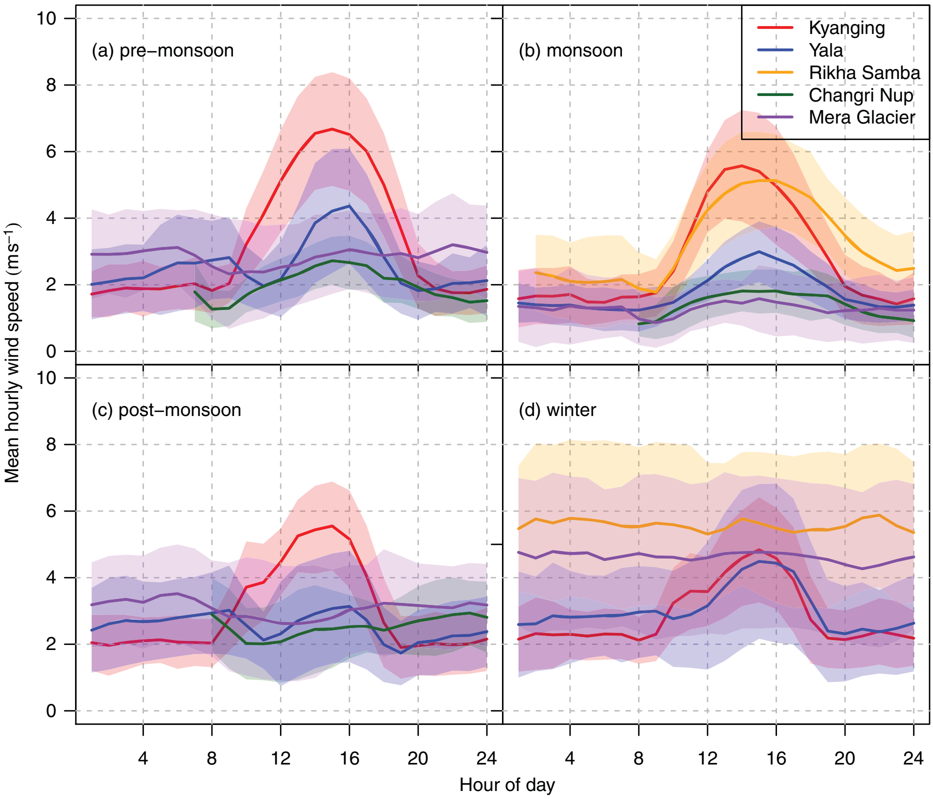

Figure 10. Mean (solid) and standard deviation (shaded) of wind speed by hour of day, for (a) pre-monsoon, (b) monsoon, (c) post-monsoon, and (d) winter seasons.

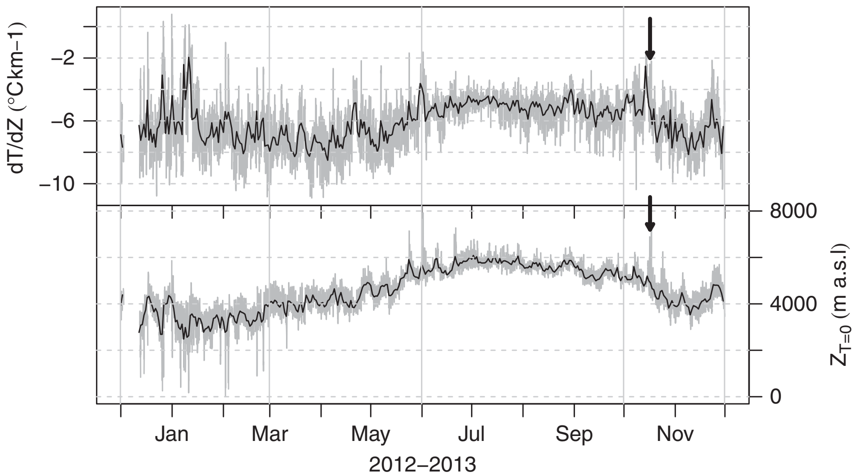

Figure 11. Temperature gradients (top panel) and height of the 0 °C isotherm (bottom panel) in the Langtang catchment, 2012–2013. Hourly values are in dark grey, and daily mean values are in black. The Typhoon Phailin event is indicated with an arrow.

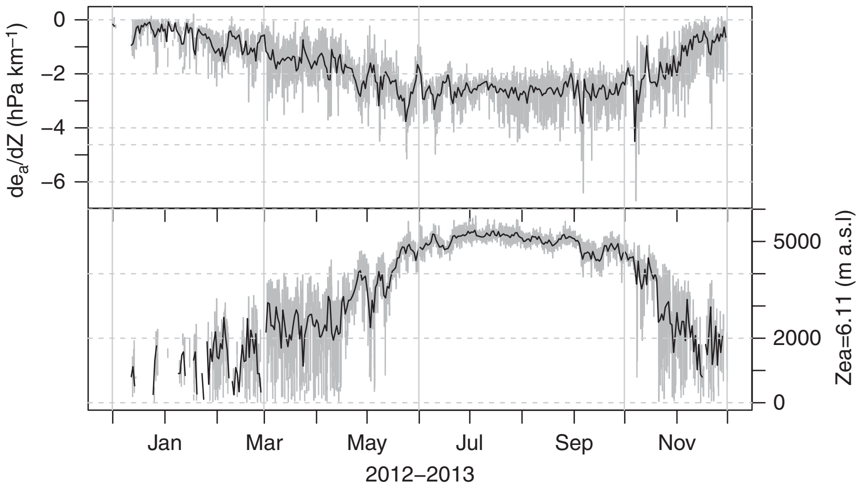

Figure 12. Gradients of vapour pressure (top panel) and height of the 6.11 hPa isoline (bottom panel) in the Langtang catchment, 2012–2013. Hourly values are in dark grey, and daily mean values are in black.

least negative at 8:00 am, and most negative in the mid-afternoon, with 1–2 °C km^{-1} differences between maximum and minimum temperature gradients. Temperature gradients are more negative when there is snow at the Yala Base Camp station, which occurs mainly during the winter and pre-monsoon months. It is probably a combination of both (a) the presence of snow that causes more negative lapse rates, and (b) the increased moisture during monsoon that results in less negative temperature gradients. Hourly temperature gradients calculated in this study show strong similarities to those reported by Fujita and Sakai (2000), though the gradients presented here are more negative.

Discussion and conclusions

Meteorological observations at high altitudes are a critical component of glacial and hydrological monitoring strategies, particularly in the Hindu Kush–Himalaya region, where standard meteorological networks exist almost exclusively at low elevations. High-altitude meteorological data are used as both input and calibration data for glacio-hydrological models (Ragettli, Pellicciotti, Bordoy, & Immerzeel, 2013) and are necessary for the evaluation of dynamically and statistically downscaled fields (Jiménez et al., 2010, Maussion et al., 2013).

Based on our analyses of seasonal and diurnal patterns of meteorological variables recorded at four stations in the Nepal Himalaya, we can make several observations that have implications for snow and ice melt modelling and dynamical downscaling. First, diurnal heating through solar radiation and valley wind circulation play significant roles in daytime temperatures and wind speed, though wind speed magnitude appears to be a function of station location in relation to the main valley axis. Both mean daily temperatures and diurnal variations are highly correlated at all sites within the study area, but sub-diurnal variations in temperature gradients (Figure 13) will strongly affect melt estimated using empirical degree-day approaches (Petersen & Pellicciotti, 2011). Wind speed extrapolations for physically based melt models or snow redistribution models remain highly uncertain.

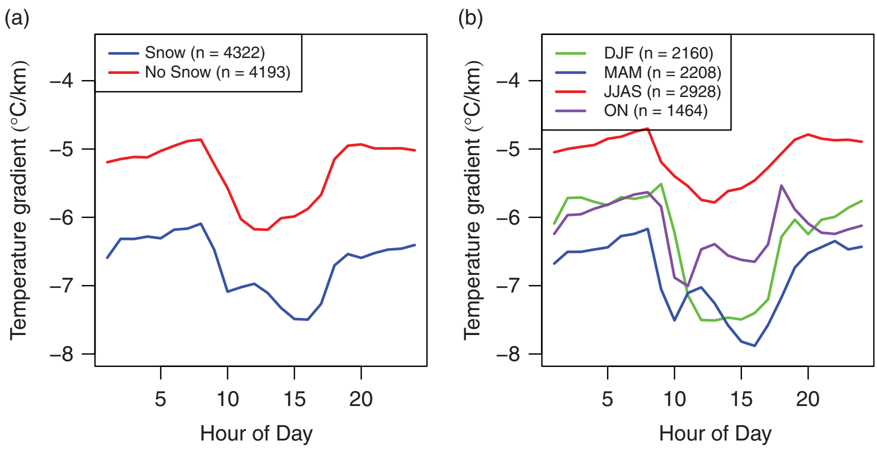

Figure 13. Mean hourly temperature gradients between Yala and Kyanging for snow-cover conditions at Yala (left), and season (right). The total number of hourly observations for each condition is given in brackets. The Yala site is snow-covered for most of the MAM period, and the latter portion of the DJF period.

Second, all sites exhibit a strong relation between daily bulk atmospheric transmissivity and vapour pressure ($r = -0.53$ to -0.83). Absorbed solar radiation at the surface is an important component of the surface energy balance at high-altitude snow and ice sites (Wagnon et al., 1999), and empirical models of atmospheric transmissivity typically rely on relatively simple measurements, such as temperature and humidity. Future research will aim to develop models of atmospheric transmissivity at these high-altitude sites and to identify the causes of different clear-sky transmissivities.

Third, our precipitation measurements support previous observations of early-morning and late-evening precipitation maxima during the monsoon in Langtang (Ueno, Shiraiwa, & Yamada, 1993). Observations from Pyramid indicate that this could be a regional phenomenon, but also raise important questions about the development of valley circulation and the precise mechanism of precipitation. At the Morimoto site, which is the farthest up-valley, the maximum precipitation frequency occurs two hours earlier than in Kyanging. Observations from multiple field trips suggest that cloud formation and condensation occur at the head of the valley first. Sustained valley circulation then drives uplift, and precipitation starts at the head of the valley before progressing to down-valley locations. Future research with high-resolution dynamical downscaling and an expanded network of precipitation stations will be able to test this hypothesis.

Fourth, the derived gradients of T, e_a and P, though computed from only two stations, shed light on the energy and mass balance of glaciers in the region. The sensible latent heat flux, for example, is expected to be positive over much of the glacierized area in the Langtang catchment as the 0 °C isotherm hovers near 6000 m asl during the monsoon. At the same time, low vapour pressure gradients during the monsoon signal that evaporation/sublimation could be an important component of the surface energy balance, as most glacierized areas will experience near-surface vapour pressures below 6.11 hPa throughout the year. Temperature gradients can also be used to identify the phase of precipitation (Higuchi, 1977) at different elevations and the resulting mass gain. Assessing the elevation of the precipitation phase change is crucial for glacier volume change studies because it has a direct impact on albedo, a key variable that controls the surface energy balance and in turn the glacier melt. The increase in precipitation between Kyanging and Yala stations observed during the monsoon is approximately 0.19 mm m^{-1}, but this increase should not be expected to be linear over the elevation range of the catchment. Future monitoring plans in the region should strongly consider the establishment of at least two, and preferably three or more, full meteorological stations at a range of elevations so that vertical gradients can be established and hourly variability in vertical gradients assessed.

Fifth, the monsoon signal is clearly visible in nearly all of the data-sets examined here, though muted in the leeward Rikha Samba site. The monsoon exerts a strong impact on mean daily temperatures and vapour pressures, on incoming short-wave and long-wave radiation, on precipitation frequency, and even on wind speeds and directions. Local topography plays a key role in the regulation of these meteorological quantities, but the synoptic setting can be clearly established by examining multiple data-sets simultaneously. In our data-sets, we observe an asymmetric shape in the onset and finish of the monsoon (Figures 2 to 4). Indeed, during the second half of the pre-monsoon, we observe a progressive build-up of the monsoon with a regular increase in precipitation frequency, temperature, vapour pressure and downwelling long-wave radiation and a simultaneous decrease in atmospheric transmissivity, mainly due to progressively increased cloudiness blocking incoming solar radiation. Conversely, the end of the monsoon is sharp. The transition between the monsoon and post-monsoon seasons, passing from cloudy, rainy and warm to clear, dry and cold, takes no more than a few days. Consequently, changes in future monsoon onset, duration and intensity (Turner &

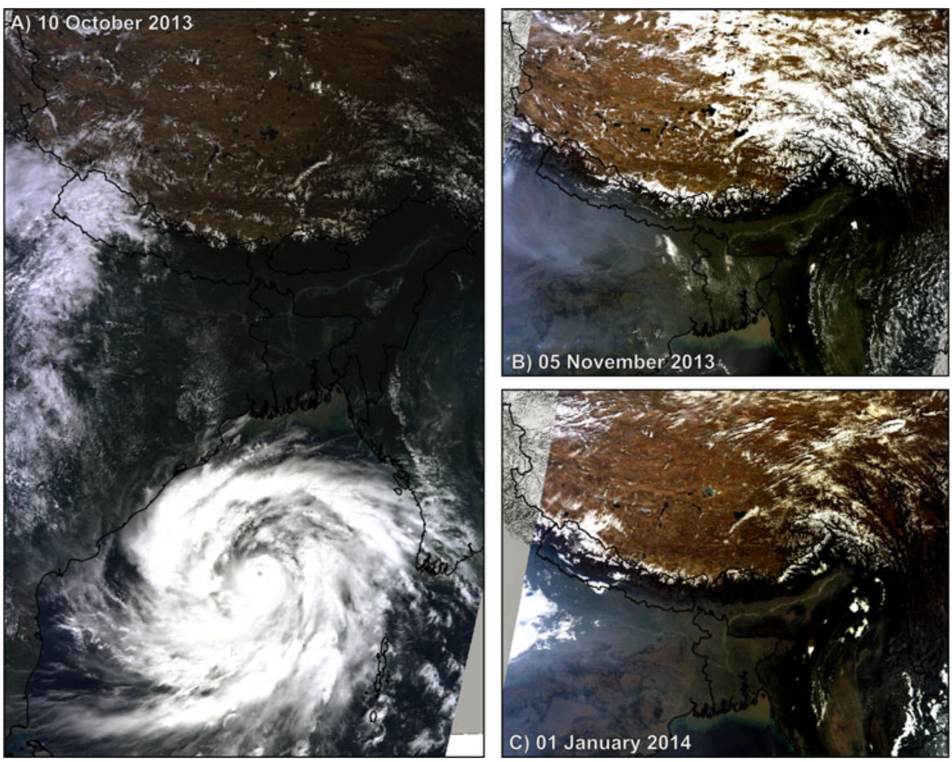

Figure 14. MODIS-TERRA RGB composites showing (a) the approach of Typhoon Phailin in the Indian Ocean, 10 October 2013; (b) extensive snow cover in middle and eastern Nepal and the Tibetan Plateau, 6 November 2013; and (c) remaining high-altitude snow cover, 1 January 2014.

Annamalai, 2012) will have significant impacts on glacier melt and accumulation processes (Diodato, Bellocchi, & Tartari, 2012).

Finally, the strong impact of the Typhoon Phailin remnants on all meteorological quantities highlights another possible area of future research. Changes in the frequency and intensity of such post-tropical storm systems may affect annual accumulation totals and glacier melt and mass balance on a regional scale. Indeed, following this rather short event (only 3 days), all the high-elevation areas of central and eastern Nepal, above approximately 4500 m asl, were covered by snow (Figure 14). In some regions this snow cover was of sufficient thickness to last until the following pre-monsoon, although the winter months are typically dry and snow cover disappears at lower elevations. Consequently, besides the direct effect on accumulation, this 3-day event affected ablation the following season. With a highly reflective snow cover on glaciers and moraine areas, melt onset was probably delayed during the following pre-monsoon period.

In conclusion, this study provides analyses of key meteorological information in a high-altitude region where data availability is severely limited. Rivers in the eastern and central Himalaya are dominated by monsoon precipitation signals (Immerzeel et al., 2013; Lutz et al., 2014), yet little is known about radiation budgets, vertical temperature and vapour pressure gradients, or precipitation mechanisms and spatial variability at high altitude. High-altitude meteorological studies are typically of limited duration, and the insights and raw data gained from our analyses can be applied to test downscaling methods and constrain key parameters in hydrological and glacier melt models. Long-term operation of these stations and their corresponding glaciological measurements will facilitate research into glacier-climate relations and long-term trends that impact regional water availability (Barry, 2012). Indeed, a regional network of high-altitude meteorological stations coupled with glacier mass balance measurements would provide critical information for future water resource assessments in the water towers of Asia.

Acknowledgements

Many thanks to an anonymous reviewer and the editor for constructive comments that have improved the original manuscript. Special thanks to Simon Wicki, Martin Heynen, Evan Miles and Eduardo Soteras for their efforts in the installation and maintenance of the Morimoto Pluvio; to Bikas Bhattarai, Sharad Joshi, Rijan Kayastha, Niraj Pradhananga and Dorothea Stumm for the installation and maintenance of the Kyanging, Yala and Rikha Samba stations; and to Yves Arnaud, Martin Ménégoz, Christian Vincent and all Pyramid staff for the installation and maintenance of Changri Nup and Pyramid Geonor stations. Yves Lejeune provided the filtered Geonor data, which is greatly appreciated. Data from the Pyramid station was made accessible through the EV-K2-CNR Project in collaboration with the Nepal Academy of Science and Technology as foreseen by a memorandum of understanding between Nepal and Italy, and thanks to contributions from the Italian National Research Council, the Italian Ministry of Education, University and Research, and the Italian Ministry of Foreign Affairs. The views and interpretations in this publication are those of the authors and are not necessarily attributable to ICIMOD.

Funding

This study was partially funded by the Netherlands Organization for Scientific Research through their VENI program and by the Research for Development (R4D) program of DFID, as well as core funds of ICIMOD (contributed by the governments of Afghanistan, Australia, Austria, Bangladesh, Bhutan, China, India, Myanmar, Nepal, Norway, Pakistan, Switzerland and the United Kingdom). The Changri Nup and Pyramid Geonor stations have been funded by the French Service d'Observation GLACIOCLIM, the French National Research Agency (ANR) through ANR-PAPRIKA, ANR-PRESHINE, and by a grant from LabexOSUG@2020 (Investissements d'avenir – ANR10 LABX56).

Supplementary information

As part of the ICIMOD publication policy, datasets used in this study will be made freely available at http://rds.icimod.org.

Disclosure statement

No potential conflict of interest was reported by the authors.

References

Ageta, Y., Ohata, T., Tanaka, Y., Ikegami, K., & Higuchi, K. (1980). Mass balance of glacier AX010 in Shorong Himal, East Nepal during the Summer Monsoon season: Glaciological expedition of Nepal, contribution no. 66. *Seppyo*, *41*, 34–41.

Azam, M. F., Wagnon, P., Vincent, C., Ramanathan, A., Linda, A., & Singh, V. B. (2014a). Reconstruction of the annual mass balance of Chhota Shigri Glacier, Western Himalaya, India, since 1969. *Annals of Glaciology*, *55*, 69–80. doi:10.3189/2014AoG66A104

Azam, M. F., Wagnon, P., Vincent, C., Ramanathan, A. L., Favier, V., Mandal, A., & Pottakkal, J. G. (2014b). Processes governing the mass balance of Chhota Shigri Glacier (Western Himalaya, India) assessed by point-scale surface energy balance measurements. *The Cryosphere Discussions*, *8*, 2195–2217. doi:10.5194/tcd-8-2867-2014

Bajracharya, S. R., Maharjan, S. B., Shrestha, F., Bajracharya, O. R., & Baidya, S. (2014). *Glacier status in Nepal and decadal change from 1980 to 2010 based on Landsat data*. Kathmandu: ICIMOD. Retrieved from: http://lib.icimod.org/record/29591/files/GSN-RR14-2.pdf

Barry, R. G. (2012). Recent advances in mountain climate research. *Theoretical and Applied Climatology*, *110*, 549–553. doi:10.1007/s00704-012-0695-x

Bolch, T., Kulkarni, A., Kääb, A., Huggel, C., Paul, F., Cogley, J. G., & … Stoffel, M. (2012). The state and fate of Himalayan glaciers. *Science*, *336*, 310–314. doi:10.1126/science.1215828

Bollasina, M., Bertolani, L., & Tartari, G. (2002). Meteorological observations at high altitude in the Khumbu Valley, Nepal, 1994–1999. *Bulletin of Glaciological Research*, *19*, 1–11.

Bolton, D. (1980). The computation of equivalent potential temperature. *Monthly Weather Review*, *108*, 1046–1053.

Bonasoni, P., Laj, P., Marinoni, A., Sprenger, M., Angelini, F. Arduini, J., … & Cristofanelli, P. (2010). Atmospheric brown clouds in the Himalayas: first two years of continuous observations at the Nepal Climate Observatory-Pyramid (5079 m). *Atmospheric Chemistry and Physics*, *10*, 7515–7531. doi:10.5194/acp-10-7515-2010

Bookhagen, B., & Burbank, D. W. (2006). Topography, relief, and TRMM-derived rainfall variations along the Himalaya. *Geophysical Research Letters*, *33*, L08405, doi:10.1029/2006GL026037

Diodato, N., Bellocchi, G., & Tartari, G. (2012). How do Himalayan areas respond to global warming? *International Journal of Climatology*, *32*, 975–982. doi:10.1002/joc.2340

Favier, V., Wagnon, P., & Ribstein, P. (2004). Glaciers of the outer and inner tropics: A different behaviour but a common response to climatic forcing. *Geophysical Research Letters*, *31*, L16403, doi:10.1029/2004GL020654

Førland, E. J., Allerup, P., Dahlström, B., Elomaa, E., Jónsson, T., Madsen, H., & … Vejen, F. (1996). Manual for operational correction of Nordic precipitation data. Report Nr. 24/96, DNMI, P.O. Box 43, Blindern, Oslo, Norway, pp. 66.

Fujita, K., Sakai, A., Air temperature environment on the debris covered area of Lirung Glacier, Langtang Valley, Nepal. Debris-Covered Glaciers (Proceedings of a workshop held at Seattle, Washington, USA, September 2000). IAHS Publ. no. 264 (pp. 83–88).

Fujita, K., Sakai, A., & Chhetri, T. B. (1997). Meterological observation in Langtang Valley, Nepal, 1996. *Bulletin of Glacier Research*, *15*, 71–78.

Gardelle, J., Berthier, E., Arnaud, Y., & Kääb, A. (2013). Region-wide glacier mass balances over the Pamir-Karakoram-Himalaya during 1999–2011. *The Cryosphere*, *7*, 1263–1286. doi:10.5194/tc-7-1263-2013

Gardner, A. S., Moholdt, G., Cogley, J. G., Wouters, B., Arendt, A. A., Wahr, J., & … Paul, F. (2013). A reconciled estimate of glacier contributions to sea level rise: 2003 to 2009. *Science*, *340*, 852–857. doi:10.1126/science.1234532

Hardy, D. R., Vuille, M. R., Braun, C. R., Keimig, F. R., & Bradley, R. S. (1998). Annual and daily meteorological cycles at high altitude on a tropical mountain. *Bulletin of the American Meteorological Society*, *79*, 1899–1913. doi:10.1175/1520-0477(1998)079<1899:AADMCA>2.0.CO;2

Hewitt, K. (2005). The Karakoram anomaly? Glacier expansion and the "elevation effect", Karakoram Himalaya. *Mountain Research and Development*, *25*, 332–340. doi:10.1659/0276-4741(2005)025[0332:TKAGEA]2.0.CO;2

Higuchi, K. (1977). Effect of nocturnal precipitation on the mass balance of the Rikha Samba Glacier, Hidden Valley, Nepal: Glaciological Expedition of Nepal, Contribution No. 38. *Seppyo*, *39*, 43–49.

Higuchi, K., Ageta, Y., Yasunari, T., & Inoue, J. (1982). Characteristics of precipitation during the monsoon season in high-mountain areas of the Nepal Himalaya. In: Hydrological Aspects of Alpine and High-Mountain Areas, IAHS Publication No. 138 (pp. 21–30).

Hock, R. (2005). Glacier melt: A review of processes and their modelling. *Progress in Physical Geography*, *29*, 362–391. doi:10.1191/0309133305pp453ra

Immerzeel, W. W., Pellicciotti, F., & Bierkens, M. F. P. (2013). Rising river flows throughout the twenty-first century in two Himalayan glacierized watersheds. *Nature Geoscience*, *6*, 742–745. doi:10.1038/ngeo1896

Immerzeel, W. W., Petersen, L., Ragettli, S., & Pellicciotti, F. (2014). The importance of observed gradients of air temperature and precipitation for modeling runoff from a glacierized watershed in the Nepalese Himalayas. *Water Resources Research*, *50*, 2212–2226. doi:10.1002/2013WR014506

Immerzeel, W. W., van Beek, L. P. H., & Bierkens, M. F. P. (2010). Climate change will affect the Asian water towers. *Science*, *328*, 1382–1385. doi:10.1126/science.1183188

Jiménez, P. A., González-Rouco, J. F., García-Bustamante, E., Navarro, J., Montávez, J. P., de Arellano, J. V. G., & Muñoz-Roldan, A. (2010). Surface wind regionalization over complex terrain: Evaluation and analysis of a high-resolution WRF simulation. *Journal of Applied Meteorology and Climatology*, *49*, 268–287. doi:10.1007/s00382-012-1326-z

Kaser, G., Grosshauser, M., & Marzeion, B. (2010). Contribution potential of glaciers to water availability in different climate regimes. *Proceedings of the National Academy of Sciences*, *107*, 20223–20227. doi:10.1073/pnas.1008162107

Kääb, A., Berthier, E., Nuth, C., Gardelle, J., & Arnaud, Y. (2012). Contrasting patterns of early twenty-first-century glacier mass change in the Himalayas. *Nature*, *488*, 495–498. doi:10.1038/nature11324

Lutz, A. F., Immerzeel, W. W., Shrestha, A. B., & Bierkens, M. F. P. (2014). Consistent increase in high Asia's runoff due to increasing glacier melt and precipitation. *Nature Climate Change*, *4*, 587–592. doi:10.1038/nclimate22372014

Marks, D., Winstral, A., Reba, M., Pomeroy, J., & Kumar, M. (2013). An evaluation of methods for determining during-storm precipitation phase and the rain/snow transition elevation at the surface in a mountain basin. *Advances in Water Resources*, *55*, 98–110. doi:10.1016/j.advwatres.2012.11.012

Marzeion, B., Jarosch, A. H., & Hofer, M. (2012). Past and future sealevel change from the surface mass balance of glaciers. *The Cryosphere*, *6*, 1295–1322. doi:10.5194/tc-6-1295-2012

Maussion, F., Scherer, D., Mölg, T., Collier, E., Curio, J., & Finkelnburg, R. (2014). Precipitation seasonality and variability over the Tibetan plateau as resolved by the High Asia Reanalysis. *Journal of Climate*, *27*, 1910–27. doi:10.1175/JCLI-D-13-00282.1.

Michelson, D. B. (2004). Systematic correction of precipitation gauge observations using analyzed meteorological variables. *Journal of Hydrology*, *290*, 161–177. doi:10.1016/j.jhydrol.2003.10.005

Mihalcea, C., Mayer, C., Diolaiuti, G., Lambrecht, A., Smiraglia, C., & Tartari, G. (2006). Ice ablation and meteorological conditions on the debris-covered area of Baltoro glacier, Karakoram, Pakistan. *Annals of Glaciology*, *43*, 292–300. doi:10.3189/172756406781812104

Moore, G. W. K., & Semple, J. L. (2004). High Himalayan meteorology: Weather at the South Col of Mount Everest. *Geophysical Research Letters*, *31*, L18109, doi:10.1029/2004GL020621

Mölg, T., Maussion, F., Yang, W., & Scherer, D. (2012). The footprint of Asian monsoon dynamics in the mass and energy balance of a Tibetan glacier. *The Cryosphere*, *6*, 1445–1461. doi:10.5194/tc-6-1445-2012

Nicholson, L. I., Prinz, R., Mölg, T., & Kaser, G. (2013). Micrometeorological conditions and surface mass and energy fluxes on Lewis Glacier, Mt Kenya, in relation to other tropical glaciers. *The Cryosphere*, *7*, 1205–1225. doi:10.5194/tc-7-1205-2013

Oerlemans, J. (2000). Analysis of a 3 year meteorological record from the ablation zone of Morteratschgletscher, Switzerland: Energy and mass balance. *Journal of Glaciology*, *46*(571–579).

Oerlemans, J. (2001). Glaciers and climate change. Lisse: A.A. Balkema.

Pellicciotti, F., Helbing, J., Rivera, A., Favier, V., Corripio, J., Araos, J., & … Carenzo, M. (2008). A study of the energy balance and melt regime on Juncal Norte Glacier, semi-arid Andes of central Chile, using melt models of different complexity. *Hydrological Processes*, *22*, 3980–3997. doi:10.1002/hyp.7085

Petersen, L., & Pellicciotti, F. (2011). Spatial and temporal variability of air temperature on a melting glacier: atmospheric controls, extrapolation methods and their effect on melt modeling, Juncal Norte Glacier, Chile. *Journal of Geophysical Research: Atmospheres (1984–2012)*, *116*, doi:10.1029/2011JD015842

Racoviteanu, A. E., Armstrong, R., & Williams, M. W. (2013). Evaluation of an ice ablation model to estimate the contribution of melting glacier ice to annual discharge in the Nepal Himalaya. *Water Resources Research*, *49*, 5117–5133. doi:10.1002/wrcr.20370

Radić, V., & Hock, R. (2011). Regionally differentiated contribution of mountain glaciers and ice caps to future sea-level rise. *Nature Geoscience*, *4*, 91–94. doi:10.1038/NGEO1052

Ragettli, S., & Pellicciotti, F. (2012). Calibration of a physically based, spatially distributed hydrological model in a glacierized basin: On the use of knowledge from glaciometeorological processes to constrain model parameters. *Water Resources Research*, *48*(3), doi:10.1029/2011WR01055

Ragettli, S., Pellicciotti, F., Bordoy, R., & Immerzeel, W. W. (2013). Sources of uncertainty in modeling the glaciohydrological response of a Karakoram watershed to climate change. *Water Resources Research*, *49*, 6048–6066. doi:10.1002/wrcr.20450

Rangwala, I., & Miller, J. R. (2012). Climate change in mountains: A review of elevation-dependent warming and its possible causes. *Climatic Change*, *114*, 527–547. doi:10.1007/s10584-012-0419-3

Rasmussen, R., Baker, B., Kochendorfer, J., Meyers, T., Landolt, S., Fischer, A. P., & … Gutmann, E. (2012). How well are we measuring snow: The NOAA/FAA/NCAR winter precipitation test bed. *Bulletin of the American Meteorological Society*, *93*, 811–829. doi:10.1175/BAMS-D-11-00052.1

Scherler, D., Bookhagen, B., & Strecker, M. R. (2011). Spatially variable response of Himalayan glaciers to climate change affected by debris cover. *Nature Geoscience*, *4*, 156–159. doi:10.1038/ngeo1068

Shea, J. M., & Moore, R. D. (2010). Prediction of spatially distributed regional-scale fields of air temperature and vapor pressure over mountain glaciers. *Journal of Geophysical Research: Atmospheres*, *115*(D23), doi:10.1029/2010JD014351

Shrestha, A. B., & Aryal, R. (2011). Climate change in Nepal and its impact on Himalayan glaciers. *Regional Environmental Change*, *11*, 65–77. doi:10.1007/s10113-010-0174-9

Takahashi, S., Motoyama, H., Kawashima, K., Morinaga, Y., Seko, K., Iida, H., & Turadahr, N. R. (1987). Meteorological features in Langtang Valley, Nepal, 1985–1986. *Bulletin of Glacier Research*, *5*, 35–40.

Takeuchi, Y. (2000). Practical prediction of ice melting beneath various thickness of debris cover on Kliumbu Glacier, Nepal, using a positive degree-day factor. In: Debris-covered Glaciers (Proceedings of an International Workshop Held at the University of Washington in Seattle, Washington, USA, 13-15 September 2000) IAHS Publ. No. 264 (pp. 53–61).

Turner, A. G., & Annamalai, H. (2012). Climate change and the South Asian summer monsoon. *Nature Climate Change*, *2*, 587–595. doi:10.1038/NCLIMATE1495

Ueno, K., Shiraiwa, T., & Yamada, T. (1993). Precipitation Environment in the LangtangValley, Nepal. In: Snow and Glacier Hydrology (Proceedings of the Kathmandu Symposium, November 1992). IAHS Publ. No. 218 (pp. 207–219).

Viviroli, D., Dürr, H. H., Messerli, B., Meybeck, M., & Weingartner, R. (2007). Mountains of the world, water towers for humanity: Typology, mapping, and global significance. *Water Resources Research*, *43*, W07447–n/a. doi:10.1029/2006WR005653

Wagnon, P., Lafaysse, M., Lejeune, Y., Maisincho, L., Rojas, M., & Chazarin, J. P. (2009). Understanding and modeling the physical processes that govern the melting of snow cover in a tropical mountain environment in Ecuador. *Journal of Geophysical Research: Atmospheres* (1984–2012), *114*(D19), doi:10.1029/2009JD012292

Wagnon, P., Ribstein, P., Francou, B., & Pouyaud, B. (1999). Annual cycle of energy balance of Zongo glacier, Cordillera Real, Bolivia. *Journal of Geophysical Research: Atmospheres* (1984–2012), *104*, 3907–3923.

Wagnon, P., Vincent, C., Arnaud, Y., Berthier, E., Vuillermoz, E., Gruber, S., & … Pokhrel, B. K. (2013). Seasonal and annual mass balances of Mera and Pokalde glaciers (Nepal Himalaya) since 2007. *The Cryosphere*, *7*, 1769–1786. doi:10.5194/tc-7-1769-2013

Whiteman, C. D. (2000). *Mountain meteorology: fundamentals and applications*. Oxford: Oxford University Press.

Yang, D., Goodison, B. E., Ishida, S., & Benson, C. S. (1998). Adjustment of daily precipitation data at 10 climate stations in Alaska: Application of World Meteorological Organization intercomparison results. *Water Resources Research*, *34*, 241–256. doi:10.1029/97WR02681

Yang, K., He, J., Tang, W., Qin, J., & Cheng, C. C. (2010). On downward shortwave and longwave radiations over high altitude regions: Observation and modeling in the Tibetan Plateau. *Agricultural and Forest Meteorology*, *150*, 38–46. doi:10.1016/j.agrformet.2009.08.004

Zhang, G., Kang, S., Fujita, K., Huintjes, E., Xu, J., Yamazaki, T., & … Yao, T. (2013). Energy and mass balance of Zhadang Glacier surface, central Tibetan Plateau. *Journal of Glaciology*, *59*, 137–148. doi:10.3189/2013JoG12J152

The Cryosphere, 9, 1105–1128, 2015
www.the-cryosphere.net/9/1105/2015/
doi:10.5194/tc-9-1105-2015

The Cryosphere
Open Access

Modelling glacier change in the Everest region, Nepal Himalaya

J. M. Shea[1], W. W. Immerzeel[1,2], P. Wagnon[1,3], C. Vincent[4], and S. Bajracharya[1]

[1]International Centre for Integrated Mountain Development, Kathmandu, Nepal
[2]Department of Physical Geography, Utrecht University, Utrecht, the Netherlands
[3]IRD/UJF – Grenoble 1/CNRS/G-INP, LTHE UMR 5564, LGGE UMR 5183, Grenoble, 38402, France
[4]UJF – Grenoble 1/CNRS, Laboratoire de Glaciologie et Géophysique de l'Environnement (LGGE) UMR 5183, Grenoble, 38041, France

Correspondence to: J. M. Shea (joseph.shea@icimod.org)

Received: 1 September 2014 – Published in The Cryosphere Discuss.: 17 October 2014
Revised: 7 April 2015 – Accepted: 8 April 2015 – Published: 27 May 2015

Abstract. In this study, we apply a glacier mass balance and ice redistribution model to examine the sensitivity of glaciers in the Everest region of Nepal to climate change. High-resolution temperature and precipitation fields derived from gridded station data, and bias-corrected with independent station observations, are used to drive the historical model from 1961 to 2007. The model is calibrated against geodetically derived estimates of net glacier mass change from 1992 to 2008, termini position of four large glaciers at the end of the calibration period, average velocities observed on selected debris-covered glaciers, and total glacierized area. We integrate field-based observations of glacier mass balance and ice thickness with remotely sensed observations of decadal glacier change to validate the model. Between 1961 and 2007, the mean modelled volume change over the Dudh Koshi basin is $-6.4 \pm 1.5\,\mathrm{km}^3$, a decrease of 15.6 % from the original estimated ice volume in 1961. Modelled glacier area change between 1961 and 2007 is $-101.0 \pm 11.4\,\mathrm{km}^2$, a decrease of approximately 20 % from the initial extent. The modelled glacier sensitivity to future climate change is high. Application of temperature and precipitation anomalies from warm/dry and wet/cold end-members of the CMIP5 RCP4.5 and RCP8.5 ensemble results in sustained mass loss from glaciers in the Everest region through the 21st century.

1 Introduction

High-elevation snow and ice cover play pivotal roles in Himalayan hydrologic systems (e.g. Viviroli et al., 2007; Immerzeel et al., 2010; Racoviteanu et al., 2013). In the monsoon-affected portions of the Himalayas, meltwater from seasonal snowpacks and glaciers provides an important source of streamflow during pre- and post-monsoon seasons, while rainfall-induced runoff during the monsoon dominates the overall hydrologic cycle (Immerzeel et al., 2013). Against this backdrop, changes in glacier area and volume are expected to have large impacts on the availability of water during the dry seasons (Immerzeel et al., 2010), which will impact agriculture, hydropower generation, and local water resources availability. In the current study, our main objectives are to calibrate and test a model of glacier mass balance and redistribution, and to present scenarios of catchment-scale future glacier evolution in the Everest region.

1.1 Study area and climate

The ICIMOD (2011) inventory indicates that the Dudh Koshi basin in central Nepal contains a total glacierized area of approximately $410\,\mathrm{km}^2$ (Fig. 1). The region contains some of the world's highest mountain peaks, including Sagarmatha (Mount Everest), Cho Oyu, Makalu, Lhotse, and Nuptse. The Dudh Koshi River is a major contributor to the Koshi River, which contains nearly one-quarter of Nepal's exploitable hydroelectric potential. Approximately $110\,\mathrm{km}^2$, or 25 % of the total glacierized area, is classified as debris-covered (Fig. 2), with surface melt rates that are typically lower than those observed on clean glaciers due to the insulating effect of the debris (Reid and Brock, 2010; Lejeune et al., 2013).

The climate of the region is characterized by pronounced seasonality of both temperature and precipitation. At 5000 m (see analysis below), mean daily temperatures range between -7 and $+10\,^{\circ}\mathrm{C}$, with minimum and maximum daily temper-

Published by Copernicus Publications on behalf of the European Geosciences Union.

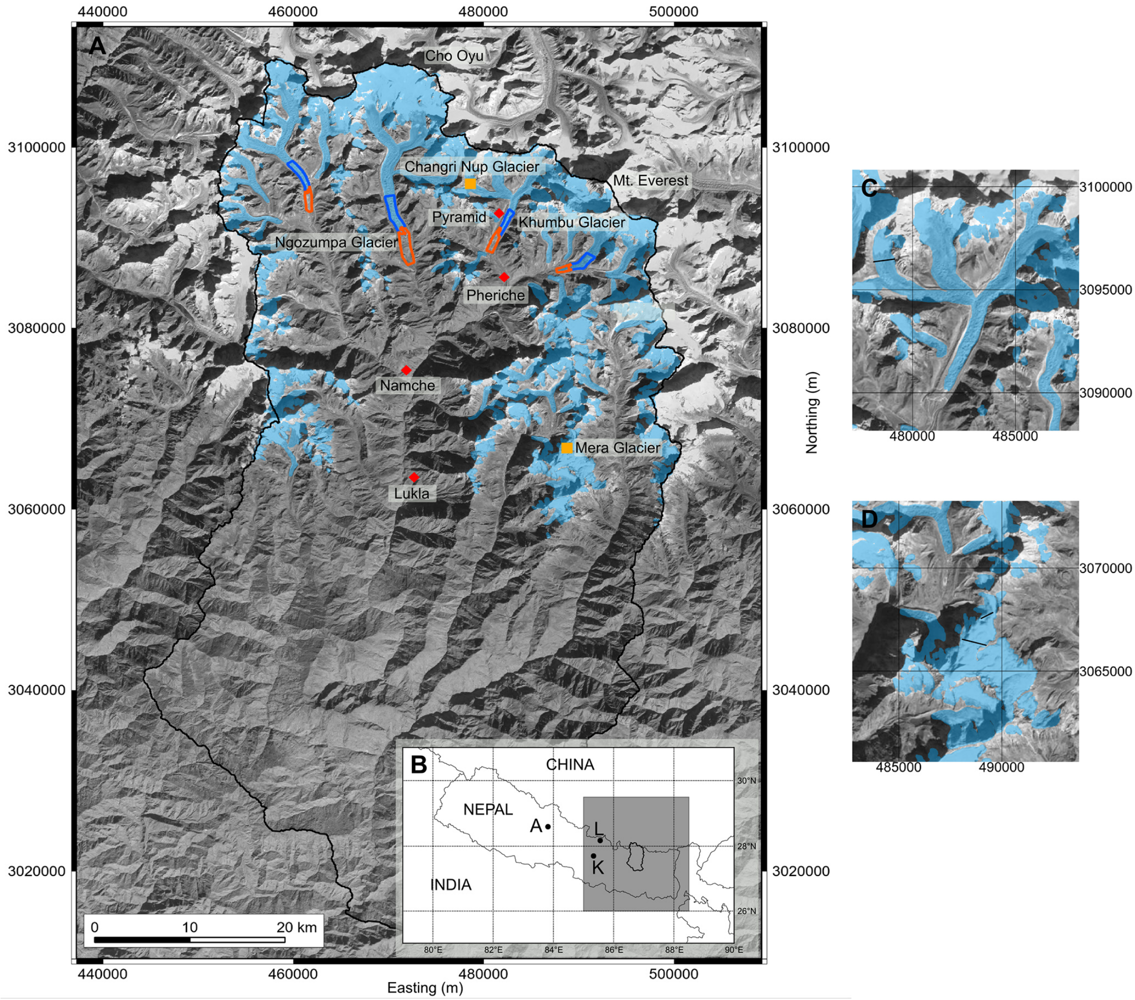

Figure 1. (a) Dudh Koshi basin, eastern Nepal, with current glacier extents in blue (ICIMOD, 2011), EVK2CNR stations (red), GPR profile sites (yellow). Extents of glacierized (blue) and non-glacierized (orange) regions used for model calibration are also shown. Coordinate system is UTM 45N. Inset map **(b)** shows the Dudh Koshi basin in relation to the APHRODITE subset (shaded), and the locations of places named in the text (A – Annapurna, L – Langtang, K – Kathmandu). Panels **(c)** and **(d)** give the location of the transverse GPR surveys (thick red lines) at Changri Nup and Mera glaciers, respectively.

atures ranging between -25 and $+10\,°C$. During the monsoon period (June–September), temperatures at 5000 m are greater than $0\,°C$ and variability is low. The majority of annual precipitation (approximately 77 %, derived from gridded climate fields, see below) falls between 1 June and 30 September during the summer monsoon (Wagnon et al., 2013). An additional 14 % of precipitation occurs during the pre-monsoon period (March–May), with little or no precipitation during the post-monsoon and winter seasons. The interaction between moisture advected from the Indian Ocean during the monsoon and the two-step topography of the Dudh Koshi region (foothills, main ranges) results in two spatial maxima of precipitation (Bookhagen and Burbank, 2006).

1.2 Himalayan glaciology

The current status of glaciers varies across the Hindu Kush Himalayan (HKH) region. Most areas have seen pronounced glacier retreat and downwasting in recent years (Bolch et al., 2012; Kääb et al., 2012; Yao et al., 2012), though some areas, such as the Karakoram and Pamir ranges, have experienced equilibrium or even slight mass gain (Gardelle et al., 2012, 2013; Jacob et al., 2012). In the Everest region (Fig. 1), Gardelle et al. (2013) find an average annual rate of mass loss of -0.26 ± 0.13 m w.e. yr^{-1} between 2000 and 2011, while Nuimura et al. (2012) estimate mass loss rates of -0.40 ± 0.25 m w.e. yr^{-1} between 1992 and 2008. Between 2003 and 2009, thinning rates of -0.40 m yr^{-1} were estimated from ICEsat data (Gardner et al., 2013), which is similar to the 1962–2002 average thinning rate of -0.33 m yr^{-1}

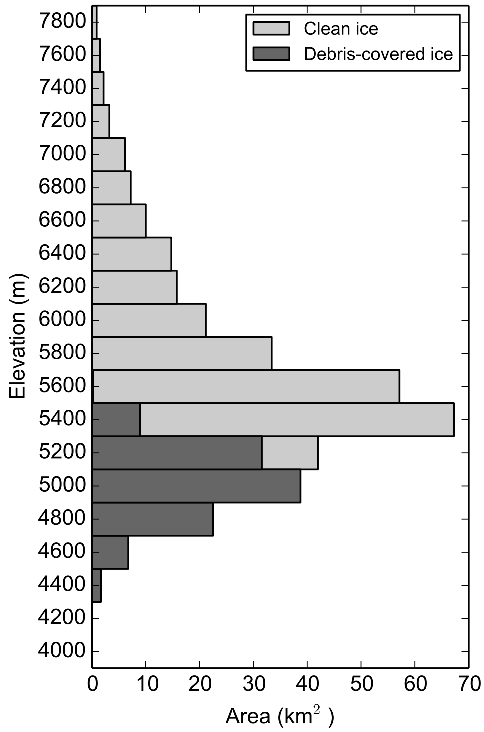

Figure 2. Area of clean and debris-covered glaciers by elevation, Dudh Koshi basin, Nepal. Extracted from SRTM 90 m DEM and glacier inventory from ICIMOD (2011)

calculated for glaciers in the Khumbu region (Bolch et al., 2008a, b). Areal extents of glaciers in Sagarmatha National Park decreased 5 % during the second half of the 20th century (Bolch et al., 2008b; Salerno et al., 2008; Thakuri et al., 2014). These estimates do not distinguish between debris-covered and clean-ice glaciers.

One consequence of glacier retreat in the Himalayas is the formation of proglacial lakes, which may pose a risk to downstream communities. Terminus retreat at Lumding and Imja glaciers, measured at -42 and $-34\,\mathrm{m\,yr^{-1}}$, respectively, between 1976 and 2000 increased to $-74\,\mathrm{m\,yr^{-1}}$ at both glaciers between 2000 and 2007 (Bajracharya and Mool, 2010). Rapid terminus retreat results in the growth of proglacial lakes which are dammed by lateral and terminal moraines (Bolch et al., 2008b; Benn et al., 2012; Thompson et al., 2012). The failure of moraine dams in the Koshi River basin has led to 15 recorded glacier lake outburst flood (GLOF) events since 1965, with flows up to 100 times greater than average annual flow (Chen et al., 2013), and the frequency of GLOFs in the Himalayas is believed to have increased since the 1940s (Richardson and Reynolds, 2000). Changes in glacier extents and volumes in response to climate change thus have important impacts not only on water resources availability but also on geophysical hazards.

The climate sensitivity of a glacier depends primarily on its mass balance amplitude. Glaciers in wetter climates typically extend to lower elevations, and are thus more sensitive to temperature changes than those in dry climates (Oerlemans and Fortuin, 1992). Himalayan glaciers, and glaciers of the Dudh Koshi in particular, present a unique challenge as observations of temperature and precipitation at high elevations are scarce. Regionally, the climate varies from monsoon-dominated southern slopes to relatively dry leeward high-elevation regions. Accordingly, equilibrium line altitudes (ELAs) in the region vary both spatially and temporally but generally range from 5200 m in the south to 5800 m in northern portions of the basin (Williams, 1983; Asahi, 2010; Wagnon et al., 2013). Nearly 80 % of the glacierized area in the Dudh Koshi basin lies between 5000 and 6000 m (Fig. 2), and the region is expected to be sensitive to climatic changes.

Table 1. EVK2CNR meteorological stations used to validate downscaled APHRODITE temperature and precipitation fields.

Site	Latitude (°)	Longitude (°)	Elevation (m)
Lukla	27.69556	86.72306	2660
Namche	27.80239	86.71456	3570
Pheriche	27.89536	86.81875	4260
Pyramid	27.95903	86.81322	5035

1.3 Historical and projected climate trends

Analyses of climate trends in the region are limited, primarily due to the lack of long-term records (Shrestha and Aryal, 2011). Available studies indicate that the mean annual temperatures have increased in the region, and particularly at high elevations (Shrestha et al., 1999; Rangwala et al., 2009; Ohmura, 2012; Rangwala and Miller, 2012). Reported mean annual temperature trends range between 0.025 and $0.06\,^{\circ}\mathrm{C\,yr^{-1}}$ for the periods 1971 to 2009 and 1977 to 1994, respectively (Shrestha and Aryal, 2011; Qi et al., 2013). Changes in temperature are particularly important for monsoon-type glaciers, which are sensitive to the elevation of the rain/snow threshold during the monsoon season (Bolch et al., 2012). Results from the CMIP5 (Climate Modelling Intercomparison Project) ensemble suggest that temperatures in the region will increase between 1.3 and 2.4 °C over the period 1961–1990 to 2021–2050 (Lutz et al., 2013), which correspond to rates of 0.021 to $0.040\,^{\circ}\mathrm{C\,yr^{-1}}$.

Precipitation amounts, timing, and phase will affect glacier responses on both annual and decadal timescales. In the greater Himalayas, trends in precipitation totals appear to be mixed and relatively weak (Mirza et al., 1998; Gautam et al., 2010; Dimri and Dash, 2012; Qi et al., 2013), though the observational network is composed mostly of low-elevation valley stations that may not reflect changes in snowfall amounts at higher elevations. General circulation model projections suggest both increased monsoon precipitation (Kripalani et al., 2007) and delayed monsoon onset

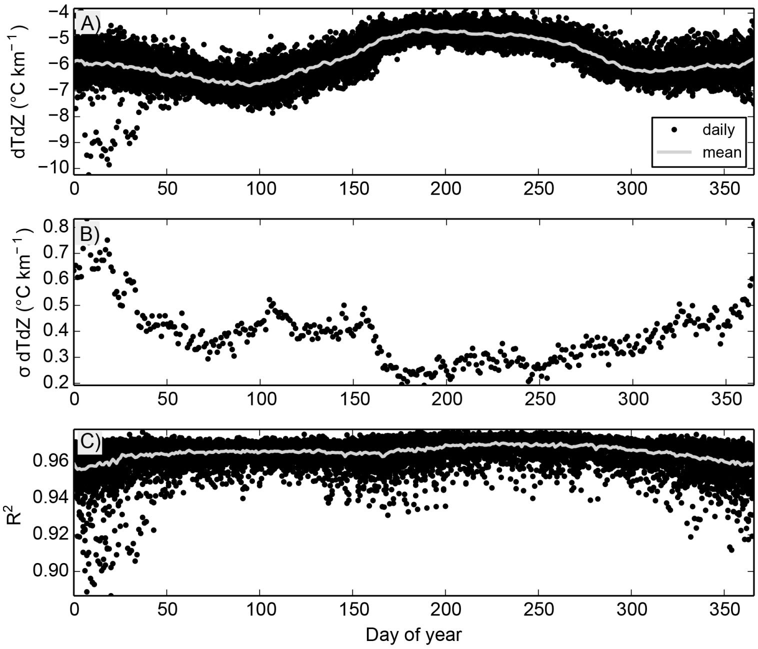

Figure 3. (a) Vertical temperature gradients (γ_T) by day of year (DOY) for all years (black) calculated from APHRODITE (1961–2007) temperature fields and resampled SRTM data, with period mean in grey, **(b)** daily standard deviation (σ) of γ_T, and **(c)** mean daily coefficient of determination (R^2) calculated from the linear regression of resampled SRTM elevations and APRHODITE cell temperatures. All temperature/elevation regressions are significant.

(Ashfaq et al., 2009; Mölg et al., 2012) in the 21st century, while the change in total annual precipitation is mixed. In the Himalayas, the CMIP5 ensemble shows projected changes in precipitation between −8 to +15 % (Lutz et al., 2013; Palazzi et al., 2013).

1.4 Models of glacier change

In spite of the recent observed changes in glaciers in the Everest region, the reported climatic trends, the expected glacier sensitivity to climatic change, and the importance of glacier water resources in the region, few studies have attempted to model the historical or future response of these glaciers to climate change (Immerzeel et al., 2012, 2013). Empirical mass balance and snowmelt and ice melt models have been developed from field observations (Ageta and Higuchi, 1984; Ageta and Kadota, 1992; Nakawo et al., 1999) and reanalysis products (Fujita and Nuimura, 2011; Rasmussen, 2013), and such approaches have been used to quantify glacier contributions to streamflow (Racoviteanu et al., 2013; Nepal et al., 2013). Projections of higher ELAs in the region (Fujita and Nuimura, 2011) and volume area-scaling approaches (Shi and Liu, 2000; Cogley, 2011) indicate continued mass wastage in the future, yet impact studies on the response of glaciers to climate change require models that link mass balance processes with representations of glacier dynamics.

One- and two-dimensional models of glacier dynamics have been applied previously to the Khumbu Glacier (Naito et al., 2000) and the East Rongbuk Glacier (Zhang et al., 2013), respectively. However, these and higher-order models of glacier dynamics are severely limited by input data availability (e.g. bed topography, ice temperatures, basal water pressure) and uncertainties in key model parameters, and have not been applied at catchment scales in the region. Debris-covered glaciers, which compose 25 % of total glacierized area, present additional modelling challenges, and validation is also limited by the availability of data. Relatively coarse methods of simulating future glacier change (e.g. Stahl et al., 2008) can be improved by applying models that can reasonably simulate key glaciological parameters (thickness, velocity, and mass redistribution).

The main objective of this study is to apply a glacier mass balance and redistribution model to the Dudh Koshi River basin, Nepal. To accomplish this, we (1) develop downscaling routines for temperature and precipitation; (2) calibrate and test the model with available field and remotely sensed observations; and (3) explore the modelled sensitivity of glaciers in the Everest region to future climate change with a suite of temperature and precipitation changes from the CMIP5 ensemble.

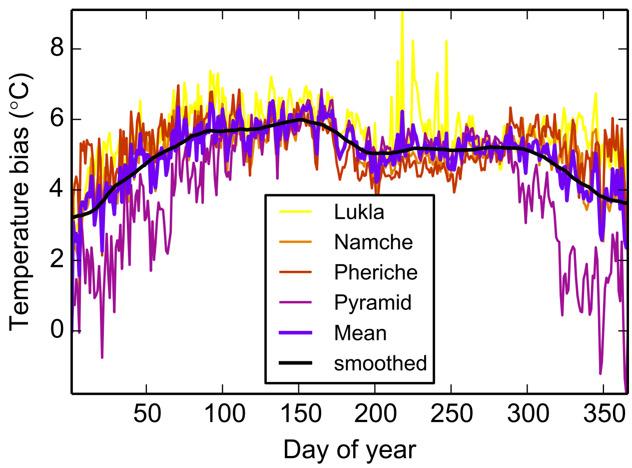

Figure 4. Average daily temperature bias (estimated – observed) for four EVK2CNR sites (2003–2007), their arithmetic mean, and a smoothed function used as a daily bias correction.

2 Data and methods

2.1 Daily climate fields

There are few observations of temperature and precipitation in the basin, and no temperature records longer than 15 years are available. To generate high-resolution fields of temperature (T) and precipitation (P) as inputs to the model, we use data from the APHRODITE (Asian Precipitation – Highly-Resolved Observational Data Integration Towards Evaluation of Water Resources) project (Yatagai et al., 2009, 2012). APHRODITE products have been previously used to test regional climate model simulations in northern India (Mathison et al., 2013) and the western Himalaya (Dimri et al., 2013), and to compare precipitation data sets in the Himalayan region (Palazzi et al., 2013). For this study, we use APHRODITE T fields (V1204R1) that are based on daily station anomalies from climatological means, interpolated on 0.05° grids and then resampled to 0.25° fields, and we refer to Yatagai et al. (2012) for more details. The APHRODITE P fields (V1101) are based on a similar technique using precipitation ratios but incorporate a weighted interpolation scheme based on topographical considerations (Yatagai et al., 2012).

To generate high-resolution fields of T and P for the glacier mass balance model, we extract a 196 (14×14) grid cell subset of the daily APHRODITE T and P fields that covers the Koshi basin (Fig. 1). Approximate elevations for each 0.25° grid cell are extracted from a resampled gap-filled Shuttle Radar Topography Mission (SRTM V4; Farr et al., 2007) digital elevation model (DEM). Based on this subset we derive relations between elevation and temperature and precipitation respectively at coarse resolution. We then use these relations in combination with the 90 m SRTM DEM to produce high-resolution daily climate fields.

2.1.1 Temperature

Downscaled temperature fields at daily 90 m resolution are computed as

$$T_Z = \gamma_T Z + T_0 - C_{\mathrm{DOY}}, \tag{1}$$

where γ_T is the daily vertical temperature gradient (Fig. 3) derived from the 0.25° APRHODITE temperatures and SRTM elevations, T_0 is the daily temperature intercept, and C_{DOY} is a bias correction based on the day of year (Fig. 4). The bias-correction factor is computed from the mean daily temperature difference between observed and estimated mean daily temperatures at four stations operated by the Italian Everest-K2-National Research Centre (EVK2CNR; Fig. 1, Table 1), and it ranges from 3 to 6 °C. The EVK2CNR stations are independent of the APHRODITE product.

2.1.2 Precipitation

To calculate high-resolution daily precipitation fields from the APHRODITE subset, we prescribe daily precipitation–elevation functions from the 0.25° APHRODITE precipitation fields and resampled SRTM data. For each day, we calculate the mean precipitation in 500 m elevation bins ($\overline{P}_{500}$) and prescribe a fitted linear interpolation function to estimate precipitation on the 90 m SRTM DEM (Fig. 5).

As APHRODITE fields are based on interpolated station data (Yatagai et al., 2012), there is a large uncertainty in the precipitation at high elevations. Independent tests of the precipitation downscaling approach were conducted by comparing precipitation observations from the EVK2CNR stations with precipitation estimated using the station elevation and the daily precipitation–elevation functions (Fig. 6). As EVK2CNR stations are not capable of measuring solid precipitation (Wagnon et al., 2013), we only examine days where only liquid precipitation ($T > 0$) is expected.

While orographic forcing of moist air masses typically produces increased precipitation with elevation, in very high-elevation regions (i.e. those greater than 4000 m) both observations and models indicate that precipitation totals will decrease above a certain elevation (Harper and Humphrey, 2003; Mölg et al., 2009). This is due in part to the drying effect from upwind orographic forcing but is also related to the low column-averaged water vapour content indicated by the Clausius–Clapeyron relation. Given that there are no precipitation observations at elevations above 5300 m, and available evidence suggests that precipitation will likely decrease at high elevations, we scale estimated precipitation using a correction factor p_{cor}:

$$P(Z) = \begin{cases} P(Z), & Z < Z_{\mathrm{c}} \\ P(Z)\,p_{\mathrm{cor}}, & Z_{\mathrm{c}} \le Z < Z_{\mathrm{m}} \\ 0, & Z \ge Z_{\mathrm{m}}, \end{cases} \tag{2}$$

where p_{cor} decreases from 1 at the height of a calibrated threshold elevation (Z_{c}; Table 2) to 0 at Z_{m}, set here to 7500 m:

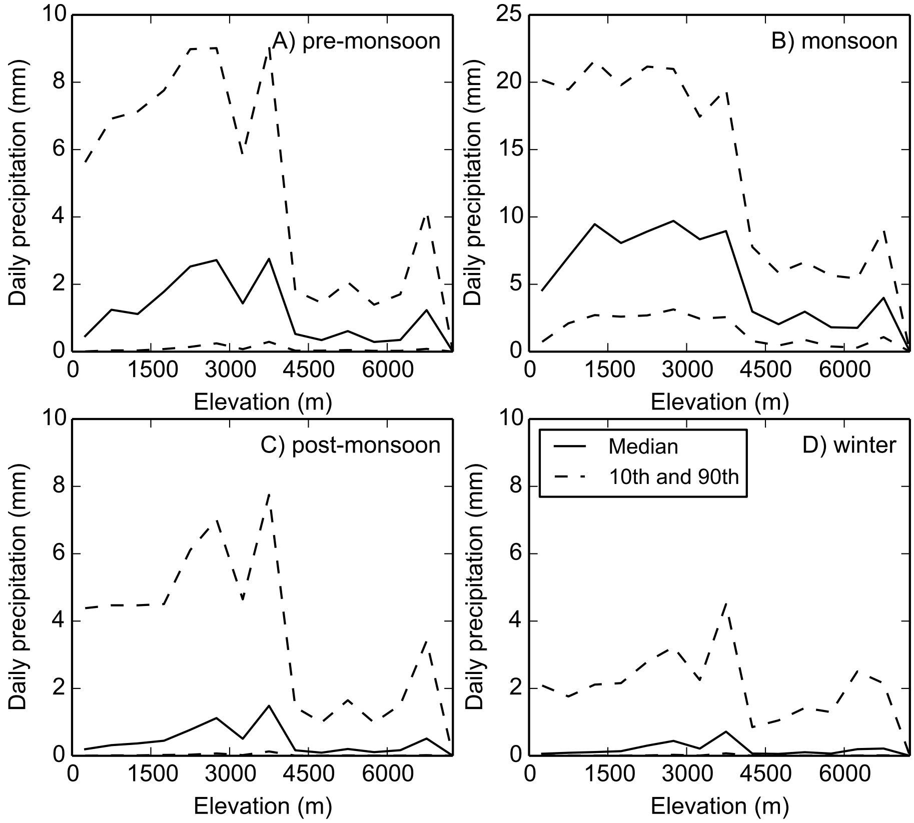

Figure 5. APHRODITE precipitation (1961–2007) binned by elevation for pre-monsoon **(a)**, monsoon **(b)**, post-monsoon **(c)**, and winter **(d)**. Median, 10th percentile, and 90th percentile of daily precipitation are shown. Note different scale for panel **(b)**.

$$p_{\mathrm{cor}} = 1 - (Z - Z_{\mathrm{c}})/(Z_{\mathrm{m}} - Z_{\mathrm{c}}). \tag{3}$$

Above 7500 m, we assume that precipitation amounts minus wind erosion and sublimation (Wagnon et al., 2013) are likely to be negligible. The total area above 7500 m represents only 1.2 % of the total basin area.

2.2 Glacier mass balance and redistribution

Following the methods of Immerzeel et al. (2012) and Immerzeel et al. (2013), daily accumulation and ablation between 1961 and 2007 are estimated from the gridded T and P fields. All calculations are based on the 90 m SRTM DEM. Daily accumulation is equal to the total precipitation when $T < 0\,°\mathrm{C}$, which is a conservative threshold with respect to other studies that have used values of 1.5 or 2 °C (Oerlemans and Fortuin, 1992), but this value has been used in previous Himalayan models (Immerzeel et al., 2012). Daily ablation is estimated using a modified degree-day factor ($\mathrm{ddf_M}$) that varies with DEM-derived aspect (θ) and surface type:

$$\mathrm{ddf_M} = \mathrm{ddf}\left(1 - R_{\exp}\cos\theta\right), \tag{4}$$

where ddf is the initial melt factor (in $\mathrm{mm\,°C^{-1}\,d^{-1}}$), and $R_{\exp}$ is a factor which quantifies the aspect (or exposure) dependence of ddf (Immerzeel et al., 2012). Initial values for melt factors for snow, ice, and debris-covered glaciers (Azam et al., 2014) are given in Table 2. The extent of debris-covered glaciers was extracted from the ICIMOD (2011) glacier inventory.

To redistribute mass from accumulation to ablation areas, we use a simplified flow model which assumes that basal sliding is the principal process for glacier movement and neglects deformational flow. While cold-based glaciers have been observed on the Tibetan Plateau (Liu et al., 2009), warm-based glaciers and polythermal regimes have been identified on the monsoon-influenced southern slopes of the Himalayas (Mae et al., 1975; Ageta and Higuchi, 1984; Kääb, 2005; Hewitt, 2007). Our assumption in this case is a necessary simplification of the sliding and deformational components of ice flow, which have not yet been modelled at the basin scale in the Himalayas.

Glacier motion is modelled as slow, viscous flow using Weertman's sliding law (Weertman, 1957), which describes glacier movement as a combination of both pressure melting and ice creep near the glacier bed. Glacier flow is assumed to be proportional to the basal shear stress (τ_{b}, Pa):

$$\tau_{\mathrm{b}} \approx v^2 R u^{\frac{2}{n+1}}. \tag{5}$$

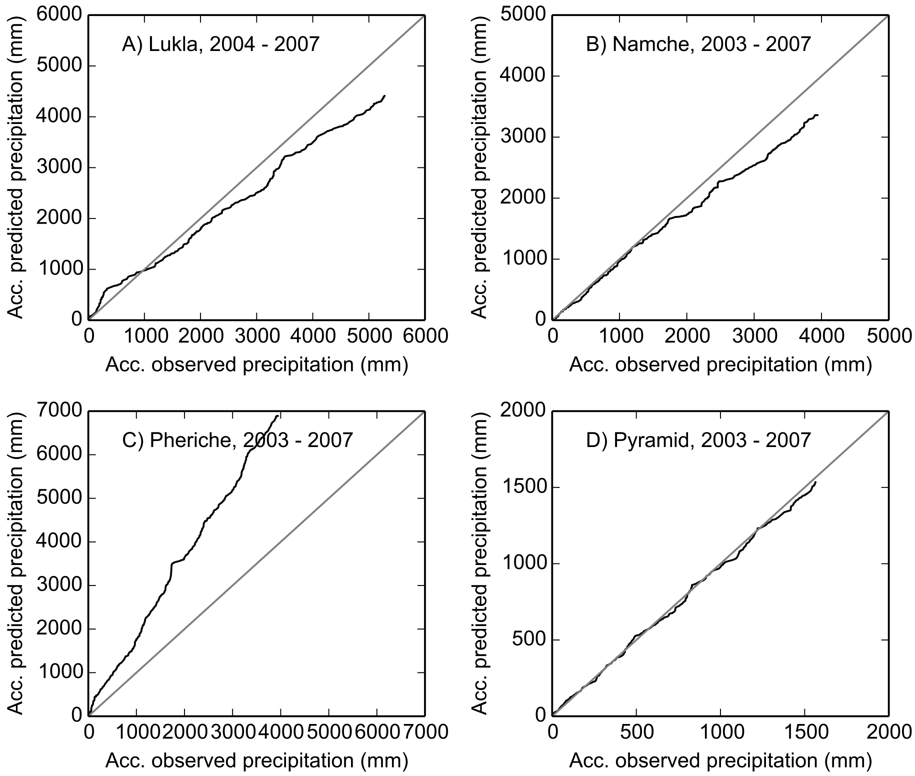

Figure 6. Accumulated observed and predicted precipitation at the EVK2CNR sites. Days where $T < 0$ or precipitation observations were missing were excluded from the analyses.

Table 2. Fixed and calibrated model parameters, with initial values, range, and final calibrated values. Degree-day factors (ddf) varied within 1 standard deviation (SD) (Supplementary Information of Immerzeel et al., 2010).

Parameter	Description	Units	Initial value	Range	Calibrated value
ρ	Ice density	$\mathrm{kg\,m^{-3}}$	916.7	–	–
g	Gravitational acceleration	$\mathrm{m\,s^{-2}}$	9.81	–	–
τ_0	Equilibrium shear stress	$\mathrm{N\,m^{-2}}$	80 000	–	–
ν	Bedrock roughness	unitless	0.1	–	–
T_S	Snow/rain limit	°C	0	–	–
γ_T	Daily vertical temperature gradient	$\mathrm{^\circ C\,m^{-1}}$	variable	–	–
C_DOY	Temperature bias correction	°C	variable	–	–
R_exp	Aspect dependence of ddf	unitless	0.2	–	–
β_TH	Threshold avalanching angle	°	50	–	–
R	Material roughness coefficient	$\mathrm{N\,m^{-2}\,s^{1/3}}$	1.80×10^9	$\pm 5.00 \times 10^8$	1.51×10^8
$\mathrm{ddf_C}$	Clean ice melt factor	$\mathrm{mm\,^\circ C^{-1}\,d^{-1}}$	8.63	±1 SD	9.7
$\mathrm{ddf_D}$	Debris-covered ice melt factor	$\mathrm{mm\,^\circ C^{-1}\,d^{-1}}$	3.34	±1 SD	4.6
$\mathrm{ddf_K}$	Khumbu Glacier melt factor	$\mathrm{mm\,^\circ C^{-1}\,d^{-1}}$	6.7		8.6
$\mathrm{ddf_S}$	Snowmelt factor	$\mathrm{mm\,^\circ C^{-1}\,d^{-1}}$	5.3	±1 SD	5.4
Z_C	Height of precipitation maximum	m a.s.l.	6000	±500	6268

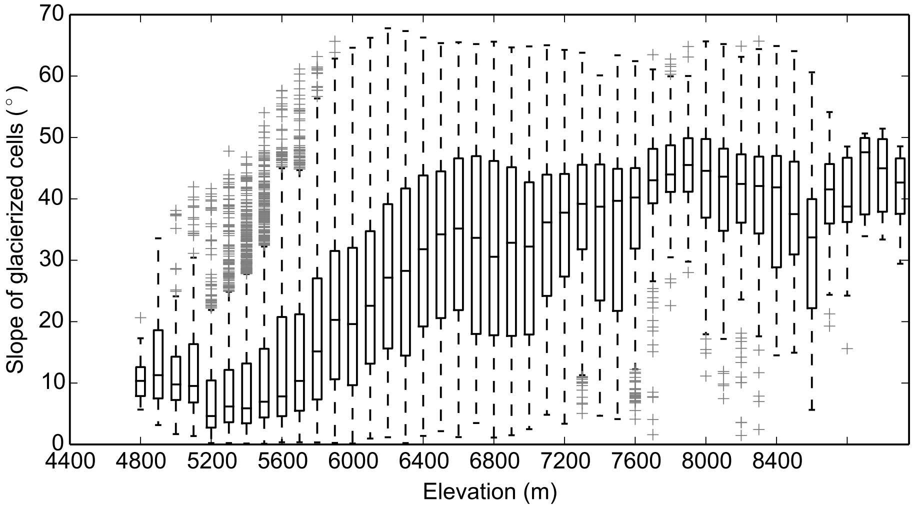

Figure 7. Boxplots of the slope of glacierized pixels in the Dudh Koshi basin, grouped by 100 m elevation bands. The boundaries of each box indicate the upper and lower quartiles, while the middle line of the box shows the median value. Whisker ends indicate the maximum (minimum) values excluding outliers, which are defined as more (less) than 3/2 times the upper (lower) quartile. Slope values were extracted from the SRTM 90 m DEM and glacier inventory from ICIMOD (2011).

Here, v (unitless) is a measure of bedrock roughness, R ($\mathrm{Pa\,m^{-2}\,s}$) is a material roughness coefficient, u is the sliding speed ($\mathrm{m\,s^{-1}}$) and n (unitless) is the creep constant of Glen's flow law, here assumed to equal 3 (Glen, 1955). The roughness of the bedrock (v) is defined as the dimension of objects on the bedrock divided by the distance between them. Smaller values for v indicate more effective regelation. R is a material roughness coefficient that controls the viscous shearing (Fowler, 2010). Basal shear stress (τ_b) is defined as

$$\tau_b = \rho g H \sin\beta, \tag{6}$$

where ρ is ice density ($\mathrm{kg\,m^{-3}}$), g is gravitational acceleration ($\mathrm{m\,s^{-2}}$), H is ice thickness (m), and β is surface slope (°). We assume that motion occurs only when basal shear stress exceeds the equilibrium shear stress ($\tau_0 = 80\,000\,\mathrm{N\,m^{-2}}$; Immerzeel et al., 2012), and combine Eqs. (5) and (6) to derive the glacier velocity:

$$u^{\frac{2}{n+1}} = \frac{\max(0, \tau_b - \tau_0)}{v^2 R}. \tag{7}$$

For each time step, glacier movement in each cell is thus modelled as a function of slope, ice thickness, and assumed bedrock roughness. The total outgoing ice flux at each time step is then determined by the glacier velocity, the horizontal resolution, and the estimated ice depth. Ice transported out of a specific cell is distributed to all neighbouring downstream cells based on slope, with steeper cells receiving a greater share of the ice flux.

As avalanches can contribute significantly to glacier accumulation in steep mountainous terrain (Inoue, 1977; Scherler et al., 2011b), the model incorporates an avalanching component which redistributes accumulated snowfall (Bernhardt and Schulz, 2010). The approach assumes that all snow in a given cell is transported to the downstream cell with the steepest slope whenever snow-holding depth and a minimum slope angle is exceeded. The snow-holding depth is deep in flat areas and shallow in steep areas and decreases exponentially with increasing slope angle.

Based on field observations and an analysis of the slopes of glacierized pixels in the catchment (Fig. 7), we assign a threshold avalanching angle (β_{TH}) of 50°. Change in ice thickness at each time step is thus the net result of ice flow through the cell, ablation, and accumulation from both precipitation and avalanching. Changes in glacier area and volume are calculated at daily time steps, and pixels with a snow water equivalent greater than 0.2 m w.e. are classified as glacier. The model does not assume steady-state conditions, and reported changes in volume and area thus represent transient states within the model.

2.3 Model initialization

Initial ice thickness for each glacierized grid cell is derived from Eq. (6):

$$H = \frac{\tau_0}{\rho g \sin\beta}, \tag{8}$$

with a minimum prescribed slope of 1.5°. We use τ_0 here, as the actual basal shear stress depends on the ice thickness. In the Dudh Koshi basin, Eq. (8) produces a total estimated glacier volume of $32.9\,\mathrm{km^3}$, based on the ICIMOD (2011) glacier inventory and SRTM DEM. While volume–area scaling relations are uncertain (Frey et al., 2013), empirical relations from Huss and Farinotti (2012) and Radić and Hock (2010) applied to individual glaciers generate basin-wide volume estimates of 31.9 and 27.5 km^3, respectively, which lends some support to the approach used here.

From the initial ice thicknesses we estimate glacier thicknesses and extents in 1961 by driving the glacier mass balance and redistribution model with modified APHRODITE temperature fields. To simulate the observed climate in the region prior to 1961, temperatures in the initialization run are decreased by $-0.025\,°C\,yr^{-1}$ (Shrestha and Aryal, 2011), for a total decrease of $-1.2\,°C$ over the 47-year initialization period. Precipitation is left unchanged in the model initialization, and we use uncalibrated model parameters (Table 2).

Mass change at the end of the 47-year initialization period is close to zero, indicating that near-equilibrium conditions have been realized. Additional runs of the initialization period, with temperatures fixed at $-1.2\,°C$, yield relatively small changes in glacier thickness (Fig. 8). However, it is possible that there are significant uncertainties in our estimates of initial (1961) thicknesses and extents, given the forcings and parameter set used, and the lag in glacier geometry responses to climate forcings.

2.4 Model calibration

From the modelled 1961 ice thicknesses and extents, the model is calibrated with six parameters: degree-day factors for clean ice (ddf_C), debris-covered ice (ddf_I), snow (ddf_S), and debris covered ice on the Khumbu Glacier (ddf_K), material roughness coefficient R, and elevation of the precipitation maximum Z_C (Table 2). Initial simulations showed anomalous flow velocities of the Khumbu Glacier, which may be due to the assumption that basal sliding is the main process of movement. This may not hold given the steep icefall above the glacier tongue and the large high-altitude accumulation area. We have corrected for this by calibrating a specific melt factor for this glacier, though improved representation of the glacier dynamics should reduce the need for a separate ddf_K. Twenty parameter sets (Table 3) were developed by varying the six calibration factors within specified ranges (Table 2). Initial values for each parameter were selected from published studies.

For each of the 20 runs (Table 4), we quantify the model skill by scoring (a) modelled and observed glacier extents at the termini of four large glaciers in the catchment (ICIMOD, 2011), (b) the geodetically derived mean basin-wide glacier mass balance of -0.40 m w.e. yr^{-1} over the period 1992–2008 (Nuimura et al., 2012), (c) a mean velocity of $10\,m\,yr^{-1}$ for debris-covered glaciers (Nakawo et al., 1999; Quincey et al., 2009), and (d) the total glacierized area in 2007 (410 km^2; ICIMOD, 2011). These tests gauge the ability of the model to accurately reproduce key glacier parameters: extent, mass change, and velocity. Scores are derived from the difference between modelled and observed quantities, with a score of zero indicating a perfect match. Scores for all four metrics are added to obtain an overall ranking of the 20 parameter sets and are weighted equally.

The glacier extent score denotes the relative deviation from a perfect match of the four large glacier termini at the end of the calibration period (Fig. 1). There are eight test polygons in total that include ice-covered and adjacent ice-free areas. For example, if only 20 % of the glacier polygons in Fig. 1 are ice covered then the score equals 0.8. The mass balance score is based on the relative offset from the catchment mean mass balance of -0.40 m w.e. yr^{-1} over the period 1992–2008:

$$S_{MB} = |(B_m/-0.4) - 1|. \tag{9}$$

If the modelled mean mass balance (B_m) equals -0.20 m w.e. yr^{-1}, then the mass balance score (S_{MB}) is 0.5. The total ice area score is based on the departure from the total glacierized area at the end of the simulation (410 km^2, ICIMOD, 2011). If the simulated ice extent is 300 km^2, then the score is 0.27 ((410–300)/410). Finally the flow velocity score quantifies the deviation from a mean glacier velocity of debris-covered tongues from 1992 to 2008 ($10\,m\,yr^{-1}$). For example, if the average simulated flow velocity is $2\,m\,yr^{-1}$, then the score is 0.8. The final score used to select the optimal parameter set is a simple addition of the four scores.

2.5 Model validation

Temperature and precipitation fields developed for this study were tested independently using point observations of mean daily temperature and total daily precipitation at the four EVK2NCR sites. We calculate mean bias error (MBE) and root mean square error (RMSE) to evaluate the skill of the elevation-based downscaling.

To validate the calibrated glacier mass balance and redistribution model, model outputs are compared against the following independent data sets:

- ice thickness profiles derived from ground-penetrating radar (GPR) at Mera Glacier (Wagnon et al., 2013) and Changri Nup Glacier (Vincent, unpublished data);
- annual mass balance and glacier mass balance gradients calculated from surface observations at Mera Glacier (Wagnon et al., 2013);
- decadal glacier extents (1990, 2000, 2010) extracted from Landsat imagery (Bajracharya et al., 2014b);
- basin-wide mean annual mass balance from 2000 to 2011 (Gardelle et al., 2013), and from 1970 to 2007 (Bolch et al., 2011).

2.6 Glacier sensitivity to future climate change

To examine the sensitivity of modelled glaciers to future climate change, we drive the calibrated model with temperature and precipitation anomalies prescribed from eight CMIP5

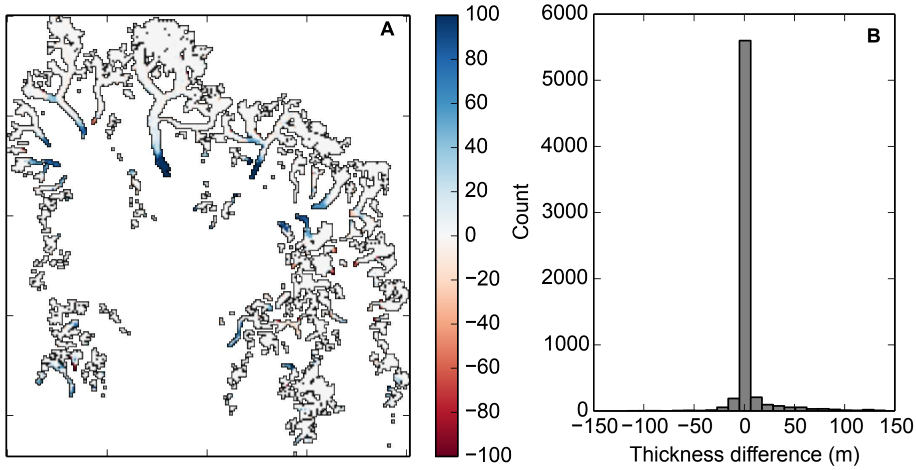

Figure 8. (a) Differences in modelled ice thickness (in m) between the end of the first initialization run (47 years) and after an additional 94 years of simulation with $\mathrm{d}T = -1.2\,°\mathrm{C}$. **(b)** Histogram of differences in modelled ice thickness.

Table 3. Parameter sets used in the calibration procedure. Degree-day factors (ddf_n) are given in units of mm $°\mathrm{C}^{-1}\,\mathrm{d}^{-1}$, R is unitless, and Z_C is in m. Mean ($\overline{x}$) and standard deviation (σ) are given at the bottom of the table.

Run	$\mathrm{ddf_C}$	$\mathrm{ddf_D}$	$\mathrm{ddf_K}$	$\mathrm{ddf_S}$	R	Z_C
1	10.1	2.4	5.7	5.1	965538934	5948
2	9.8	3.7	6.8	4.6	862185519	5974
3	9.2	4.1	8.5	3.6	1326340408	5544
4	8.8	1.7	5.3	5.7	2115148902	6392
5	9.7	4.6	8.6	5.4	1507211339	6268
6	8.9	1.9	6.8	4.3	1757035837	5712
7	9.3	3.6	7.3	6.6	1602852068	5810
8	8.9	2	7	5.3	1891517886	7175
9	9.3	2.9	8.2	5.7	965461867	6663
10	8.1	3.1	9	5.8	1966902971	6339
11	9.3	4.1	7	5.1	2119160369	5804
12	10.1	3.3	6.4	4.7	1183544033	5774
13	10.2	2.2	5.7	5.1	2027971886	5960
14	9.3	5.2	6.6	6.4	1642592045	5887
15	8.5	3.2	6.7	3.9	1674708607	5466
16	8.1	4.3	4.2	5.5	1278943171	6877
17	10.2	3.5	5.4	5.6	1687134148	6314
18	10.7	2	6.2	5.3	1920883676	6270
19	7.6	2.9	7.2	4.6	2402645369	5586
20	10.8	3.5	6	6.4	1885850339	5673
$\overline{x}$	9.3	3.2	6.7	5.2	1639181469	6072
σ	0.87	0.98	1.23	0.8	428282810	459

climate simulations that represent cold/warm and dry/wet end-members (Table 5; Immerzeel et al., 2013). Decadal T and P anomalies relative to 1961–1990 are extracted from the CMIP5 end-members. Temperature trends are strong in all CMIP5 simulations, with ensemble mean temperature increases to 2100 as great as $+8\,°\mathrm{C}$ in late winter and early spring (January–April). Precipitation anomalies do not show any significant trends and vary between 0.4 and 1.8 times the baseline period. Uncertainties in our scenarios of future climate change are examined through the mean and standard deviation of modelled ice areas and volumes derived from the eight CMIP5 models. As the model is empirically based and we assume only changes in T and P (all other state and input variables remain unchanged), we stress that the resulting glacier change realizations are a reflection of the modelled sensitivity to climate change, as opposed to physically based projections.

Table 4. Scores (unitless) from the 20 calibration runs versus independent calibration data. Calibration targets were observed extents of four large termini, basin-wide net mass balance of −0.40 m (Nuimura et al., 2012), total glacier area of 410 km^2 in 2010 (ICIMOD, 2011), and mean velocity of 10 m yr^{-1} on debris-covered tongues (Quincey et al., 2009). Mean and standard deviation (σ) of scores are provided at the bottom of the table, and scores for the selected run are in bold.

Run	Terminus extents	B_a	Total area	Velocity	Total score
1	0.20	0.46	0.04	3.44	4.14
2	0.19	0.31	0.03	2.78	3.31
3	0.19	0.26	0.01	0.34	0.79
4	0.19	0.69	0.04	0.38	1.30
5	**0.17**	**0.19**	**0.06**	**0.05**	**0.47**
6	0.20	0.58	0.01	0.75	1.54
7	0.18	0.23	0.09	0.10	0.59
8	0.19	0.70	0.03	0.88	1.80
9	0.20	0.46	0.05	3.13	3.83
10	0.18	0.45	0.05	0.01	0.69
11	0.18	0.24	0.05	0.47	0.94
12	0.19	0.33	0.04	1.21	1.76
13	0.19	0.52	0.04	0.08	0.84
14	0.17	0.05	0.09	0.44	0.75
15	0.19	0.39	0.00	0.08	0.65
16	0.18	0.44	0.04	0.72	1.37
17	0.18	0.36	0.06	0.02	0.63
18	0.19	0.56	0.05	0.37	1.18
19	0.19	0.46	0.02	0.36	1.03
20	0.18	0.20	0.10	0.37	0.85
$\bar{x}$	0.19	0.39	0.04	0.80	1.42
σ	0.01	0.18	0.03	0.87	0.90

Table 5. Projected mean annual temperature and precipitation changes from 1961–1990 to 2021–2050, extracted from RCP4.5 and RCP8.5 CMIP5 runs. See Supplementary Information from Immerzeel et al. (2013) for more information.

Scenario	Description	dP (%)	dT (°C)	Model	Ensemble
RCP4.5	Dry, Cold	−3.2	1.5	HADGEM2-CC	r1i1p1
RCP4.5	Dry, Warm	−2.3	2.4	MIROC-ESM	r1i1p1
RCP4.5	Wet, Cold	12.4	1.3	MRI-CGCM3	r1i1p1
RCP4.5	Wet, Warm	12.1	2.4	IPSL-CM5A-LR	r3i1p1
RCP8.5	Dry, Cold	−3.6	1.7	HADGEM2-CC	r1i1p1
RCP8.5	Dry, Warm	−2.8	3.1	IPSL-CM5A-LR	r2i1p1
RCP8.5	Wet, Cold	15.6	1.8	CSIRO-MK3-60	r1i1p1
RCP8.5	Wet, Warm	16.4	2.9	CAN-ESM2	r2i1p1

3 Results

3.1 APHRODITE downscaling

Daily vertical temperature gradients calculated from the APHRODITE temperature fields and resampled SRTM range from −0.010 to −0.004 °C m^{-1} and are highly significant (Fig. 3). Calculated γ_T values are most negative in the pre-monsoon (mid-April) and least negative during the active phase of the summer monsoon (mid-June to late August). This is likely a function of the increased moisture advection in the monsoon and pre-monsoon periods, which results in a less negative moist adiabatic lapse rate. These findings are consistent with temperature gradient observations between −0.0046 °C m^{-1} (monsoon) and −0.0064 °C m^{-1} (pre-monsoon) in a nearby Himalayan catchment (Immerzeel et al., 2014b). The standard deviation in calculated γ_T is lowest during the monsoon and greatest in the winter.

At all four EVK2CNR stations, daily temperatures estimated from APHRODITE vertical gradients are greater than observed, with mean daily differences ranging from −1 to +8 °C (Fig. 4). Micro-meteorological conditions may contribute to the larger biases observed at Pyramid (winter) and Pheriche (summer). During the summer monsoon period (mid-June to mid-September), the mean difference for all stations is approximately 5 °C. We develop a bias correction for the day of year (DOY) based on the mean temperature bias from the four stations, which ranges from 3.22 to 6.00 °C. The largest bias coincides with the approximate onset of the summer monsoon (DOY 150, or 31 May). A possible mechanism for this is the pre-monsoon increase in humidity at lower elevations, which would be well-represented in the gridded APHRODITE data but not at the higher elevation EVK2CNR stations. The increased humidity would result in a less negative derived temperature gradient, and thus greater errors at the high-elevation stations. The variability in calculated temperature gradients is sharply reduced at onset of the monsoon, which supports this hypothesis. Bias-corrected estimates of daily temperature (Fig. 9) have root mean squared errors (RMSE) of 1.21 to 2.07 °C and mean bias errors (MBE) of −0.87 to 0.63 °C.

Based on the calculated daily temperature gradients, intercepts, and the bias correction, we estimate the height of the 0 °C isotherm ($Z_{T=0}$) for the period 1961–2007 to examine melt potential and snow-line elevations. Mean monthly values of $Z_{T=0}$ range from 3200 m (January) to 5800 m (July), though it can reach elevations of over 6500 m on occasion. This corresponds to meteorological observations from Langtang Valley, Nepal (Shea et al., 2015), and from the Khumbu Valley (http://www.the-cryosphere-discuss.net/7/C1879/2013/tcd-7-C1879-2013.pdf).

Daily precipitation–elevation functions (Fig. 5) exhibit strong decreases in precipitation above 4000 m, particularly in the monsoon and pre-monsoon periods. Absolute precipitation totals are greatest during the monsoon period, but large precipitation events can still occur in the post-monsoon period (October–November). As often observed in high-elevation environments, daily precipitation totals observed at the EVK2CNR stations are not well captured by the downscaling process (Fig. 6). This is likely due to the difficulties in estimating precipitation in complex terrain (Immerzeel et al., 2012; Pellicciotti et al., 2012) and to errors in the precipitation measurements. For daily liquid precipitation ($T > 0$ °C), RMSEs range between 2.05 and 8.21 mm, while MBEs range from −0.85 to 1.77 mm. However, accumulated precipitation totals (Fig. 6) and mean monthly precipitation values show greater coherence, which lends some support for the downscaling approach used. At Pyramid (5035 m), the highest station with precipitation observations, the fit between cumulative predicted and observed precipitation is quite close. However, at Pheriche (4260 m), predicted precipitation is nearly double that observed over the period of record, which suggests that further refinements to the precipitation downscaling method are needed.

3.2 Model results and validation

For the calibration runs, we report here volume and area values averaged between 1 November and 31 January. Reported uncertainties are the standard deviation in modelled values from the 20 simulations. Modelled ice volumes from the 20 calibration runs (Fig. 10) decrease from 41.0 km^3 in 1961 to between 31.6 and 37.1 km^3 in 2007, with a 20-member mean of 34.5 ± 1.5 km^3 at the end of the simulation period. The ensemble mean modelled glacierized area in the calibration runs decreases from 499 km^2 to 392 ± 11 km^2, with a final range of 374 to 397 km^2.

Parameters for the calibrated model were chosen from Run 5, which had the lowest additive score of the 20 parameter sets (Table 4). Run 5 generates glacier volume and area totals that are lower but within 1 standard deviation of the model mean (Fig. 10). The selected parameter set contains degree-day factors (Table 2) that are all slightly higher than those observed by Azam et al. (2014) at Chhota Shigri Glacier but are similar to values obtained for snow and ice by Singh et al. (2000) at Dokriani Glacier, Garhwal Himalaya. The value of the material roughness coefficient in the selected parameter set lies between the values used previously in Baltoro (Pakistan) and Langtang (Nepal, Fig. 1) catchments (Immerzeel et al., 2013, Supplementary Information).

Spatially distributed output from the calibrated model (Run 5), 1961–2007, is summarized in Fig. 11. Mean annual ablation (Fig. 11a) ranges from 0 to 4.00 m w.e. yr^{-1}, though most modelled values are less than 1.80 m w.e. yr^{-1}. Debris-covered termini, despite having lower degree-day factors, are nevertheless subjected to large melt rates due to their relatively low elevation and consequently higher temperatures. Our model generates maximum melt rates at the transition between debris-covered and clean glacier ice, at elevations of approximately 5000 m (Fig. 2). This is consistent with geodetic observations of mass change in the catchment (e.g. Bolch et al., 2008b). Maximum mean annual snowfall (Fig. 11b) amounts of up to 0.50 m w.e. yr^{-1} are observed at 6268 m (the calibrated value of Z_C, Table 2), but due to the precipitation scaling function (Eq. 2) the highest peaks receive zero snowfall amounts. The calibrated height of Z_C (6268 m) is similar to the elevation of maximum snowfall (between 6200 and 6300 m) estimated for the Annapurna range in mid-Nepal (Fig. 1; Harper and Humphrey, 2003).

Modelled glacier velocities during the calibration period are less than 10 m yr^{-1} over debris-covered glacier termini and between 30 and 100 m yr^{-1} between the accumulation and ablation zones. While there are differences in both the spatial pattern and magnitude of modelled and observed velocities (e.g. Quincey et al., 2009), we feel that our simplification of glacier dynamics is unavoidable in the current study, and the development of higher-order physically based models will lead to improved representations of glacier flow.

3.2.1 Mass balance

Over the entire domain, modelled mean annual mass balances (b_a; Fig. 11c) range from −4.6 to +3.0 m w.e. yr^{-1},

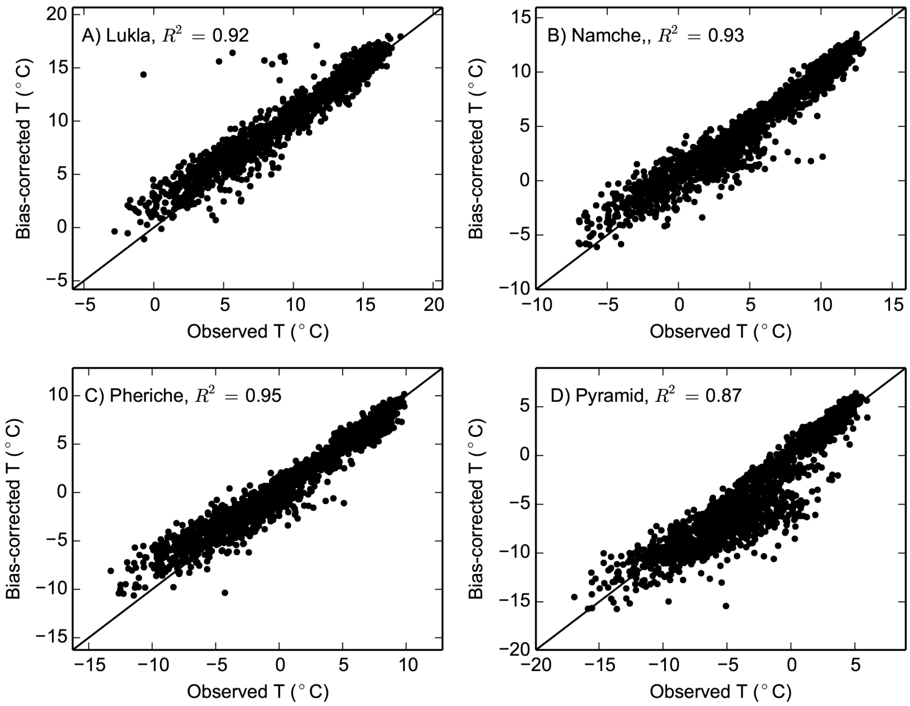

Figure 9. Mean daily temperatures observed at EVK2CNR sites (2003–2007) versus bias-corrected temperatures estimated from APHRODITE temperature fields.

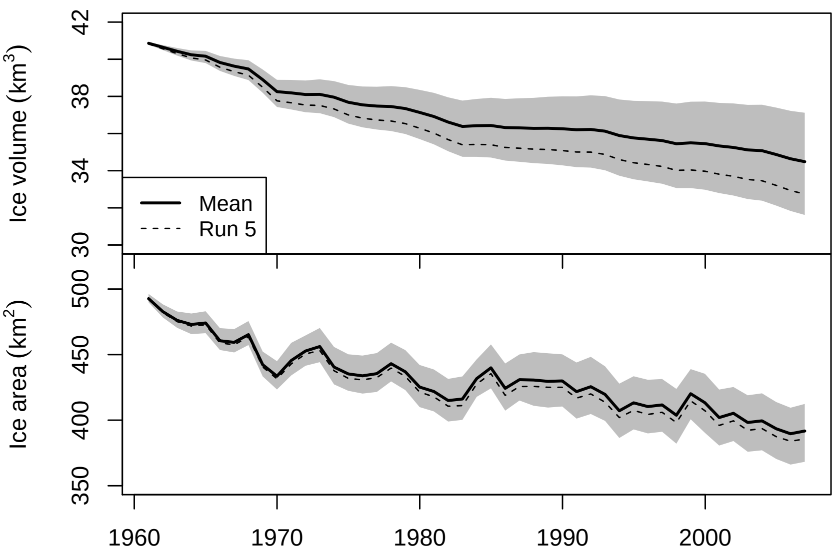

Figure 10. Top panel: modelled mean (1 November–31 January) ice volumes from the 20 calibration runs, 1961–2007, with multi-model mean (black line), minimum and maximum modelled volumes (shaded area), and results from Run 5 (dashed line). Bottom panel: as above but for modelled glacier areas from the 20 calibration runs.

with the majority of values falling between −1.4 and +0.1 m w.e. yr^{-1}. The spatial patterns of modelled annual mass balance are consistent with the geodetic estimates of mass change between 2000 and 2010, and our modelled basin-wide mass balance of −0.33 m w.e. yr^{-1} is only slightly more negative than the basin-wide estimates of -0.26 ± 0.13 m w.e. yr^{-1} given by Gardelle et al. (2013) and -0.27 ± 0.08 m w.e. yr^{-1} given by Bolch et al. (2011) for the Khumbu region only.

The overall Dudh Koshi mass balance gradient (Run 5), calculated from median modelled b_a for all glacierized cells in 100 m intervals between 4850 and 5650 m, is equiva-

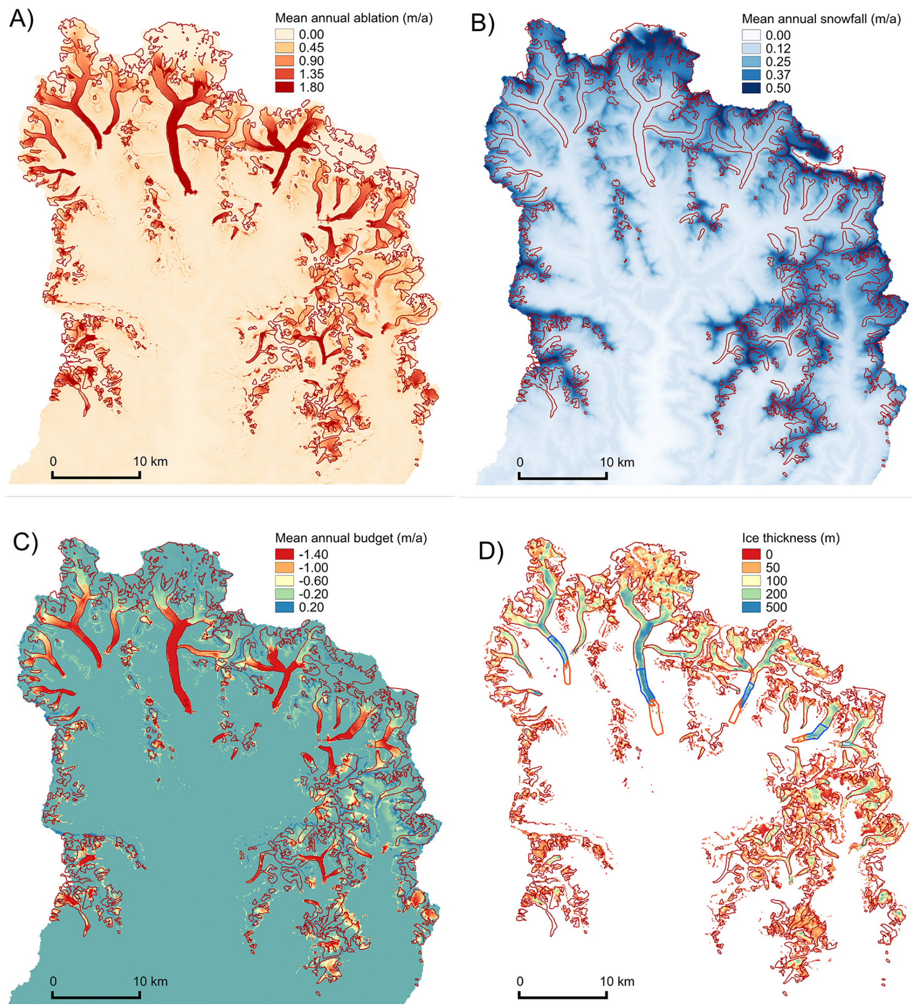

Figure 11. Results from the calibrated model run, 1961–2007. **(a)** Mean annual ablation, **(b)** mean annual snowfall, **(c)** mean annual mass budget, and **(d)** final ice thickness. Extents of glacierized and non-glacierized calibration regions are shown in **(d)**.

lent to 0.27 m w.e. $(100\,\mathrm{m})^{-1}$ (Fig. 12). The range of mass balance gradients for the other 19 parameter sets ranges from 0.10 to 0.34 m w.e. $(100\,\mathrm{m})^{-1}$. The mass balance gradient from Run 5 gives a basin-wide ELA at approximately 5500 m, which agrees with previously published estimates (Williams, 1983; Asahi, 2010; Wagnon et al., 2013). Mass balance gradients (Run 5) at Mera and Naulek glaciers are approximately 0.40 and 0.68 m w.e. $(100\,\mathrm{m})^{-1}$, respectively, between 5350 and 5600 m. These values compare well with the gradients of 0.48 and 0.85 m w.e $(100\,\mathrm{m})^{-1}$ observed over the same elevation range at Mera and Naulek between 2007 and 2012 (Wagnon et al., 2013). Calculated mass balance gradients from the different parameter sets range from 0.31 to 0.35 m w.e. $(100\,\mathrm{m})^{-1}$ at Mera Glacier and from 0.46 to 0.72 m w.e. $(100\,\mathrm{m})^{-1}$ at Naulek Glacier (Fig. 12).

Modelled annual mass balances (B_a) at Mera Glacier (1961–2007) range between -1.45 and $+0.11$ m w.e. (Fig. 13), with low variability amongst the different parameter sets. Surface mass balance observations at the same site from 2007 to 2012 range between -0.67 and $+0.46$ m w.e. (Wagnon et al., 2013). As model and observation periods do not overlap, direct comparisons between modelled and observed mass balances are not possible. However, the mean mass balance observed at Mera Glacier between 2007 and 2012 is -0.08 m w.e., whereas the mean modelled mass balance between 2000 and 2006 is -0.16 m w.e. We note that our reconstructed mass balance series at Mera Glacier shows strong similarities to the reconstructed mass balance at Chhota Shigri Glacier (Azam et al., 2014), with balanced conditions in the late 1980s and early 1990s. Standard deviations of observed and modelled mass balance are 0.51 and 0.29 m w.e., respectively, and the greater variability in observed b_a is likely linked to the short observation period (5 years) and to enhanced local variability which cannot be captured with downscaled climate fields. The mass balance model, although it may underestimate the

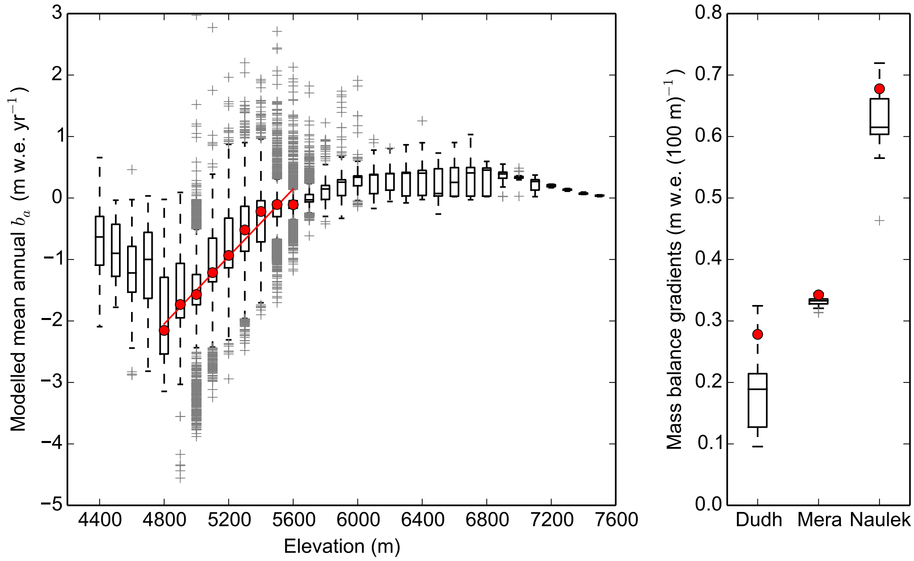

Figure 12. Left: boxplots of modelled mean annual mass balance (m w.e. yr^{-1}) calculated for 100 m intervals (1961–2007) for the entire Dudh Koshi basin. Calculated mass balance gradient of 0.27 m w.e. (100 m)$^{-1}$ between 4850 and 5650 m is shown in red. Right: boxplots of mass balance gradients calculated for all 20 calibration model runs for the entire Dudh Koshi (between 4850 and 5650 m), Mera Glacier (between 5350 and 5600 m), and Naulek Glacier (between 5350 and 5600 m). The gradients calculated for Run 5 are shown in red.

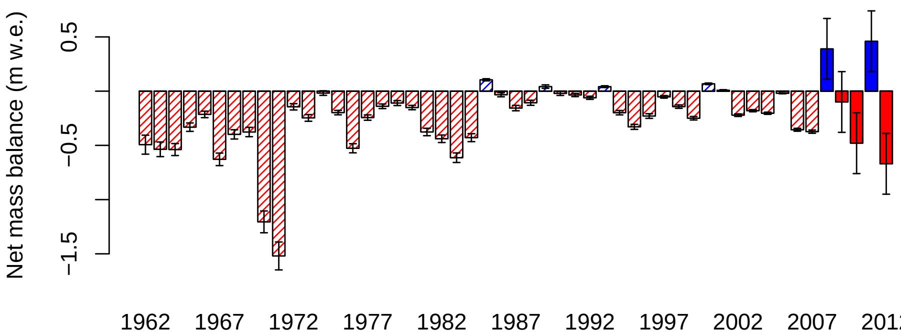

Figure 13. Modelled (dashed) and observed (solid) annual net mass balance at Mera Glacier, 1961–2007. Error bars for the modelled mass balances derived from the standard deviation of the annual mass balances extracted from 20 calibration runs, and error bars for the observed mass balances are from Wagnon et al. (2013).

inter-annual variability, is able to simulate a surface mass balance that is in a plausible and realistic range.

3.2.2 Modelled and observed glacier thickness

At the end of the calibrated run (1961–2007), modelled ice thicknesses range between 0 and 620 m, though 98 % of these are less than 205 m (Fig. 11d). Similar ice thicknesses have been estimated for the large debris-covered Gangotri Glacier, Indian Himalaya, using slope, surface velocities, and simple flow laws (Gantayat et al., 2014). Due to the model formulation, low-angle slopes on glacier termini may result in unrealistic estimates of ice depth, and a minimum surface slope of 1.5° is prescribed in the model. Radio-echo surveys in 1999 indicated that centerline ice thicknesses on the Khumbu Glacier decreased from approximately 400 m at Everest Base Camp to less than 100 m near the terminus (Gades et al., 2000). Our model accurately captures this decrease in the upper portions but overestimates ice thickness in the relatively flat terminus. Recent observations of ice thickness obtained from ground penetrating radar (GPR) surveys in the basin are examined in detail below.

Estimates of glacier thickness extracted from the calibrated model and are compared with depth profiles found with GPR surveys conducted at Mera Glacier (Wagnon et al., 2013) and Changri Nup Glacier (C. Vincent, unpublished data). To facilitate the comparison, we obtained surface elevations and bedrock depths from the GPR surveys, and we matched these to the modelled ice thicknesses of the corresponding pixels (Fig. 14). At the lower elevation profile on Mera Glacier (5350 m), the shape of the bedrock profile is

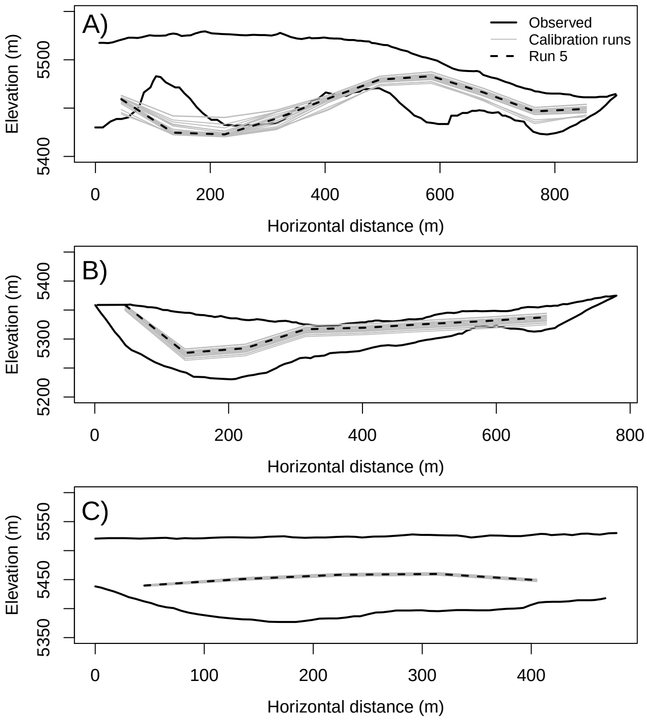

Figure 14. Glacier depths estimated from transverse ground-based GPR surveys and the mass balance and redistribution model, for **(a)** profile at 5350 m on Mera Glacier, **(b)** profile at 5520 m on Mera Glacier, and **(c)** profile at Changri Nup Glacier (Fig. 1). Ice depth estimates for all 20 calibration runs are given in grey, and the results for Run 5 are shown as a dashed black line.

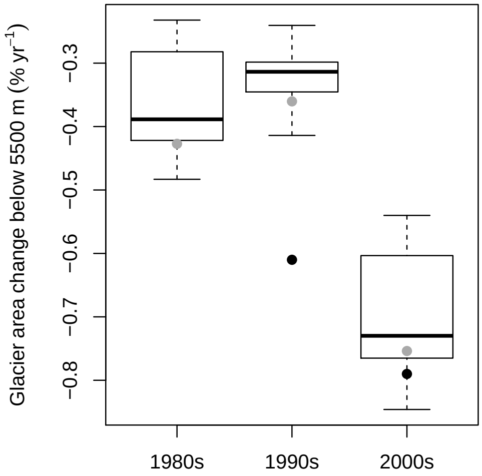

Figure 15. Rates of historical glacier area change below 5500 m (% yr^{-1}) from the 20 model runs. Remotely sensed rates of glacier area change and Run 5 results are shown as black and grey points, respectively. The 1980's inventory contained inaccuracies related to the resolution of the imagery and the misclassification of snow as glacier ice, and an observed rate of change from 1980 to 1990 is not included here.

similar to the model, but ice thicknesses are approximately half what is observed or less. This may be due in part to the surface slope extracted from the DEM, which controls the modelled ice thickness. The transect at 5350 m was collected in a flat section between two steeper slopes, which would likely be mapped as a steep slope in the DEM. For the profile at 5520 m both the shape and the depths of the bedrock profile are generally well-captured by the model. At the Changri Nup cross section, which lies on a relatively flat section of the main glacier body, modelled ice depths are approximately two-thirds of the observed. Modelled ice depths do not appear to be highly sensitive to the range of model parameters used in the 20 calibration runs, though variability is higher for Mera Glacier than for Changri Nup.

3.2.3 Modelled and observed glacier extents and shrinkage

Modelled historical changes in glacier area (Fig. 10) exhibit greater variability than modelled ice volumes. This is largely due to the sensitivity of the modelled glacier area to large snowfall events, as snowfall amounts greater than the 0.2 m w.e. threshold are classified as glacier. To compare modelled and observed extents we use the mean extent at the end of the ablation season (1 November–31 January).

Using semi-automated classifications of Landsat imagery, glacier extents in the Dudh Koshi basin were constructed for 1990, 2000, and 2010 (ICIMOD, 2011; Bajracharya et al., 2014a, available at rds.icimod.org). As the glacier change signal is greatest at lower elevations, and errors in glacier delineation due to persistent snow cover are possible at higher elevations, we consider the change in glacier area below 5500 m, which roughly equals the equilibrium line altitude in the catchment.

Below 5500 m, the observed rate of glacier area change in the Dudh Koshi was -0.61 % yr^{-1} between 1990 and 2000, and -0.79 % yr^{-1} between 2000 and 2010. For the 20 parameter sets, modelled rates of glacier area change below 5500 m (Fig. 15) vary between -0.24 % and 0.41 % yr^{-1} (1990–2000) and -0.54 and -0.85 % yr^{-1} (2000–2007) for the 20 parameter sets. The calibrated run (Run 5) gives area change rates of -0.36 and -0.75 % yr^{-1} for the 1990–2000 and 2000–2007 periods, respectively. Both modelled and observed glacier change are of similar magnitudes, and both show a consistent trend of increasing area loss, which is corroborated by other studies in the region (Bolch et al., 2008b; Thakuri et al., 2014). Salerno et al. (2014) cite a weakened monsoon with reduced accumulation at all elevations as a main reason for the increased mass loss in recent years. Differences between modelled and observed rates of glacier shrinkage can be attributed to errors in the glacier inventory, e.g. geometric correction and interpretation errors, uncertainty in our estimates of initial ice volumes, and other model errors which are discussed below.

Table 6. Mean ($\overline{x}$) and standard deviation (σ) in percent modelled glacier volume change for RCP4.5 and RCP8.5 end-members at 2050 and 2100.

Scenario	$\overline{x}_{2050}$	σ_{2050}	$\overline{x}_{2100}$	σ_{2100}
RCP4.5	−39.3	16.8	−83.7	11.2
RCP8.5	−52.4	14.5	−94.7	4.2

3.3 Glacier sensitivity to future climate change

Decadal temperature and precipitation anomalies extracted from members of the CMIP5 ensemble that capture a range of climate scenarios (Table 5) are applied to the historical APHRODITE T and P fields. The calibrated glacier mass and redistribution model is then used to explore the sensitivity of modelled glaciers to future climate change in the Dudh Koshi basin. From initial glacier volumes and extents (Eq. 8), the mean projected changes in total ice volume at 2050 are −39.3 and −52.4 % for RCP4.5 and RCP8.5 emissions scenarios, respectively (Table 6). The minimum projected volume change at 2050 is −26 % (cold/wet), and the maximum is −70 % (warm/dry). At 2100 the projected mean total volume loss is estimated at −83.7 % for RCP4.5 scenarios, and −94.7 % for RCP8.5, with a range between −70 and −99 %. Radić et al. (2014) and Marzeion et al. (2012), respectively, estimate mean glacier volume changes in south-east Asia of −50 and −60 % for RCP4.5 scenarios and −75 and −70 % for RCP8.5 by 2100. In all scenarios presented here, the rate of ice loss decreases towards the end of the simulation period (Fig. 16), which indicates a shift towards equilibrium mass balance conditions.

Increased precipitation may slow the rate of future mass loss, but it is not sufficient to offset the increases in glacier melt due to increased temperatures. Changes in the timing and magnitude of monsoon precipitation may thus be less important than previously believed (Mölg et al., 2012; Bolch et al., 2012). The main difference between the RCP4.5 and RCP8.5 scenarios is the magnitude of the temperature increase, which leads to greater losses of ice volume in the RCP8.5 scenarios. This is due in part to the increased melt but also to the expansion of the ablation area and the change in precipitation phase from solid to liquid. Based on the daily temperature gradients and projected monthly temperature increases, the elevation of the 0 °C isotherm may increase by 800 to 1200 m by 2100. A potential snow-line elevation of 7000 m in August would expose 90 % of the current glacierized area to melt and severely restrict snow accumulation during the monsoon.

With a distributed model we can examine the possible impact of future climate change on Everest-region glacier area and thickness with respect to elevation. The patterns of decreases in ice area (Fig. 17) and ice thickness (Fig. 18) with elevation illustrate the combined effects of increased melt rates due to warmer temperatures and the insulating effect of debris cover. The greatest losses in glacier area, both relative and absolute, are expected at elevations close to the current ELA (approx. 5500 m), where the greatest amount of debris-free ice area currently exists. At lower elevations, where glaciers are exclusively debris-covered (Fig. 2), modelled glacier thicknesses are greater (Fig. 11), melt rates are lower, and modelled changes in glacier area and volume will be less than those near the ELA.

Wet and cool scenarios for both the RCP4.5 and RCP8.5 scenarios show the possible survival of debris-covered glaciers between 4000 and 4500 m, albeit with greatly reduced thicknesses (Fig. 18). In both warm and dry scenarios, glaciers below 5500 m could be eliminated, and in the RCP8.5 scenario, glacier thicknesses between 6000 and 6500 m could experience reductions by the year 2100. According to these scenarios, no changes are expected in the glacier volumes at elevations above 7000 m.

Our most conservative realization (RCP4.5 dry/cold, $T+1.5$°C, $P+12.3$ % by 2050) shows virtually no change in glaciers above 6000 m (Fig. 17b). However, glacierized area near the current ELA (5500 m) may see declines of up to 80 %, and thinning will occur below 5750 m (Fig. 18). Debris-covered termini may see area reductions of 40 % by 2100. The RCP8.5 warm/dry scenario (+3.1 °C, −2.8 % P by 2050) is the worst-case realization, in which glaciers below 6500 m are essentially eliminated by 2100 (Fig. 17c).

4 Discussion

Through a multi-parameter calibration and validation with independent data sets, we model the mass balance and mass redistribution of glaciers in the Dudh Koshi basin over the period 1961–2007. Temperature and precipitation changes specified from end-members of the CMIP5 ensemble are applied to historical climate fields to examine the sensitivity of glaciers in the region to future climate change. Expected increases in temperature will result in sustained mass losses that are only partially offset by increases in precipitation. We can identify three main sources of uncertainty in our approach: parametric, structural, and climate inputs. These are discussed below. Although considerable progress is made in this study by the systematic integration of field-based observations into our modelling approach, there are still a number of key challenges to be addressed in the future.

4.1 Structural uncertainty

The glacier mass balance and redistribution model used in this study has precedents in other studies (Immerzeel et al., 2012, 2013) and has been calibrated here with observational data. While the model is a simplification of complex ice flow and dynamical processes, it is an important tool that can be used to explore the sensitivity of glaciers in the region

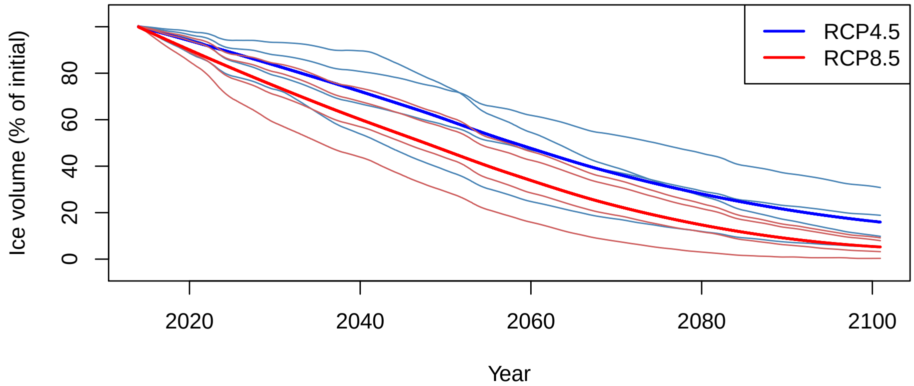

Figure 16. Sensitivity of modelled glacier volumes to decadal T and P anomalies from four RCP4.5 (blue) and four RCP8.5 (red) ensemble members (see Table 5 for details). Realizations are given as thin lines, and ensemble means are thick lines. All realizations are smoothed with a loess filter (span = 0.05) to minimize interannual variations.

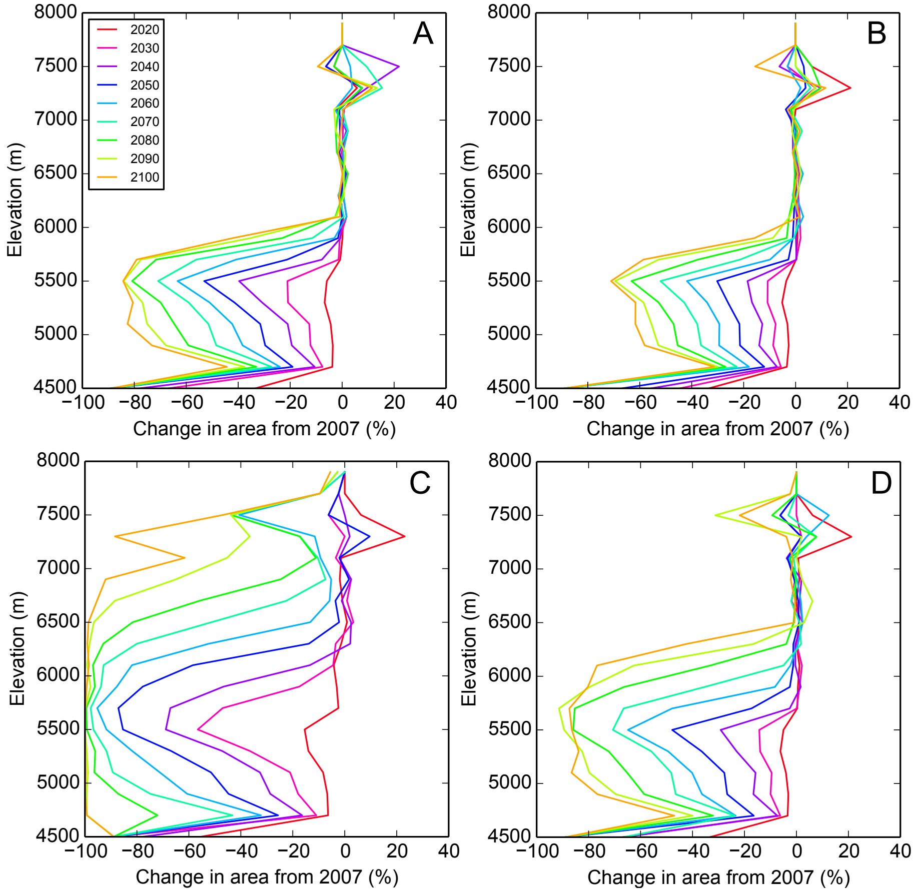

Figure 17. Change in glacier area versus elevation for **(a)** the dry/warm RCP4.5 scenario, **(b)** the wet/cool RCP4.5 scenario, **(c)** the dry/warm RCP8.5 scenario, and **(d)** the wet/cool RCP8.5 scenario.

to future climate change. Given the forcings (−1.2 °C over 47 years) and parameter set (uncalibrated) used in the initialization, and the lag in actual glacier geometry response to climate change, it is possible that there are additional uncertainties in our estimates of initial ice volumes.

Our assumption of stationary debris cover may also be incorrect in the long-term, as glacier wastage typically leads to increased debris concentrations and the development of a debris cover. However, the median glacier slope above 5500 m is greater than 20° (Fig. 7), and the development of debris

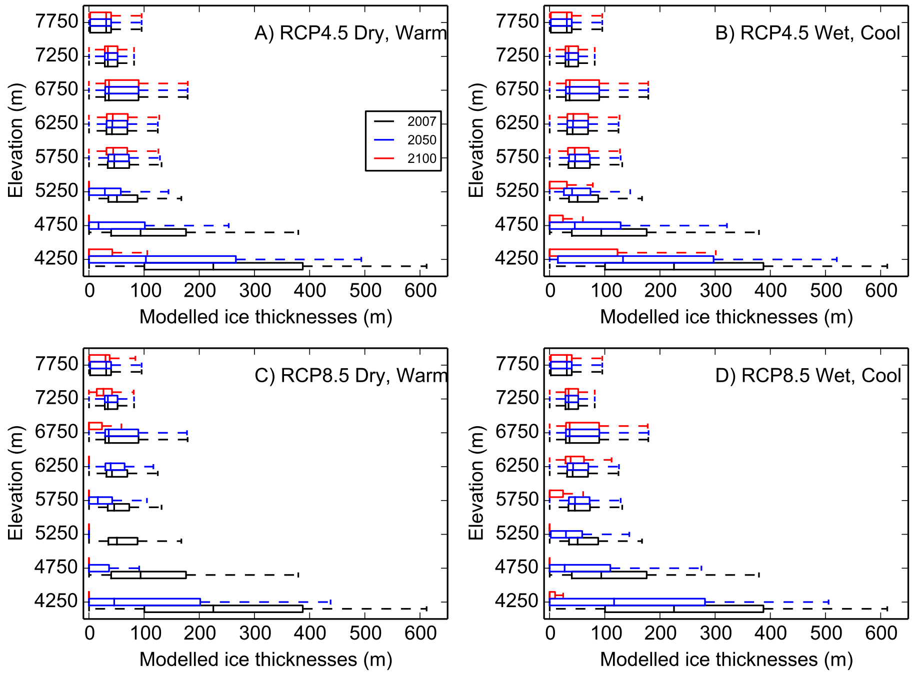

Figure 18. Distribution of modelled ice thicknesses by elevation band, for 2007 (initialization), 2050, and 2100. **(a)** Dry/warm RCMP4.5 scenario, **(b)**, wet/cool RCP4.5 scenario, **(c)** dry/warm RCP8.5 scenario, and **(d)** wet/cool RCP8.5 scenario.

cover on such slopes is unlikely (cf. Fig. 3b, Scherler et al., 2011a) as de-glaciation proceeds. Until higher-order models of glacier dynamics (e.g. Adhikari and Huybrechts, 2009; Clarke et al., 2015) are sufficiently advanced and explicitly include the effects of debris cover, and the additional input data (bedrock topography, ice temperatures) are well-constrained, simple modelling approaches will still be required for basin-scale analyses of glacier change scenarios.

4.2 Parametric uncertainty

Our calibration approach relies on 20 sets of six different parameters with values taken randomly from pre-assigned initial values and ranges (Table 3). Model results from the 20 parameter sets (Figs. 12, 13, 14) suggest that the parametric uncertainty is well-constrained. The selected set of calibrated parameters is similar to those used in other regions (Immerzeel et al., 2012, 2013), but a much larger and more computationally expensive Monte Carlo-type simulation must be undertaken to reduce the parametric uncertainty. Additional calibration data sets would also be beneficial, and these could include a greater number of ice depth measurements from debris-covered and clean-ice glaciers, remotely sensed snow cover, and glacier mass balance.

4.3 Input climate data uncertainty

The lack of high-elevation temperature and precipitation data to force the mass balance model is one of the key challenges that nearly all Himalayan modelling studies face. In this study, we derive temperature gradients and precipitation–elevation functions from the 0.25° gridded APHRODITE data, which in turn is based primarily on low-elevation stations. The downscaling approach is then tested with semi-independent station data from the EVK2CNR network of stations in the Dudh Koshi basin. While temperatures can be skillfully modelled after applying a bias correction based on the day of year, our ability to predict precipitation ranges from very good (at Pyramid) to very poor (at Pheriche). Difficulty in quantifying precipitation and precipitation gradients in high-mountain areas is likely one of the largest sources of uncertainty in mountain hydrology (Immerzeel et al., 2012; Nepal et al., 2013). Further investigations into high-elevation precipitation gradients, through field studies, remote sensing derivatives, and/or the use of high-resolution numerical weather models, will help to increase our understanding of glacier nourishment in the region. An analysis of the sensitivity of modelled glacier change to the rain/snow threshold temperature is also recommended.

4.4 Response times

Glaciers in the region are highly sensitive to temperature changes. Precipitation increases of 15 % (mostly during the monsoon season) will be unable to counter the loss of glacier mass due to increased melt rates. For intense warming scenarios, our ensemble mean volume change is more negative than regional estimates given by both Marzeion et al. (2012) and Radić et al. (2014). The potential loss of lower-elevation glaciers in the study area raises the question of glacier response times. The actual response times of glaciers in the region can be approximated from modelled thicknesses and mass balance rates near the glacier terminus, following the methods of Jóhannesson et al. (1989):

$$\tau = \frac{-H'}{\dot{b}_\mathrm{a}}, \tag{10}$$

where H' is a representative glacier thickness and $\dot{b}_\mathrm{a}$ ($\dot{b}_\mathrm{a} > 0$) is the mean annual mass balance near the terminus. Given our modelled ice thicknesses and mean annual mass balances at the termini of glaciers throughout the catchment, Eq. (10) suggests that the smaller glaciers in the southern portions of the basin have total glacier response times on the order of 20–50 years, while the large debris-covered glaciers have response times of 200–500 years. These first-order estimates reflect the time it takes the glaciers to reach a new equilibrium state in response to a step change in climate (Cogley et al., 2011) and are in agreement with the modelled persistence of debris-covered termini and loss of smaller, low-elevation glaciers.

Our scenarios suggest that future reductions in glacier area will occur mainly in clean ice regions between accumulation areas and debris-covered termini. We anticipate that the hypsometric distribution of ice will become bi-modal as glacier mass loss proceeds: debris-covered tongues will continue to exist (in reduced states) at low elevations but will become separated from their high-elevation accumulation zones (Kääb, 2005). Current examples of this type of glacier change can be found at Chorabari Glacier, Garhwal Himalaya (Dobhal et al., 2013), and at Lirung Glacier (central Nepal) in nearby Langtang Valley (Immerzeel et al., 2014a), where glacier wastage above the debris-covered termini has left stagnant debris-covered ice below and small high-elevation ice masses above. Model scenarios from this study are thus consistent with field observations and suggest that this will become a familiar picture in the coming decades.

5 Conclusions

In the mountains of high Asia, changes in glacier volumes will impact the timing and magnitude of streamflows, particularly in the pre-monsoon period (Immerzeel et al., 2013). Our study advances the current understanding of Himalayan glacier evolution under climate change and examines the basin-scale evolution of glaciers in the Dudh Koshi basin of central Nepal using a distributed glacier mass balance and redistribution model. We constrain the glacier model parameters with observations where possible and calibrate against observations of net glacier mass change, velocities on debris-covered termini, and glacier extents. Our work represents a first-order estimate of future glacier change and is subject to considerable uncertainty from a number of sources.

Temperature and precipitation anomalies from end-member scenarios extracted from the CMIP5 RCP4.5 and RCP8.5 ensemble (Immerzeel et al., 2013) are applied to historical downscaled climate fields, and the model is used to explore the sensitivity of glaciers in the Dudh Koshi basin to future climate change. Modelled glacier sensitivity to temperature change is high, with large decreases in ice thicknesses and extents for even the most conservative climate change scenario. Future climate scenarios with increased precipitation and reduced warming result in decreased mass losses, though increases in precipitation are insufficient to offset the dramatic increase in mass loss through increased melting.

Glaciers in the region appear to be highly sensitive to changes in temperature, and projected increases in precipitation are insufficient to offset the increased glacier melt. While we have identified numerous sources of uncertainty in the model, the signal of future glacier change in the region is clear and compelling. Advancements in the representation of ice dynamics (Clarke et al., 2015) and understanding of high-altitude precipitation will result in improved catchment-scale estimates of glacier sensitivity to future climate change in high mountain Asia.

Acknowledgements. We gratefully acknowledge the Royal Norwegian Embassy at Kathmandu for funding the Cryosphere Monitoring Project at the ICIMOD and the contributions of Finu Shrestha and Sudan Maharajan to the glacier inventory work. This study was partially funded by the Netherlands Organization for Scientific Research through their VENI program and by the research for development (R4D) program of DFID, as well as core funds of ICIMOD contributed by the governments of Afghanistan, Australia, Austria, Bangladesh, Bhutan, China, India, Myanmar, Nepal, Norway, Pakistan, Switzerland, and the United Kingdom. Mera and Changri Nup glacier research was supported by the French Service d'Observation GLACIOCLIM and the French National Research Agency through ANR-09-CEP-005-01/PAPRIKA. This study was carried out within the framework of the Ev-K2-CNR Project in collaboration with the Nepal Academy of Science and Technology as foreseen by the Memorandum of Understanding between Nepal and Italy, and thanks to contributions from the Italian National Research Council, the Italian Ministry of Education, University and Research, and the Italian Ministry of Foreign Affairs. We also acknowledge the World Climate Research Programme's Working Group on Coupled Modelling, which is responsible for CMIP, and we thank the climate modelling groups for producing and making available their model outputs. The views and interpretations in this publication are those of the authors and are not necessarily attributable to ICIMOD. Ben Marzeion, Anne Rowan, Graham Cogley, Franco Salerno, and an anonymous reviewer provided invaluable comments and suggestions on previous versions of the manuscript.

Edited by: T. Bolch

References

Adhikari, S. and Huybrechts, P.: Numerical modelling of historical front variations and the 21st-century evolution of glacier AX010, Nepal Himalaya, Ann. Glaciol., 50, 27–34, 2009.

Ageta, Y. and Higuchi, K.: Estimation of mass balance components of a summer-accumulation type glacier in the Nepal Himalaya, Geografiska Annaler Series A. Physical Geography, 66A, 249–255, 1984.

Ageta, Y. and Kadota, T.: Predictions of changes of glacier mass balance in the Nepal Himalaya and Tibetan Plateau: a case study of air temperature increase for three glaciers, Ann. Glaciol., 16, 89–94, 1992.

Asahi, K.: Equilibrium-line altitudes of the present and Last Glacial Maximum in the eastern Nepal Himalayas and their implications for SW monsoon climate, Quaternary Int., 212, 26–34, doi:10.1016/j.quaint.2008.08.004, 2010.

Ashfaq, M., Shi, Y., Tung, W.-w., Trapp, R. J., Gao, X., Pal, J. S., and Diffenbaugh, N. S.: Suppression of south Asian summer monsoon precipitation in the 21st century, Geophys. Res. Lett., 36, L01704, doi:10.1029/2008GL036500, 2009.

Azam, M. F., Wagnon, P., Vincent, C., Ramanathan, A., Linda, A., and Singh, V. B.: Reconstruction of the annual mass balance of Chhota Shigri glacier, Western Himalaya, India, since 1969, Ann. Glaciol., 55, 69–80, doi:10.3189/2014AoG66A104, 2014.

Bajracharya, S. R. and Mool, P.: Glaciers, glacial lakes and glacial lake outburst floods in the Mount Everest region, Nepal, Ann. Glaciol., 50, 81–86, doi:10.3189/172756410790595895, 2010.

Bajracharya, S., Maharjan, S., and Shrestha, F.: The status and decadal change of glaciers in Bhutan from the 1980s to 2010 based on satellite data, Ann. Glaciol., 55, 159–166, doi:10.3189/2014AoG66A125, 2014a.

Bajracharya, S., Maharjan, S., Shrestha, F., Bajracharya, O., and Baidya, S.: Glacier Status in Nepal and Decadal Change from 1980 to 2010 Based on Landsat Data, ICIMOD, available at: lib.icimod.org/record/29291, last access: 29 August 2014b.

Benn, D. I., Bolch, T., Hands, K., Gulley, J., Luckman, A., Nicholson, L. I., Quincey, D., Thompson, S., Toumi, R., and Wiseman, S.: Response of debris-covered glaciers in the Mount Everest region to recent warming, and implications for outburst flood hazards, Earth Sci. Rev., 114, 156–174, doi:10.1016/j.earscirev.2012.03.008, 2012.

Bernhardt, M. and Schulz, K.: SnowSlide: A simple routine for calculating gravitational snow transport, Geophys. Res. Lett., 37, L11502, doi:10.1029/2010GL043086, 2010.

Bolch, T., Buchroithner, M., Pieczonka, T., and Kunert, A.: Planimetric and volumetric glacier changes in the Khumbu Himal, Nepal, since 1962 using Corona, Landsat TM and ASTER data, J. Glaciol., 54, 592–600, doi:10.3189/002214308786570782, 2008a.

Bolch, T., Buchroithner, M. F., Peters, J., Baessler, M., and Bajracharya, S.: Identification of glacier motion and potentially dangerous glacial lakes in the Mt. Everest region/Nepal using spaceborne imagery, Nat. Hazards Earth Syst. Sci., 8, 1329–1340, doi:10.5194/nhess-8-1329-2008, 2008b.

Bolch, T., Pieczonka, T., and Benn, D. I.: Multi-decadal mass loss of glaciers in the Everest area (Nepal Himalaya) derived from stereo imagery, The Cryosphere, 5, 349–358, doi:10.5194/tc-5-349-2011, 2011.

Bolch, T., Kulkarni, A., Kääb, A., Huggel, C., Paul, F., Cogley, J. G., Frey, H., Kargel, J. S., Fujita, K., Scheel, M., Bajracharya, S., and Stoffel, M.: The state and fate of Himalayan glaciers, Science, 336, 310–314, doi:10.1126/science.1215828, 2012.

Bookhagen, B. and Burbank, D.: Topography, relief, and TRMM-derived rainfall variations along the Himalaya, Geophys. Res. Lett., 33, L08405, doi:10.1029/2006GL026037, 2006.

Chen, N. Sh., Hu, G. Sh., Deng, W., Khanal, N., Zhu, Y. H., and Han, D.: On the water hazards in the trans-boundary Kosi River basin, Nat. Hazards Earth Syst. Sci., 13, 795–808, doi:10.5194/nhess-13-795-2013, 2013.

Clarke, G. K. C., Jarosch, A. H., Anslow, F. S., Radic, V., and Menounos, B.: Projected deglaciation of western Canada in the twenty-first century, Nat. Geosci., doi:10.1038/ngeo2407, in press, 2015.

Cogley, J. G.: Present and future states of Himalaya and Karakoram glaciers, Ann. Glaciol., 52, 69–73, doi:10.3189/172756411799096277, 2011.

Cogley, J., Hock, R., Rasmussen, L., Arendt, A., Bauder, A., Braithwaite, R., Jansson, P., Kaser, G., Möller, M., Nicholson, L., and Zemp, M.: Glossary of glacier mass balance and related terms. IHP-VII Technical Documents in Hydrology No. 86, IACS Contribution No. 2, UNESCO-IHP, 126 pp., 2011.

Dimri, A. and Dash, S.: Wintertime climatic trends in the western Himalayas, Clim. Change, 111, 775–800, doi:10.1007/s10584-011-0201-y, 2012.

Dimri, A., Yasunari, T., Wiltshire, A., Kumar, P., Mathison, C., Ridley, J., and Jacob, D.: Application of regional climate models to the Indian winter monsoon over the western Himalayas, Sci. Total Environ., 468, S36–S47, doi:10.1016/j.scitotenv.2013.01.040, 2013.

Dobhal, D., Mehta, M., and Srivastava, D.: Influence of debris cover on terminus retreat and mass changes of Chorabari Glacier, Garhwal region, central Himalaya, India, J. Glaciol., 59, 961–971, doi:10.3189/2013JoG12J180, 2013.

Farr, T. G., Rosen, P. A., Caro, E., Crippen, R., Duren, R., Hensley, S., Kobrick, M., Paller, M., Rodriguez, E., Roth, L., Seal, D., Shaffer, S., Shimada, J., Umland, J., Werner, M., Oskin, M., Burbank, D., and Alsdorf, D.: The Shuttle Radar Topography Mission, Rev. Geophys., 45, RG2004, doi:10.1029/2005RG000183, 2007.

Fowler, A. C.: Weertman, Lliboutry and the development of sliding theory, J. Glaciol., 56, 965–972, doi:10.3189/002214311796406112, 2010.

Frey, H., Machguth, H., Huss, M., Huggel, C., Bajracharya, S., Bolch, T., Kulkarni, A., Linsbauer, A., Salzmann, N., and Stoffel, M.: Ice volume estimates for the Himalaya-Karakoram region: evaluating different methods, The Cryosphere Discuss., 7, 4813–4854, doi:10.5194/tcd-7-4813-2013, 2013.

Fujita, K. and Nuimura, T.: Spatially heterogeneous wastage of Himalayan glaciers, P. Natl. Acad. Sci., 108, 14011–14014, doi:10.1073/pnas.1106242108, 2011.

Gades, A., Conway, H., Nereson, N., Naito, N., and Kadota, T.: Radio echo-sounding through supraglacial debris on Lirung and Khumbu Glaciers, Nepal Himalayas, Proceedings of International Workshop on Debris Covered Glaciers, IAHS-AISH Publication, 264, 13–22, 2000.

Gantayat, P., Kulkarni, A., and Srinivasan, J.: Estimation of ice thickness using surface velocities and slope: case study at Gangotri Glacier, India, J. Glaciol., 60, 277–282, doi:10.3189/2014JoG13J078, 2014.

Gardelle, J., Berthier, E., and Arnaud, Y.: Slight mass gain of Karakoram glaciers in the early twenty-first century, Nat. Geosci., 5, 322–325, doi:10.1038/ngeo1450, 2012.

Gardelle, J., Berthier, E., Arnaud, Y., and Kääb, A.: Region-wide glacier mass balances over the Pamir-Karakoram-Himalaya during 1999–2011, The Cryosphere, 7, 1263–1286, doi:10.5194/tc-7-1263-2013, 2013.

Gardner, A. S., Moholdt, G., Cogley, J. G., Wouters, B., Arendt, A. A., Wahr, J., Berthier, E., Hock, R., Pfeffer, W. T., Kaser, G., Ligtenberg, S. R. M., Bolch, T., Sharp, M. J., Hagen, J. O., Van Den Broeke, M., and Paul, F.: A reconciled estimate of glacier contributions to sea level rise: 2003 to 2009, Science, 340, 852–857, doi:10.1126/science.1234532, 2013.

Gautam, M. R., Acharya, K., and Tuladhar, M. K.: Upward trend of streamflow and precipitation in a small, non-snow-fed, mountainous watershed in Nepal, J. Hydrol., 387, 304–311, 2010.

Glen, J. W.: The creep of polycrystalline ice, Royal Soc. London Proc. Series A, 228, 519–538, doi:10.1098/rspa.1955.0066, 1955.

Harper, J. T. and Humphrey, N. F.: High altitude Himalayan climate inferred from glacial ice flux, Geophys. Res. Lett., 30, 1764, doi:10.1029/2003GL017329, 2003.

Hewitt, K.: Tributary glacier surges: an exceptional concentration at Panmah Glacier, Karakoram Himalaya, J. Glaciol., 53, 181–188, doi:10.3189/172756507782202829, 2007.

Huss, M. and Farinotti, D.: Distributed ice thickness and volume of all glaciers around the globe, J. Geophys. Res.-Earth Surf., 117, F04010, doi:10.1029/2012JF002523, 2012.

ICIMOD: The status of glaciers in the Hindu Kush-Himalayan region, ICIMOD, available at: http://lib.icimod.org/record/9419/files/icimod-the_status_of_glaciers_in_the_hindu_kush-himalayan_region%5B1%5D.pdf, 2011.

Immerzeel, W. W., van Beek, L. P. H., and Bierkens, M. F. P.: Climate change will affect the Asian water towers, Science, 328, 1382–1385, doi:10.1126/science.1183188, 2010.

Immerzeel, W., van Beek, L., Konz, M., Shrestha, A., and Bierkens, M.: Hydrological response to climate change in a glacierized catchment in the Himalayas, Clim. Change, 110, 721–736, doi:10.1007/s10584-011-0143-4, 2012.

Immerzeel, W., Pellicciotti, F., and Bierkens, M.: Rising river flows throughout the twenty-first century in two Himalayan glacierized watersheds, Nat. Geosci., 6, 742–745, doi:10.1038/ngeo1896, 2013.

Immerzeel, W., Kraaijenbrink, P., Shea, J., Shrestha, A., Pellicciotti, F., Bierkens, M., and de Jong, S.: High-resolution monitoring of Himalayan glacier dynamics using unmanned aerial vehicles, Remote Sens. Environ., 150, 93–103, 2014a.

Immerzeel, W. W., Petersen, L., Ragettli, S., and Pellicciotti, F.: The importance of observed gradients of air temperature and precipitation for modeling runoff from a glacierized watershed in the Nepalese Himalayas, Water Resour. Res., 50, 2212–2226, doi:10.1002/2013WR014506, 2014b.

Inoue, J.: Mass budget of Khumbu Glacier: glaciological expedition of Nepal, Contribution No. 32, Seppyo, 39, 15–19, 1977.

Jacob, T., Wahr, J., Pfeffer, W., and Swenson, S.: Recent contributions of glaciers and ice caps to sea level rise, Nature, 482, 514–518, doi:10.1038/nature10847, 2012.

Jóhannesson, T., Raymond, C., and Waddington, E.: Time-scale for adjustment of glaciers to changes in mass balance, J. Glaciol., 35, 355–369, 1989.

Kääb, A.: Combination of SRTM3 and repeat ASTER data for deriving alpine glacier flow velocities in the Bhutan Himalaya, Remote Sens. Environ., 94, 463–474, 2005.

Kääb, A., Berthier, E., Nuth, C., Gardelle, J., and Arnaud, Y.: Contrasting patterns of early twenty-first-century glacier mass change in the Himalayas, Nature, 488, 495–498, doi:10.1038/nature11324, 2012.

Kripalani, R. H., Oh, J. H., Kulkarni, A., Sabade, S. S., and Chaudhari, H. S.: South Asian summer monsoon precipitation variability: Coupled climate model simulations and projections under IPCC AR4, Theor. Appl. Climatol., 90, 133–159, doi:10.1007/s00704-006-0282-0, 2007.

Lejeune, Y., Bertrand, J.-M., Wagnon, P., and Morin, S.: A physically based model of the year-round surface energy and mass balance of debris-covered glaciers, J. Glaciol., 59, 327–344, doi:10.3189/2013JoG12J149, 2013.

Liu, Y., Hou, S., Wang, Y., and Song, L.: Distribution of borehole temperature at four high-altitude alpine glaciers in central Asia, J. of Mountain Sci., 6, 221–227, 2009.

Lutz, A. F., Immerzeel, W. W., Gobiet, A., Pellicciotti, F., and Bierkens, M. F. P.: Comparison of climate change signals in CMIP3 and CMIP5 multi-model ensembles and implications for Central Asian glaciers, Hydrol. Earth Syst. Sci., 17, 3661–3677, doi:10.5194/hess-17-3661-2013, 2013.

Mae, S., Wushiki, H., Ageta, Y., and Higuchi, K.: Thermal drilling and temperature measurements in Khumbu Glacier, Nepal Himalayas, Seppyo, 37, 161–169, 1975.

Marzeion, B., Jarosch, A. H., and Hofer, M.: Past and future sea-level change from the surface mass balance of glaciers, The Cryosphere, 6, 1295–1322, doi:10.5194/tc-6-1295-2012, 2012.

Mathison, C., Wiltshire, A., Dimri, A., Falloon, P., Jacob, D., Kumar, P., Moors, E., Ridley, J., Siderius, C., Stoffel, M., and Yasunari, T.: Regional projections of North Indian climate for adaptation studies, Sci. Total Environ., 468, S4–S17, doi:10.1016/j.scitotenv.2012.04.066, 2013.

Mirza, M., Warrick, R., Ericksen, N., and Kenny, G.: Trends and persistence in precipitation in the Ganges, Brahmaputra and Meghna river basins, Hydrol. Sci. J., 43, 845–858, 1998.

Mölg, T., Chiang, J. C. H., Gohm, A., and Cullen, N. J.: Temporal precipitation variability versus altitude on a tropical high mountain: Observations and mesoscale atmospheric modelling, Q. J. Roy. Meteorol. Soc., 135, 1439–1455, doi:10.1002/qj.461, 2009.

Mölg, T., Maussion, F., Yang, W., and Scherer, D.: The footprint of Asian monsoon dynamics in the mass and energy balance of a Tibetan glacier, The Cryosphere, 6, 1445–1461, doi:10.5194/tc-6-1445-2012, 2012.

Naito, N., Nakawo, M., Kadota, T., and Raymond, C. F.: Numerical simulation of recent shrinkage of Khumbu Glacier, Nepal Himalayas, in: Debris-covered Glaciers: Proceedings of an International Workshop Held at the University of Washington in Seattle, Washington, USA, 13–15 September 2000, Vol. 264, p. 245, International Association of Hydrological Sciences, 2000.

Nakawo, M., Yabuki, H., and Sakai, A.: Characteristics of Khumbu Glacier, Nepal Himalaya: recent change in the debris-covered area, Ann. Glaciol., 28, 118–122, 1999.

Nepal, S., Krause, P., Flügel, W.-A., Fink, M., and Fischer, C.: Understanding the hydrological system dynamics of a glaciated alpine catchment in the Himalayan region using the J2000 hydrological model, Hydrol. Process., 28, 1329–1344, doi:10.1002/hyp.9627, 2013.

Nuimura, T., Fujita, K., Yamaguchi, S., and Sharma, R. R.: Elevation changes of glaciers revealed by multitemporal digital elevation models calibrated by GPS survey in the Khumbu region, Nepal Himalaya, 1992–2008, J. Glaciol., 58, 648–656, doi:10.3189/2012JoG11J061, 2012.

Oerlemans, J. and Fortuin, J. P. F.: Sensitivity of glaciers and small ice caps to greenhouse warming, Science, 258, 115–117, 1992.

Ohmura, A.: Enhanced temperature variability in high-altitude climate change, Theor. Appl. Climatol., 110, 499–508, doi:10.1007/s00704-012-0687-x, 2012.

Palazzi, E., Hardenberg, J., and Provenzale, A.: Precipitation in the Hindu-Kush Karakoram Himalaya: Observations and future scenarios, J. Geophys. Res.-Atmos., 118, 85–100, doi:10.1029/2012JD018697, 2013.

Pellicciotti, F., Buergi, C., Immerzeel, W., Konz, M., and Shrestha, A.: Challenges and uncertainties in hydrological modeling of remote Hindu Kush-Karakoram-Himalayan (HKH) basins: suggestions for calibration strategies, Mountain Res. Develop., 32, 39–50, doi:10.1659/MRD-JOURNAL-D-11-00092.1, 2012.

Qi, W., Zhang, Y., Gao, J., Yang, X., Liu, L., and Khanal, N. R.: Climate change on the southern slope of Mt. Qomolangma (Everest) region in Nepal since 1971, J. Geogr. Sci., 23, 595–611, 2013.

Quincey, D. J., Luckman, A., and Benn, D.: Quantification of Everest region glacier velocities between 1992 and 2002, using satellite radar interferometry and feature tracking, J. Glaciol., 55, 596–606, doi:10.3189/002214309789470987, 2009.

Racoviteanu, A., Armstrong, R., and Williams, M.: Evaluation of an ice ablation model to estimate the contribution of melting glacier ice to annual discharge in the Nepalese Himalaya, Water Resour. Res., 49, 5117–5133, doi:10.1002/wrcr.20370, 2013.

Radić, V. and Hock, R.: Regional and global volumes of glaciers derived from statistical upscaling of glacier inventory data, J. Geophys. Res.-Earth Surf., 115, F01010, doi:10.1029/2009JF001373, 2010.

Radić, V., Bliss, A., Beedlow, A. C., Hock, R., Miles, E., and Cogley, J. G.: Regional and global projections of twenty-first century glacier mass changes in response to climate scenarios from global climate models, Clim. Dynam., 42, 37–58, doi:10.1007/s00382-013-1719-7, 2014.

Rangwala, I. and Miller, J.: Climate change in mountains: a review of elevation-dependent warming and its possible causes, Clim. Change, 114, 527–547, doi:10.1007/s10584-012-0419-3, 2012.

Rangwala, I., Miller, J. R., Russell, G. L., and Xu, M.: Using a global climate model to evaluate the influences of water vapor, snow cover and atmospheric aerosol on warming in the Tibetan Plateau during the twenty-first century, Clim. Dynam., 34, 859–872, doi:10.1007/s00382-009-0564-1, 2009.

Rasmussen, L. A.: Meteorological controls on glacier mass balance in High Asia, An. Glaciol., 54, 352–359, doi:10.3189/2013AoG63A353, 2013.

Reid, T. D. and Brock, B. W.: An energy-balance model for debris-covered glaciers including heat conduction through the debris layer, J. Glaciol., 56, 903–916, doi:10.3189/002214310794457218, 2010.

Richardson, S. D. and Reynolds, J. M.: An overview of glacial hazards in the Himalayas, Quaternary Int., 65, 31–47, 2000.

Salerno, F., Buraschi, E., Bruccoleri, G., Tartari, G., and Smiraglia, C.: Glacier surface-area changes in Sagarmatha national park, Nepal, in the second half of the 20th century, by comparison of historical maps, J. Glaciol., 54, 738–752, doi:10.3189/002214308786570926, 2008.

Salerno, F., Guyennon, N., Thakuri, S., Viviano, G., Romano, E., Vuillermoz, E., Cristofanelli, P., Stocchi, P., Agrillo, G., Ma, Y., and Tartari, G.: Weak precipitation, warm winters and springs impact glaciers of south slopes of Mt. Everest (central Himalaya) in the last two decades (1994–2013), The Cryosphere Discuss., 8, 5911–5959, doi:10.5194/tcd-8-5911-2014, 2014.

Scherler, D., Bookhagen, B., and Strecker, M. R.: Spatially variable response of Himalayan glaciers to climate change affected by debris cover, Nat. Geosci., 4, 156–159, doi:10.1038/ngeo1068, 2011a.

Scherler, D., Bookhagen, B., and Strecker, M. R.: Hillslope-glacier coupling: The interplay of topography and glacial dynamics in High Asia, J. Geophys. Res.-Earth Surf., 116, F02019, doi:10.1029/2010JF001751, 2011b.

Shea, J., Wagnon, P., Immerzeel, W., Biron, R., Brun, F., and Pellicciotti, F.: A comparative high-altitude meteorological analysis from three catchments in the Nepalese Himalaya, Int. J. Water Resour. Manage., doi:10.1080/07900627.2015.1020417, 2015.

Shi, Y. and Liu, S.: Estimation on the response of glaciers in China to the global warming in the 21st century, Chinese Sci. Bull., 45, 668–672, doi:10.1007/BF02886048, 2000.

Shrestha, A. B. and Aryal, R.: Climate change in Nepal and its impact on Himalayan glaciers, Reg. Environ. Change, 11, 65–77, doi:10.1007/s10113-010-0174-9, 2011.

Shrestha, A. B., Wake, C. P., Mayewski, P. A., and Dibb, J. E.: Maximum temperature trends in the Himalaya and its vicinity: an analysis based on temperature records from Nepal for the period 1971-94, J. Climate, 12, 2775–2786, doi:10.1175/1520-0442(1999)012<2775:MTTITH>2.0.CO;2, 1999.

Singh, P., Kumar, N., Ramasastri, K., and Singh, Y.: Influence of a fine debris layer on the melting of snow and ice on a Himalayan Glacier, in: Debris Covered Glaciers, Vol. 264 of IAHS Proceedings, 63–69, IAHS, 2000.

Stahl, K., Moore, R. D., Shea, J. M., Hutchinson, D., and Cannon, A. J.: Coupled modelling of glacier and streamflow response to future climate scenarios, Water Resour. Res., 440, W02422, doi:10.1029/2007WR005956, 2008.

Thakuri, S., Salerno, F., Smiraglia, C., Bolch, T., D'Agata, C., Viviano, G., and Tartari, G.: Tracing glacier changes since the 1960s on the south slope of Mt. Everest (central Southern Himalaya) using optical satellite imagery, The Cryosphere, 8, 1297–1315, doi:10.5194/tc-8-1297-2014, 2014.

Thompson, S. S., Benn, D. I., Dennis, K., and Luckman, A.: A rapidly growing moraine-dammed glacial lake on Ngozumpa Glacier, Nepal, Geomorphology, 145, 1–11, doi:10.1016/j.geomorph.2011.08.015, 2012.

Viviroli, D., Dürr, H. H., Messerli, B., Meybeck, M., and Weingartner, R.: Mountains of the world, water towers for humanity: Typology, mapping, and global significance, Water Resour. Res., 43, W07447, doi:10.1029/2006WR005653, 2007.

Wagnon, P., Vincent, C., Arnaud, Y., Berthier, E., Vuillermoz, E., Gruber, S., Ménégoz, M., Gilbert, A., Dumont, M., Shea, J.

M., Stumm, D., and Pokhrel, B. K.: Seasonal and annual mass balances of Mera and Pokalde glaciers (Nepal Himalaya) since 2007, The Cryosphere, 7, 1769–1786, doi:10.5194/tc-7-1769-2013, 2013.

Weertman, J.: On the sliding of glaciers, J. Glaciol., 3, 33–38, 1957.

Williams, V. S.: Present and former equilibrium-line altitudes near Mount Everest, Nepal and Tibet, Arctic Alpine Res., 15, 201–211, 1983.

Yao, T., Thompson, L., Yang, W., Yu, W., Gao, Y., Guo, X., Yang, X., Duan, K., Zhao, H., Xu, B.and Pu, J., Lu, A., Xiang, Y., Kattel, D., and Joswiak, D.: Different glacier status with atmospheric circulations in Tibetan Plateau and surroundings, Nat. Clim. Change, 2, 663–667, doi:10.1038/NCLIMATE1580, 2012.

Yatagai, A., Arakawa, O., Kamiguchi, K., Kawamoto, H., Nodzu, M. I., and Hamada, A.: A 44-year daily gridded precipitation dataset for Asia based on a dense network of rain gauges, Sola, 5, 137–140, doi:10.2151/sola.2009-035, 2009.

Yatagai, A., Kamiguchi, K., Arakawa, O., Hamada, A., Yasutomi, N., and Kitoh, A.: APHRODITE: Constructing a Long-Term Daily Gridded Precipitation Dataset for Asia Based on a Dense Network of Rain Gauges, B. Am. Meteorol. Soc., 93, 1401–1415, doi:10.1175/BAMS-D-11-00122.1, 2012.

Zhang, T., Xiao, C., Colgan, W., Qin, X., Du, W., Sun, W., Liu, Y., and Ding, M.: Observed and modelled ice temperature and velocity along the main flowline of East Rongbuk Glacier, Qomolangma (Mount Everest), Himalaya, J. Glaciol., 59, 438–448, doi:10.3189/2013JoG12J202, 2013.

Hydrol. Earth Syst. Sci. Discuss., 12, 4755–4784, 2015
www.hydrol-earth-syst-sci-discuss.net/12/4755/2015/
doi:10.5194/hessd-12-4755-2015

Hydrology and Earth System Sciences
Discussions
Open Access

This discussion paper is/has been under review for the journal Hydrology and Earth System Sciences (HESS). Please refer to the corresponding final paper in HESS if available.

Reconciling high altitude precipitation in the upper Indus Basin with glacier mass balances and runoff

W. W. Immerzeel[1,3], N. Wanders[1], A. F. Lutz[3], J. M. Shea[2], and M. F. P. Bierkens[1]

[1]Utrecht University, Department of Physical Geography, Heidelberglaan 2, P.O. Box 80115, Utrecht, the Netherlands
[2]International Centre for Integrated Mountain Development (ICIMOD), P.O. Box 3226, Kathmandu, Nepal
[3]FutureWater, Costerweg 1V, 6702 AA Wageningen, the Netherlands

Received: 30 March 2015 – Accepted: 8 April 2015 – Published: 4 May 2015

Correspondence to: W. W. Immerzeel (w.w.immerzeel@uu.nl)

Published by Copernicus Publications on behalf of the European Geosciences Union.

Abstract

Mountain ranges in Asia are important water suppliers, especially if downstream climates are arid, water demands are high and glaciers are abundant. In such basins, the hydrological cycle depends heavily on high altitude precipitation. Yet direct observations of high altitude precipitation are lacking and satellite derived products are of insufficient resolution and quality to capture spatial variation and magnitude of mountain precipitation. Here we use glacier mass balances to inversely infer the high altitude precipitation in the upper Indus Basin and show that the amount of precipitation required to sustain the observed mass balances of the large glacier systems is far beyond what is observed at valley stations or estimated by gridded precipitation products. An independent validation with observed river flow confirms that the water balance can indeed only be closed when the high altitude precipitation is up to a factor ten higher than previously thought. We conclude that these findings alter the present understanding of high altitude hydrology and will have an important bearing on climate change impact studies, planning and design of hydropower plants and irrigation reservoirs and the regional geopolitical situation in general.

1 Introduction

Of all Asian basins that find their headwaters in the greater Himalayas, the Indus Basin depends most strongly on high altitude water resources (Immerzeel et al., 2010; Lutz et al., 2014). The largest glacier systems outside the polar regions are found in this area and the seasonal snow cover is the most extensive of all Asian basins (Immerzeel et al., 2009). In combination with a semi-arid downstream climate, a high demand for water owing to the largest irrigation scheme in the world and a large and quickly growing population, the importance of the upper Indus Basin (UIB) is evident (Immerzeel and Bierkens, 2012). The hydrology of the UIB (4.37×10^5 km^2) is, however, poorly understood and the magnitude and distribution of high altitude precipitation is one of its largest unknowns (Hewitt, 2005, 2007; Winiger et al., 2005; Ragettli and Pellicciotti, 2012; Immerzeel et al., 2013; Mishra, 2015). Annual precipitation patterns in the UIB result from the intricate interplay between synoptic scale circulation and valley scale topography-atmosphere interaction resulting in orographic precipitation and funnelling of air movement (Barros et al., 2004; Hewitt, 2013). At the synoptic scale, annual precipitation originates from two sources: the south-eastern monsoon during the summer and moisture transported by the westerly jet stream over central Asia (Scherler et al., 2011; Mölg et al., 2013) during winter. The relative contribution of westerly disturbances to the total annual precipitation increases from south-east to north-west, and the anomalous behaviour of Karakoram glaciers are commonly attributed to changes in winter precipitation (Scherler et al., 2011; Yao et al., 2012). At smaller scales the complex interaction between the valley topography and the atmosphere dictates the spatial distribution of precipitation (Bookhagen and Burbank, 2006; Immerzeel et al., 2014). Valley bottoms, where stations are located, are generally dry and precipitation increases up to a certain maximum altitude (HMAX) above which all moisture has been orographically forced out of the air and precipitation decreases again. In westerly dominated rainfall regimes HMAX is generally higher, which is likely related to the higher tropospheric altitude of the westerly airflow (Harper, 2003; Hewitt, 2005, 2007; Winiger et al., 2005; Scherler et al., 2011). Gridded precipitation products are the de facto standard in hydrological assessments, and they are either based on observations (e.g. APHRODITE; Yatagai et al., 2012), remote sensing (e.g. the Tropical Rainfall Monitoring Mission; Huffman et al., 2007) or reanalysis (e.g. ERA-Interim; Dee et al., 2011) (Fig. 1c to e). In most cases the station data strongly influence the distribution and magnitude of the precipitation in those data products, however the vast majority of the UIB is located at elevations far beyond the average station elevation (Fig. 1a and b). The few stations that are at elevations above 2000 m are located in dry valleys and we hypothesize that the high altitude precipitation is considerably underestimated (Fig. 1c–e). Moreover, remote sensing based products, such as TRMM, are insufficiently capable of capturing snowfall (Bookhagen and Burbank, 2006; Huffman

et al., 2007) and the spatial resolution (25 to 75 km^2) of most rainfall products (and the underlying models) is insufficient to capture topography-atmosphere interaction at the valley scale (Fig. 1c–e). Thus, there is a pressing need to improve the quantification of high altitude precipitation, preferably at large spatial extents and at high resolution. Earlier work at the small scale suggested that the glacier mass balance may be used to reconstruct precipitation in its catchment area (Harper, 2003; Immerzeel et al., 2012b). Figure 1a and b shows that the glaciers are located at elevations that are in higher parts of the UIB, which are not covered by station data. Therefore the mass balances of the glaciers contain important information on high altitude accumulation in an area that is inaccessible, ungauged, but very important from an hydrological point of view. In this study we further elaborate this approach by inversely modeling average annual precipitation from the mass balance of 550 large ($> 5\,km^2$) glacier systems located throughout the UIB. We perform a rigorous uncertainty analysis and we validate our findings using independent observation of river runoff.

2 Methods

We use regionally-averaged glacier mass balance (MB) data from ICESat (Kääb et al., 2012) in combination with daily air temperature fields, a degree day melt model and a detailed elevation model to optimize the precipitation gradient (PG) so as to match the simulated and observed glacier mass balances. We apply geostatistical conditional simulation (Goovaerts, 1997) to spatially interpolate the PG estimates to high-resolution PG fields, which are then used to estimate the high-altitude precipitation. To account for uncertainties in the estimated precipitation we randomly sample six critical parameters and generate 10 000 equiprobable precipitation fields and we validate our results using observed river runoff data.

2.1 Datasets

Glacier mass balance trends based on ICESat (Kääb et al., 2012) are recomputed for the period 2003 until 2008 for the three major mountain ranges in the UIB: the Karakoram, the Hindu-Kush and the Himalaya (Fig. 1). For each zone the mass balance is computed including a regional uncertainty estimate (Kääb et al., 2012). From the zonal uncertainty (σ_z) we estimate the SD between glaciers within a zone (σ_g) as

$$\sigma_g = \sigma_z \sqrt{n} \quad (1)$$

Where n is the number of glaciers within a zone. The σ_g values used in the uncertainty analysis are shown in Table 1.

Glacier outlines area based on the glacier inventory of the International Centre for Integrated Mountain Development (Bajracharya and Shrestha, 2011). We use runoff data and actual evapotranspiration (ETa) data for the validation of our results. For runoff we compiled all available published data, which we complemented with data made available by the Pakistan Meteorological Department and the Pakistan Water and Power Development Authority. To account for uncertainty in gridded ETa estimates we used four different products which we resampled to a 1 km^2 resolution at which we perform all our analysis:

- ERA-Interim reanalysis (Dee et al., 2011): ERA-Interim uses the HTESSEL land surface scheme (Dee et al., 2011) to compute actual evapotranspiration (ETa). For transpiration a distinction is made between high and low vegetation in the HTESSEL scheme and these are parameterized from the Global Land Cover Characteristics database at a nominal resolution of 1 km^2.
- MERRA reanalysis (Rienecker et al., 2011): the MERRA reanalysis product of NASA applies the state-of-the-art GEOS-5 data assimilation system that includes many modern observing systems in a climate framework. MERRA uses the GEOS-5 catchment LSM land surface scheme (Koster et al., 2000) to compute actual ET.

- ET-Look (Bastiaanssen et al., 2012): the ET-Look remote sensing model infers information on ET from combined optical and passive microwave sensors, which can observe the land-surface even under persistent overcast conditions. A two-layer Penman–Monteith forms the basis of quantifying soil and canopy evaporation. The dataset is available only for the year 2007, but it was scaled to the 2003–2007 average using the ratio between the 2003–2007 average and the 2007 annual ET based on ERA-INTERIM.
- PCRGLOB-WB (Wada et al., 2014): the global hydrological model PCRGLOB-WB computes actual evapotranspiration using potential evapotranspiration based on Penman–Monteith, which is further reduced based on available soil moisture.

The average annual ET for the period 2003–2007 for each of the four products is shown in Fig. 2. The spatial patterns show good agreement, but the magnitudes differ considerably. The average ET for the entire upper Indus equals 359 ± 107 mm yr^{-1}.

The daily APHRODITE precipitation (Yatagai et al., 2012) and air temperature datasets (Yasutomi et al., 2011) from 2003 until 2007 are used as reference datasets to ensure maximum temporal overlap with the ICESat based glacier mass balance dataset (Kääb et al., 2012). The precipitation dataset is resampled from the nominal resolution of 25 km^2 to a resolution of 1 km^2 using the nearest neighbour algorithm. The air temperature dataset is then bias-corrected using monthly linear regressions with independent station data to account for altitudinal and seasonal variations in air temperature lapse rates (Fig. 3).

2.2 Model description

We use the PC-Raster spatial–temporal modelling environment (Karssenberg et al., 2001) to model the mass balance of the major glaciers in each zone and subsequently estimate precipitation gradients required to sustain the observed mass balance. The model operates at a daily time step from 2003 until 2007 and a spatial resolution of 1 km^2. For each time step the total accumulation and total melt are aggregated over the entire glacier surface. Only glaciers with a surface area above 5 km^2 are included in the analysis (Karakoram = 232 glaciers, Hindu-Kush = 119, Himalaya = 204 glaciers) to avoid scale problems. The model is forced by the spatial precipitation and temperature fields. The precipitation fields are corrected using a precipitation gradient (PG, $\% m^{-1}$). Precipitation is positively lapsed using a PG between a reference elevation (HREF) to an elevation of maximum precipitation (HMAX). At elevations above HMAX the precipitation is negatively lapsed from its maximum at HMAX with the same PG. HREF and HMAX values are derived from literature (Table 1) including its uncertainty. HMAX varies per zone and lies at a lower elevation in the Himalayas than in the other two zones (Table 1). We spatially interpolate HMAX from the zonal values to cover the entire UIB. The melt is modelled over the glacier area using the positive degree day (PDD) method (Hock, 2005), with different degree day factors (DDF) for debris-covered (DDFd) and debris-free (DDFdf) glaciers derived from literature (Table 1). To account for uncertainty in DDF, the DDFd and DDFdf are taken into account separately in the uncertainty analysis. At temperatures below the critical temperature of 2 °C (Singh and Bengtsson, 2004; Immerzeel et al., 2013) precipitation falls in the form of snow and contributes to the accumulation. Avalanche nourishment of glaciers is a key contributor for UIB glaciers (Hewitt, 2005, 2011) and to take this process into account, we extend the glacier area with steep areas directly adjacent to the glacier with a slope over an average threshold slope (TS) of 0.2 $m m^{-1}$. This average threshold slope is derived by analyzing the slopes of all glacierised pixels in the basin (Fig. 4). To account for uncertainty in TS this parameter is taken into account in the uncertainty analysis.

For each glacier system we execute transient model runs from 2003 until 2007 and we compute the average annual mass balance from the total accumulation and melt over this period. We make two different runs for each glacier system with two different PGs (0.3 $\% m^{-1}$ and 0.6 $\% m^{-1}$) and we use the simulated mass balances of these two runs and the observed mass balances based on ICESat to optimize the PG per glacier, such that the simulated mass balance matches the observed. To interpolate the glacier-specific PG-values to PG-fields we use geostatistical conditional simula-

tion (Goovaerts, 1997) with a standardized semi-variogram. In the semi-variogram, the nugget and the range are fixed and the sill is set equal to the variance of the PGs of all glaciers. The spatial PG fields are then used in combination with a digital elevation model to generate the corrected precipitation field.

2.3 Uncertainty analysis

A rigorous uncertainty analysis is performed to take into account the uncertainty in parameter values and uncertainty in regional patterns. To account for parameter uncertainty we perform a 10 000 member Monte Carlo simulation on the parameters given in Table 1. For each run we randomly sample the parameter space based on the average (μ) and the SD (σ), which are based on literature values. For the positively-valued parameters we use a log-Gaussian distribution and a Gaussian distribution in case parameter values can be negative. We take into account uncertainty in the following key parameters (HREF, HMAX, DDFd, DDFdg, TS) for the PG as well as uncertainty in the mass balance against which the PG is optimized (MB). Based on the results of the 10 000 simulations we derive the average corrected precipitation field and the associated uncertainty in the estimates.

To account for uncertainty in spatial correlation and the presence of spatial patterns in the parameters we perform a sensitivity analysis where we consider three cases:

- fully correlated: we assume the parameters are spatially fully correlated within a zone, e.g. for each of the 10 000 simulation a parameter has the same value within a zone;
- uncorrelated: we assume the parameters are spatially uncorrelated and within each zone each glacier system is assigned a random value;
- intermediate case: we use geostatistical unconditional simulation (Goovaerts, 1997) with a standardized semi-variogram (nugget = 0, sill = variance of parameter, range = 120 km).

2.4 Validation

We estimate the average annual runoff (Q) for sub-basins in the UIB from

$$Q = P_{\text{cor}} - \text{ET} + \text{MB} \tag{2}$$

Where P_{cor} is the corrected average precipitation, ET is the average annual evapotranspiration based on the four products and MB is the glacier mass balance expressed over the sub-basin area. We then compare the estimated runoff values to the observed time series (Table 2).

3 Results and discussion

The average annual precipitation based on 10 000 conditionally simulated fields reveals a striking pattern of high altitude precipitation. The amount of precipitation required to sustain the large glacier systems is much higher than either the station observations or the gridded precipitation products imply. For the entire UIB the uncorrected average annual precipitation (Yatagai et al., 2012) for 2003–2007 is 437 mm yr^{-1} (191 $\text{km}^3\,\text{yr}^{-1}$), an underestimation of more than 200 % compared with our corrected precipitation estimate of 913 ± 323 mm yr^{-1} (399 ± 141 $\text{km}^3\,\text{yr}^{-1}$; Fig. 5). The greatest corrected annual precipitation totals in the UIB (1271 mm yr^{-1}) are observed in the elevation belt between 3750 to 4250 m compared to 403 mm yr^{-1} for the uncorrected case. In absolute terms the main water producing region is located in the elevation belt between 4250 and 4750 m where approximately 78 km^3 of rain and snow precipitates annually.

In the most extreme case, precipitation is underestimated by a factor 5 to 10 in the region where the Pamir, Karakorum and Hindu-Kush ranges intersect (Fig. 5). Our inverse modelling shows that the large glacier systems in the region can only be sustained if snowfall in their accumulation areas totals around 2000 mm yr^{-1} (Hewitt, 2007). This is in sharp contrast to precipitation amounts between 200 and 300 mm yr^{-1} that are reported by the gridded precipitation products (Fig. 1). Our results match well with the few

studies which are available. Annual accumulation values between 1000 and 3000 mm are reported for accumulation pits above 4000 m in the Karakoram (The Batura Glacier Investigation Group, 1979; Wake, 1989; Winiger et al., 2005). Our results show that the highest precipitation amounts are found along the monsoon-influenced southern Himalayan arc with values up to 3000 mm yr^{-1}, while north of the Himalayan range the precipitation decreases quickly towards a vast dry area in the north-eastern part of the UIB (Shyok sub-basin). In the north-western part of the UIB, westerly storm systems are expected to generate considerable amounts of precipitation at high altitude.

We estimated the uncertainty in the modelled precipitation field with the SD (σ) of the 10 000 realizations (Fig. 5). The signal to noise ratio is satisfactory in the entire domain, e.g. the σ is always considerably smaller than the average precipitation with an average coefficient of variation of 0.35. The largest absolute uncertainty is found along the Himalayan arc and this coincides with the precipitation pattern found here. Strikingly, the region where the underestimation of precipitation is largest, at the intersection of the three mountain ranges in the northern UIB, is also an area where the uncertainty is small even though precipitation gradients are large. By running a multiple regression analysis after optimizing the PGs we quantify the contribution of each parameter to the total uncertainty. The largest source of uncertainty in our estimate of UIB high altitude precipitation stems from the MB estimates, followed by the DDFdf, DDFd, TS, HREF and HMAX, although regional differences are considerable (Fig. 6). The MB constrains the precipitation gradients and thereby exerts a strong control on the corrected precipitation fields, in particular because the intra-zonal variation in MB is relatively large (Table 1). Thus, improved spatial monitoring techniques of the MB are expected to greatly improve precipitation estimates.

Figure 7 shows the result of uncertainty analysis associated to the spatial correlation of the parameters, which reveals that the impact on the average corrected precipitation is limited. Locally there are minor differences in the corrected precipitation amounts, but overall the magnitude and spatial patterns are similar. However, there are considerable differences in the uncertainty. The lowest uncertainty is found for the fully uncorrelated

Discussion Paper | Discussion Paper | Discussion Paper | Discussion Paper |

case, the fully correlated case has the highest uncertainty whereas the intermediate case is in between both. For the fully correlated case all glacier systems have the same parameter set for the specific realization and this results in a larger final uncertainty. In the uncorrelated case each glacier system has a different randomly sampled parameter set and this reduces the overall uncertainty as it spatially attenuates the variation in precipitation gradients.

The corrected precipitation is validated independently by a comparison to published average annual runoff data of 27 stations (Table 2). Runoff estimates based on the corrected precipitation agree well with the average observed annual runoff (Fig. 8). The runoff estimated for the uncorrected APHRODITE is consistently lower than the observed runoff, and in some occasions even negative. Runoff estimates were also made based on the ERA-INTERIM and TRMM precipitation products. The TRMM results yield a similar underestimation as the uncorrected APHRODITES product, but the runoff estimate based on the ERA-INTERIM precipitation agrees reasonably well with the observations. However the coarse resolution (70 km^2) (Fig. 1) is problematic and cannot be used to reproduce the mass balance (Fig. 9). Averaged over large catchments the precipitation may be applied for hydrological modeling, but at smaller scales there are likely very large biases. As a result, the observed glacier mass balances cannot be reproduced when the ERA-INTERIM dataset is used.

Our results reveal a strong relation between elevation and precipitation with a median PG for the entire upper Indus of 0.0989 $\% m^{-1}$, but with larger regional differences. Median precipitation gradients in the Hindu-Kush and Karakoram ranges (0.260 $\% m^{-1}$and 0.119 $\% m^{-1}$ respectively) are significantly larger than those observed in the Himalayan range, e.g 0.044 $\% m^{-1}$ (Fig. 10). In the Hindu-Kush, for example, for every 1000 m elevation rise, precipitation increases by 260 % with respect to APHRODITE, which is based on valley floor precipitation. In combination with a higher HMAX in the Hindu-Kush and the Karakoram (e.g. 5500 m vs. 4500 m in the Himalayas; Winiger et al., 2005; Hewitt, 2007; Seko, 1987; Putkonen, 2004; Immerzeel et al., 2014) this suggests that westerly airflow indeed has a higher tropospheric altitude and that the interplay

between elevation and precipitation is stronger for this type of precipitation. Further research should thus focus on the use of high resolution cloud-resolving weather models (Mölg et al., 2013) for this region to further resolve seasonal topography-precipitation interaction at both synoptic and valley scales.

4 Conclusions

In this study we inversely model high altitude precipitation in the upper Indus Basins from glacier mass balance trends derived by remote sensing. Although there are significant uncertainties, our results unambiguously show that high altitude precipitation in this region is underestimated and that the large glaciers here can only be sustained if high altitude accumulation is much higher than most commonly used gridded data products.

Our results have an important bearing on water resources management studies in the region. The observed gap between precipitation and streamflow (Immerzeel et al., 2009) (with stream flow being larger) cannot be attributed to the observed glacier mass balance (Kääb et al., 2012), but is most likely the result of an underestimation of precipitation, as also follows from this study. With no apparent decreasing trends in precipitation (Archer and Fowler, 2004) the observed negative trends in stream flow in the glacierised parts of the UIB should thus be primarily attributed to decreased glacier and snow melt (Sharif et al., 2013) and increased glacier storage (Gardelle et al., 2012). In a recent study the notion of of negative trends in UIB runoff was contested and based on a recent analysis (1985–2010) it was concluded that runoff of Karakoram rivers is increasing (Mukhopadhyay and Khan, 2014a). The study suggests that increase glacier melt during summer is the underlying reason, which in combination with positive precipitation trends in summer does not contradict the neutral glacier mass balances in the region. From all of these studies it becomes apparent that precipitation is the key to understanding behavior of glacier and hydrology at large in the UIB. The precipitation we estimate in this study differs considerably, in magnitude and spatial distribution, from datasets that are commonly used in design of reservoirs for hydropower and irrigation and as such it may have a significant impact and improve such planning processes.

The water resources of the Indus River play an important geopolitical role in the region, and our results could contribute to the provision of independent estimates of UIB precipitation. We conclude that the water resources in the UIB are even more important and abundant than previously thought. Most precipitation at high altitude is now stored in the glaciers, but when global warming persists and the runoff regime becomes more rain dominated, the downstream impacts of our findings will become more evident.

Acknowledgements. This study was funded by the Netherlands Organization for Scientific Research through their VENI program and user support program for space research and by the UK Department for International Development (DFID). This study was also partially supported by core funds of ICIMOD contributed by the governments of Afghanistan, Australia, Austria, Bangladesh, Bhutan, China, India, Myanmar, Nepal, Norway, Pakistan, Switzerland, and the UK. The views and interpretations in this publication are those of the authors and are not necessarily attributable to ICIMOD. The authors acknowledge the Pakistan Meteorological Department and the Pakistan Water and Power Development Authority for providing meteorological and hydrological data. The authors are grateful to Andreas Kääb for calculating the zonal mass balances based on the IceSat data, to Rianne Giesen for organizing the glacier mass balance data, to Samjwal Bajracharya for providing the glacier boundaries and to Philip Kraaijenbrink for assisting with the figures.

References

Archer, D.: Contrasting hydrological regimes in the upper Indus Basin, J. Hydrol., 274, 198–210, doi:10.1016/S0022-1694(02)00414-6, 2003. 4774

Archer, D.R. and Fowler, H.J.: Spatial and temporal variations in precipitation in the Upper Indus Basin, global teleconnections and hydrological implications, Hydrol. Earth Syst. Sci., 8, 47–61, doi:10.5194/hess-8-47-2004, 2004. 4766

Azam, M. F., Wagnon, P., Ramanathan, A., Vincent, C., Sharma, P., Arnaud, Y., Linda, A., Pottakkal, J. G., Chevallier, P., Singh, V. B., and Berthier, E.: From balance to imbalance:

a shift in the dynamic behaviour of Chhota Shigri glacier, western Himalaya, India, J. Glaciol., 58, 315–324, doi:10.3189/2012JoG11J123, 2012. 4773

Bajracharya, S. and Shrestha, B.: The Status of Glaciers in the Hindu Kush-Himalayan Region, Tech. rep., ICIMOD, Kathmandu, 2011. 4759

Barros, A. P., Kim, G., Williams, E., and Nesbitt, S. W.: Probing orographic controls in the Himalayas during the monsoon using satellite imagery, Nat. Hazards Earth Syst. Sci., 4, 29–51, doi:10.5194/nhess-4-29-2004, 2004. 4757

Bastiaanssen, W. G. M., Cheema, M. J. M., Immerzeel, W. W., Miltenburg, I. J., and Pelgrum, H.: Surface energy balance and actual evapotranspiration of the transboundary Indus Basin estimated from satellite measurements and the ETLook model, Water Resour. Res., 48, W11512, doi:10.1029/2011WR010482, 2012. 4760

Bookhagen, B. and Burbank, D. W.: Topography, relief, and TRMM-derived rainfall variations along the Himalaya, Geophys. Res. Lett., 33, 1–5, doi:10.1029/2006GL026037, 2006. 4757

Dee, D. P., Uppala, S. M., Simmons, A. J., Berrisford, P., Poli, P., Kobayashi, S., Andrae, U., Balmaseda, M. A., Balsamo, G., Bauer, P., Bechtold, P., Beljaars, A. C. M., van de Berg, L., Bidlot, J., Bormann, N., Delsol, C., Dragani, R., Fuentes, M., Geer, A. J., Haimberger, L., Healy, S. B., Hersbach, H., Hólm, E. V., Isaksen, L., Kå llberg, P., Köhler, M., Matricardi, M., McNally, A. P., Monge-Sanz, B. M., Morcrette, J.-J., Park, B.-K., Peubey, C., de Rosnay, P., Tavolato, C., Thépaut, J.-N., and Vitart, F.: The ERA-Interim reanalysis: configuration and performance of the data assimilation system, Q. J. Roy. Meteor. Soc., 137, 553–597, doi:10.1002/qj.828, 2011. 4757, 4759, 4775

Gardelle, J., Berthier, E., and Arnaud, Y.: Slight mass gain of Karakoram glaciers in the early twenty-first century, Nat. Geosci., 5, 322–325, doi:10.1038/ngeo1450, 2012. 4766

Goovaerts, P.: Geostatistics for Natural Resources Evaluation, Oxford University Press, New York – Oxford, 1997. 4758, 4762

Hagg, W., Mayer, C., Lambrecht, A., and Helm, A.: Sub-debris melt rates on southern Inylchek Glacier, central Tian Shan, Geogr. Ann. A, 90, 55–63, doi:10.1111/j.1468-0459.2008.00333.x, 2008. 4773

Harper, J. T.: High altitude Himalayan climate inferred from glacial ice flux, Geophys. Res. Lett., 30, 3–6, doi:10.1029/2003GL017329, 2003. 4757, 4758

Hewitt, K.: The Karakoram anomaly? Glacier expansion and the 'elevation effect,' Karakoram Himalaya, Mt. Res. Dev., 25, 332–340, doi:10.1659/0276-4741(2005)025[0332:TKAGEA]2.0.CO;2, 2005. 4757, 4761

Hewitt, K.: Tributary glacier surges: an exceptional concentration at Panmah Glacier, Karakoram Himalaya, J. Glaciol., 53, 181–188, doi:10.3189/172756507782202829, 2007. 4757, 4763, 4765, 4773
Hewitt, K.: Glacier change, concentration, and elevation effects in the Karakoram Himalaya, upper Indus Basin, Mt. Res. Dev., 31, 188–200, doi:10.1659/MRD-JOURNAL-D-11-00020.1, 2011. 4761, 4773
Hewitt, K.: The regional context, in: Glaciers of the Karakoram Himalaya, chap. 1, Springer, Dordrecht, 1–33, doi:10.1007/978-94-007-6311-1, 2013. 4757
Hock, R.: Glacier melt: a review of processes and their modelling, Prog. Phys. Geog., 29, 362–391, doi:10.1191/0309133305pp453ra, 2005. 4761
Huffman, G. J., Adler, R. F., Bolvin, D. T., Gu, G., Nelkin, E. J., Bowman, K. P., Hong, Y., Stocker, E. F., and Wolff, D. B.: The TRMM Multisatellite Precipitation Analysis (TMPA): quasi-global, multiyear, combined-sensor precipitation estimates at fine scales, J. Hydrometeorol., 8, 38–55, doi:10.1175/JHM560.1, 2007. 4757, 4775
Immerzeel, W. W. and Bierkens, M. F. P.: Asia's water balance, Nat. Geosci., 5, 841–842, doi:10.1038/ngeo1643, 2012. 4756
Immerzeel, W., Droogers, P., De Jong, S. M., and Bierkens, M.: Large-scale monitoring of snow cover and runoff simulation in Himalayan river basins using remote sensing, Remote Sens. Environ., 113, 40–49, doi:10.1016/j.rse.2008.08.010, 2009. 4756, 4766
Immerzeel, W., Van Beek, L., and Bierkens, M.: Climate change will affect the Asian water towers, Science, 328, 1382–1385, doi:10.1126/science.1183188, 2010. 4756
Immerzeel, W., Beek, L. P. H., Konz, M., Shrestha, A. B., and Bierkens, M. F. P.: Hydrological response to climate change in a glacierized catchment in the Himalayas, Climatic Change, 110, 721–736, doi:10.1007/s10584-011-0143-4, 2012a. 4773
Immerzeel, W. W., Pellicciotti, F., and Shrestha, A. B.: Glaciers as a proxy to quantify the spatial distribution of precipitation in the Hunza Basin, Mt. Res. Dev., 32, 30–38, doi:10.1659/MRD-JOURNAL-D-11-00097.1, 2012b. 4758
Immerzeel, W., Pellicciotti, F., and Bierkens, M.: Rising river flows throughout the twenty-first century in two Himalayan glacierized watersheds, Nat. Geosci., 6, 742–745, doi:10.1038/NGEO1896, 2013. 4757, 4761, 4773
Immerzeel, W., Petersen, L., Ragettli, S., and Pellicciotti, F.: The importance of observed gradients of air temperature and precipitation for modeling runoff from a glacierised watershed in

the Nepalese Himalayas, Water Resour. Res., 50, 2212–2226, doi:10.1002/2013WR014506, 2014. 4757, 4765, 4773
Kääb, A., Berthier, E., Nuth, C., Gardelle, J., and Arnaud, Y.: Contrasting patterns of early twenty-first-century glacier mass change in the Himalayas, Nature, 488, 495–498, doi:10.1038/nature11324, 2012. 4758, 4759, 4760, 4766, 4773
Karssenberg, D., Burrough, P. A., Sluiter, R., and de Jong, K.: The PCRaster software and course materials for teaching numerical modelling in the environmental sciences, Transactions in GIS, 5, 99–110, doi:10.1111/1467-9671.00070, 2001. 4760
Khattak, M., Babel, M., and Sharif, M.: Hydro-meteorological trends in the upper Indus River Basin in Pakistan, Clim. Res., 46, 103–119, doi:10.3354/cr00957, 2011. 4774
Koster, R., Suarez, M., Ducharne, A., Stieglitz, M., and Kumar, P.: A catchment-based approach to modeling land surface processes in a general circulation model structure, J. Geophys. Res., 105, 24809–24822, 2000. 4759
Lutz, A. F., Immerzeel, W. W., Shrestha, A. B., and Bierkens, M. F. P.: Consistent increase in High Asia's runoff due to increasing glacier melt and precipitation, Nat. Clim. Change, 4, 1–6, doi:10.1038/NCLIMATE2237, 2014. 4756
Mihalcea, C., Mayer, C., Diolaiuti, G., Lambrecht, A., Smiraglia, C., and Tartari, G.: Ice ablation and meteorological conditions on the debris-covered area of Baltoro Glacier, Karakoram, Pakistan, Ann. Glaciol., 43, 292–300, 2006. 4773
Mishra, V.: Climatic uncertainty in Himalayan Water Towers, J. Geophys. Res.-Atmos., doi:10.1002/2014JD022650, in press, 2015. 4757
Mölg, T., Maussion, F., and Scherer, D.: Mid-latitude westerlies as a driver of glacier variability in monsoonal High Asia, Nat. Clim. Change, 4, 68–73, doi:10.1038/nclimate2055, 2013. 4757, 4766
Mukhopadhyay, B. and Khan, A.: Rising river flows and glacial mass balance in central Karakoram, J. Hydrol., 513, 191–203, 2014a. 4766
Mukhopadhyay, B. and Khan, A.: A quantitative assessment of the genetic sources of the hydrologic flow regimes in upper Indus Basin and its significance in a changing climate, J. Hydrol., 509, 549–572, doi:10.1016/j.jhydrol.2013.11.059, 2014b. 4774
Nicholson, L. and Benn, D.: Calculating ice melt beneath a debris layer using meteorological data, J. Glaciol., 52, 463–470, doi:10.3189/172756506781828584, 2006. 4773

Discussion Paper | Discussion Paper | Discussion Paper | Discussion Paper |

Putkonen, J. K.: Continuous snow and rain data at 500 to 4400 m altitude near Annapurna, Nepal, 1991–2001, Arct. Antarct. Alp. Res., 36, 244–248, doi:10.1657/1523-0430(2004)036, 2004. 4765, 4773

Ragettli, S. and Pellicciotti, F.: Calibration of a physically based, spatially distributed hydrological model in a glacierized basin: on the use of knowledge from glaciometeorological processes to constrain model parameters, Water Resour. Res., 48, 1–20, doi:10.1029/2011WR010559, 2012. 4757

Rienecker, M. M., Suarez, M. J., Gelaro, R., Todling, R., Bacmeister, J., Liu, E., Bosilovich, M. G., Schubert, S. D., Takacs, L., Kim, G.-K., Bloom, S., Chen, J., Collins, D., Conaty, A., da Silva, A., Gu, W., Joiner, J., Koster, R. D., Lucchesi, R., Molod, A., Owens, T., Pawson, S., Pegion, P., Redder, C. R., Reichle, R., Robertson, F. R., Ruddick, A. G., Sienkiewicz, M., and Woollen, J.: MERRA: NASA's Modern-Era Retrospective Analysis for Research and Applications, J. Climate, 24, 3624–3648, doi:10.1175/JCLI-D-11-00015.1, 2011. 4759

Scherler, D., Bookhagen, B., and Strecker, M. R.: Spatially variable response of Himalayan glaciers to climate change affected by debris cover, Nat. Geosci., 4, 156–159, doi:10.1038/ngeo1068, 2011. 4757

Seko, K.: Seasonal variation of altitudinal dependence of precipitation in Langtang Valley, Nepal Himalayas, Bulletin of Glacier Research, 5, 41–47, 1987. 4765, 4773

Sharif, M., Archer, D. R., Fowler, H. J., and Forsythe, N.: Trends in timing and magnitude of flow in the Upper Indus Basin, Hydrol. Earth Syst. Sci., 17, 1503–1516, doi:10.5194/hess-17-1503-2013, 2013. 4766, 4774

Singh, P. and Bengtsson, L.: Hydrological sensitivity of a large Himalayan basin to climate change, Hydrol. Process., 18, 2363–2385, doi:10.1002/hyp.1468, 2004. 4761

The Batura Glacier Investigation Group: The Batura glacier in the Karakoram mountains and its variations, Sci. Sinica, 22, 958–974, 1979. 4764

Wada, Y., Wisser, D., and Bierkens, M. F. P.: Global modeling of withdrawal, allocation and consumptive use of surface water and groundwater resources, Earth Syst. Dynam., 5, 15–40, doi:10.5194/esd-5-15-2014, 2014. 4760

Wake, C.: Glaciochemical investigations as a tool to determine the spatial variation of snow accumulation in the central Karakoram, Northern Pakistan, Ann. Glaciol., 13, 279–284, 1989. 4764

Winiger, M., Gumpert, M., and Yamout, H.: Karakorum-Hindukush-western Himalaya: assessing high-altitude water resources, Hydrol. Process., 19, 2329–2338, doi:10.1002/hyp.5887, 2005. 4757, 4764, 4765, 4773

Yao, T., Thompson, L., Yang, W., Yu, W., Gao, Y., Guo, X., Yang, X., Duan, K., Zhao, H., Xu, B., Pu, J., Lu, A., Xiang, Y., Kattel, D. B., and Joswiak, D.: Different glacier status with atmospheric circulations in Tibetan Plateau and surroundings, Nat. Clim. Change, 2, 663–667, doi:10.1038/nclimate1580, 2012. 4757

Yasutomi, N., Hamada, A., and Yatagai, A.: Development of a long-term daily gridded temperature dataset and its application to rain/snow discrimination of daily precipitation, Global Environ. Res., 3, 165–172, 2011. 4760, 4777

Yatagai, A., Yasutomi, N., Hamada, A., Kitoh, A., Kamiguchi, K., and Arakawa, O.: APHRODITE: constructing a long-term daily gridded precipitation dataset for Asia based on a dense network of rain gauges, Geophysical Research Abstracts, 14, 1401–1415, 2012. 4757, 4760, 4763, 4775

Discussion Paper | Discussion Paper | Discussion Paper | Discussion Paper |

Table 1. Averages (μ) and SDs (σ) of predictors for the precipitation gradient. Values and ranges are based on literature as follows: HREF, HMAX: (Seko, 1987; Putkonen, 2004; Winiger et al., 2005; Hewitt, 2007, 2011; Immerzeel et al., 2012a, 2014), DDF_d, DDF_{df} (Mihalcea et al., 2006; Nicholson and Benn, 2006; Hagg et al., 2008; Azam et al., 2012; Immerzeel et al., 2013), MB (Kääb et al., 2012).

Variable	Acronym	Distribution	μ	σ
Reference elevation (m)	HREF	log-Gaussian	2500	500
Maximum elevation (m)	HMAX	log-Gaussian		
Himalayas			4500	500
Karakoram			5500	500
Hindu-Kush			5500	500
Degree day factor debris (mm °C^{-1} day^{-1})	DDF_d	log-Gaussian	2	2
Degree day factor debris free (mm °C^{-1} day^{-1})	DDF_{df}	log-Gaussian	7	2
Threshold slope (m m^{-1})	TS	log-Gaussian	0.2	0.05
Mass balance (m w.e. yr^{-1})	MB	Gaussian		
Himalayas			−0.49	0.57
Karakoram			−0.21	0.76
Hindu-Kush			−0.07	0.61

Table 2. Runoff stations used for validation. Catchment areas are delineated based on SRTM DEM.

Station	LAT	LON	Area (km^2)	Observed Q (m^3 s^{-1})	Period
Besham Qila[a]	34.906	72.866	198 741	2372.2	2003–2007
Tarbela inflow[a]	34.329	72.856	203 014	2370.3	2003–2007
Mangla inflow[a]	33.200	73.650	29 966	831.8	2003–2007
Marala inflow[a]	32.670	74.460	29 611	956.5	2003–2007
Dainyor bridge[a]	35.925	74.372	14 147	331.8	1966–2004
Skardu – Kachura[b]	35.435	75.468	146 200	1074.2	1970–2010
Partab Bridge[b]	35.767	74.597	177 622	1787.9	1962–2009
Yogo[b]	35.183	76.100	64 240	359.4	1973–2010
Kharmong[b]	34.933	76.217	70 875	452.3	1982–2010
Gilgit[b]	35.933	74.300	13 174	286.7	1980–2010
Doyian[b]	35.550	74.700	4000	135.7	1974–2009
Chitral[c]	35.867	71.783	12 824	271.9	1964–1996
Kalam[c]	35.467	72.600	2151	89.6	1961–1997
Naran[c]	34.900	73.650	1181	48.1	1960–1998
Alam bridge[b]	35.767	74.600	28 201	644.0	1966–2010
Chakdara[c]	34.650	72.017	5990	178.9	1961–1997
Karora[c]	34.900	72.767	586	21.2	1975–1996
Garhi Habibullah[c]	34.450	73.367	2493	101.8	1960–1998
Muzafferabad[c]	34.430	73.486	7604	357.0	1963–1995
Chinari[c]	34.158	73.831	14 248	330.0	1970–1995
Kohala[c]	34.095	73.499	25 820	828.0	1965–1995
Kotli[c]	33.525	73.890	2907	134.0	1960–1995
Shigar[b]	35.422	75.732	6681	202.6	1985–1998
Phulra[d]	34.317	73.083	1106	19.2	1969–1996
Daggar[d]	34.500	72.467	534	6.9	1969–1996
Warsak[e]	34.100	71.300	74 092	593.0	1967–2005
Shatial Bridge[b]	35.533	73.567	189 263	2083.2	1984–2009

[a]: Calculated based on discharge provided by the Pakistan Water and Power Development (WAPDA).
[b]: Based on Mukhopadhyay and Khan (2014b).
[c]: Based on Sharif et al. (2013).
[d]: Based on Archer (2003).
[e]: Based on Khattak et al. (2011).

Discussion Paper | Discussion Paper | Discussion Paper | Discussion Paper |

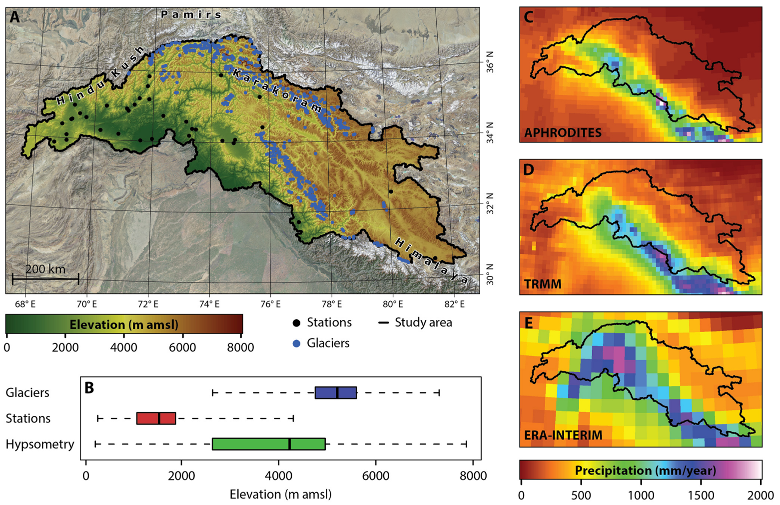

Figure 1. Overview of the UIB, basin hypsometry and three gridded precipitation products. **(a)** shows the digital elevation model and the location of the major glacier systems (area > 5 km^2) and the available stations in the Global Summary of the Day (GSOD) of the World Meteorological Organization (WMO). **(b)** shows boxplots of the elevation distribution of the basin, the large glacier systems and the GSOD stations. (**c** to **e**) show the average gridded annual precipitation between 1998–2007 for the APHRODITE (Yatagai et al., 2012), TRMM (Huffman et al., 2007) and ERA-INTERIM (Dee et al., 2011) datasets.

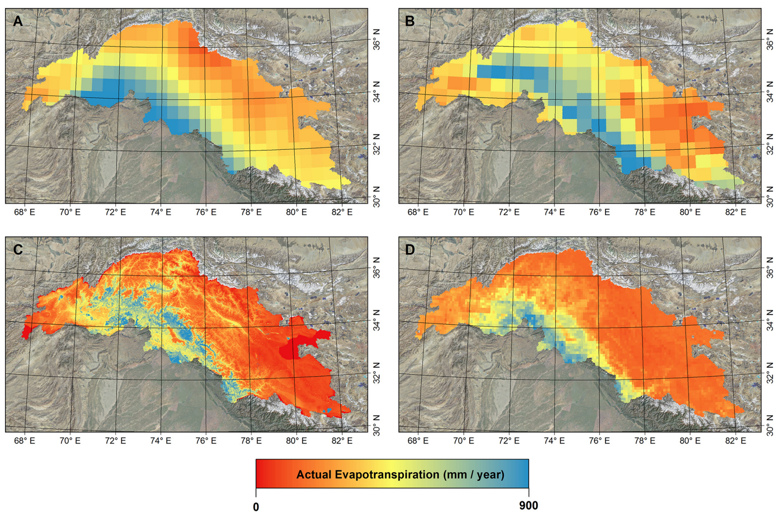

Figure 2. Average annual actual evapotranspiration between 2003 and 2007 for ERA-Interim **(a)**, MERRA **(b)**, ET-Look **(c)** and PCRGLOB-WB **(d)**.

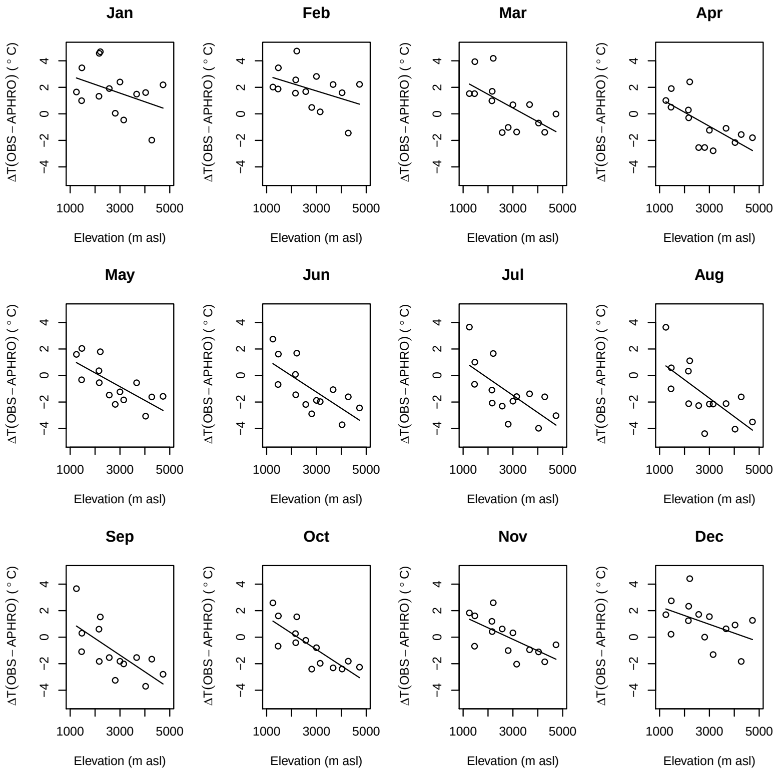

Figure 3. Monthly relation between observed temperatures at meteorological stations (OBS) and the APHRODITE temperature fields (APHRO) (Yasutomi et al., 2011).

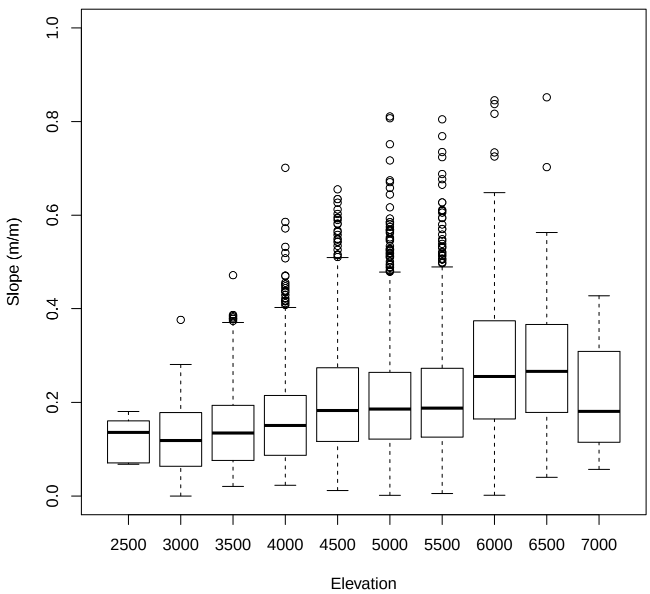

Figure 4. Boxplots of slopes of glacierised areas per elevation bin.

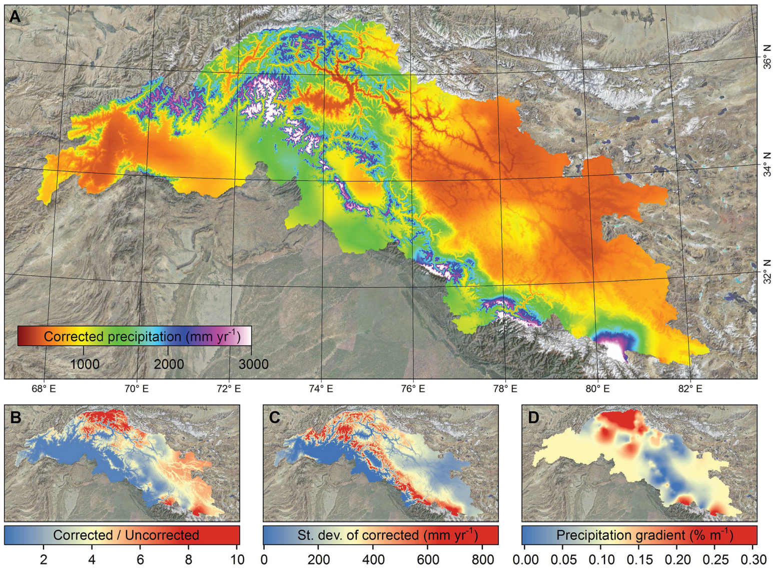

Figure 5. Corrected precipitation and estimated uncertainty for the UIB for the case with intermediate spatial correlation between model parameters. **(a)** shows the average modelled precipitation field based on 10 000 simulations for the period 2003–2007, **(b)** shows the ratio of corrected precipitation to the uncorrected APHRODITE precipitation for the same period, **(c)** shows the SD of the 10 000 simulations and **(d)** shows the average precipitation gradient.

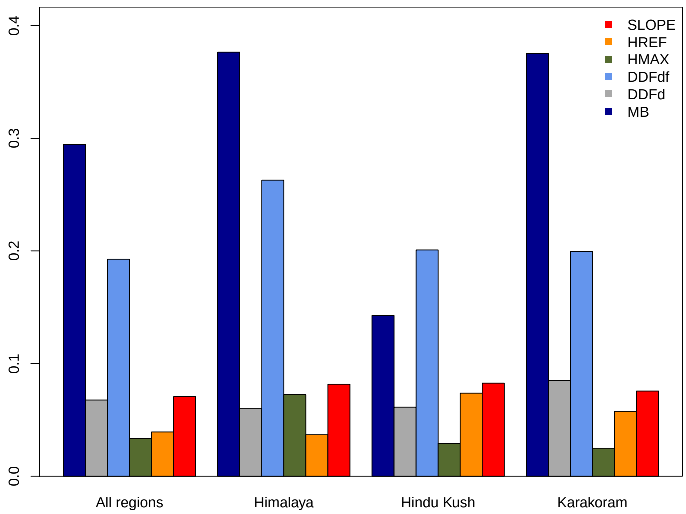

Figure 6. Normalized weights of multiple regression of the precipitation gradients by the predictors slope (slope threshold for avalanching to contribute to accumulation), HREF (base elevation from which lapsing starts), HMAX (elevation with peak precipitation), DDFd (degree day factor for debris covered glaciers), DDFdf (degree day factor for debris free glaciers) and the MB (mass balance of the glacier).

Discussion Paper | Discussion Paper | Discussion Paper | Discussion Paper |

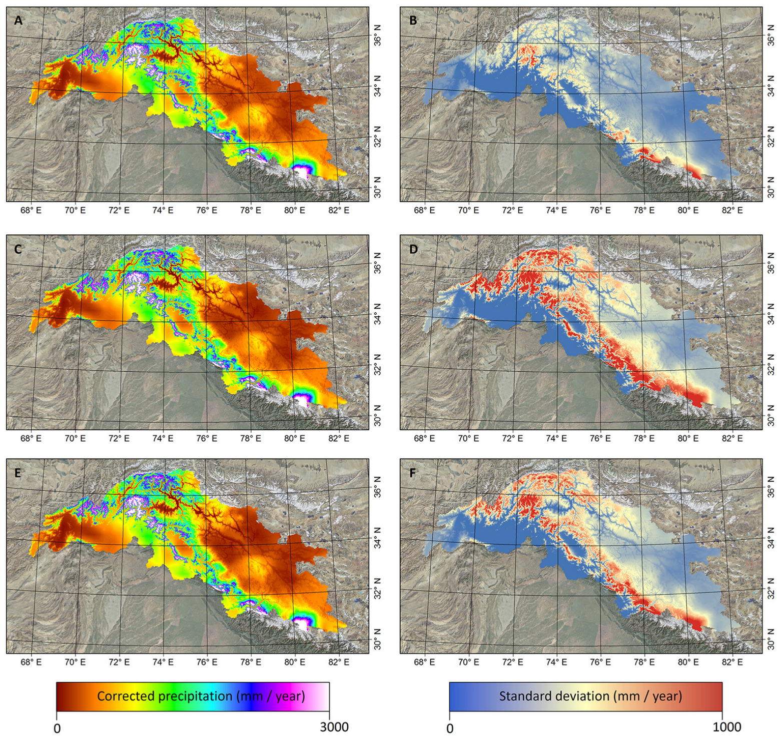

Figure 7. Impact of spatial correlation of parameters on the corrected precipitation field and associated uncertainty. The top panels show the corrected precipitation field **(a)** and uncertainty **(b)** for the fully uncorrelated case. The middle panels **(d, e)** for the fully correlated case and the bottom panels **(e, f)** for the intermediate case.

Discussion Paper | Discussion Paper | Discussion Paper | Discussion Paper |

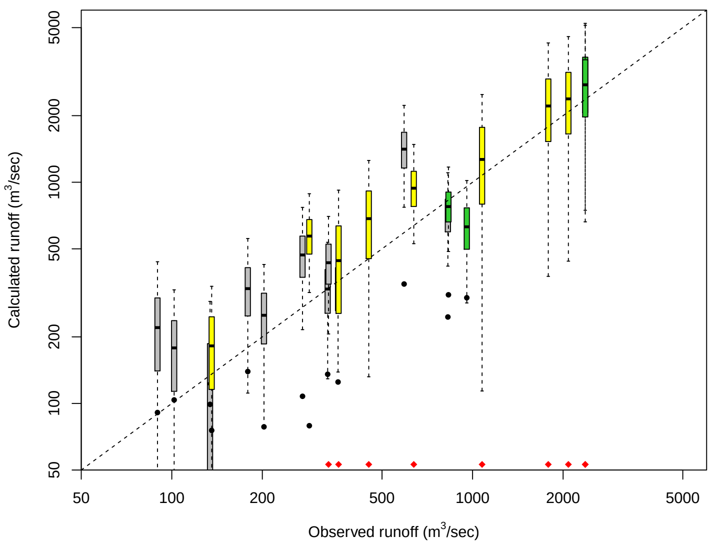

Figure 8. Validation of the precipitation correction using observed discharge (Table 2). The box plots are based on the runoff estimate based on 10 000 corrected precipitation fields (grey: stations for which the observed record does not coincide with the 2003–2007 period, yellow: stations for which the 2003–2007 period is part of the observational record, green: stations for which the observations are based precisely on the 2003–2007 period). The black dots and red diamonds (estimated runoff below 50 $m^3 s^{-1}$) show the estimated runoff based on the uncorrected precipitation.

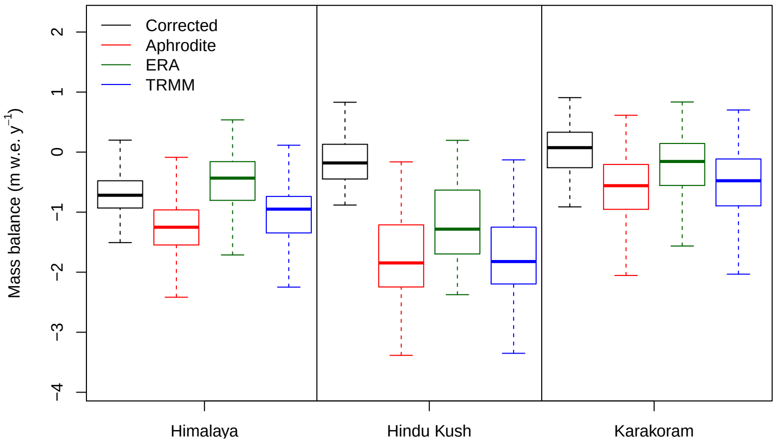

Figure 9. Reconstructed mass balances based on the corrected, APHRODITE, ERA-INTERIM and TRMM datasets. The black horizontal dotted line shows the observed mass balance for each zone.

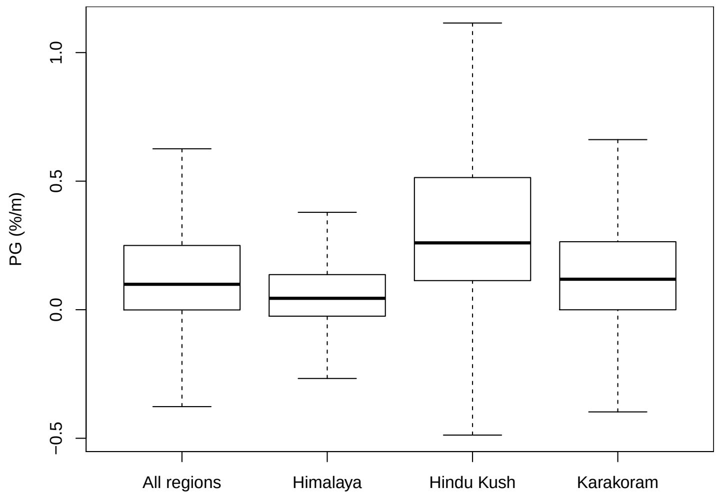

Figure 10. Box plots of precipitation gradients for the entire UIB and for the three regions separately

ANNEX 2: MANUAL PLUVIOMETER

MANUAL:
PLUVIOMETER WITH
SATELLITE CONNECTION

Contents

TOOLS & CABLES:

Wrenches: 10 mm, 11 mm, 13 mm

Small adjustable wrench

Allen key: 8

Screwdrivers: big head screwdriver

Small slotted screwdriver (Campbell)

Measuring tape

Rubber/ piece of bike tube

Cable ties / wire straps

Vulcanizing tape

Spare screws

Mason's level

Key for data logger box

Water pliers

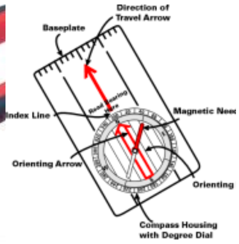

Compass

CABLES:

- USB to serial adapter (make sure you have installed the driver for the adapter)
- Cable to connect logger to laptop (RS232) – serial to serial (female to male)
- Ethernet cable
- Cable to connect antenna to the datalogger (***This cable should never be bent too much!)***
- UDG device and Temperature device cables (These are already attached to the datalogger box)

LOWER STRUCTURE PLUVIOMETER

Goal

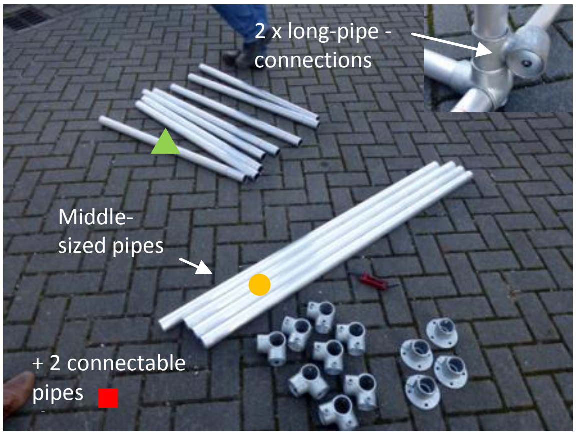

Pieces needed

Fix 90°-connection parts and feet to the middle-sized pipes (Allen key 8)

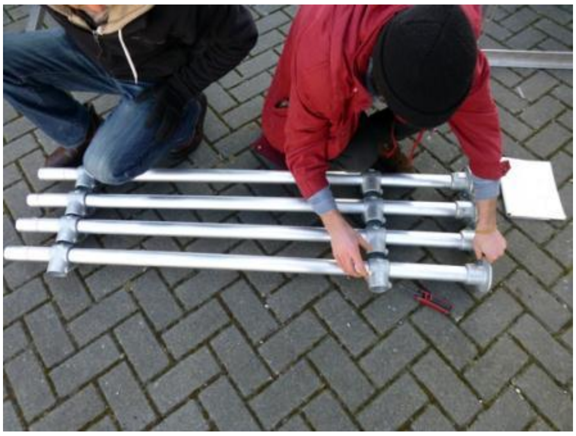

They should all be at the same height in a dist. of 1 m. Leave all connections 'loose' for now so that you can adjust the whole structure later!

Build 2 rectangle structures out of 2 middle-sized and 2 short pipes each

…

…

Attach 4 short pipes to one of the structures

Put 2 long- pipe- connection parts on opposite sides – see also next picture

Put the other frame on top and adjust, tighten everything. Orange circle: Long-pipe-connection parts

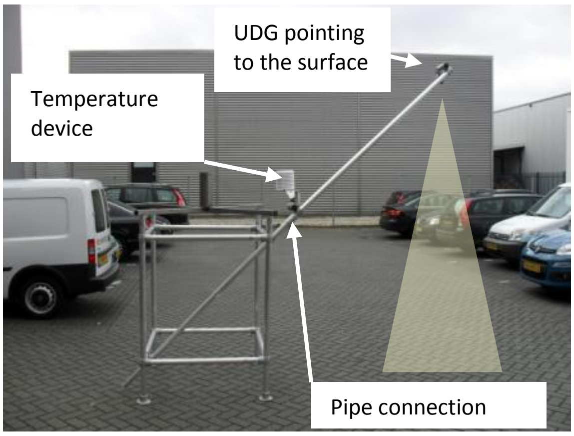

Goal: Long pipe with temperature sensor and UDG

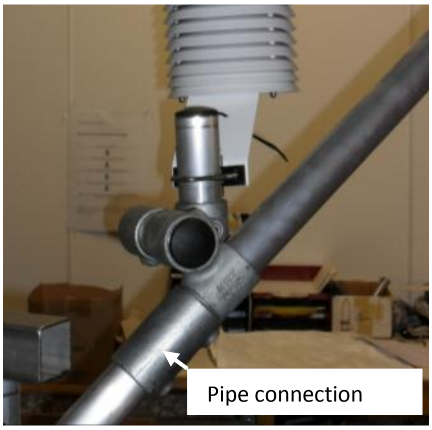

First connect the two longest pipes to one long pipe. Before attaching the long pipe to the lower structure mount the temperature device right next to the pipe connection

(picture from a different pluviometer) To install the temperature sensor in the shield remove the plastic nut below

(picture from a different pluviometer) Attach the black element to the sensor, put the sensor inside the shield an fix the plastic nut again

...

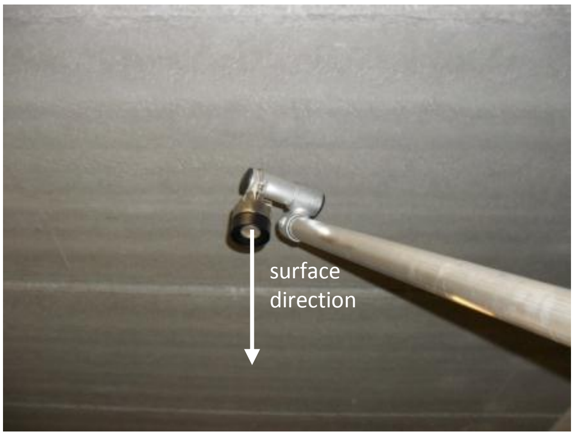

Attach the UDG device to the end of the pipe on the same side of the pipe connection as the temperature sensor

(picture from a different pluviometer) Connect the UDG cable to the UDG device and fix the cable with a cable strap at the long pipe

Attach the long pipe with the attached sensors to the lower structure (sensors are not attached in this picture)

... (sensors are not attached in this picture)

CROSS STEEL STRUCTURE


Place the steel structure with the cylinder on top


If it does not fit, loosen some of the corner connections of the lower structure to make it fit and then tighten everything again

UPPER STRUCTURE PLUVIOMETER


Goal


Screws

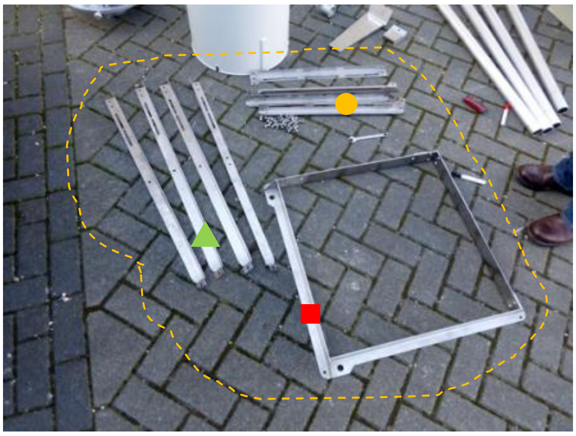
Pieces needed


Put the frame on the floor and attach the 4 long pieces to the corners of the frame (wrench 13). Make sure that all the pieces marked with box which have extra holes are together on one side as in the big picture below.

Attach 3 short pieces on the outsides leave 1 piece opposite to where the box belongs out for now to later place the weighing system and the bucket!

Circles: extra holes, Orange rectangle: where the box belongs

FIX UPPER STRUCTURE TO LOWER STRUCTURE

Place the upper structure on the lower structure

Screws

Match the marked parts

Attach with 4 long screws

Tighten everything and fix the whole structure with rocks etc. to make it stable before you put the weighing system! It should be more or less leveled already (check with **Mason's level)*!***

MOUNT THE BOX

Attach the data logger box (without battery!) with 4 long screws

Screws

MOUNT THE PRECEPITATION BALANCE

Put the cable through the steel cylinder

…

Place the weighing system on the steel cylinder

Put the cable from below through the cylinder and out

Hand tighten upper screws around the cylinder

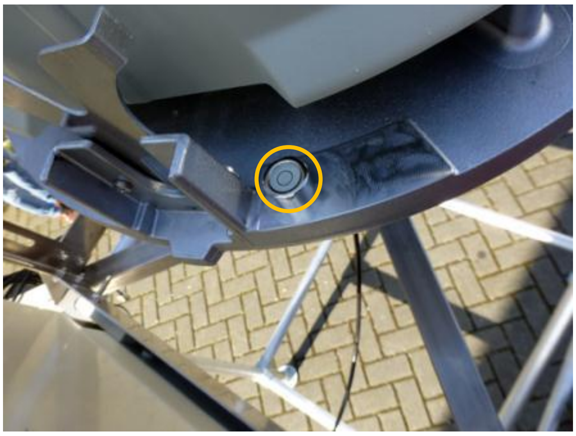

Level and fix the system with the lower screws around the cylinder, the bubble should be in the middle

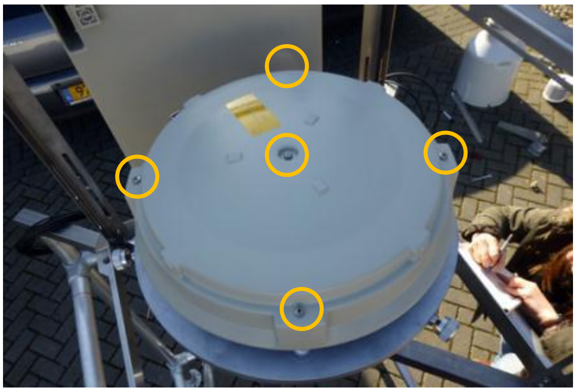

Remove the 4 transportation screws and the one in the middle (head screwdriver)

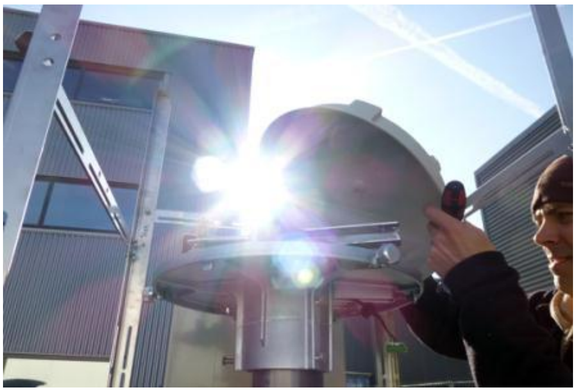

Remove the top

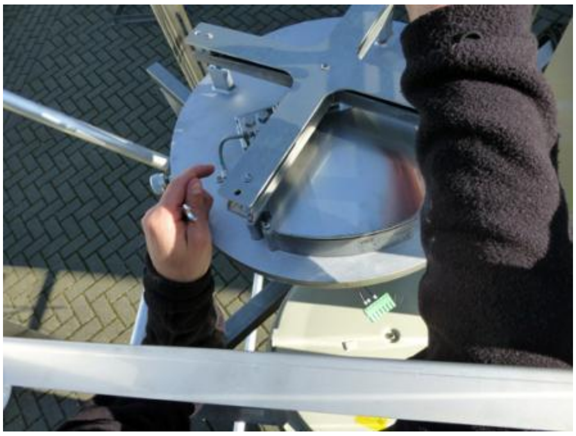

Remove the small metal plate without removing the screws completely

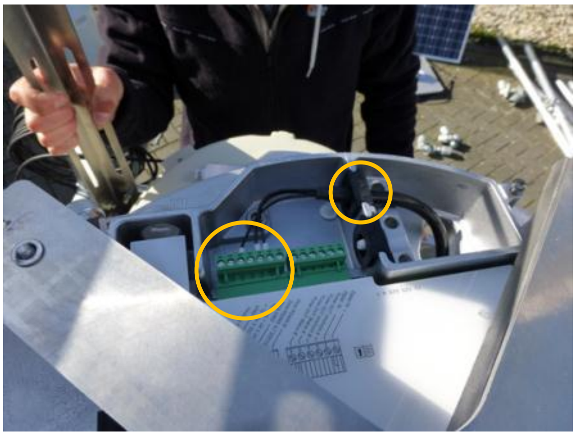

Plug the cable and fix the rubber cable stabilizer

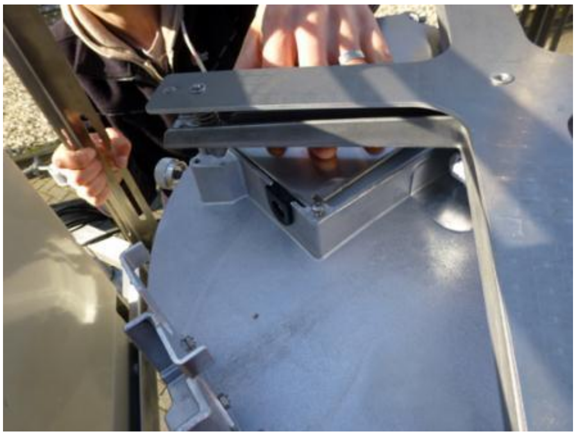

Attach the small metal plate back again

Put the plastic top back (it only fits one way) and attach the middle screw - **DO NOT ATTACH AGAIN THE 4 TRASPORT SCREWS ON THE OUTSIDE!**

Place plastic bucket on top of the weighing system

Place the plastic cylinder on top and tighten the hand screws

Attach the last bar of the upper structure

THE WIND SHIELD

Goal

Screws

Attach all wind flaps in the right order with the small screws

…

Put the whole wind shield on top of the structure and attach it with the hand screws from the inside to the upper structure

One person can go on top, one person should step on the structure on the opposite site to balance out the weight!

Recheck if the balance is still leveled out

MOUNT THE SOLAR PANEL / ANTENNA STRUCTURE

Goal

4 long pipes each with two connection pieces and a foot
2 middle-sized pipes, 90 cm
2 small pipes, 65 cm
1 pipe 75 cm

If not already adjusted fix the connection pieces to each of the long pipes like in the picture depicted
Tighten everything loose until you can fit the whole structure!

Build two A on the floor out of 2 long pipes and 1 middle-sized pipe each. Place the two small pipes on top of one A and tighten a bit

Put the second A on top

Adjust everything to make it fit

Add the solar panel with the 75 cm pipe

Attach the arm for the antenna on the side of the structure with the U-connections, the arm should look up (wrench 10 and 11)

Put some rubber between the connection pieces and the tube to prevent sliding along the pipe!

SOLAR PANEL CABLE & ANTENNA CABLE

Attach the cable (***The cable should never be bent too much!)*** to the antenna, pull it through the big hole on the bottom of the data logger box and connect it to the modem. **Put vulcanizing tape around the connection of the antenna**

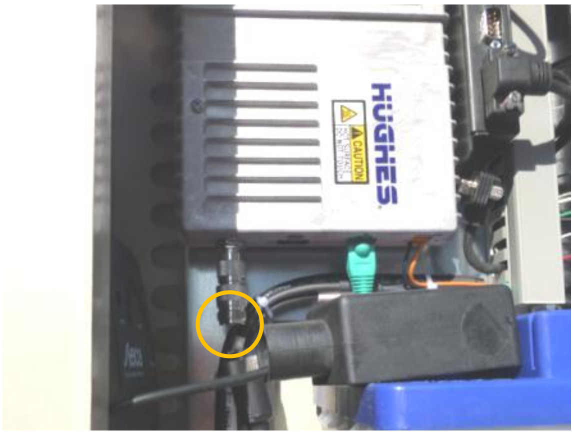

Orange circle: where to connect the antenna to the modem

Pull the solar panel cable through the hole on the bottom of the data logger box and attach the cables to the solar charge controller (little Campbell screw driver):
Positive – red (on the left)
Negative – blue (on the right)

CONNECT TEMPERATURE SENS. & UDG CABLE

The cable of the UDG and temperature sensor are already connected to the datalogger. They just need to be strapped to the frame and the temperature sensor needs to be inserted into the radiation shield and the UDG connected to the cable.

CONNECT THE BATTERY

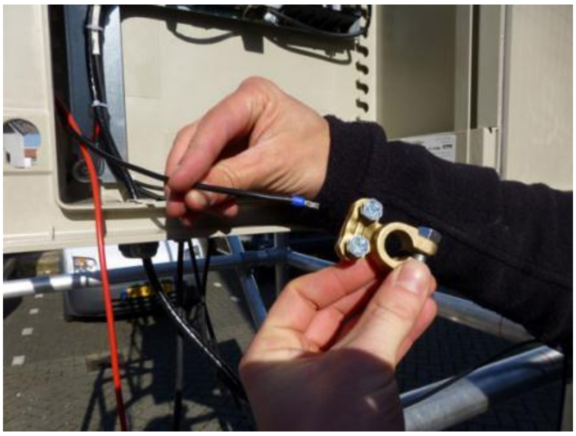

Attach battery adapters if possible – If the battery has a different connection system make sure the connections are tight!

Place the battery in the data logger box
Attach the cables to the battery and put the rubber caps on top
Negative – black (on the left)

Positive – red (on the right)

…

CLEAN UP ALL CABLES WITH CABLE TIES / WIRE STRAPS!

TEST SATELLITE CONNECTION / ANTENNA ALIGNMENT

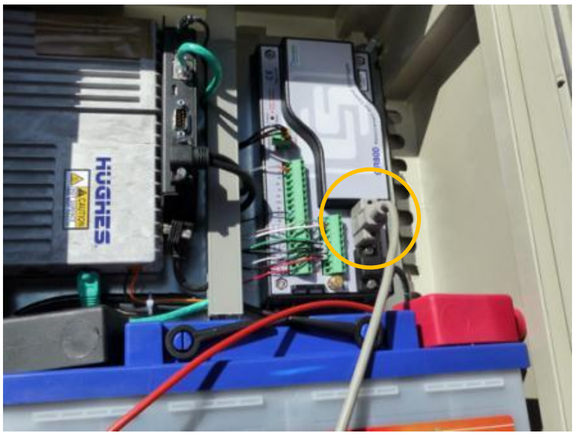

Connect the data logger to the laptop (with cable and USB-to-serial adapter, make sure you have installed the driver for the adapter)

Start the software PC200W
- Add the data logger device: add ComPort, PakbusPort, CR800series
- Select ComPort, apply
- Send the new datalogger program first!!!

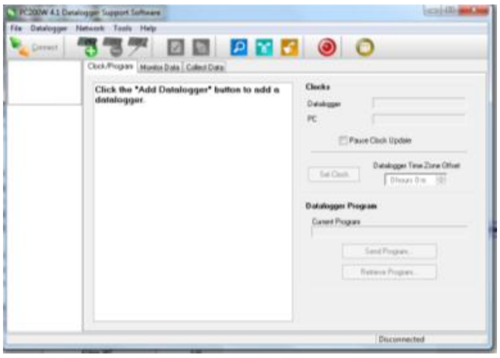

- Get table definitions
- Box “included for schedule collection” should be checked if that table should be transmitted during collection time
- Go to Monitor Data
- Type ‘1’ in manual modem on
- Wait until the modem turns on (maximum 15 minutes)

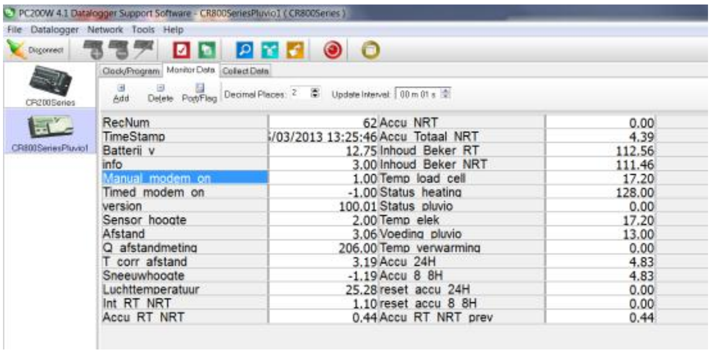

RecNum	62	Accu NRT	0.00
TimeStamp	/03/2013 13:25:46	Accu Totaal NRT	4.39
Batterij v	12.75	Inhoud Beker RT	112.56
info	3.00	Inhoud Beker NRT	111.46
Manual modem on	1.00	Temp load cell	17.20
Timed modem on	-1.00	Status heating	128.00
version	100.01	Status pluvio	0.00
Sensor hoogte	2.00	Temp elek	17.20
Afstand	3.06	Voeding pluvio	13.00
Q afstandmeting	206.00	Temp verwarming	0.00
T corr afstand	3.19	Accu 24H	4.83
Sneeuwhoogte	-1.19	Accu 8 8H	4.83
Luchttemperatuur	25.28	reset accu 24H	0.00
Int RT NRT	1.10	reset accu 8 8H	0.00
Accu RT NRT	0.44	Accu RT NRT prev	0.44

- On the modem the three green LED's should be flashing

Right: Modem
Middle: GPS
Left: Connection to satellite

Antenna alignment procedure:
Before the M2M modem can be used to transfer data, the antenna must be correctly aligned to the appropriate satellite. WARNING: Alignment mode disables all transmissions from the terminal, ensuring the antenna is safe to approach/handle from all sides – For safety reasons, do not attempt to align the antenna without alignment mode enabled.

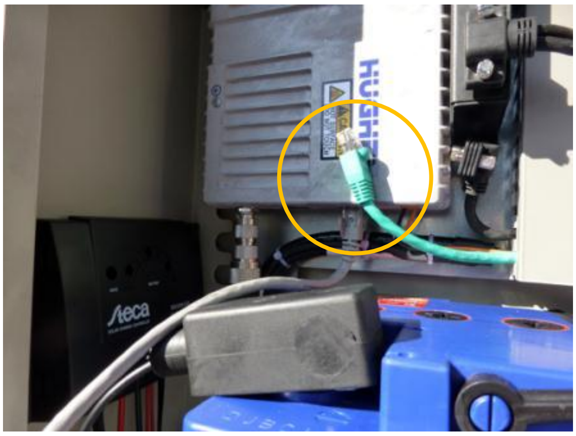

Plug out the green cable on the modem and plug in the ethernet cable to establish a direct connection to the laptop

To place the modem in alignment mode, ensure the modem is powered on and then short press the black button (for less than 2 seconds), the terminal will indicate that it is in alignment mode by blinking the power, GPS and net LED's.

Once a GPS fix has been obtained, the GPS LED will then remain constantly illuminated whilst the others will continue to flash, note that a valid GPS fix is required before commencing antenna alignment.

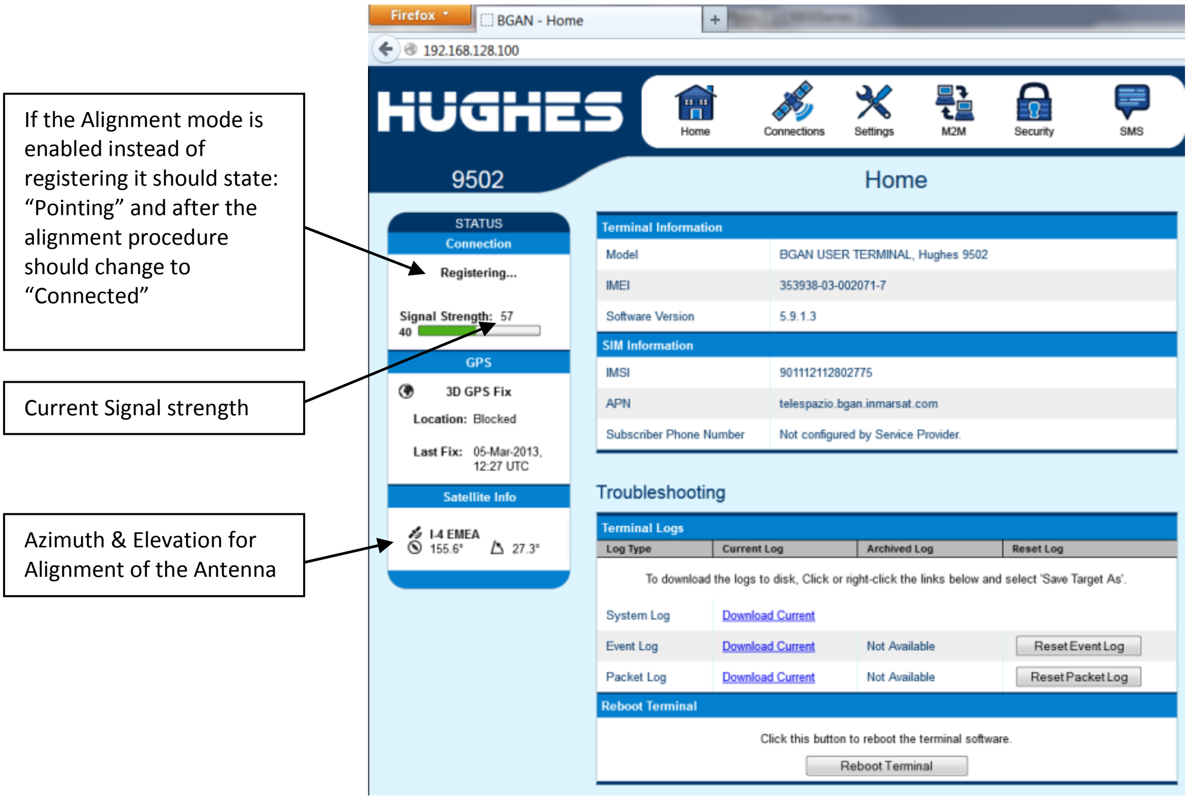

Open an internet browser and type in the IP-Number (the same for all 3 Pluviometers): **192.168.128.100**
Try to get the highest signal strength possible by adjusting the antenna according to the proposed Azimut & Elevation.
The Signal strength has to be > 50dB!

Once the antenna has been successfully aligned (Signal Strength is reported as greater than 50dB) the terminal can be **switched back to operational mode by short pressing the black button again** – when all three LED’s go solid the terminal is successfully connected to the network and a data session has been established.

Don’t forget to plug again the green cable into the interface

After doing this put the power off the system by loosening one of battery poles. Then put the power on again. This is needed so that the modem is assigned the correct IP.

- Go to the software PC200W
- Go to Monitor Data
- Type ‘0’ in manual modem on

SETUP ON PC WHICH WILL BE USED TO COLLECT THE DATA:

- Start the LoggerNet software

- Set up > add Boot > IPPort, PakBus Portlogger, CR800Series

Loggernet clock settings

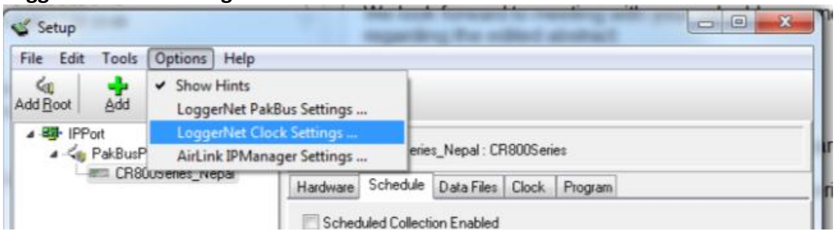

- Set to GMT

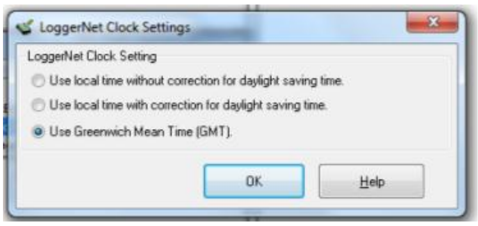

IPPort :

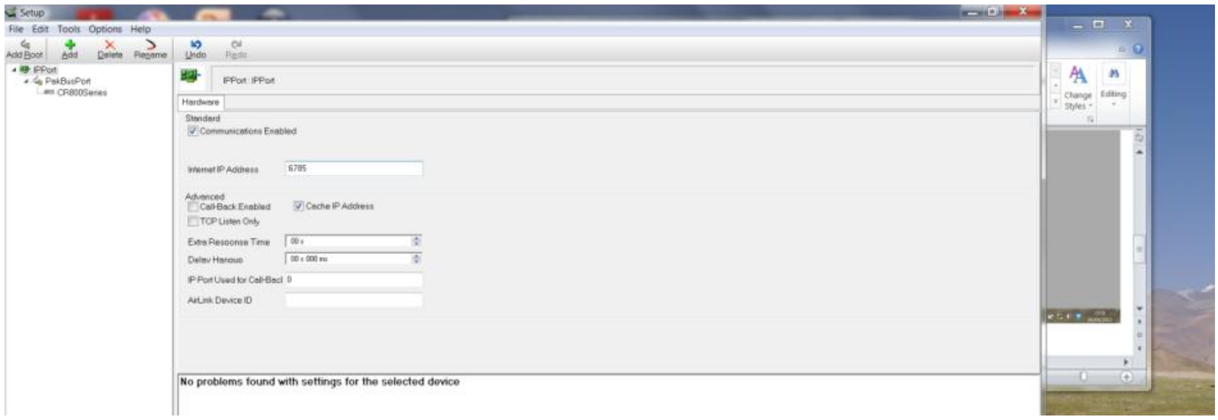

- Box 'communication enabled' should be checked
- Hardware: fill in the IP-Number "IPNumber:6785"

Pakistan Pluviometer 1
IMSI: 901112112802775
IMEI: 353938030020717
SIM: 898709912412802775
IP: 85.90.236.18

Pakistan Pluviometer 2:
IMSI: 901112112802777
IMEI: 353938030021327
SIM: 898709912412802777
IP: 85.90.236.20

Nepal Pluviometer (blue stickers):
IMSI: 901112112802776
IMEI: 353938030021269
SIM: 898709912412802776
IP: 85.90.236.19

PakBusPort:
- Box ‘call-back enabled’ should NOT be checked
- Maximum Packet size should be left at 1000 as long as no problems are occurring

CR800series:

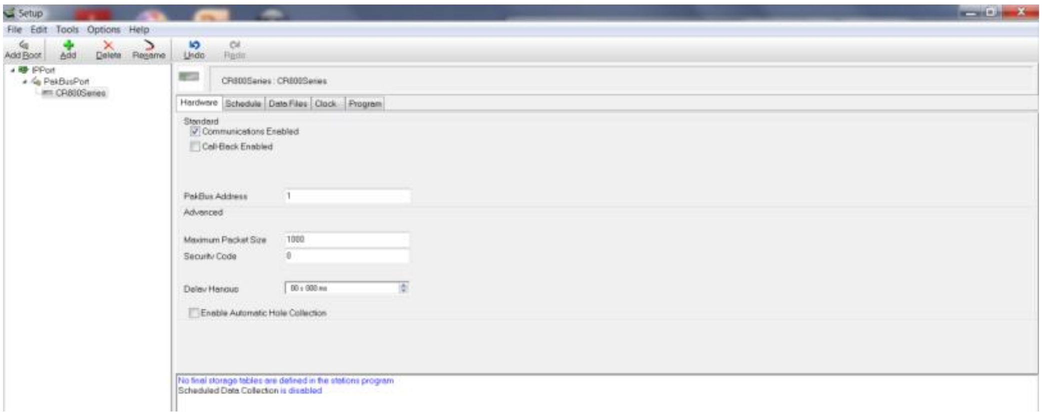

- Box ‘call-back enabled’ should NOT be checked

CR800series -> Tab Schedule

Nepal:

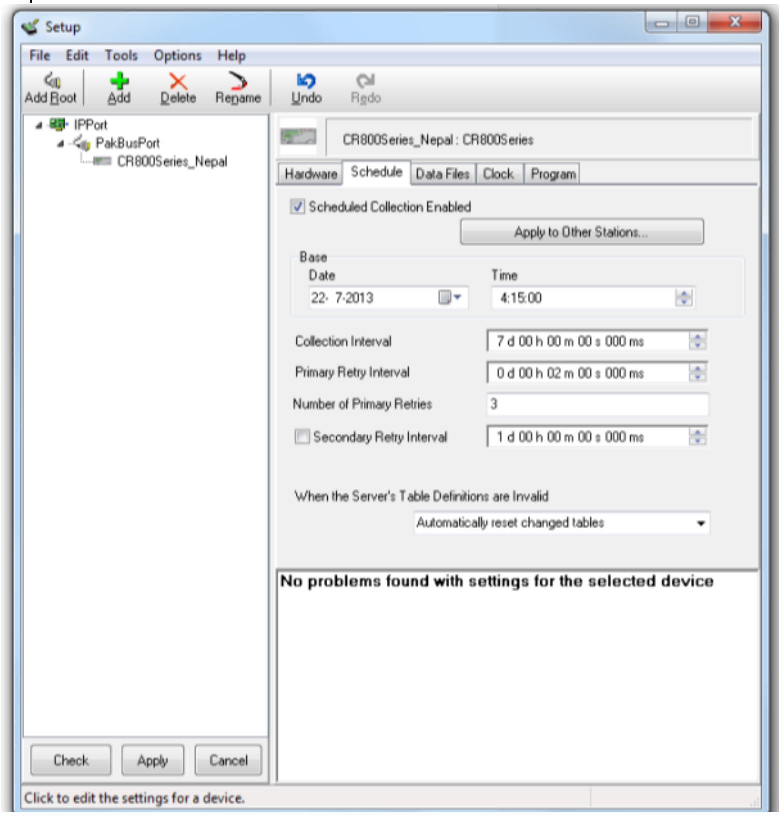

Pakistan:

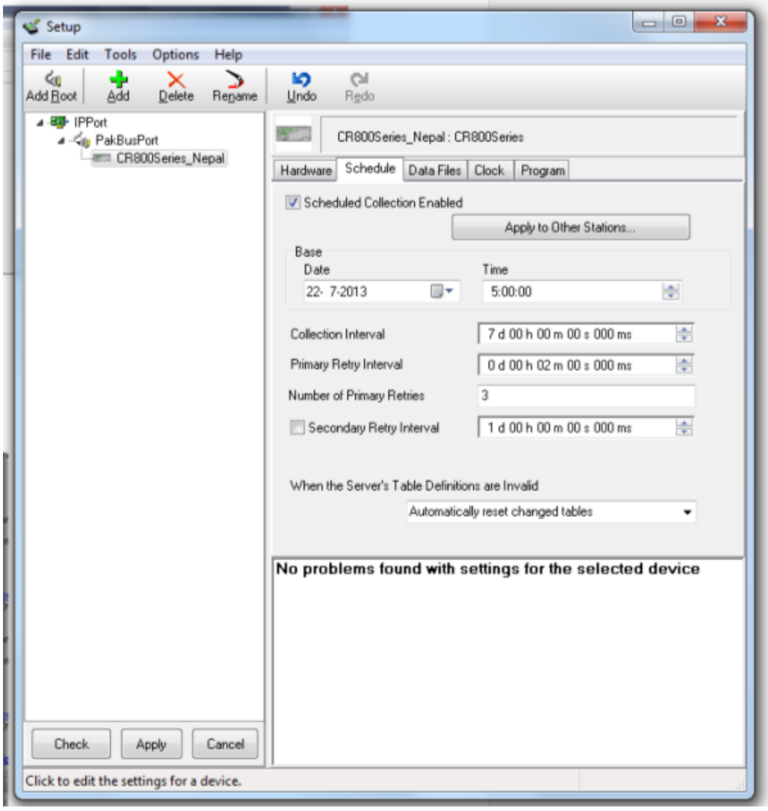

CR800series -> Tab "Data files"

specify where to save

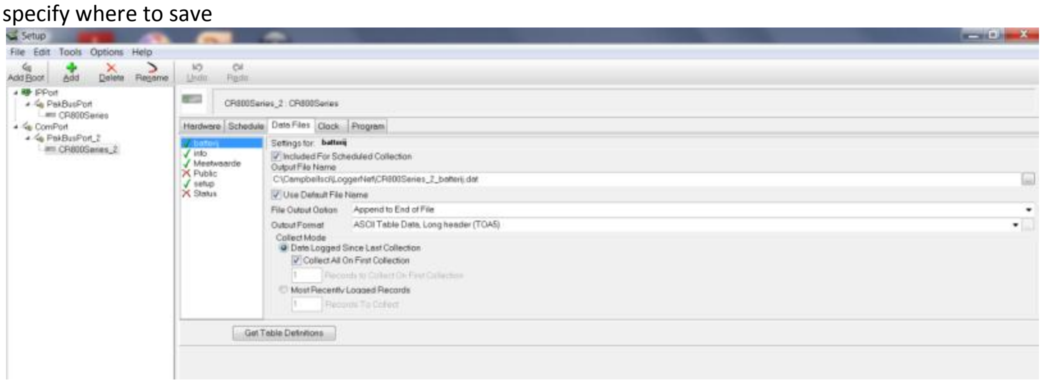

CR800series -> Tab "Clock"

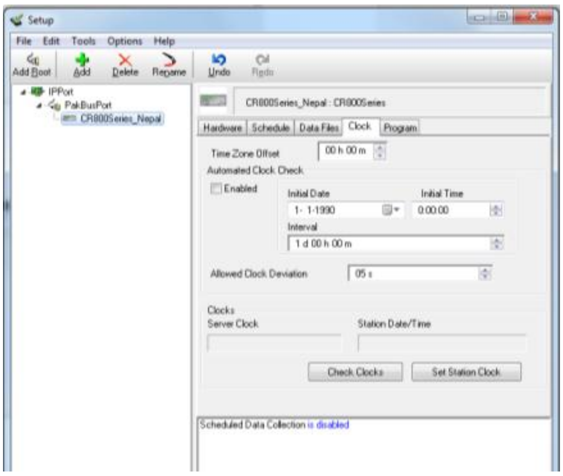

- Check clocks can be done manually
- Make sure the datalogger clock is on UTC/GMT
- Clock: Box 'enable' should NOT be checked

ANNEX 3: IGS SYMPOSIUM REPORT

CONFERENCE REPORT

THE INTERNATIONAL SYMPOSIUM ON GLACIOLOGY IN HIGH MOUNTAIN ASIA

KATHMANDU, NEPAL, 1 -6 MARCH 2015

IGS 2015 KATHMANDU

IGS

ICIMOD

This document was prepared by Dr. Joseph Shea (Glacier Hydrologist), with materials provided by Michelle Laurie, (conference facilitator), Tanuja Shrestha (conference assistant), Jitendra Bajracharya (KMC), and Nasana Badyakar (KMC).

CONTENTS

SUMMARY

From 1 March to 6 March 2015, 245 scientists, researchers, and students met in Kathmandu, Nepal for the International Glaciological Society Symposium on Glaciology in High Mountain Asia. The symposium was sponsored and hosted by the International Centre for Integrated Mountain Development, and additional funding for student travel support was provided by a number of international agencies.

The symposium was designed to highlight research advances in glaciology, with a particular focus on the glaciers of High Mountain Asia. The HMA region includes the Himalayas, the Hindu Kush, the Karakoram, the Pamirs, the Tien Shan, and the Tibetan Plateau. The glaciers of HMA were a notable 'blank spot' in the 2007 IPCC report, and while some research had been conducted in time for the 2013 IPCC report, there had not been a scientific symposium focused specifically on the glaciers of the region.

With an innovative conference format that included less formality, time for discussions and synthesis, networking opportunities, and fantastic science, the IGS Symposium has had a major impact on both the science of glaciology in the region, and on the way scientific symposia should operate. The forthcoming papers of the Annals of Glaciology related to glaciology in High Mountain Asia will ensure that the region receives greater scientific attention and scrutiny.

INTRODUCTION

The idea to host a symposium about Himalayan glaciers in Kathmandu was first discussed in 2012. The International Glaciological Society (IGS) was approached in March 2013, and the symposium was fully endorsed by ICIMOD in June 2013. The IGS had indicated early on that it wanted the symposium to have an important legacy, both scientific and developmental. This document summarizes the organization, program, and outcomes of the symposium, and provides key indicators of the scientific and developmental legacy.

The scientific program of the symposium was focused on the following key themes:

1) Past, present, and future glacier change (reconstructions, observations, projections)
2) Observations and models of glacier dynamics (including glacier response times, and thickness and volume of ice)
3) Glacier and snow melt processes (debris cover, supraglacial lakes, black carbon, etc.)
4) Hydrology of glacierized catchments
5) High-altitude meteorology, climate downscaling, and climatic change (ice core records, etc.)
6) Glacial hazards (GLOFs, avalanches, mass movements)
7) Permafrost studies (measurement, modeling, distribution)
8) Impacts of cryospheric change (local and regional water resources, ecosystems, etc.)

While the early scientific steering committee developed the scientific themes and the circulars that advertised the symposium, the conference program was developed with the assistance of Michelle Laurie, a conference facilitator hired by ICIMOD. With Ms. Laurie, the local organizing committee brainstormed ideas, hopes, and goals for the IGS Symposium in February and March 2014.

A key goal for the IGS symposium in Kathmandu was to provide a different experience than a typical scientific conference. There was a desire to have longer talks and time for Q&A, time for reflection and internalization of the information provided, sense making of the various talks to see if larger patterns and key messages emerge. In addition, efforts to help people network, build contacts and connect on topics important to them both during the event and after were seen as important elements to foster.

The final program reflects the inputs of the scientific steering committee, the local organizing committee, and the work of Michelle Laurie. The success of the symposium, as indicated by the outcomes, the comments, and the thanks received afterwards, is certainly a legacy of which ICIMOD can be proud.

PARTICIPANTS AND PROGRAM

PARTICIPANTS

In total, 245 participants registered for the IGS Symposium. Forty (40%) of the total number of participants were students, and nearly half (49%) were from ICIMOD regional member countries (primarily India, Nepal, and China). A breakdown of the registration statistics is given in Table 1.

Table 1: IGS registration statistics

Number of participants:	245
Number of students:	98
Number of RMC participants:	119
Number of female participants:	67
Number of ICIMOD sponsored participants (Registration):	59
Number of students with travel support:	62

PROGRAM

The conference program included 65 oral presentations and 160 poster presentations spread over four days (Appendix 1). A mid-week Open Spaces session on Wednesday morning promoted discussions and conversations.

Other events included:

- Media Panel (1 March)
- Breaking the Ice: Young Scientists on Glaciology in High Mountain Asia (public event, 1 March)
- ICIMOD Reception Dinner (1 March)
- Documentary screening and Q+A : "The Himalayas: the abode of snows" (public event, 4 March)
- IGS Reception Dinner (5 March) and IACS student presentation awards

SPEAKER POLICY: GENDER BALANCE AND REGIONAL BALANCE

The local organizing committee developed a speaker policy to guide the selection of speakers:

"The local organizing committee will work to ensure balance in all aspects of the IGS Symposium. The final conference programme represents our honest attempt to reflect both the gender balance and geographic distribution of the conference participants, and to promote students and early-career scientists."

How did we do? Of the 65 scheduled presentations:

- 39% of the talks were given by RMC residents (versus 48% registered)
- 32% of the talks were given by females (versus 27% registered)
- 35% of the talks were given by students (versus 40% of registered)

OUTCOMES

In addition to having five days of scientific presentations, discussions, and interactions between regional and international scientists and students, the symposium generated an important number of tangible outcomes. These included:

- "Where do you work?" map of study sites in High Mountain Asia, showing a concentration of sites in Nepal, but very few observations from the Pamirs, the Karakoram, the Tibetan Plateau, and Nyenchen Tangla (eastern end of the Himalayas).

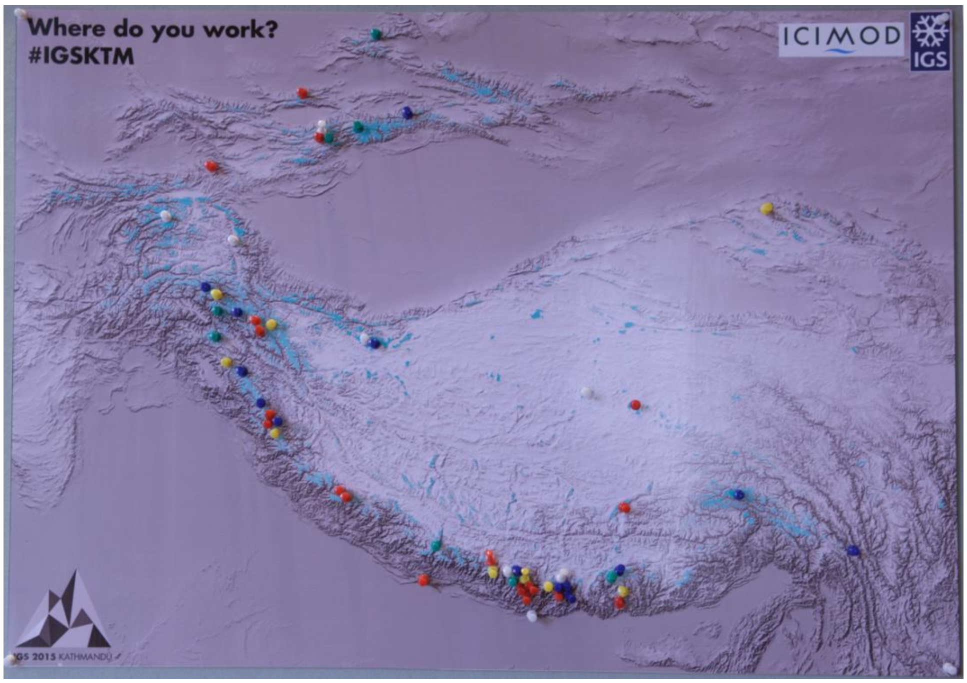

Figure 1: Map of "Where do you work"?, from the IGS Symposium.

- Glaciology Roster
- Media Release
    - http://www.icimod.org/?q=17276
- Synthesis (Annals of Glaciology Editorial)
    - In progress, expected date of publication is January 2016.
- Student Travel Support
    - $24,000 USD in travel support distributed to 62 students who were first-author presenters at the IGS Symposium
    - Funds were provided from ICIMOD (through Norway Support for Cryosphere and Department For International Development, DFID-UK), Institute de Réserche pour le Développement (IRD-France), Laboratoire d'Etude des Transferts en Hydrologie et Environnement (LTHE; France), Labex OSUG@2020 (Investissements d'avenir – ANR10 LABX56; France), and United Nations Development Program (UNDP) - Pakistan
- Young Scientists Panel Video

    - In preparation, will be released through ICIMOD in April 2015
- Student Presentation Awards
    - http://www.icimod.org/?q=17294
- Blog posts
    - http://michellelaurie.com/2015/03/30/sense-making-friend-making-and-glaciers/

PRESS RELEASE AND MEDIA COVERAGE

[The following press release was drafted on Friday 6 March, and released on Monday 9 March on the ICIMOD website, www.icimod.org/?q=17276]

Narrowing the Knowledge Gap on Glaciers in High Mountain Asia

(9 March 2015, Kathmandu, Nepal)

Researchers and students from around the globe met in Kathmandu last week to assemble a more complete picture of glaciers and glacier changes throughout high mountain Asia. Two-hundred and forty scientists from 26 countries came together between 1 and 6 March 2015 for the International Symposium on Glaciology in High-Mountain Asia, organized by the International Glaciological Society (IGS) and hosted by the International Centre for Integrated Mountain Development (ICIMOD), to share the latest findings on glaciers, glacier change, glacier contribution to river flow, and mountain hazards in the region. While knowledge gaps across the region are gradually being filled, additional questions are being raised. "We are making progress on understanding the region as a whole, but when we look at glacier change in more detail, new uncertainties emerge", said Joseph Shea, a glacier hydrologist at ICIMOD and Chair of the Local Organizing Committee.

The integration of different disciplines has led to studies that capture both regional and local changes in glaciers, snow, and water availability. Multiple researchers presented evidence of the retreat of glaciers in the eastern Himalayas, but suggested that river flows will not decline significantly in the coming decades, as melt rates and precipitation are projected to increase. The Karakoram was also highlighted as a region where glaciers are not retreating, and future research will attempt to explain this anomaly. "Glaciers in high mountain Asia are the highest on earth, and we have built a strong foundation for future research through this symposium", said Doug MacAyeal, President of the IGS. However, questions remain about the role of debris cover and black carbon in glacier melt, and the limited number of high-altitude precipitation observations. Researchers agreed that more field observations, improved models, intercomparisons of models, and regional data sharing are among the most critical directions and needs for future research.

"ICIMOD is proud to host the first IGS symposium in Kathmandu and help facilitate regional knowledge sharing on the state of our glaciers as well as their impacts on people. We, along with our partners, are working to develop the most accurate and complete picture of the glaciers", said David Molden, Director General of ICIMOD.

The IGS gathers scientists from around the world several times a year to bring together their knowledge of glaciers in different regions. Results from the symposium will be published in a special edition of the peer-reviewed journal *Annals of Glaciology*, set to be released next year, as well as through the IGS website in August. *[end]*

The press release was covered in a number of online news sites and aggregators, including the following:

- Himalayan glaciers retreating in eastern region says report
  http://www.ibtimes.co.uk/himalayan-glaciers-retreating-eastern-region-says-report-1491224
  International Business Times, Jayalakshmi , 10 March 2015
- Narrowing the Knowledge Gap on Glaciers in High Mountain Asia
  http://www.enepalikhabar.com/english-headline/2015/03/36582
  enepalikhabar.com, 10 March 2015
- Evidence of glacier retreat in Himalayas
  https://in.news.yahoo.com/evidence-glacier-retreat-himalayas-133405544.html
  Indo Asian News Service, IANS, 9 March 2015
- Glaciers are melting in eastern Himalayas: Report [posted on FB]
  http://timesofindia.indiatimes.com/home/environment/Glaciers-are-melting-in-eastern-Himalayas-Report/articleshow/46506693.cms
  Times of India, IANS, 9 March 2015
- Evidence of glacier retreat in Himalayas
  http://zeenews.india.com/news/sci-tech/evidence-of-glacier-retreat-in-himalayas_1558782.html
  Zeenews.india, Monday, IANS, 9 March 2015
- Evidence of glacier retreat in Himalayas
  http://www.daijiworld.com/news/news_disp.asp?n_id=302539
  Daijiworld.com, IANS, 9 March 2015
- Narrowing the Knowledge Gap on Glaciers in High Mountain Asia
  http://www.nepalmountainnews.com/cms/2015/03/11/narrowing-the-knowledge-gap-on-glaciers-in-high-mountain-asia/
  Nepal Mountain News, 11 March 2015
- Narrowing the knowledge gap on glaciers
  www.htsyndication.com/htsportal/article/Narrowing-the-knowledge-gap-on-glaciers/6865026
  Hindustan Times Syndication, 10 March 2015
- Narrowing the Knowledge Gap on Glaciers in High Mountain Asia
  http://www.dnd.com.pk/narrowing-the-knowledge-gap-on-glaciers-in-high-mountain-asia/88874
  Dispatch News Desk, 10 March 2015
- Narrowing the knowledge gap on glaciers (Blog)

http://blogs.hindustantimes.com/kurakani-in-kathmandu/2015/03/10/narrowing-the-knowledge-gap-on-glaciers/
Hindustan Times, Utpal Parashar, 10 March 2015

- Glaciers in eastern Himalayas undergoing change
  http://www.gizmodo.in/indiamodo/Glaciers-in-eastern-Himalayas-undergoing-change/articleshow/46513714.cms
  Gizmodo India Bureau, 10 March 2015

THANK YOU LETTER FROM THE IGS

International Glaciological Society

Scott Polar Research Institute,
Lensfield Road,
Cambridge, CB2 1ER, UK
Tel: +44 (0)1223 355 974
Fax: +44 (0)1223 354 931
E-mail: igsoc@igsoc.org
Web: http://www.igsoc.org

Dr D Molden
ICIMOD
G.P.O. Box 3226
Khumaltar
Kathmandu
Nepal

27 March 2015

Dear David

It has now been three weeks since the Kathmandu symposia closed. The excitement has dissipated and we can now look back dispassionately and with a clear head.

This really was a fantastic symposium, one of the best. The innovative approach to engage the delegates was superb and something we aim to emulate in future symposia. The venue was very appropriate and well suited to such an event as ours.

But what stands out is competence and congeniality of the local organisers. You and your staff deserve a huge thank you for what you have accomplished. The event was very well organised and a credit to the ICIMOD team.

The IGS is proud to have participated in the organisation of this symposium and we look forward to working with ICIMOD again in the not too distant future. The huge success of the meeting, judging by the many positive comments we have received, warrants that we start thinking about a follow up symposium in a few years.

Another valuable result achieved by the symposium is the participation of scientists, old and in particular young ones from the region. It exposed the world to the science being conducted there and similarly the 'locals' are being exposed to science from the rest of the world. Some very valuable lessons were learned.

When the idea of organising a symposium in Nepal was initially being discussed the IGS Council was adamant that such a symposium should leave behind a legacy that would benefit the region. It certainly did so and it also left a legacy for the worldwide scientific community. And that is largely thanks to you and your team.

Thank you again very much

Yours sincerely.

Douglas R. MacAyeal

Douglas R. MacAyeal
IGS President

Magnús Már Magnússon.
Secretary General

Registered Charity 231043

SPONSORS

The local organizing committee would like to sincerely thank the following organizations for their generous financial and logistical support:

- ICIMOD and its core donors (Afghanistan, Bangladesh, Bhutan, China, India, Myanmar, Nepal, Pakistan)
- Norwegian Ministry of Foreign Affairs
- L'Institut de Recherche pour le Développement (IRD; France)
- Laboratoire d'Etude des Transferts en Hydrologie et Environnement (LTHE; France)
- Labex OSUG@2020 (Investissements d'avenir – ANR10 LABX56; France)
- Department For International Development (DFID; United Kingdom)
- Kathmandu University (Nepal)
- Tribhuvhan University (Nepal)
- Department of Hydrology and Meteorology (DHM; Nepal)
- United Nations Development Program – Pakistan
- Divecha Centre for Climate Change (India)
- International Association of Cryospheric Sciences (IACS)

ANNEX 4: LANGTANG STATUS REPORT

Langtang Valley Status Report
June 2015

NORWEGIAN EMBASSY

ICIMOD 30

UKaid from the British people

This report was prepared by Dr. Joseph Shea and Dr. Patrick Wagnon, of the International Centre for Integrated Mountain Development (ICIMOD). The field visit was supported by the Norwegian Ministry of Foreign Affairs and partners.

International Centre for Integrated Mountain Development (ICIMOD)

Cover photograph: Langtang Khola near Langshisha Karka, 7 June 2015.

Contents

1 Introduction

A magnitude 7.8 earthquake struck central Nepal on 25 April 2015. The earthquake caused significant losses of life and property throughout central Nepal, and Langtang Valley was the site of devastating avalanches, landslides, and rockfalls that killed more than 350 people.

Langtang Valley has been the focus of intense glaciological, meteorological, and hydrological fieldwork over the past four years as part of the Norwegian-supported cryosphere monitoring project. Numerous high-impact publications stemming from the research conducted in the valley are evidence of the success of the comprehensive research focus, and both regional and international post-graduate students have been trained through research conducted in this program. The research and student training has been conducted by ICIMOD and national and international partners, including Kathmandu University, Department of Hydrology and Meteorology (Nepal), Utrecht University, and ETH-Zurich. Additional funding for research in the valley has come from the United Kingdom Department For International Development (DFID), the American Embassy in Kathmandu, USAID, and others.

This report summarizes the status of meteorological and hydrological stations visited during a 5-day field visit to Langtang Valley on 4 - 8 June 2015. Aerial and ground-based photographs are used to document the impacts of the earthquake and associated avalanches on hydro-meteorological equipment maintained in Langtang Valley. The station survey team was

Station	Damages	Cost Estimate
AWS-Kyanging	Tower, CNR4, anemometer, Jennoptik, Pluvio (?)	
AWS-Lirung (ETH)	everything; datalogger returned to KTM	
AWS-Yala Base Camp	Tower, Pluvio base and windscreen; CNR4 still malfunctioning due to AEM	
AWS-Yala Glacier	Anemometer, other components unknown; no data retrieved	
AWS-Langtang (ETH)	Incoming solar radiation	
Pluvio-Yala	everything; datalogger returned to KTM and data retrieved	
Pluvio-Ganga La	Frame, Pluvio, SR50, 1/2 solar panels, anemometer.	
Pluvio-Morimoto	None.	
Pluvio-Langshisha	Unknown	
HS-Lirung	Station pole and fencing bent, sensor ok	
HS-Kyanging	RTS installation unsatisfactory	
HS-Langshisha	None	

composed of Dr. Joseph Shea (ICIMOD), Dr. Patrick Wagnon (ICIMOD/IRD), Mr. Gyalbu Tamang (Kyanging), and Mr. Djornay Lama (Langtang).

An overview map of the station locations is given below. We estimate that roughly 75% of the variables from the three main station types (AWS, HS, and Pluvio) will not be collected this season. Based on our survey, the following stations will be functioning (fully or partially) during the 2015 monsoon:

- AWS-Kyanging (T/RH only)
- AWS-Yala (no radiation)
- AWS-Langtang
- Pluvio-Morimoto (limited duration)
- Tipping buckets, T-loggers
- HS-Kyanging (requires maintenance)
- HS-Lirung
- HS-Langshisha

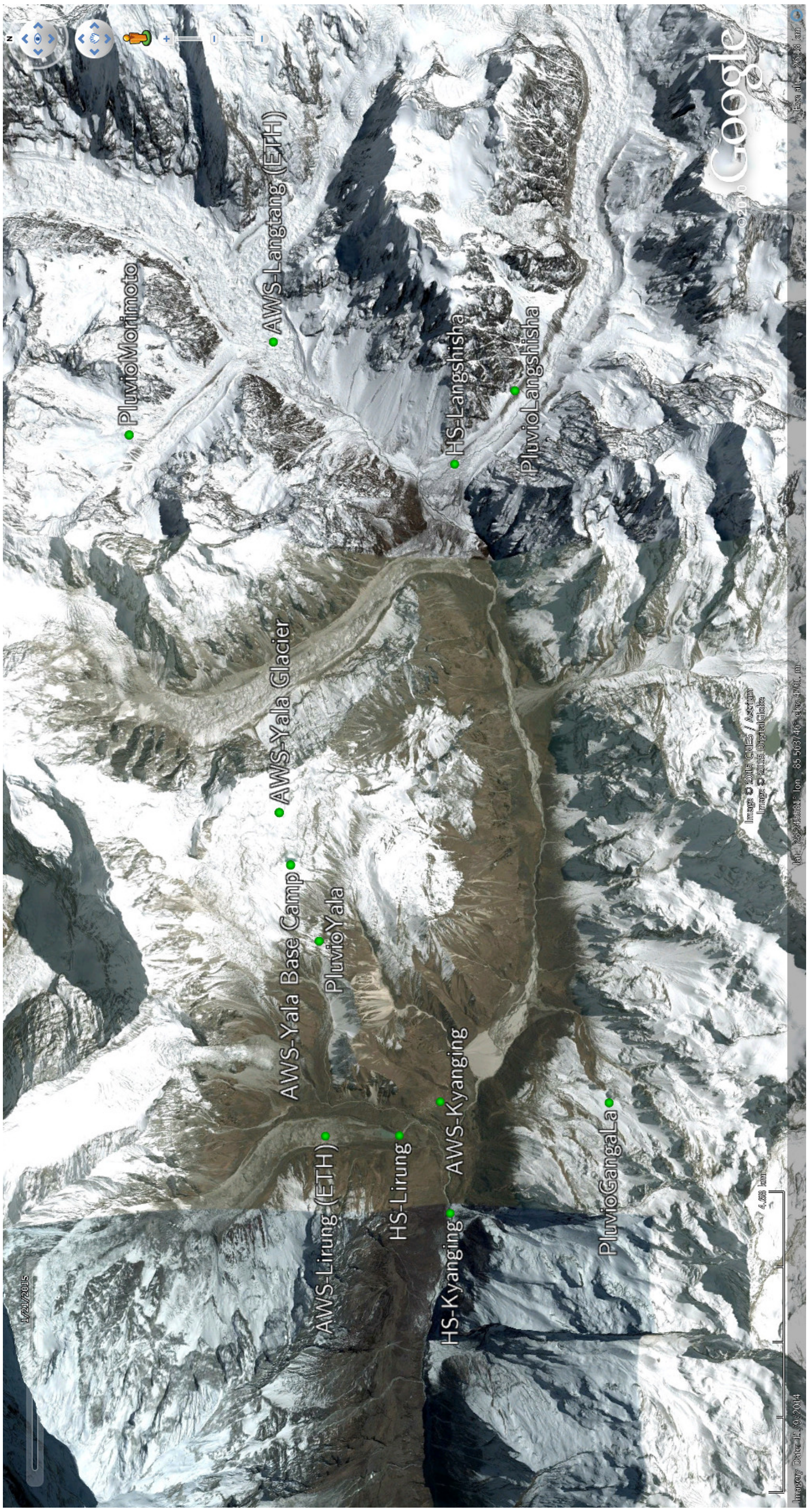

Langtang Valley with AWS, HS, and Pluvio station locations (Google Earth)

2 Station Summaries

2.1 AWS-Kyanging and DHM Base House

An avalanche from the east ridge of Langtang-Lirung (photo) created an air blast that hit Lirung Glacier valley and Kyanging. A hanging glacier below the ridge appears to be the source of the avalanche, and fracture marks on the glacier indicate that future ice avalanches and and associated wind blasts could occur.

East ridge of Langtang-Lirung, with suspected source of avalanche and air blast that affected Lirung Glacier and Kyanging.)

The Kyanging weather station was heavily affected, as were many hotels in Kyanging. Tin roofing and wood framing was found inside the DHM compound (photo), and was also found across the river on the other side of the valley (photo).

Details:

- Station mast snapped at base and in middle, thrown 2 meters from the base (photo)
- CNR4 and wind sensor gone (photos)
- T/RH, solar panel appears OK (photos)
- Pluvio tilted (photo), reset and calibrated with direct connection. Cable from Pluvio to datalogger was damaged (photo) exposing the 12V power supply and the SDI ground. Data are not being transmitted from Pluvio to datalogger, possible short? Removed damaged section of cable and rewired Pluvio, but still NA being reported on datalogger.
- Laser snow depth sensor brought back to Kathmandu for testing and calibration.
- Battery at 12.0 V, but no power to datalogger. Disconnected and reconnected, and datalogger came back on. T/RH sensor, solar panel, and Iridium were remounted on a

portable tripod (see photo), with datalogger box on the ground.

The DHM Base House was badly damaged by the earthquake and the air blast (photo). No ICIMOD equipment was found inside the remains of the base house, but it is unclear if the equipment (steam drill, generator) was moved somewhere else after the earthquake.

AWS-Kyanging station and pluvio after remounting and repair

Tin roofing and lumber inside the AWS-Kyanging fencing.

Pluvio at AWS-Kyanging

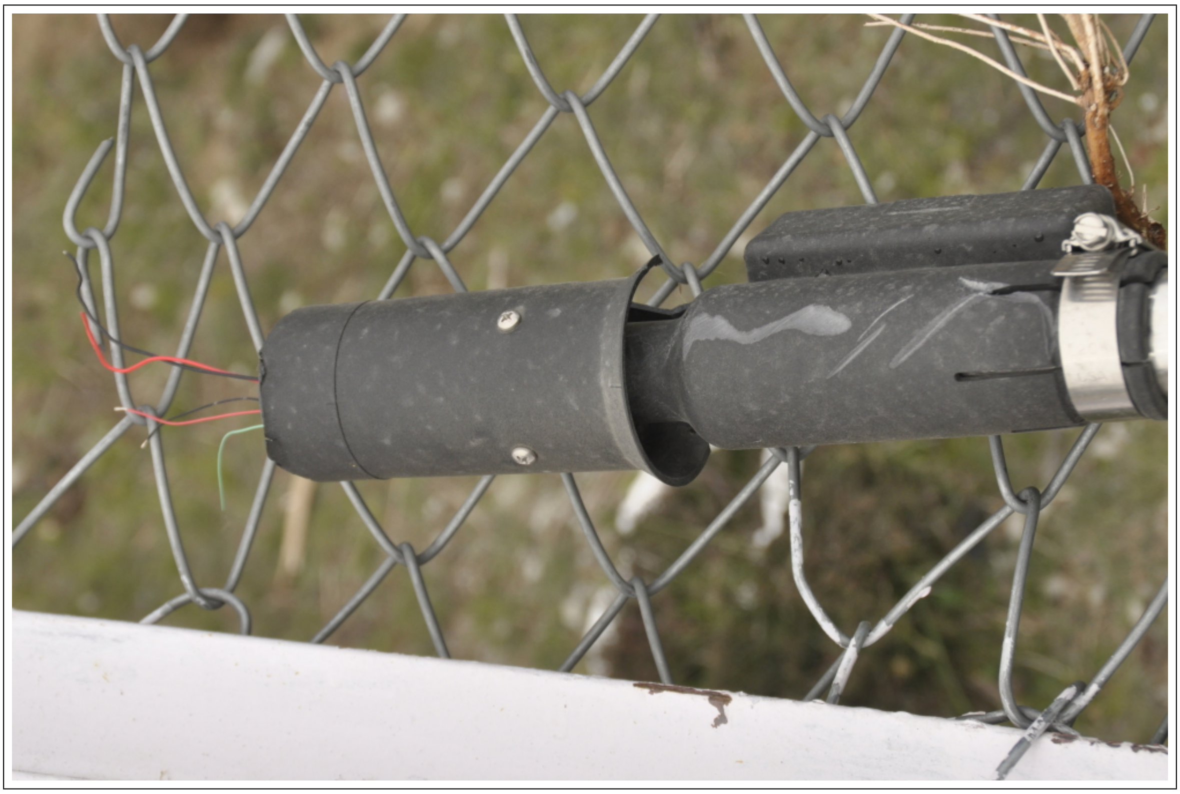

AWS-Kyanging wind sensor

AWS-Kyanging net radiometer

Damaged Pluvio data cable

AWS-Kyanging station

DHM Base House in Kyanging

DHM Base House in Kyanging

2.2 AWS-Lirung (ETH) and T-loggers

Also affected by the same air blast, the AWS-Lirung was found scattered across Lirung Glacier, up to 200 m from its original location.

Details

- Pole with snow depth sensor bent, but in place; Box with Multiplexer on site, and OK; Hobo sensors damaged and carried down to Ktm
- The black box with the battery was 15 m away, not damaged except the connexion of the grey cable partly broken (see photo)
- The tripod with all sensors has been blown away on the other side of the glacier (left bank) more than 200 m from the initial position
- Tripod, CNR4, CR1000, wind sensor, solar panel, thermometer: all destroyed; CNR4 and CR1000 were brought down to Kathmandu and data could not be retrieved. Logger needs to be sent to manufacturer to download the data.
- T-loggers: 2 retrieved, 1 located 50 m south of AWS, put back vertical; one located close to cliff 1, at 200 m from AWS position: broken
- Cliffs 1 and 2; lake Anna: see photos, cliff 1 buried below debris, cliff 2 and lake Anna still visible

AWS-Lirung SR50 and solar panel

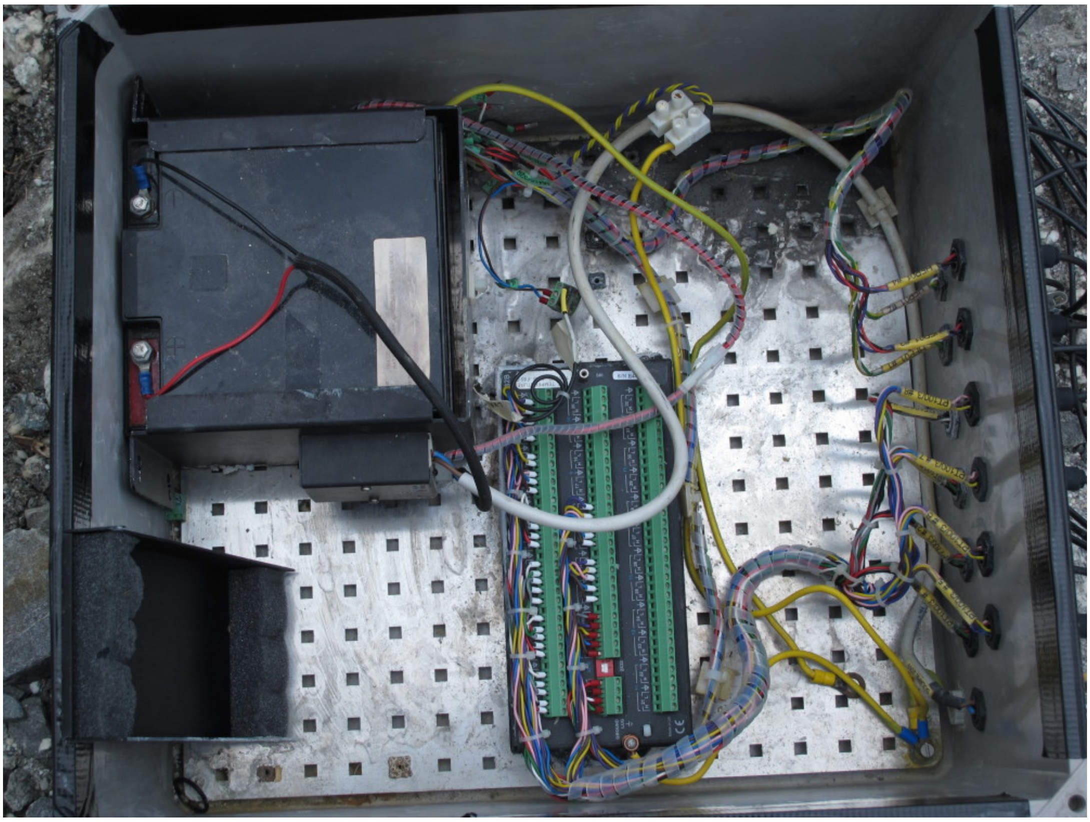

AWS-Lirung multiplexer (box was closed and left as is)

AWS-Lirung pelican case

AWS-Lirung tripod and datlogger box

Cliff and lake on Lirung Glacier


Cliff and lake on Lirung Glacier


Cliff and lake on Lirung Glacier

2.3 AWS-Yala Base Camp

The AWS at Yala Base camp appears to have been hit by an air blast from a large avalanche off of Yansa Tsenji summit, 6500 m asl.

Details

- Visit at 10:40 LT, download of the data (extremely slow, more than 2 hours to collect all data); cautious: there is a 6 min difference between AWS clock and local time (10:46 AWS = 10:40 LT); Battery = OK, 14.3V
- Pluvio bent 20° toward South. Put back vertical at 14:00 LT
- all sensors are fine but the station was lying down on the snow (see photo); one of the 3 leg connections of the mast broke; station put back vertical at 13:00LT
- CNR4 does not record correct data: this is not due to the quake, but to pre-existing data-logger malfunction

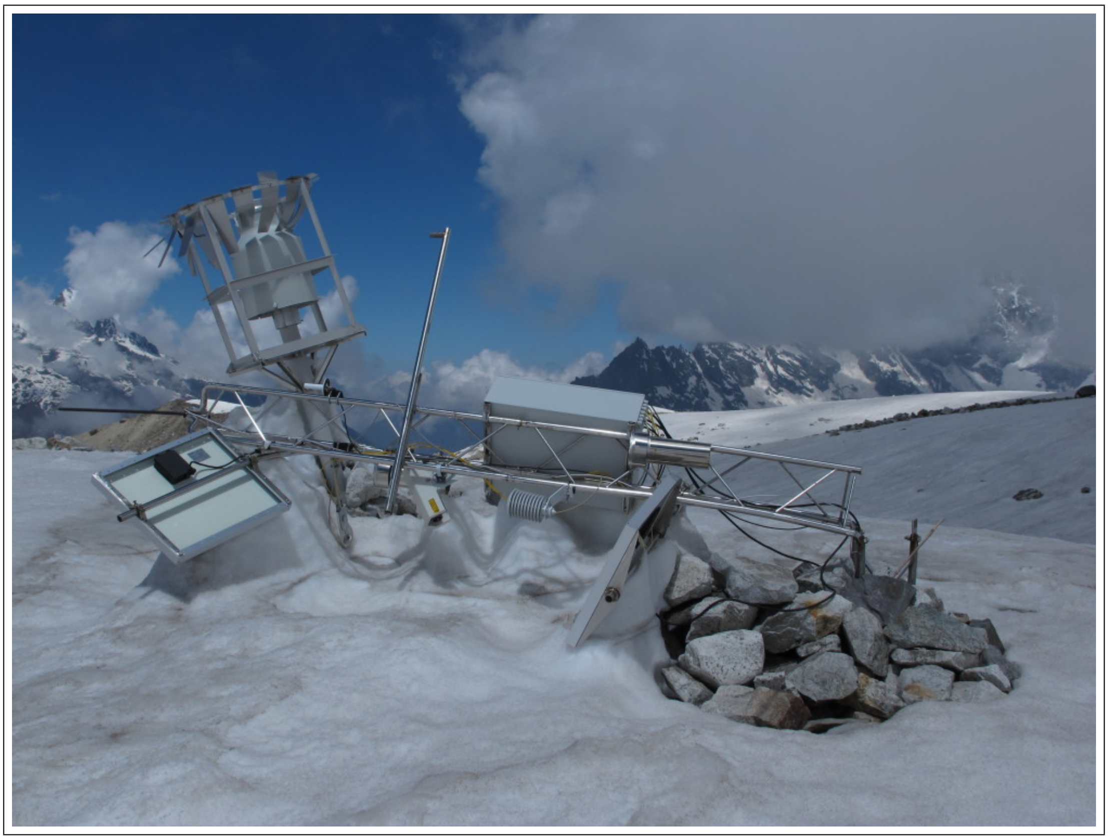

AWS-Yala Base Camp

AWS-Yala Base Camp

AWS-Yala Base Camp standing tall

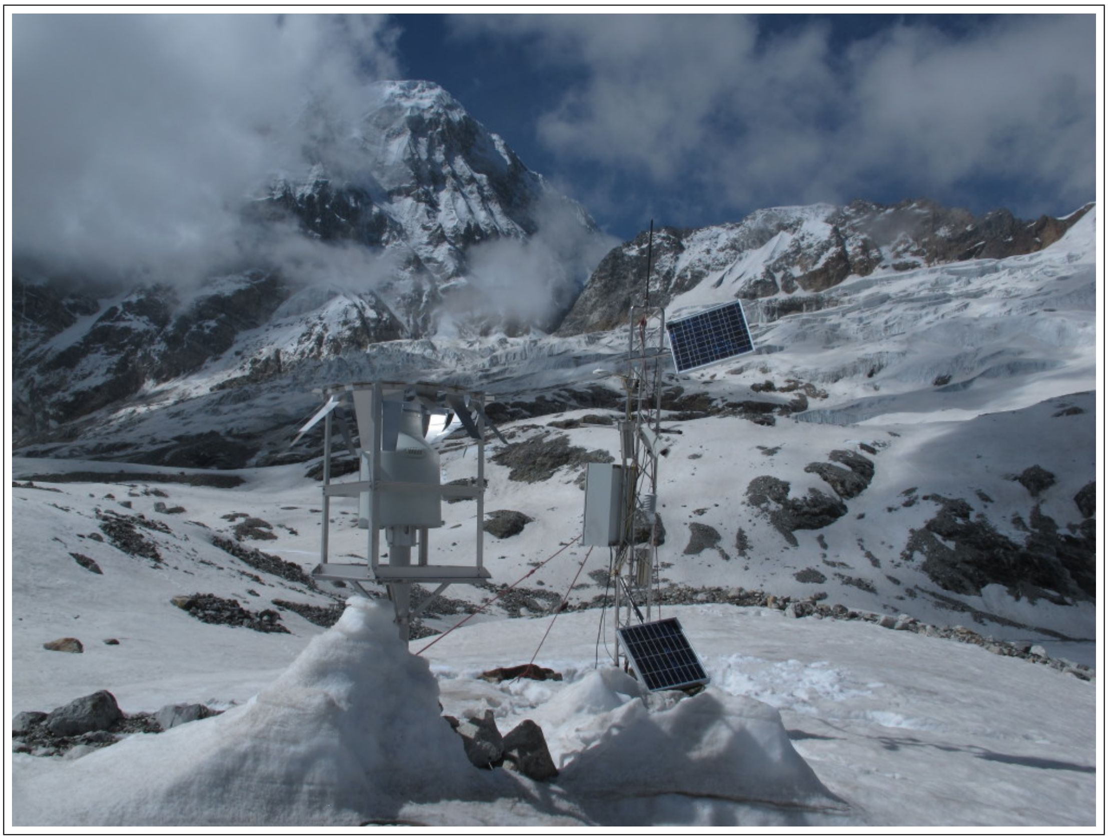

AWS-Yala Base Camp and Pluvio after repair

2.4 AWS-Yala Glacier

Station was found almost completely buried under the seasonal snowpack. It was unaffected by the earthquake or avalanches.

Details

- Visit at 13:00 LT 5 June, almost entirely buried, only wind sensor Young 05103 (broken) emerging 5 cm above the surface
- shoveled 40 cm, tripod appears to be standing, but no data being collected

Yala Glacier AWS, buried in the snow

2.5 AWS-Langtang (ETH)

The AWS on Langtang suffered minor damage from an air blast that stemmed from avalanches on the eastern side of Langtang Glacier. Avalanche debris was found filling depressions on the western half of the glacier (photo), and at the Morimoto Base Camp.

Details

- Albedometer was tilted towards the blast, and the incoming pyranometer suffered damage (photos)
- All other sensors appeared to be okay
- Battery was fully charged (14.46 V), and the ventilation fan started up after the power was connected (though it waited until the next measurement interval
- Due to Serial-USB issues, could not connect to datalogger to verify
- Albedometer screws are tightened, but the pipe can still rotate 5-10°?
- Datalogger box was wired to the tripod

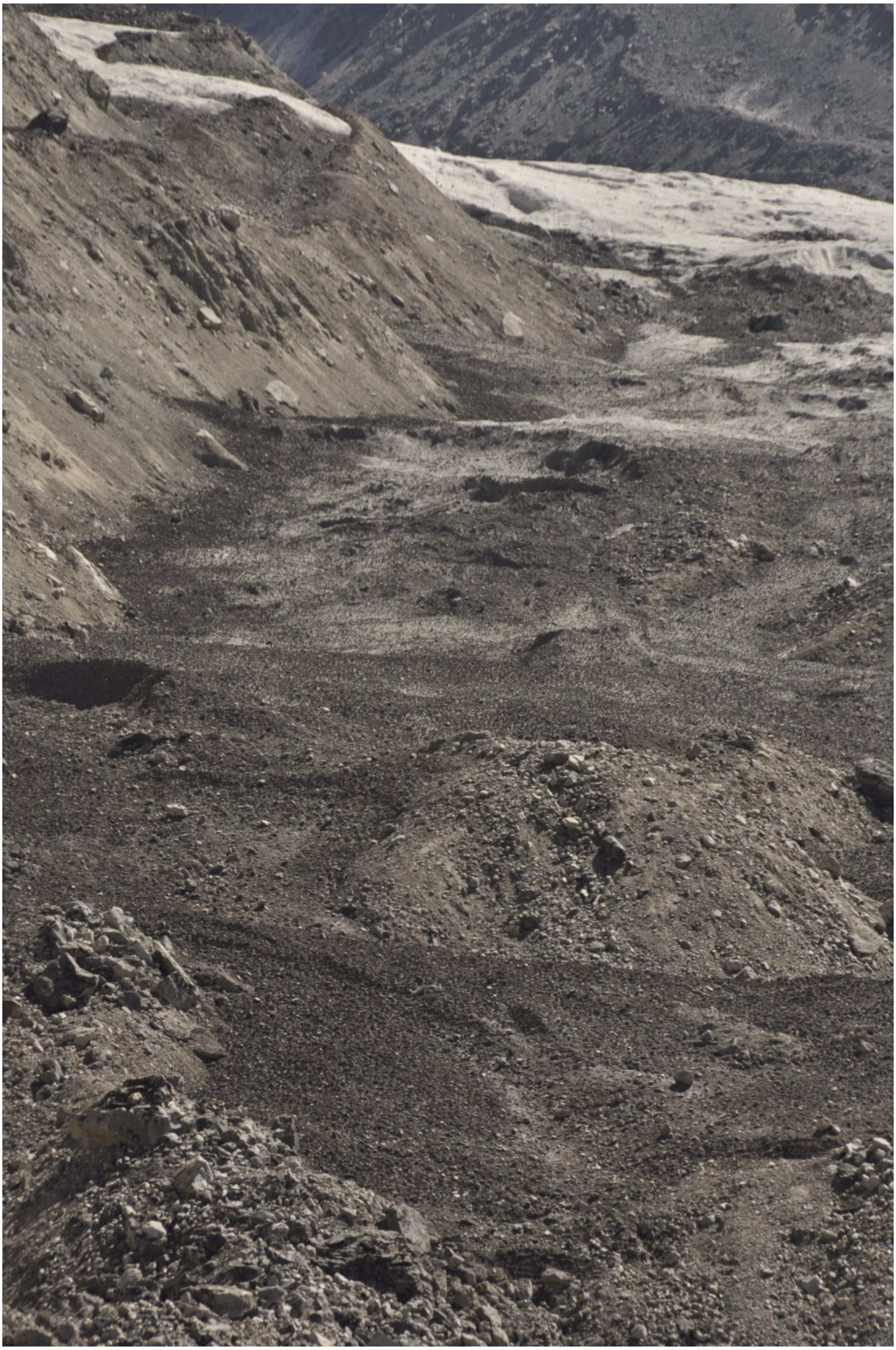

Avalanche debris on the western half of Langtang Glacier. Looking northward

Tilted albedometer at AWS-Langtang

Damaged incoming pyranometer at AWS-Langtang

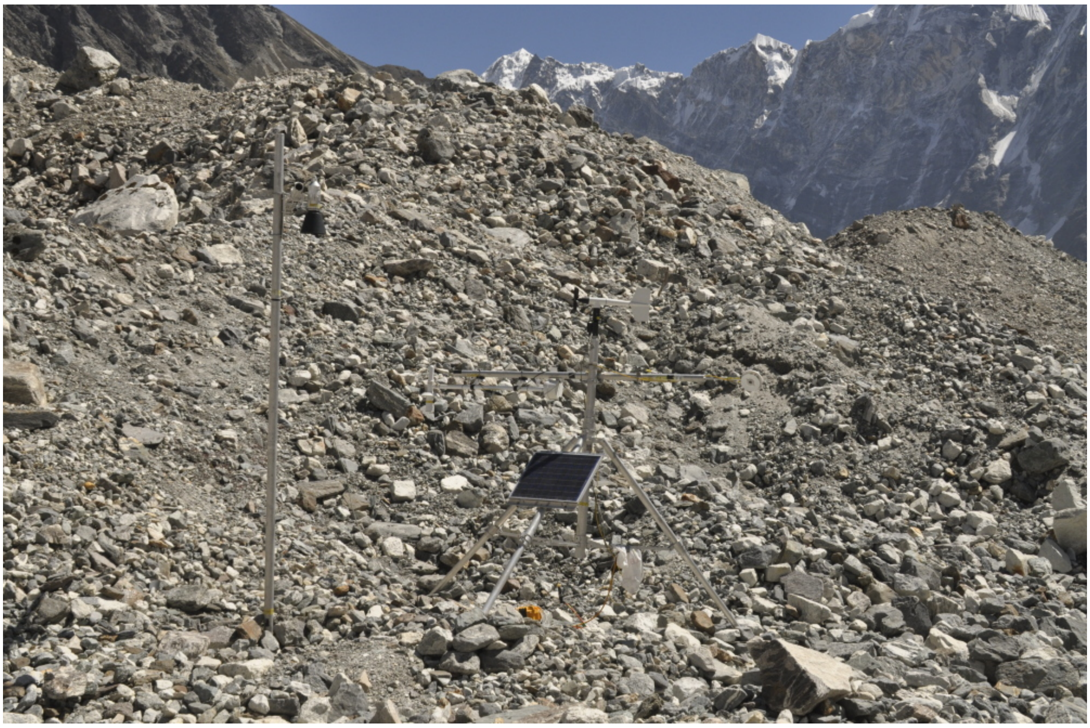

AWS-Langtang

Datalogger connections, and attachment to tripod

2.6 Pluvio-Yala

Part of the Yala Pluvio was identified during the aerial survey on 12 May. The site visit showed extensive damage to the station and the Pluvio weighing gauge, bucket and shield have not been found. We suspect that a large avalanche from the Yansa Tsenji summit, 6500 m asl was coincident with the earthquake (photo).

Details

- Visit at 16:00 LT on 5 June. SR50 and temperature sensors still on the pole (bent toward south)
- Only the base of the pluvio was remaining, the metallic upper part, the datalogger, and the 2 sets of batteries were found 50 m to 200 m from the station;
- The SR50, datalogger, and battery sets have been brought down to Kathmandu
- Data have been downloaded from the CR200 datalogger

Avalanche deposit on the plateau between Yala Glacier Base Camp and the Yala Pluvio

Yala Pluvio datalogger

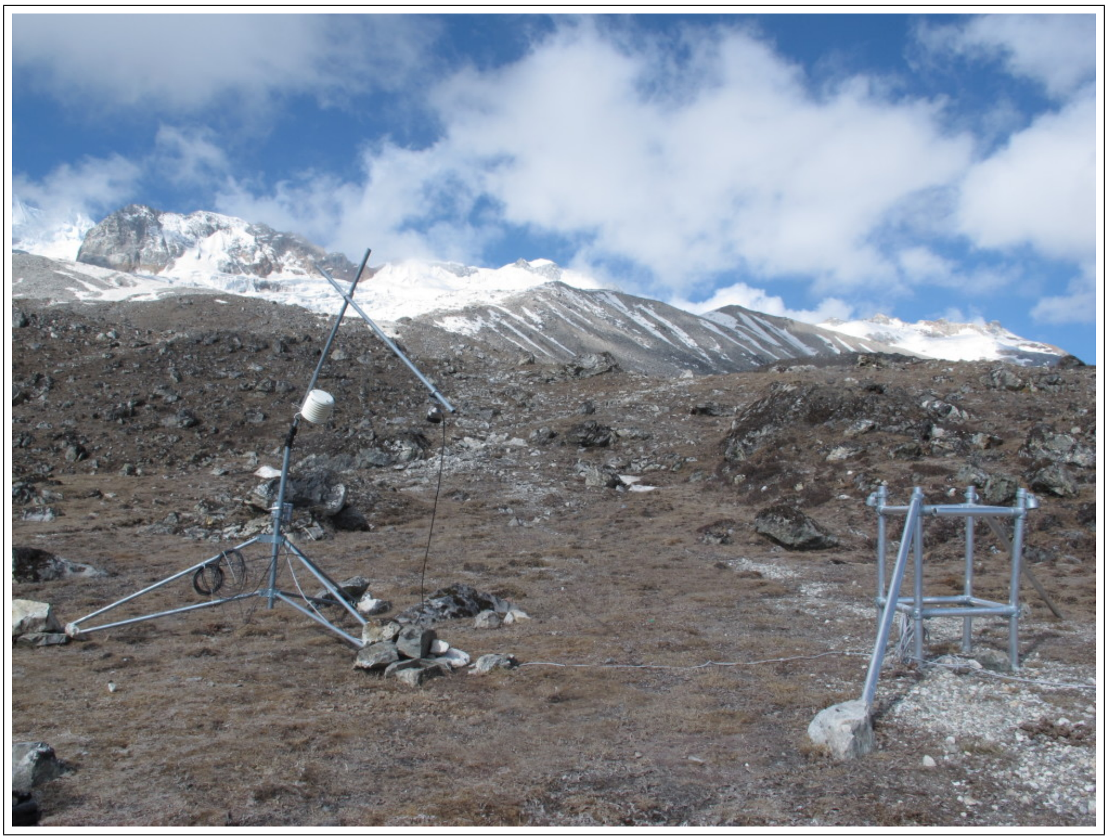

Yala Pluvio structure and tripod with T/RH sensor and SR50

2.7 Pluvio-Ganga La

As the Ganga La Pluvio was found approximately 30 m downhill (northeast) of its original location, we presume that a large avalanche from Naya Kanga (photo) created an air blast that moved the station.

Details

- Frames bent/sheared, Pluvio windscreen damaged (frame appears ok)
- Pluvio bucket and cover ok.
- Wind sensor missing cups, SR50 damaged and brought back to Kathmandu for testing
- Battery still had power, but download in field did not work (USB-serial issues). Datalogger returned to Kathmandu and downloaded. Station stopped recording on 2 January 2015, but battery power was still at 12.86 V??
- wired remaining solar panel to charge controller to maintain battery charge

(a) Original location of Ganga La Pluvio (foreground), and location after the earthquake/air blast (circled on right).

Ganga La Pluvio station

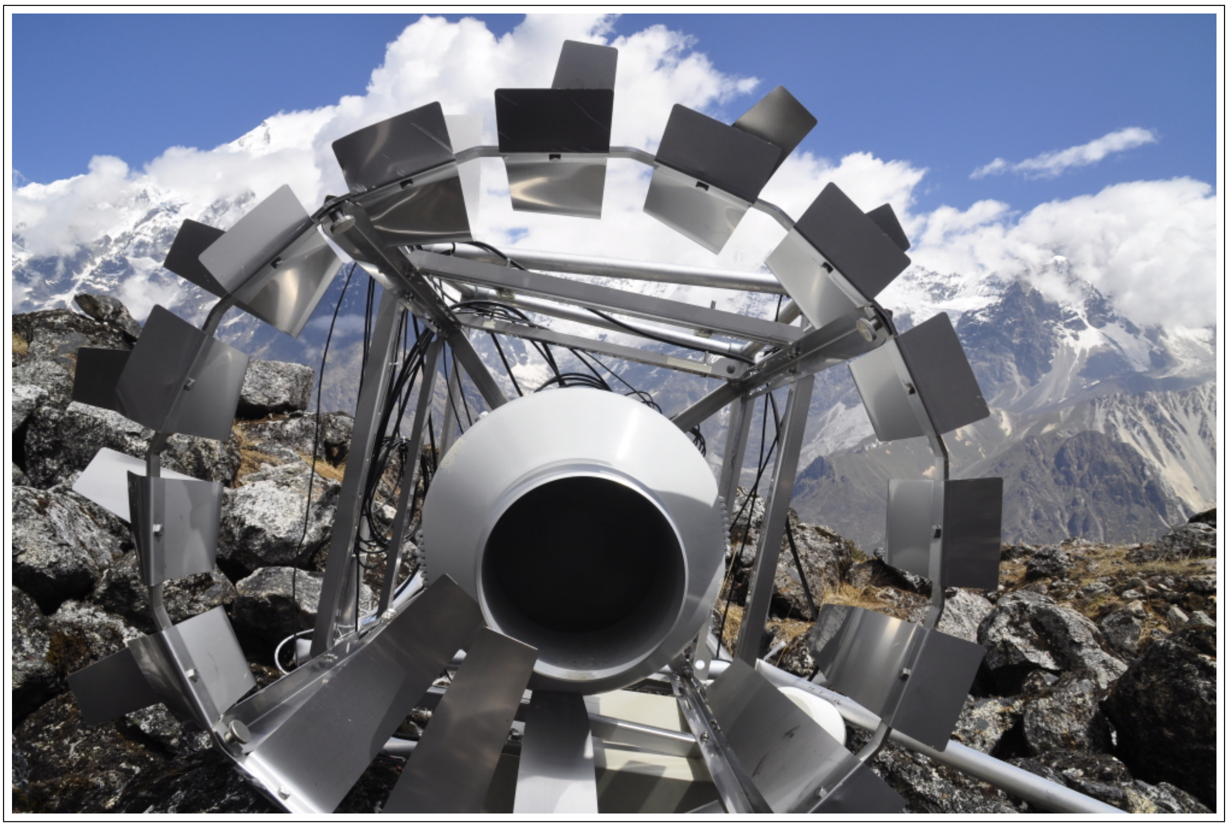

Ganga La Pluvio windscreen

2.8 Pluvio-Morimoto

Details

- Visit at 10:15LT 7 June
- No power. Connected spare battery and downloaded data from 2013 until 10/10/2014 6:00
- 2 additional datapoints on 28/10/2014 at 14:00 and 14:15
- Problem with solar charging system? main battery disconnected and a new 12V/7Ah battery connected to the datalogger, but without any solar charging system connected.
- Station was working and recording when I left but for how long???

Morimoto Pluvio on 7 June 2015

2.9 Pluvio-Langshisha

The Langshisha Pluvio, T-logger, and tipping bucket were not visited as the Langtang River was too high to cross safely. Aerial recon from 12 May 2014 suggest that all equipments at the site were tipped over during the earthquake, and was not affected by avalanche activity.

Given the fact that the Ganga La datalogger survived its 30 m slide, it is likely that the Langshisha station is in working condition, but just needs to be set upright and calibrated.

Aerial photo of toppled Langshisha Pluvio station, T-logger, and tipping bucket on 12 May 2015

2.10 HS-Lirung

Lirung hydrological station was also affected by the Kyanging air blast.

Details:

- visit at 9h50 LT, download of the data, AWS clock on time; Battery = OK, 14.5V
- solar panel facing W put back in S position
- Damages: the pole is bent toward south, should be put in vertical position again; fence not damaged but slightly bent, gate damaged and should be repaired.

Lirung hydrological station

2.11 HS-Kyanging

The Kyanging hydrological station was not affected by the earthquake or any avalanche activity. However, the installation by RTS in February 2015 has led to additional problems.

Details

- The aluminum pipe used to mount the radar level sensor (RLS) was the wrong diameter for the mount installed on the rock (or the mount was the wrong size for the pipe)
- To make the aluminum pipe fit properly, a 10 cm rectangle was cut from the bottom of the pipe, and it was squeezed into the bedrock mount (photo)
- As a result, the aluminum pipe is bent already, and the length of the pipe results in significant movement in the wind
- The guy wire was also completely slack, and the RLS was not perpendicular to the water surface. Adding tension to the guywire pulled the pipe upwards, but resulted in greater sensor tilt
- The pipe was rotated to set the RLS perpendicular, but the sensor was still tilted away from the bank, and could not be adjusted.

HS-Kyanging mounting pipe and rock anchor

HS-Kyanging rock attachment, showing bent pipe

HS-Kyanging RLS tilted on 5 June 2015

HS-Kyanging guy-wire anchor. Guy-wire is not secured, and is slack.

2.12 HS-Langshisha

The hydrological station at the Langshisha outlet was also not visited during this trip due to the high water levels on Langtang Khola. However, the aerial survey of 12 May 2015 suggested that the station was unaffected by the earthquake. A proper rating curve has not yet been developed for this site.

HS-Langshisha from aerial survey on 12 May 2015

3 Tipping Buckets and T-Loggers

The survey team also downloaded Tipping bucket and T-Loggers where possible. It was not possible to download the older version of the tipping buckets, as we did not have the appropriate cables). The sites visited include the following:

- Ganga La (three ground T-loggers and 3 tipping buckets)
- Langtang Valley (Jathang T-logger and TB; Lanshisha Karka TB; Morimoto Base Camp TB and T-logger)

4 Yala Glacier Stake Observations

On 5 June 2015, P. Wagnon made glacier stake observations. These are summarized in the table below.

Stake name	Emerging length (cm)	Snow depth (cm)	Comments
Stakes located on the usual trail going to AWS			
1_nov14	97	57	This is the lowest stake on the main trail, wet snow, approx density of 0.4/0.45 1 single piece emerging
2_nov14	76	60	10m below, there is an old broken stake wet snow, approx density of 0.4/0.45 1 single piece emerging
No name	160	60	20 m above 2_nov14 Very bent, almost horizontal above the slope 1 single piece emerging
No name	198	NA	Between 2_nov14 and 3_nov13 Very bent, almost horizontal above the slope 1 single piece emerging
Metallic (site 3)	337	103	This is the long metallic stake 40 m from AWS Less wet snow, approx density of 0.35/0.4
A_nov13 or3_nov13?	302	103	10 m above Metallic
No name	216	103	3 m from A_nov13
Stakes located 150 m W from the usual trail going to AWS			
1B_nov14	64	55	wet snow, approx density of 0.4/0.45 1 single piece emerging
1B_may14	73	55	3 m from 1B_nov14 wet snow, approx density of 0.4/0.45 1 single piece emerging
No name	127	NA	150 above 1B 2 pieces at least